

**STRUCTURAL AND HYPERFINE INTERACTION  
STUDIES IN TRANSITION METAL BORATES  
AND MALEATES BY MÖSSBAUER  
AND E.S.R. SPECTROSCOPY**

**A THESIS  
SUBMITTED FOR THE DEGREE OF  
DOCTOR OF PHILOSOPHY**

By  
**M. VITHAL**

SCHOOL OF CHEMISTRY  
**UNIVERSITY OF HYDERABAD**  
HYDERABAD - 500 134  
INDIA

**March, 1985**

Dedicated to:

My Parents  
and  
Teachers



## CONTENTS

STATEMENT	...	i
CERTIFICATE	...	ii
ACKNOWLEDGEMENTS	...	iii
PREFACE	...	vi
CHAPTER 1 -- INTRODUCTION		
1.1	The Mössbauer Effect	1
1.2	Basic features of Mössbauer spectroscopy	2
1.3	A review of work done on boroferrites	12
CHAPTER 2 -- EXPERIMENTAL METHODS AND METHODOLOGY		
2.1	Experimental Techniques	
2.1.1	Mössbauer measurements	24
2.1.2	Cryostat	27
2.1.3	Furnace	30
2.1.4	X-ray measurements	30
2.1.5	Optical spectra	30
2.2	Methodology used for the analysis of the spectra	
2.2.1	Temperature dependence of quadrupole splitting	31
2.2.2	Hyperfine fields in substituted systems	37
2.2.3	Mössbauer spectra in fluctuating environments	39
2.2.4	Field distribution in model independent method	47

CHAPTER 3 - MÖSSBAUER STUDIES OF  $\text{Fe}_{1-x}\text{M}_x\text{BO}_3$   
( $x=0, 0.1$ ;  $\text{M}=\text{Al}, \text{Ga}$  and  $\text{Cr}$ )

3.1	Introduction	54
3.2	Experimental	55
3.3	Results and Discussion	57
3.4	Conclusions	87

CHAPTER 4 - A MÖSSBAUER STUDY OF HYPERFINE  
INTERACTIONS IN THE BORO-FERRITE  
 $\text{Fe}_{3-x}\text{Ga}_x\text{BO}_6$  ( $x=0, 0.12$ )

4.1	Introduction	94
4.2	Experimental procedure and analysis of data	95
4.3	Results and discussion	97
4.3.1	Nature of spin transition	107
4.3.2	Temperature dependence of hyperfine field	113
4.3.3	The critical exponents	113
4.3.4	Mössbauer studies of the substituted compound $\text{Fe}_{2.88}\text{Ga}_{0.12}\text{BO}_6$	115
4.4	Conclusions	122

CHAPTER 5 - ORGANIC ACID COMPLEXES: A REVIEW

5.1	Introduction	128
5.2	Structural features	128
5.3	Mössbauer studies	135
5.4	Electron spin resonance studies	137

## CHAPTER 6 - EXPERIMENTAL METHODS AND METHODOLOGY

6.1	Experimental measurements	
6.1.1	Electron spin resonance measurements	149
6.1.2	Differential thermal analysis	150
6.1.3	Thermogravimetric measurements	150
6.2	Methodology	
6.2.1	Total Hamiltonian and the effective spin Hamiltonian	153
6.2.2	$\text{Cu}^{2+}$ ( $3d^9$ ) case	155
6.2.3	$\text{Mn}^{2+}$ ( $3d^5$ ) case	158
6.2.4	Analysis of angular variation data for the case of $\text{Cu}^{2+}$	164
6.2.5	Analysis of angular variation data for the case of $\text{Mn}^{2+}$	169

## CHAPTER 7 - PREPARATION AND MÖSSBAUER STUDIES OF FERROUS MALEATE TETRAHYDRATE ( $\text{Fe}(\text{C}_4\text{H}_3\text{O}_4)_2 \cdot 4\text{H}_2\text{O}$ )

7.1	Introduction	179
7.2	Experimental	180
7.3	Results and Discussion	
7.3.1	X-ray studies	181
7.3.2	Mössbauer studies	185
7.3.3	Optical spectra	192
7.3.4	Decomposition studies	195
7.4	Conclusions	198

CHAPTER 8 - ESR STUDY OF $\text{Cu}^{2+}$ DOPED IN ZINC MALEATE TETRAHYDRATE		
8.1	Introduction	203
8.2	Experimental	205
8.3	Results and Discussion	207
8.4	Conclusions	218
CHAPTER 9 - AN ESR STUDY OF $\text{Mn}^{2+}$ DOPED IN ZINC MALEATE TETRAHYDRATE		
9.1	Introduction	224
9.2	Experimental	225
9.3	Results and Discussion	228
9.4	Conclusions	238
APPENDIX I		242
APPENDIX II		247
APPENDIX III		252
APPENDIX IV		257
APPENDIX Va		262
APPENDIX Vb		266
VITAE		xiii

STATEMENT

I hereby declare that the matter embodied in this thesis is the result of investigations carried out by me in School of Chemistry, University of Hyderabad, Hyderabad, India, under the supervision of Dr. R. Jagannathan.

In keeping with the general practice of reporting scientific observations, due acknowledgement has been made wherever the work described is based on the findings of other investigators.


Hyderabad  
April 1985




M. VITHAL

CERTIFICATE

Certified that the work 'STRUCTURAL AND HYPERFINE INTERACTION STUDIES IN TRANSITION METAL BORATES AND MALEATES BY MÖSSBAUER AND ESR SPECTROSCOPY' has been carried out by Mr. M. Vithal under my supervision and the same has not been submitted elsewhere for a degree.

  
D e a n  
School of Chemistry

  
Dr. R. JAGANNATHAN  
Thesis Supervisor

ACKNOWLEDGEMENTS

I express my deep sense of gratitude and profound thanks to Dr. R. Jagannathan for suggesting interesting problems and guiding through their solutions. I gratefully recall many of the stimulating discussions I had with him and his words of encouragement during my travails.

Thanks are due to,

Prof. G. Mehta, Dean, School of Chemistry for his constant encouragement and the support extended ever since I joined this lively Department in August 1979.

Prof. D. Balasubramanian, former Dean, School of Chemistry for his encouragement.

Prof. A.K. Bhatnagar, Dean, School of Physics for helpful discussions and permission to avail of the CIL facilities even during odd hours.

Dr. M.V. Rajasekharan of School of Chemistry, Dr. S. Dattagupta and Dr. C.S. Sunandana of School of Physics for their discussions, suggestions and help in some of the experimental works, all the faculty members of School of Chemistry for their help and encouragement.

Dr. L. May, Catholic University of America, Washington D.C. for providing the Least Square Fit programme which is used in this thesis.

Prof. H.G. Devare, TIFR, Bombay for his help in recording the low temperature Mössbauer spectra presented in Chapter 7.

Dr. V. Ramanan, IISc, Bangalore for his help in sending computer output for refinement of cell parameters reported in Chapter 7.

Dr. B. Rama Rao for his help in recording various X-ray diffractograms by way of characterising the samples.

Dr. N. Ravi for his constant encouragement and inspiring suggestions.

Dr. Sajid Husain, Regional Research Laboratory, Hyderabad for his help and understanding in course of the last phase of this work.

Technical staff, Mr. W.A. Khan, Mr. C. Prabhakar Rao, Mr. Arun Kumar, Mrs. Vijayalaxmi, Mrs. Nirmala, Mr. C.S. Murthy and Mr. P. Anand for their help in collecting various spectral data and cooperation.




Mr. T.V. Gopal for typing the thesis carefully and Mr. Ananta Rao for drawing the figures.

Mr. Bhaskara Rao, Mr. Prasad and other staff members of School of Chemistry for their cooperation and help.

My friends Drs. K. Sambasiva Rao, Ch. Mohan Rao, P. Mitra and K.V. Subba Rao and Messers A. Ramachandraiah, T.G. Narendrababu, M. Vaman Rao, C. Linga Reddy, Y. Koteswara Rao, J.A.R.P. Sarma, C. Narayana, P. Venkataiah, P. Sivaram, V. Prabhakar, B. Bhanu Prasad and Miss Mary Elizabathe, Anita and Achuta Kumari for their lively company and timely help.

U.G.C. and C.S.I.R., New Delhi for the financial assistance from August 1980 to September 1983 and October 1983 to February 1985 respectively.

Finally I appreciate my wife Kausalya Devi for her cooperation and patience.

  
M. VITHAL

## PREFACE

The thesis presents structural and hyperfine interaction studies in iron borates or more appropriately borofer-rites and transition metal maleates by Mössbauer Spectroscopy and electron spin resonance (ESR) measurements. The interest in the boroferrites stems from the fact that boron in these materials can exist as planar  $\text{BO}_3^{3-}$  or  $\text{BO}_4^{5-}$  tetrahedra giving rise to unusual magnetic interactions leading to ferromagnetism, antiferromagnetism, spin-reorientation etc. Further the boroferrites exhibit unusual combination of physical properties of fundamental interest such as, for example, ferromagnetism-ferroelectricity in the boracites, magneto-optical properties in iron borate  $\text{FeBO}_3$  etc., which make these materials worthy of detailed investigations. It is only natural to choose Mössbauer Spectroscopy as the technique, for the method provides a powerful probe for investigations pertaining to iron-bearing magnetic materials. The first part of the thesis pertains to the Mössbauer studies of boroferrites and presented in four chapters which include in the first chapter (i) a very brief introduction to the effect and the hyperfine interactions followed by a review on the boroferrites pointing out the salient features of their structural aspects and physical properties and in

the second chapter (ii) details of experimental procedures employed and presentation of the mathematical steps involved in (a) the analysis of temperature dependence of quadrupole splitting for the  $3d^6$  case (b) the analysis of hyperfine fields in substituted systems by static method due to Coey and model independent approach due to Window and line shape analysis to account for relaxation effects.

Chapter 3 deals with the Mössbauer investigations of  $\text{FeBO}_3$  and the substituted borates  $\text{Fe}_{0.9}\text{M}_{0.1}\text{BO}_3$  ( $\text{M}=\text{Al}, \text{Ga}$  and  $\text{Cr}$ ). Ferric borate,  $\text{FeBO}_3$ , is of considerable interest as it is the only candidate in borates to be a transparent magnetic material with a lot of potential magneto-optic applications. The Mössbauer spectra of  $\text{FeBO}_3$  as well as its solid solutions close to  $T_c$  have been looked into with a view to understand the effect of substitution on relaxation process and/or superparamagnetism. The Curie temperatures of  $\text{FeBO}_3$ ,  $\text{Fe}_{0.9}\text{Ga}_{0.1}\text{BO}_3$ ,  $\text{Fe}_{0.9}\text{Al}_{0.1}\text{BO}_3$  and  $\text{Fe}_{0.9}\text{Cr}_{0.1}\text{BO}_3$  have been determined to be 352, 319, 317 and 335 K respectively. The reduced hyperfine field vs reduced temperature follows the Brillouin behaviour for  $S = 5/2$  for all the cases. It is shown that Coey's model is inadequate in simulating the Mössbauer spectra of solid solutions close to  $T_c$ . In the parent material viz.,  $\text{FeBO}_3$ ,

relaxation effects are found to be important only very close to  $T_c$  i.e.  $1^\circ$  below  $T_c$ . The model due to Blume and Tjon fairly reproduces the line profiles near  $T_c$  in this case. On the other hand, analyses of the Mössbauer spectra close to  $T_c$  of  $\text{Fe}_{0.9}\text{Al}_{0.1}\text{BO}_3$  and  $\text{Fe}_{0.9}\text{Ga}_{0.1}\text{BO}_3$  have been found to require the introduction of the additional order parameter  $\eta$ , proposed by van der Woude and Dekker. Estimates of activation energies for the spin-flip process have been found to be  $9.93 \times 10^{-13}$  and  $5.87 \times 10^{-13}$  erg/degree for  $\text{Fe}_{0.9}\text{Al}_{0.1}\text{BO}_3$  and  $\text{Fe}_{0.9}\text{Ga}_{0.1}\text{BO}_3$  respectively. In the solid solutions the relaxation effects dominate even  $15^\circ$  below  $T_c$ . These results have been interpreted to arise from dominant superparamagnetic relaxation effects due to the presence of clusters produced by substitution of magnetic by non-magnetic ions. Evidence for the cluster formation is also obtained by comparing the distribution in the hyperfine fields by the model independent approach due to Window in analysing the spectra. Simple relaxation models have been found to be inadequate in fully reproducing the experimental spectra close to  $T_c$  for  $\text{Fe}_{0.9}\text{Cr}_{0.1}\text{BO}_3$  and the possible reasons are presented in the light of existing literature.

Chapter 4 gives an account of Mössbauer investigations on  $\text{Fe}_3\text{BO}_6$  and 4%  $\text{Ga}^{3+}$  substituted  $\text{Fe}_3\text{BO}_6$  carried out keeping

particularly in mind the spin-reorientation phenomena exhibited by the parent material at 418 K. Mössbauer measurements of hyperfine parameters close to spin-reorientation temperature ( $T_{SR}$ ) have been shown to display no hysteresis effects in spite of the reorientation following a first order phase transformation. However, as is characteristic of first order change, significant change in structure is indicated by the changes in the quadrupole interactions. 4% substitution of  $Fe^{3+}$  by  $Ga^{3+}$  brings down  $T_{SR}$  from 418 to 403 K. The temperature dependence of hyperfine field for the 8d site follows closely the Brillouin function for  $S = 5/2$  both for the parent as well as the substituted compound. The deviation of the 4c site from the Brillouin curve has been explained by including the biquadratic exchange interaction giving rise to  $j/J = 0.015$ . It is found that  $Ga^{3+}$  has no site preference. Unlike in the case of experimental spectra close to  $T_c$  it is found that the static model due to Coey can be employed for simulating the experimental spectra at temperatures far away from  $T_c$ . An exchange constant  $J \sim 10 \text{ cm}^{-1}$  has been obtained on the basis of this model.

The second part of the thesis presents structural and hyperfine interaction studies in acid complexes formed

between maleic acid and transition metal ions. The interest in these systems stems from the observations that (i) organic acids give rise to a variety of structures with transition metal ions enabling a comparative study of complexes of same carboxylic acid with different metal ions and of different carboxylic acids with the same metal ion, (ii) the work has scope for a comparative study of transition metal ions with the rare-earths, (iii) in many instances single crystals can be prepared leading to studies with unambiguous conclusions, (iv) furthermore the decomposition of these complexes into metallic oxides provide interest both from the preparatory point of view of the oxides/ ferrites and also scope for solid state studies regarding the bearing of structures on the differences in their decomposition behaviour.

This part of the thesis is presented in five chapters. The first chapter of this part (Chapter 5) provides a comprehensive review of the literature on the carboxylic acid complexes focussing attention on these features of interest to facilitate discussion of the results presented. This is followed by a chapter on the methodology relevant to the analysis of ESR spectra of single crystal studies employing  $\text{Cu}^{2+}$  and  $\text{Mn}^{2+}$  as ESR probes giving an account of

the desired expressions for obtaining chemical information and analysing forbidden ESR transitions, which are of particular interest in  $\text{Mn}^{2+}$  systems.

The next chapter deals with the preparation and temperature dependent Mössbauer measurements of iron(II) maleate tetrahydrate. From the analysis of the temperature dependence of quadrupole splitting and optical spectral data, the crystal field parameters viz., the 10 Dq, tetragonal field, rhombic field and the splitting of the  $e_g$  levels have been derived. Results of powder X-ray diffractograms establishing the isomorphism of ferrous maleate tetrahydrate with manganese maleate tetrahydrate have been presented. The results of differential thermal analysis and thermogravimetric analysis on ferrous maleate tetrahydrate and the independent decomposition studies are submitted.

Chapter 8 presents the results of a single crystal ESR studies of  $\text{Cu}^{2+}$  doped in zinc maleate tetrahydrate. Copper maleate tetrahydrate and zinc maleate tetrahydrate are not isomorphous. From the single crystal ESR measurements it is concluded that  $\text{Cu}^{2+}$  in zinc maleate tetrahydrate occupies a substitutional position with a micro-symmetry dictated by the parent lattice. The ground state of  $\text{Cu}^{2+}$  in zinc maleate tetrahydrate is derived to be  $0.724|3z^2-r^2\rangle + 0.173|x^2-y^2\rangle$ .

In the last chapter the single crystal ESR results of  $\text{Mn}^{2+}$  doped in zinc maleate tetrahydrate are presented. The low symmetry of the  $\text{Mn}^{2+}$  ion is found to give rise to a number of forbidden transitions in addition to the allowed five sextets of 30 transitions. Further the orientation along the principal Z-axis also is achieved when a neat and simple 30 line spectrum eliminating the appearance of any forbidden transitions is obtained which is used for detailed analysis of the spectra. The line positions were analysed to obtain the hyperfine parameters viz., A, g, D, E and 'a' which are the hyperfine splitting constant, the g-factor, axial component of zero field splitting, rhombic component of zero field splitting and cubic field term respectively. The sign of D is found to be positive indicating that  $\text{Mn}^{2+}$  like  $\text{Cu}^{2+}$  goes into substitutional site and occupies axially compressed octahedron. An analysis of the forbidden transitions also is presented which leads to  $Q' = 1.69$  and  $Q'' = 0.304$  for the values of the axial and rhombic components respectively of the quadrupole coupling constant.



PART - I

## CHAPTER 1

### INTRODUCTION

#### 1.1 The Mössbauer Effect

Rudolph L. Mössbauer discovered in 1957 the phenomenon of recoilfree nuclear resonance fluorescence [1]. This observation, referred to as the Mössbauer effect, has gained fundamental importance and shown unique potentiality ever since Kistner and Sunyar established the role of hyperfine interactions underlying the effect [2]. The hyperfine interactions appear as a shift in the centre of gravity of the spectrum, splitting of the lines and line broadening effects. The interactions leading to shifting and splitting of the lines have resulted in the application of the technique particularly to problems of chemical and structural interest. The applications have also been extended from static to dynamic effects, rendered possible due to sharply defined energy of the gamma radiation leading to changes in the profiles due to time dependent

effects. In this chapter a brief introduction to the hyperfine interactions in Mössbauer spectroscopy is given. Detailed discussions of fundamental aspects and applications are available in literature [3-7].

## 1.2. Basic features of Mössbauer spectroscopy

### 1.2.1. The Technique

In a classical model, a  $\gamma$ -ray emitter in the excited state may be treated as a damped oscillator emitting electromagnetic radiation. The energy distribution of the emitted radiation is given by

$$I(\omega) \propto \left| \int_0^{\infty} E(t) e^{-i\omega t} dt \right|^2$$

$$I(\omega) \propto \frac{1}{(E - E_\gamma)^2 + (\Gamma_{\text{nat}}/2)^2} \quad \dots (1.1)$$

where  $E(t)$  is the electric field of the  $\gamma$ -radiation,  $E = \hbar\omega$ ,  $E_\gamma$  is the nuclear transition energy,  $\hbar$  is the Planck's constant and the natural width  $\Gamma_{\text{nat}} = \frac{\hbar}{\tau_n}$  where  $\tau_n$  is the mean lifetime of the excited nucleus. Eq.(1.1) represents a lorentzian line centered at  $E_\gamma$  with full-width at half-maximum (FWHM) equal to  $\Gamma_{\text{nat}}$ .

A distinct feature in Mössbauer spectroscopy is the use of Doppler effect; the source is given a velocity  $V$  with respect to the absorber and the energy of the emitted radiation  $E_\gamma$  as seen by the absorber is given by

$$E(V) = E_\gamma \left(1 + \frac{V}{C}\right) \quad \dots (1.2)$$

where  $V$  and  $C$  are the velocities of source and light respectively. Thus the intensity of the unabsorbed  $\gamma$ -radiation vs the Doppler velocity provides the spectral profile in a transmission experiment. Energy differences are expressed in terms of the Doppler velocity. The properties of interest for the case of  $^{57}\text{Fe}$  are given in Table 1.1.

### 1.2.2. Hyperfine Interactions

#### i) Isomer Shift

The electrostatic interaction between the Mössbauer nucleus and the surrounding electric charges give rise to isomer shift and quadrupole splitting effects of the nuclear levels. The electronic charge density at the nucleus  $-e|\psi(0)|^2$  gives rise to energy shifts of the nuclear levels which depend on the nuclear radius. As the size of the nucleus changes

Table 1.1 Properties of the  $^{57}\text{Fe}$  nucleus [12].

---

natural isotopic abundance	2.14 %
Gamma-ray energy	14.413 keV
natural line width ( $\Gamma_0$ )	0.194 mm/Sec
internal conversion coefficient ( $\alpha$ )	8.2
maximum resonance cross section ( $\sigma_0$ )	$3.45 \times 10^{-19} \text{ cm}^2$
nuclear quadrupole moment ( $Q^e$ )	$0.21 \times 10^{-24} \text{ m}^2$
magnetic moment ( $\mu_g$ )	+0.0903 nm
( $\mu_e$ )	-0.1547 nm.
half-life time of parent $^{57}\text{Co}$ nucleus ( $t_{1/2}$ )	270 days.
energy conversion factor	$1 \text{ mm/sec} = 7.7019 \times 10^{-27} \text{ J}$ $= 4.8077 \times 10^{-8} \text{ eV.}$

---

during decay, the effect results in a shift in the nuclear transition energy given by

$$\delta E = \frac{2\pi}{3} Ze^2 |\psi(0)|^2 (\langle r_e^2 \rangle - \langle r_g^2 \rangle) \quad \dots (1.3)$$

where  $Z$  is the atomic number of the Mössbauer atom and  $\langle r_e \rangle$  and  $\langle r_g \rangle$  are the mean square radii of the nucleus in the excited and ground states respectively, in a point charge model [8]. If the Mössbauer atoms in the source and absorber are different, eq. 1.3. may be rewritten as

$$\delta = \frac{2\pi}{3} Ze^2 (|\psi_a(0)|^2 - |\psi_s(0)|^2) (\langle r_e^2 \rangle - \langle r_g^2 \rangle) \quad \dots (1.4)$$

where the subscripts  $a$  and  $s$  represent absorber and source respectively.  $\delta$ , the isomer shift is proportional to the difference between the electronic charge densities at the source and absorber nuclei. Isomer shift has not been completely characterised although it is known to be influenced by (a) the effects due to overlaps of the orbitals in bonding [9] (b) covalency effects due to partial transfer of electrons from the ligand to the Mössbauer atom or vice versa (c) potential distortion and (d) relativistic effects etc. [10].

## ii) Quadrupole interaction

Any nucleus with a quantum number  $I > 1/2$  has a non-spherical charge distribution, which when expanded in a series of multipoles contains a quadrupole term. The electrostatic interaction energy  $E_Q$ , between the quadrupole moment and the electric field gradient tensor, may be written as [5]

$$E_Q = 1/6 \sum_i \sum_j Q_{ij} V_{ij} \quad \dots (1.5)$$

where  $Q_{ij}$  and  $V_{ij}$  are the components of the Quadrupole moment tensor and e.f.g tensor respectively given by

$$Q_{ij} = \int_{V_N} (3x_i x_j - \delta_{ij} r^2) \rho(r) d\tau$$

$$\text{and } V_{ij} = \frac{\partial^2 V}{\partial x_i \partial x_j}.$$

Here  $V_N$  is the volume of the nucleus and  $\rho(r)$  is its charge density and a value of  $1/6$  gets associated in the series expansion. The energy levels of  $E_Q$  can be calculated as the expectation values of the operator  $H_Q$ , that corresponds with  $E_Q$ , working on the wave function of the whole system. In the principal axes system the interaction energy can be written as

$$E_Q = 1/6 \sum_i V_{ii} Q_{ii} \quad \dots (1.6)$$

The corresponding Hamiltonian assumes the form,

$$H_Q = \frac{eQV_{zz}}{4I(2I-1)} [3I_z^2 - I(I+1) + \frac{\eta}{2} (I_+^2 + I_-^2)] \quad \dots (1.7)$$

where  $Q$  corresponds to  $Q_{zz}$ ,  $\eta = \frac{V_{xx} - V_{yy}}{V_{zz}}$  and  $I_+$  and  $I_-$  are the shift operators. For the  $^{57}\text{Fe}$  case the splitting due to the quadrupole interaction reduces to

$$Q.S = \frac{1}{2}eV_{zz}Q\sqrt{1 + \frac{\eta^2}{3}} \quad \dots (1.8)$$

where  $V_{zz}$  is the expectation value of  $V_{zz}$ . The details of evaluation of  $V_{zz}$  for the  $3d^6(\text{Fe}^{2+})$  configuration, relevant to our own studies on iron maleate, are given in the next chapter.

The experimental evaluation of quadrupole splitting in the absence of magnetic field is straight forward. The evaluation in the case when a magnetic field is present and the influence of quadrupole interaction appears through shifts in the line positions in the hyperfine split spectra are briefly discussed in the next chapter.



### iii) Magnetic hyperfine interactions

The Zeeman interaction of the nuclear magnetic dipole moment with a magnetic field  $H_n$  in the Z-direction at the nucleus completely lifts the degeneracy of the nuclear states. The shifts in the energies of the nuclear substates are given by

$$E_m = -g_n \mu_N H_n m \quad \dots (1.9)$$

where  $g_n$  is the gyromagnetic ratio,  $\mu_N$  is the nuclear magneton and  $m$  is an eigen-value of the nuclear spin operator  $I_z$ . The splitting of the levels results, for instance in  $^{57}\text{Fe}$ , six allowed transitions as the excited state with  $I_e = 3/2$  and ground state with  $I_g = 1/2$  split into 4 and 2 non-degenerate levels respectively. The relaxing of selection rules due to mixing of the levels in the presence of combined magnetic dipole and electric quadrupole interactions are discussed in literature [11]. In such a case, the Hamiltonian is given by

$$H = H_0 + H_M + H_Q \quad \dots (1.10)$$

where  $H_0$  represents the energy of the nuclear state in the absence of the last two terms.  $H_M$  and  $H_Q$  represent the magnetic dipolar and electric quadrupolar terms respectively. When both nuclear quadrupole and Zeeman interactions are present,

the Hamiltonian describing the hyperfine interaction is given by

$$H = -g_n \mu_n \vec{H}_n \cdot \vec{I} + \frac{eQ_n V_{zz}}{4I(2I-1)} [3\hat{I}_z^2 - \hat{I}^2 + \eta(I_+^2 + I_-^2)/2] \dots (1.11)$$

### 1.2.3. Relaxation Effects in Mössbauer Spectroscopy

Figure 1.1 gives the appropriate frequency ranges of the relaxation rates for various **spin** fluctuation processes and the techniques used for their study. The effect of electron spin on Mössbauer spectra is implied in the magnetic interaction  $H_M$  in eq. 1.10. In the spin-Hamiltonian formalism  $H_M$  may be written as

$$H_M = \vec{I} \cdot \vec{A} \cdot \vec{S}$$

where  $A$  is the hyperfine coupling tensor and  $S$ , the effective electron spin. The effective electron spin of electrons in an electronic state can be replaced by the expectation value in the state  $\langle S \rangle$ . When transition between different electronic states occur, the orientation of the electron spin changes in time and the hyperfine interaction becomes time dependent. The simplest case is to visualise the relaxation process occurring between two levels with opposed electron spin quantum numbers, inducing a reorientation of the electron spin and the

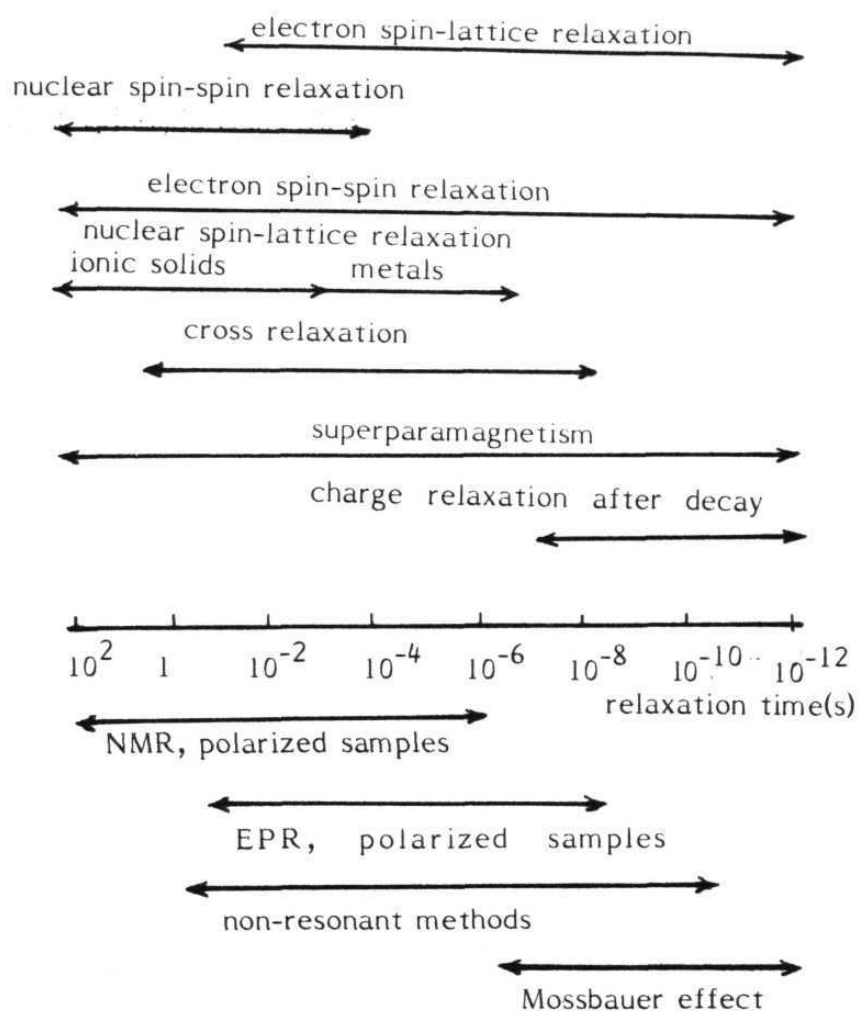


**Fig.1.1 Typical ranges of relaxation times of various relaxation processes and the appropriate experimental methods.**

hyperfine field. This is called the spin flip process. The shape of the Mössbauer spectra in the presence of relaxation is determined by the frequency of the spin flips,  $\omega_{SF}$ , the Larmor precession frequency,  $\omega_L$ , and the nuclear life-time of the excited state,  $\tau_N$ . Simple or complex spectra appear depending upon the relative values of  $\omega_{SF}$ ,  $\omega_L$  and  $1/\tau_N$ . Among the various relaxation processes electron spin relaxation and superparamagnetic fluctuation influence most the Mössbauer spectral line shape. The two common forms of electron spin relaxation are the spin-lattice and spin-spin relaxation. Information about the relaxation process is generally obtained by studying relaxation times as a function of temperature, magnetic field or concentration. A large number of theoretical papers dealing with the influence of time dependent hyperfine interactions on the Mössbauer line shape may be found in literature [13]. The most general theories are based on stochastic or perturbation models. On the basis of a stochastic model Blume arrives at general line-shape expressions employing a formalism in which super operators (Lioville operators) are used. In a closely related treatment Dekker and van der Woude and Dekker have developed line shape expressions who have also taken into account the possible difference in the probabilities of finding the electron between two given states in magnetic materials. We have used the line shape

expressions developed by these authors to analyse the spectra of substituted borates. A brief outline of their models and final line shape expressions obtained are presented in the next chapter.

### 1.3. A review of work done on boroferrites

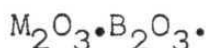
Our own Mössbauer studies pertain to hyperfine interactions in some of the boroferrites. It would be appropriate at this stage, a brief survey of the boroferrites, bringing out the salient features of their structural aspects and physical properties pointing out why we embarked on a study of these materials.

Preparation, characterization and detailed investigations of structure and physical properties of the anhydrous transition metal borates are scattered in literature. But the available studies show very many interesting and unusual properties worthy of detailed investigations in these materials. One of the attractive features in the borates is the possibility to study materials exhibiting coexistence of magneto-optic-electric properties. The simplest iron borate for example  $\text{FeBO}_3$  is a magneto-optic material and the naturally occurring

mineral boracite shows the unusual combination of ferromagnetism and ferroelectricity [14,15]. That boron can exist as planar  $\text{BO}_3^{3-}$  or  $\text{BO}_4^{5-}$  tetrahedra provides scope for exhibition of strongly anisotropic magnetic interactions by the so called boroferrites. One of the most fascinating fields of current interest happens to be the study of amorphous materials. Borates present a situation where attempts can be made to prepare glassy and crystalline materials with closely related compositions rendering interesting comparisons of physical properties in related ordered and amorphous materials. An extension of the studies from the transition metal to the rare earths provide further scope as many of them show lasing properties. With these points of view in mind a beginning is made on the study of simple and substituted boroferrites, as these materials are suitable for detailed investigations by Mössbauer spectroscopy. We scan below the literature pertaining to boroferrites and related materials bringing out features of interest.

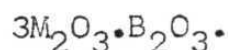
Most of the anhydrous transition metal borates may be comprehended to occur as  $x.\text{MO} \cdot y.\text{M}_2\text{O}_3 \cdot z.\text{B}_2\text{O}_3$ . Interestingly the ratio of the metal oxides to the  $\text{B}_2\text{O}_3$  exhibit a wide range, as illustrated by the examples given below. An extensive study of the infrared spectra of the crystalline inorganic

borates was first reported by Weir and Schroeder [16]. Their studies show that the coordination of boron deciding whether it exists as planar  $\text{BO}_3^{3-}$  or tetrahedral  $\text{BO}_4^{5-}$  can be reliably fixed from the infrared spectra. The crystal structure and related works on the anhydrous transition metal borates of interest are discussed below.

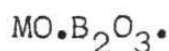


One of the early candidates to be prepared in this series is  $\text{Fe}_2\text{O}_3 \cdot \text{B}_2\text{O}_3$  or more simply  $\text{FeBO}_3$ . Bernal synthesised this monoborate and showed it to have the calcite structure [17]. Kurtzig et al established this material to be a green, room temperature ferromagnet [14]. Muller established a simpler synthetic technique for preparing this monoborate and the isomorphous  $\text{CrBO}_3$  and  $\text{InBO}_3$  and their solid solutions [18]. He also reported detailed susceptibility studies of these borates. An early account of Mössbauer studies on the pure iron borate was reported by Eibschutz and Lines [19].

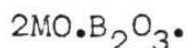
It is interesting to note that in this system partial substitution of  $\text{Fe}_2\text{O}_3$  by 0.25  $\text{La}_2\text{O}_3$  and 0.5  $\text{La}_2\text{O}_3$  ( $\text{La}=\text{Y}, \text{Gd}, \text{Sm}, \text{Dy}$ ) leads to totally different crystal structures from the parent compound. The former gives rise to huntite and the latter to the dolomite structure [20,21].



$3Fe_2O_3 \cdot B_2O_3$  happens to be the only known member of this composition. White et al determined its crystal structure [22]. Unlike in  $FeBO_3$ , boron has a tetrahedral configuration in this case and the material is magnetic. The phase transformation in the magnetic state has been studied by susceptibility and Mössbauer techniques [23-25]. These reports however do not agree on the order of the phase transformation.



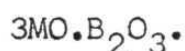
Monoborates of this class, referred to as the metaborates, are well characterised where  $M = Zn^{2+}, Cu^{2+}$ . In both cases boron has tetrahedral symmetry. However  $Zn^{2+}$  occurs in one type of site with tetrahedral symmetry whereas  $Cu^{2+}$  occurs in two types of sites, one of which is octahedral and the other square planar [26,27].



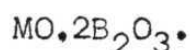
Monoborates of this class, referred to as the pyroborates commonly occur with divalent ions such as  $Mg^{2+}, Fe^{2+}, Co^{2+}, Ni^{2+}$ , and  $Mn^{2+}$ . Boron in these isomorphous borates have



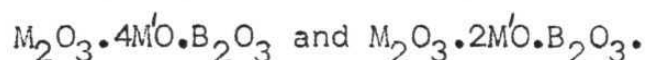
planar geometry. The metal ions are situated in more than one type of sites with octahedral symmetry [28].



Monoborates of this type referred to as the orthoborates also occur with divalent ions of  $\text{Co}^{2+}$ ,  $\text{Mg}^{2+}$  and  $\text{Mn}^{2+}$ . These are highly coloured transparent materials but their optical properties in the visible have not been characterised. These orthoborates are isomorphous unlike their zinc analogue. In these cases  $\text{M}^{2+}$  occupies two inequivalent octahedral sites in orthorhombic unit cell [29-31]. In the case of zinc compound,  $\text{Zn}^{2+}$  occupies three inequivalent sites with tetrahedral symmetry in a monoclinic unit cell [32]. Mitchell has characterised the infrared spectra of some of these orthoborates in detail [33].



Diborates of this class contain  $[\text{B}_4\text{O}_7]^{2-}$  anions with the boron atoms occurring both in tetrahedral as well as in planar geometry, and differ in this from all other systems discussed in literature. The metal ions in these cases occupy distorted tetrahedral symmetry [34].



Borates of these general formulae occur naturally with  $M = Mn^{3+}$ ,  $Fe^{3+}$  and  $M' = Mg^{2+}$ ,  $Fe^{2+}$ ,  $Mn^{2+}$ . The crystal structures of these minerals viz., ludwigite and pinakiolite were first characterised in detail by Takeuchi et al and Bertaut [35,36]. Compounds with analogous structures containing other transition metal ions,  $M' = Co^{2+}$ ,  $Cu^{2+}$  and  $Ni^{2+}$  have also been synthesised [36]. Relatively recently the magnetic properties of ludwigite have been looked into by Apostolov et al and Weidenmann and Burlet [37,38]. It is shown that partial substitution of  $Mg^{2+}$  by transition metal ions leads to the observation of more than one antiferromagnetic transition, the one taking place at the higher temperature arising due to one dimensional M-M interaction and the other at the lower temperature resulting due to three dimensional M-M interaction [37]. The latter authors have suggested spin-glass behaviour in these systems on the basis of susceptibility, Mössbauer, neutron diffraction and specific heat data. Although the absence of three dimensional ordering has been claimed by Apostolov et al on the basis of Mössbauer data, no details are presented [37]. Abe et al studied more extensively by susceptibility and Mössbauer spectral measurements the borates of the formula  $Fe_2O_3 \cdot B_2O_3 \cdot 4NiO$  and  $Fe_2O_3 \cdot B_2O_3 \cdot 2NiO$  [39].

These authors observed that the bulk susceptibility measurements in these cases gave significantly lower  $T_N$  values than the values derived from Mössbauer measurements and attributed to relaxation phenomena in these low dimensional magnetic materials [39]. Weidenmann and Burlet suggested that inversion of  $\text{Fe}^{3+}$  and  $\text{Mg}^{2+}$  in these structures lead to spin-glass behaviour. Abe et al found no evidence for any significant inversion from their Mössbauer study [39].

References:

1. R.L. Mössbauer, Z. Physik. 151, 124 (1958).
2. O.C. Kistner and A.W. Sunyar, Phys. Rev. Lett. 4, 229 (1960).
3. Advances in Mössbauer Spectroscopy, edited by B.V. Thosar, P.K. Iyengar, J.K. Srivastava and S.C. Bhargava (Elsevier, New York, 1983).
4. T.C. Gibb, Principles of Mössbauer Spectroscopy (Chapman and Hall, London, 1976).
5. G.K. Wertheim, Mössbauer Effect: Principles and Applications (Academic Press, New York, 1964).
6. N.N. Greenwood and T.C. Gibb, Mössbauer Spectroscopy (Chapman and Hall, London, 1971).
7. V.I. Goldanskii and R.H. Herber, Chemical Applications of Mössbauer Spectroscopy (Academic Press, New York, 1963).
8. G. Breit, Rev. Mod. Phys. 30, 507 (1958).
9. R. Jagannathan and K.N. Srivastava, Hyp. Inter. 7, 377 (1979).
10. Mössbauer Isomer Shifts, Edited by G.K. Shenoy and F.E. Wagner ( North Holland, 1978).

11. J. van Donger Torman, R. Jagannathan and J.M. Trooster, Hyp. Inter. 1, 135 (1975).
12. J.G. Stevens and V.E. Stevens, Mössbauer Effect Data Index, Covering the 1976 literature (Plenum Press, New York, 1978).
13. S. Morup, Paramagnetic and Superparamagnetic Relaxation Phenomena Studied by Mössbauer Spectroscopy, D.Sc. thesis, Technical University, Denmark, 1981, and references therein.
14. A.J. Kurtzig, R. Wolfe, R.C. LeCraw and J.W. Nielsen. Appl. Phys. Lett. 14, 350 (1969).
15. H. Schmid, in Magnetoelectric Interaction Phenomena in Crystals, edited by A.J. Freeman and H. Schmid (Gordon and Breach, New York, 1975), p.121.
16. C.E. Weir and R.A. Schroeder, J. Res. Nat. Bur. Std-A. 68A, 465 (1964).
17. I. Bernal, C.W. Struck and J.G. White, Acta Crystallogr. 16, 849 (1963).
18. O. Muller, M.P.O'Horo and J.F.O'Neill, J. Solid State Chem. 23, 115 (1978).
19. M. Eibschutz and M.E. Lines, Phys. Rev. 7, 4907 (1973).

20. T. Takahashi, O. Yamada and K. Ametani, Mater. Res. Bull. 10, 153 (1975).
21. O. Muller and J.F.O'Neill, in The Rare Earth in Modern Science and Technology, edited by G.J. McCarthy and J.J. Rhyne (Plenum Press, New York, 1978), p.173.
22. J.G. White, A. Miller and R.E. Nielsen, Acta Crystallogr. 19, 1060 (1965).
23. R. Wolfe, R.D. Pierce, M. Eibschutz and J.W. Nielsen, Solid State Commun. 7, 949 (1969).
24. A.S. Kamzin and V.A. Bokov, Sov. Phys. Solid State 19, 1247 (1977).
25. C. Voigt, Phys. Lett. 53A, 223 (1975).
26. P. Smith, S. Garcia-Blanco and L. Rivoir, Zeit. Kristallogr. 119, 375 (1964).
27. M. Martinez - Ripoll, S. Martinez - Carrera and S. Garcia-Blanco, Acta Crystallogr. B27, 677 (1971).
28. S. Block, G. Burley, A. Perloff and D. Mason. Jr, J. Res. Nat. Bur. Std. 62, 95 (1959).
29. S.V. Berger, Acta Chem. Scand. 3, 660 (1949).
30. R.E. Newnham, R.P. Santoro, P.F. Seal and G.R. Stallings, Phys. Status Solidi 16, K17 (1966).

31. J. Pardo, M. Martinez - Ripoll and S. Garcia - Blanco, Acta Crystallogr. B30, 37 (1974).
32. S. Garcia - Blanco and J. Fayos, Zeit. Kristallogr. 127, 145 (1968).
33. A. Mitchell, Trans. Faraday Soc. 62, 530 (1966).
34. M. Martinez - Ripoll, S. Martinez - Carrera and S. Garcia - Blanco, Acta Crystallogr. B27, 672 (1971).
35. Y. Takeuchi, T. Watanabe and T. Ito, Acta Crystallogr. 3, 98 (1950).
36. E.F. Bertaut, Acta Crystallogr. 3, 473 (1950).
37. A.V. Apostolov, M.T. Mihov and P.T. Tcholakov, J. Mag. Mag. Mater. 15-18, 1309 (1980).
38. A. Weidenmann and P. Burlet, J. de Phys. Colloque C6, supplement no. 8, pC6-720 (1978).
39. M. Abe, K. Kaneta, M. Gomi and S. Nomura, Mater. Res. Bull. 14, 519 (1979).

## CHAPTER 2

### EXPERIMENTAL METHODS AND METHODOLOGY

#### Abstract

The experimental details pertaining to the Mössbauer spectrometer used and variable temperature measurements made from 77 to 900 K and powder X-ray diffractogram measurements are presented. Some of the details of (a) calculation of temperature dependence of quadrupole splitting for  $3d^6$  case in different crystal fields (b) the line shape expressions based on the relaxation models due to (i) Blume and Tjon and (ii) van der Woude and Dekker, (c) the static model of Coey and (d) the model independent approach due to Window in the analysis of hyperfine field distribution are presented.



## 2.1. Experimental Techniques

### 2.1.1. Mössbauer measurements

In recording the Mössbauer spectra the source is moved with respect to the absorber or vice versa to achieve the Doppler shift and the intensity transmitted through the absorber is measured as a function of velocity. The spectra reported here were measured using a constant acceleration spectrometer (Elscint), a block diagram of which is given in Figure 2.1. The spectrometer consists of (i) the drive assembly consisting of two coupled loudspeakers (model MVT-3) one having the driving coil and the other having the sensing coil giving rise to a feed-back signal, wound around the same rod freely suspended with two phosphor-bronze leafsprings. The velocity of the rod is proportional to a reference voltage delivered by the driving unit (MD-3). A function generator (MFG-3) produces the desired wave-forms and the necessary timing signals, (ii) a multi-channel analyser (Promeda) which receives the timing signals for opening the 512 channels of the MCA periodically and the desired  $\gamma$ -ray pulses. In this system the motion of the source is independent of the MCA and during data accumulation synchronisation between velocity and channel number is established over every period of the drive signal, (iii) the detection system consisting of a 'Cento' xenon proportional

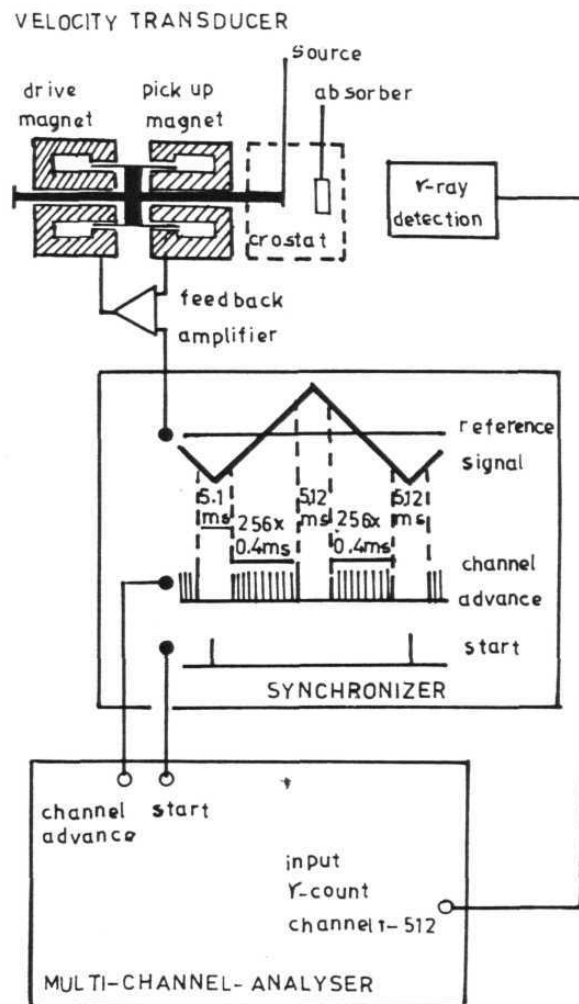


Fig.2.1 Schematic diagram of the Mössbauer spectrometer.

counter. The amplitude of the pulses produced in the counter is proportional to the energy of the photons. The pulses are amplified and fed into a single channel analyser (SCA-N-3) which selects the 14.4 keV peak for the  $^{57}\text{Co}$  isotope and transforms into standard pulses which are received and counted by the MCA (Promeda). The recording of the spectra could be carried out without interference due to external disturbances. A hard copy of the data was obtained as a print out using a Teletype typewriter.

A source of  $^{57}\text{Co}$  in rhodium matrix with a strength of 25 mCi is employed. The absorbers were prepared by sandwiching thoroughly ground powder material into a perspex absorber holder of 2 cm dia. For high temperature measurements, copper ring holders with thin aluminium windows were employed. In all the absorbers the iron content was kept at  $\sim 10 \text{ mg/cm}^2$ .

The spectrometer was standardised recording spectra of samples of  $\alpha\text{-Fe}_2\text{O}_3$ , iron-foil,  $\text{K}_4\text{Fe}(\text{CN})_6$  and sodium nitroprusside dihydrate and comparing the peak positions with values reported in literature [1,2]. A standard spectrum of the iron foil is recorded for each measurement. The per-channel velocity is obtained by taking the splittings of the outer most lines in terms of mm/sec and equating with peak positions

obtained in terms of channel numbers for the measured standard spectra using a least square fit programme [3]. The errors quoted in line positions correspond to the standard deviation obtained by an error analysis, details of which are discussed in literature [4]. Some of the standard spectra are shown in Figure 2.2.

#### 2.1.2. Cryostat

A simple cryostat constructed in our laboratory for Mössbauer measurements at liquid-nitrogen temperature ( $-196^{\circ}\text{C}$ ) is shown in Figure 2.3. The copper vessel of 10 cm diameter and 21 cm height is surrounded by a thermocole and inserted into a wooden box. A copper block of 5 x 4 x 2 cm is welded to the bottom of the copper vessel through a cold finger (1 cm dia and 3.5 cm long). In this block a provision is made for the absorber which could be firmly fixed by a screwable cylindrical ring. The thermocouple junction is kept in a thin hole inside the copper block close to the absorber. The thermocouple reading was measured with a digital multimeter (Keithley 174). The temperature remained stable to  $\pm 0.5^{\circ}\text{C}$  during the measurements. The liquid nitrogen consumption was about 0.5 litre per hour.

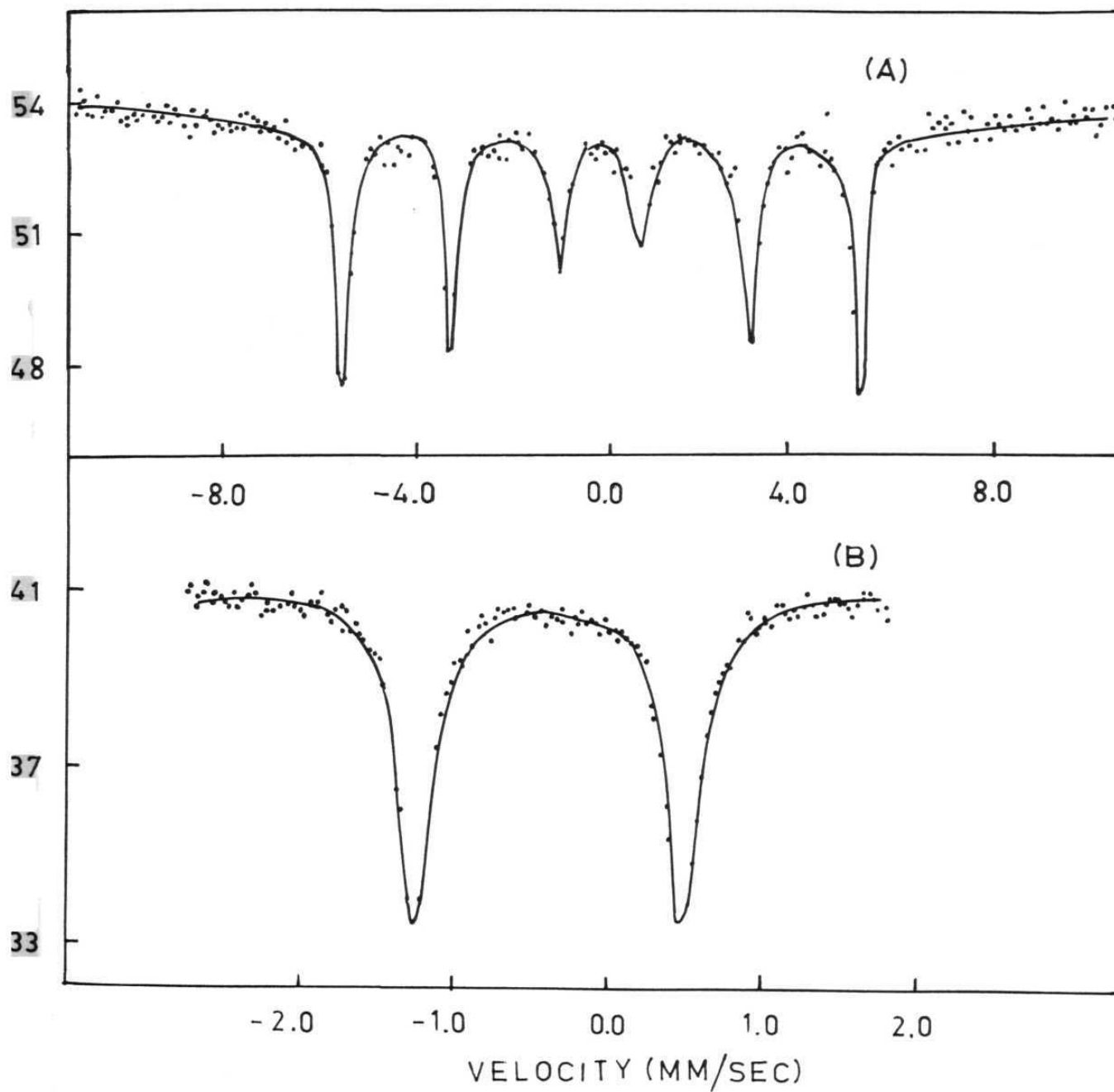


Fig.2.2 Mössbauer spectra of (a) Iron foil and (b) sodium nitro prusside dihydrate.

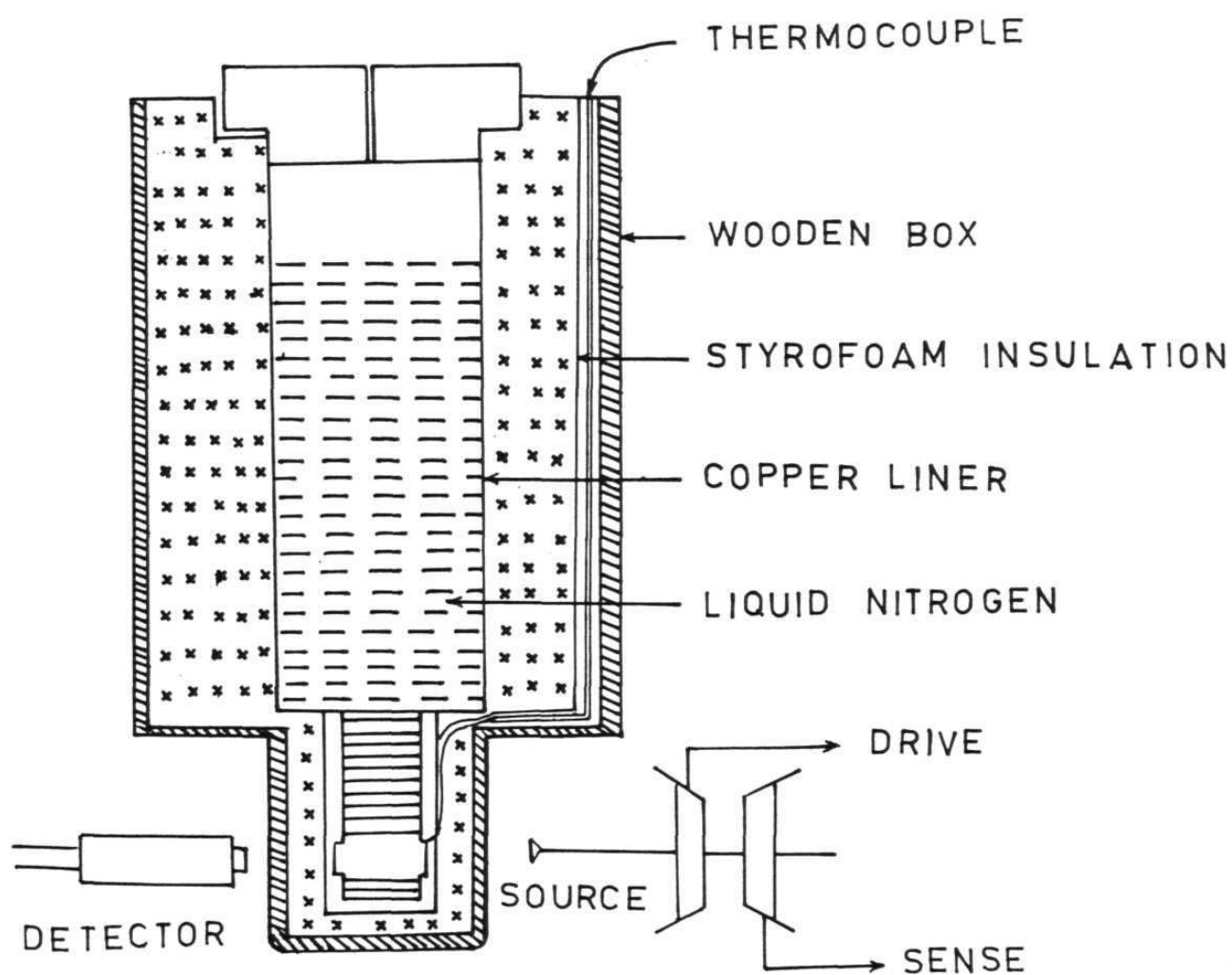


Fig.2.3 A cryostat assembly for low temperature Mössbauer measurements

### 2.1.3. Furnace

For measurements at temperatures above 300 K a stainless Ricor vacuum furnace (MF-2A) is used. It has two thin windows for allowing the 14.4 keV  $\gamma$ -rays without attenuation. Thermal shielding is obtained with thin aluminised keptone. The sample was heated in vacuum with a low resistance heating element. A chromel-alumel thermocouple is used for monitoring the temperature. The temperature is controlled manually ( $\pm 0.5^\circ$ ) by adjusting the input voltage to the heating element.

### 2.1.4. X-ray measurements.

The powder X-ray diffraction patterns were obtained using the Philips X-ray diffraction unit consisting of PW 1010 generator, PW 1055/25 wide angle goniometer and PW 1051 diffractometer. A Geiger-Müller counter and nickel-filtered Cu-K $\alpha$  radiation were employed.

### 2.1.5. Optical spectra

The photoacoustic spectra (PAS) were recorded on a Princeton Applied Research model 6001 instrument. The spectra are corrected for black absorption and normalized using carbon

black as reference. The normalization corrects the observed spectrum for the power variation in the source over the spectral region of interest.

Optical spectra for solutions were recorded in a Cary-17 model spectrometer employing a quartz cell of one centimeter path length.

## 2.2. Methodology used for the analysis of spectra.

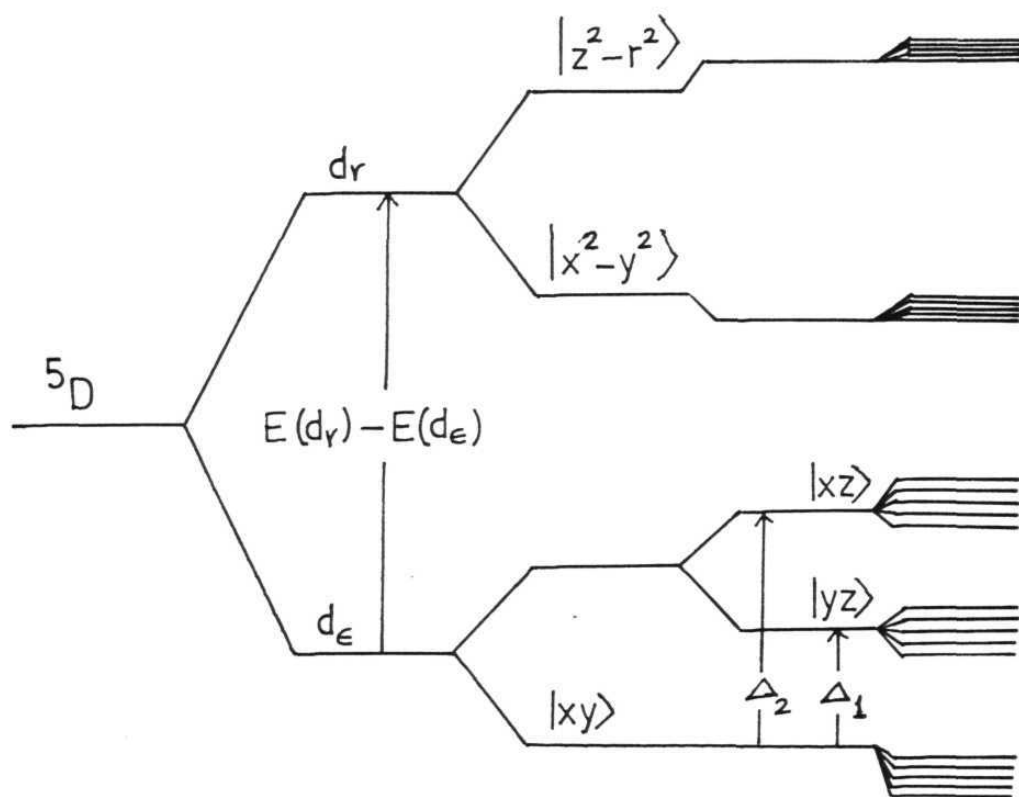
### 2.2.1. Temperature dependence of quadrupole splitting

A computer programme is written on the basis of the formalism discussed in literature to obtain the crystal field terms from a measurement of quadrupole splitting as a function of temperature. This is required for the purpose of analysing the results of our measurements on ferrous maleate tetrahydrate presented in chapter 7. A brief description of the formalism and the steps involved in writing the programme are given below.

The energy level scheme for high spin  $\text{Fe}^{2+}(\text{3d}^6)$  case is given in Figure 2.4. The expression given for the quadrupole splitting in eq. 1.8 may be rewritten as

$$\text{Q.S.} = \frac{1}{2} e^2 Q(1-R_{3d}) V_{zz}(T) \sqrt{1 + \frac{\eta^2(T)}{3}} \quad \dots (2.1)$$





Free ion + Cubic field + Axial field + Rhombic field + Spin-Orbit coupling

Fig.2.4 Energy level scheme for  $Fe^{2+}$  ion

A factor of  $(1-R_{3d})$  arises due to polarization of inner closed shells and the lattice charges, referred to as the Sternheimer effect [5]. Thus to evaluate (2.1) it is required to obtain  $V_{xx}$ ,  $V_{yy}$  and  $V_{zz}$  as  $\eta = \frac{|V_{xx}| - |V_{yy}|}{|V_{zz}|}$ . The electronic contributions to the e.f.g may be denoted by

$$V_{ii}(el) = \langle \psi | \sum_k V_{ii}(\vec{r}_k) | \psi \rangle \quad \dots (2.2)$$

where the wave function  $\psi$  describes the distribution of all electrons considered and for the present case can be written as

$$V_{ii}(el) = \sum_u N_u \langle \phi_u(\vec{r}) | V_{ii}(el) | \phi_u(\vec{r}) \rangle \quad \dots (2.3)$$

where  $V_{ii}(el) = \frac{e}{4\pi\epsilon_0} \left( \frac{3(x_i)^2 - |r|^2}{|r|^5} \right)$ ,  $N_u$  is the number of electrons in the  $u$ -th molecular orbital and  $\phi_u$  in the LCAO-MO approximation is given by  $\phi_u = \sum_p C_{pu} \phi_p$ , the sum being taken over all atomic orbitals of all nuclei considered but the calculations are usually restricted to the atoms to which the orbitals are localized. Expression (2.3) may be written as

$$V_{ii} = - \sum_a N(a) V_{ii}^{aa} - 2 \sum_a \sum_{a'} n(a, a') V_{ii}^{aa'} + \frac{1}{4\pi\epsilon_0} \sum_B (q_B \frac{3(x_i)_B^2 - R_B^2}{R_B^5}) \quad \dots (2.4)$$

where  $n(a, a') = \sum_u N_u C_{au} C_{a'u}$ . The first term represents the valence contribution to the e.f.g tensor at the site of the nucleus and the second term denotes the so called lattice contribution.

For the high spin  $Fe^{2+}(3d^6)$  case under crystal field approximation eq(2.4) can be written as [6]

$$V_{ii} = -(1-R_{3d}) \sum_a n(3d_a) V_{ii}^{aa} - (1-R_{3d}) \sum_a \sum_{a'} n(3d_a, 3d_{a'}) V_{ii}^{aa'} \quad \dots (2.5)$$

where  $V_{ii}^{aa}$  and  $V_{ii}^{aa'}$  are the diagonal and non-diagonal terms. The diagonal terms are given by

$$V_{ii}^{aa} = -\frac{e}{4\pi\epsilon_0} \langle R(\vec{r}) | \frac{1}{r^3} R(\vec{r}) \rangle \langle Y_{1m}(\theta, \phi) | 3 \cos^2 \theta - 1 | Y_{1m}(\theta, \phi) \rangle \quad \dots (2.6)$$

where  $Y_{1m}(\theta, \phi)$  are the spherical harmonics. The non-diagonal terms are given by

$$\langle d_z^2 | 3 \cos^2 \theta - 1 | d_{x^2-y^2} \rangle = \langle d_z^2 | 3 \cos^2 \theta - 1 | d_{x^2-y^2} \rangle = \frac{8}{7} \sqrt{3} \quad \dots (2.7)$$

Evaluating the matrix elements eqs. (2.6) and (2.7) are rewritten as follows

$$(V_{zz})_{3d} = -4/7 \frac{e}{4\pi\epsilon_0} \langle r^{-3} \rangle_{3d} (1-R_{3d}) \times \\ [n(3d_z^2) - n(3d_{x^2-y^2}) - n(3d_{xy}) + \frac{1}{2} n(3d_{xz}) + \frac{1}{2} n(3d_{yz})] \quad \dots (2.8)$$

$$(V_{xx} - V_{yy})_{3d} = \frac{2}{7} \frac{e}{4\pi\epsilon_0} \langle r^{-3} \rangle_{3d} (1 - R_{3d}) \times \\ [3n(3d_{yz}) - 3n(3d_{xz}) + 4\sqrt{3n(3d_z^2, 3d_x^2 - y^2)}] \dots (2.9)$$

The required matrix elements for computing the electronic population in the 15 levels and evaluating the above components is done by considering the Hamiltonian [7]

$$H = H_{\text{axial}} + H_{\text{rhombic}} + H_{\text{s.o.}} \\ = -|\lambda| L_z S_z - \frac{|\lambda|}{2} (L_+ S_- + L_- S_+) + \delta L_z^2 - \frac{\epsilon}{4} (L_+^2 + L_-^2) \\ \dots (2.10)$$

where  $\lambda$  is the spin-orbit coupling constant and  $\delta$  and  $\epsilon$  represent axial and rhombic splitting of the  ${}^5T_{2g}$  levels (Figure 2.4) for the  ${}^5D$  term. There will be  $(2L+1)(2S+1) = 25$  energy levels, but only contributions from the 15 levels arising from  ${}^5T_{2g}$  term in a distorted octahedral field are considered. The 15 x 15 matrix is set up in terms of  $\lambda$ ,  $\delta$  and  $\epsilon$  which are the input parameters. The atomic orbital net population for the different orbitals are calculated using the appropriate transformations in the basis set and the relationships,

$$n_i(3d_{xy}) = \sum_{m_s} C_{xy}^2, m_s \\ n_i(3d_{xz}) = \sum_{m_s} C_{xz}^2, m_s$$

$$n_i(3d_{yz}) = \sum_{m_s} C_{yz, m_s}^2 \quad \text{and}$$

$$n_i(3d_z^2) = n_i(3d_x^2 - y^2) = n_i(3d_z^2, 3d_x^2 - y^2) = 0 \quad \dots (2.11)$$

where the coefficients are obtained from the eigen-vectors after the diagonalization. For the 15 energy levels  $\phi_i$ , the e.f.g tensor contributions are calculated using the relationships (2.8), (2.9) and (2.11). The temperature dependence is introduced by assuming a Boltzmann distribution for the population and obtaining the contributions to the e.f.g. which take the form

$$V_{zz}(T) = \frac{\sum_{i=0}^{14} (V_{zz})_i e^{-(E_i - E_0)/kT}}{\sum_i e^{-(E_i - E_0)/kT}}$$

$$(V_{xx} - V_{yy})(T) = \frac{\sum_{i=0}^{14} (V_{xx} - V_{yy})_i e^{-(E_i - E_0)/kT}}{\sum_i e^{-(E_i - E_0)/kT}} \quad \dots (2.12)$$

Substitution of these values in eq.(2.1) thus leads to the temperature dependence of quadrupole splitting. In our calculations we used  $r^{-3} = 32.5 \text{ \AA}^{-3}$  [8],  $Q = 0.21b$  [9],  $(1-R_{3d}) = 0.68$  [10]. The data were fitted to get the best fit with measured q.s. values at different temperatures by varying  $\delta$  and  $\epsilon$ . Computation and curve fitting were achieved using a computer programme written for this purpose in this laboratory [11].

### 2.2.2. Hyperfine fields in substituted systems.

There is a range of temperature and concentration in which diamagnetically substituted magnetically ordered oxide materials show anomalous Mössbauer spectra. Several attempts have been made to reproduce such line shapes from a simple local molecular field theory assuming a binomial distribution in the coordination and calculating the corresponding hyperfine fields to obtain the composed Mössbauer spectra [12,13]. In this model no time dependent phenomena such as relaxation effects discussed earlier were assumed. This static model, originally put forward by Coey is tested in our systems at low substitution of diamagnetic ions in a magnetic lattice both at near  $T_c$  as well as away from  $T_c$ .

If the magnetic ions such as  $\text{Fe}^{3+}$  and diamagnetic ions such as  $\text{Al}^{3+}$  or  $\text{Ga}^{3+}$  are denoted by f and g and the concentration of second species expressed as a fraction x, assuming a binomial distribution the probability  $P_N(Z)$  of a particular site ion being surrounded by Z f-ions and (N-Z) g-ions may be written as

$$P_N(Z) = \frac{N!}{Z! (N-Z)!} (1-x)^Z (x)^{N-Z} \quad \dots (2.13)$$

where  $N$  is the coordination number. The magnetisation of ions in different environments may be calculated using a local molecular field theory. Introducing the reduced parameters  $\sigma(Z) = \bar{S}_Z/Z$ ,  $\langle \sigma \rangle_{av} = \langle \bar{S}_Z \rangle / S$ ,  $\Upsilon = T/T_c = \frac{3kT}{2S(S+1)J\langle Z \rangle_{av}}$ , the magnetization can be expressed as

$$\sigma(Z) = \beta_s \frac{3S\langle \sigma \rangle_{av}Z}{(S+1)\Upsilon\langle Z \rangle_{av}} \quad \dots (2.14)$$

where  $\beta_s$  represents the Brillouin function.  $\bar{S}_Z$  in (2.14) is the time average of the spin of an iron ion along the magnetic axis and  $\langle \dots \rangle$  denotes an average over all the iron sites in the bulk,  $S$  is the spin of the magnetic ion i.e.  $5/2$  for  $\text{Fe}^{3+}$  case and  $J$  is the exchange constant. Using the above equation the magnetic fields for various near neighbours were calculated self-consistently. It is then assumed that each near neighbour gives rise to a six line pattern with the corresponding hyperfine field and the composite spectrum is result of these sub-spectra. After introducing the line broadening effects caused on account of the range of values about  $H(Z)$  given by

$$\beta = \frac{6\gamma S}{(S+1)\langle Z \rangle_{av}\Upsilon} \frac{d\beta_s}{dy} \sqrt{Z \sum_{i=1}^6 P_6^i(Z) [\sigma(Z) - \langle \sigma \rangle_{av}]^2} \quad \dots (2.15)$$

where  $P'_6(Z) = P_6(Z)/(1-P_6(0))$  and  $\gamma = 1$  for lines 1 and 6, 0.579 for 2 and 5 and 0.157 for 3 and 4. The composite spectra were calculated and compared with the experimental spectra. The value of  $\bar{T}$  is altered to get a good fit with experimental points. Expression (2.14) gives the hyperfine field due to each coordination. The value of  $\bar{T}$  leads to the average value of exchange constant  $J$ . An attempt is made to analyse the spectra of substituted  $\text{FeBO}_3$  and  $\text{Fe}_3\text{BO}_6$  in the range of concentration and temperature under investigation using this model and the validity of the model pointed out. A computer programme based on this formalism written for the purpose of analysis of the Mössbauer data is used [11].

### 2.2.3. Mössbauer spectra in fluctuating environments.

As discussed in the earlier chapter the stochastic model of ionic spin relaxation has been used for analysing 'anomalous' lineshapes in Mössbauer spectroscopy. In this formalism the case when the time dependent hyperfine Hamiltonian at different instances commute with each other has been found to be simple and widely employed for explaining relaxation spectra. Such a case referred to as the adiabatic or secular case has been treated by several authors at different levels of approximations [14-27]. These authors considered a Hamiltonian  $\hat{H}_0$



containing all the time-dependent interactions of the nucleus and the surrounding electrons and a time dependent Hamiltonian which gives rise to transitions among the eigen states of  $\hat{H}_0$  at random instants of time. The result of the calculations is formally expressed by [24]

$$I(\omega) = \langle A^+ ( \frac{1}{2} T_{nat} - i\omega - \hat{W} - i\hat{H}_0^X )^{-1} A \rangle \quad \dots (2.16)$$

where  $\hat{W}$  is an operator describing the relaxation among the eigen states of the system,  $H_0^X$  is called the Liouville operator corresponding to the Hamiltonian  $\hat{H}_0$ , and  $\hat{A}$  is an operator describing the interaction of the system with the electromagnetic field. Equation (2.16) may also be expressed in terms of matrix elements of the form

$$I(\omega) = \sum_{\substack{\mu, \nu \\ \mu', \nu'}} P(\nu) \langle \nu | \hat{A}^+ | \mu \rangle [\mu | ( \frac{1}{2} T_{nat} - i\omega - \hat{W} - i\hat{H}_0^X )^{-1} | \mu' \nu' ] \times \langle \mu' | A^+ | \nu' \rangle \quad \dots (2.17)$$

where  $P(\nu)$  is the probability that the system initially is in the state  $|\nu\rangle$ . In principle the matrix elements corresponding to the second term has a dimension of  $(2S+1)^2 (2I_e+1) (2I_g+1)$ . In practice only approximate methods are used. The calculation is simplified assuming that the magnetic field fluctuates only along the Z-direction and the e.f.g. is axially symmetric with

symmetry axis lying parallel to Z[14]. Under these circumstances  $\hat{H}_n$  given in (1.11) is modified as

$$\hat{H}_n = Q'[3I_Z^2 - I(I+1) - g_n \mu_N \hat{I}_Z H_n(t)] \quad \dots (2.18)$$

where  $Q' = \frac{eQV_{zz}}{4I(2I-1)}$  and the magnetic field at the nucleus,  $H_n(t)$  is a random function of time.  $H_n$  may be written in the form

$$H_n = a_0 M + H \quad \dots (2.19)$$

where  $n$  corresponds to the number of spin states and  $M$  assumes values corresponding to each spin. The spectral component corresponding to a specific nuclear transition  $m_g \rightarrow m_e$  may then be calculated using a modified expression of (2.17) given by [14, 17, 28-32].

$$I(\omega) = \text{Re} \left[ \sum_{M, M'} P(M) A_{MM'}^{-1}(\omega) \right] \quad \dots (2.20)$$

where  $P(M)$  is the thermal population of the electronic state  $|M\rangle$ , and the matrix elements  $A_{MM'}$  are given by

$$A_{MM'} = [i(\omega_M - \omega) + \frac{1}{2} T_{\text{nat}}] \delta_{M, M'} - J_{MM'}^2 \quad \dots (2.21)$$

where  $\hbar\omega_M$  is the nuclear transition energy when the ion is in

the state  $M$ , and  $\Omega_{MM'}$  is the transition probability rate for the ionic spin transition  $|M\rangle \rightarrow |M'\rangle$ . This line shape expression has been shown to reduce to the form [26]

$$I(P) = \text{Re} \sum_{M_1 M_0} \langle M_1 | A^+ | M_0 \rangle^2 \left[ p + i\alpha + \frac{\beta^2}{(p+i\alpha+2)} \right]^{-1} \dots (2.22)$$

where  $M_1$  and  $M_0$  are the angular momentum quantum numbers in the excited and ground states of the nucleus respectively and  $\lambda$  is the relaxation rate,

$$p = -i\omega + T/2$$

$$\alpha(M_1) = Q(3M_1^2 - I(I+1))$$

$$\beta(M_0, M_1) = \mu(g_0 M_0 - g_1 M_1)h$$

and the matrix elements  $\langle M_1 | A^+ | M_0 \rangle$  are the Clebsch-Gordon coefficients.  $g_0$  and  $g_1$  are the nuclear  $g$ -factors for ground and excited states respectively. It is assumed that the spin jumps at random between the values of  $+h$  and  $-h$ . The above expression may be written in a more explicit form as

$$F(\omega) = \sum_{i=1}^6 \frac{\left(\frac{T}{2} + 2\lambda\right) \left[\frac{T^2}{4} + \lambda T - (\alpha - \omega)^2 + \beta^2\right] + (\alpha - \omega)^2 (T + 2\lambda)}{\left(\frac{T^2}{4} + T\lambda - (\alpha - \omega)^2 + \beta^2\right)^2 + (\alpha - \omega)^2 (2\lambda + T)^2} \dots (2.23)$$

Expressing all the quantities in units of  $T$ , a computer programme written using the above expression for simulation of the relaxation spectra is given in Appendix I. Figure 2.5 shows representative relaxation spectra simulated using the above expression for different values of  $\lambda$ .

A modified form of the line shape expression (2.20) has been derived for simulation of line profiles in magnetically ordered material within the molecular field model by Dekker, and van der Woude and Dekker, incorporating the concept of partial order [19,28]. For the simple case of  $S_Z = 1/2$  the order parameter  $\eta$ , may be introduced such that the probabilities for  $S_Z$  to be  $+1/2$  or  $-1/2$  are  $(1+\eta)/2$  and  $(1-\eta)/2$  respectively with  $0 < \eta < 1$ . The A matrix in expression (2.20) for this case may be written as

$$\vec{A} = \begin{bmatrix} i(\omega_2 - \omega) - \Omega_f & \Omega_s \\ -\Omega_f & i(\omega_1 - \omega) - \Omega_s \end{bmatrix} / \det \vec{A} \quad \dots (2.24)$$

where  $\omega_1$  and  $\omega_2$  correspond to the frequencies emitted by the nucleus due to fluctuations in the spin state,  $\Omega_f$  and  $\Omega_s$  give the probability for the frequencies to have the values  $\omega_1$  and  $\omega_2$  respectively. Introducing a convenient frequency scale using the relationship

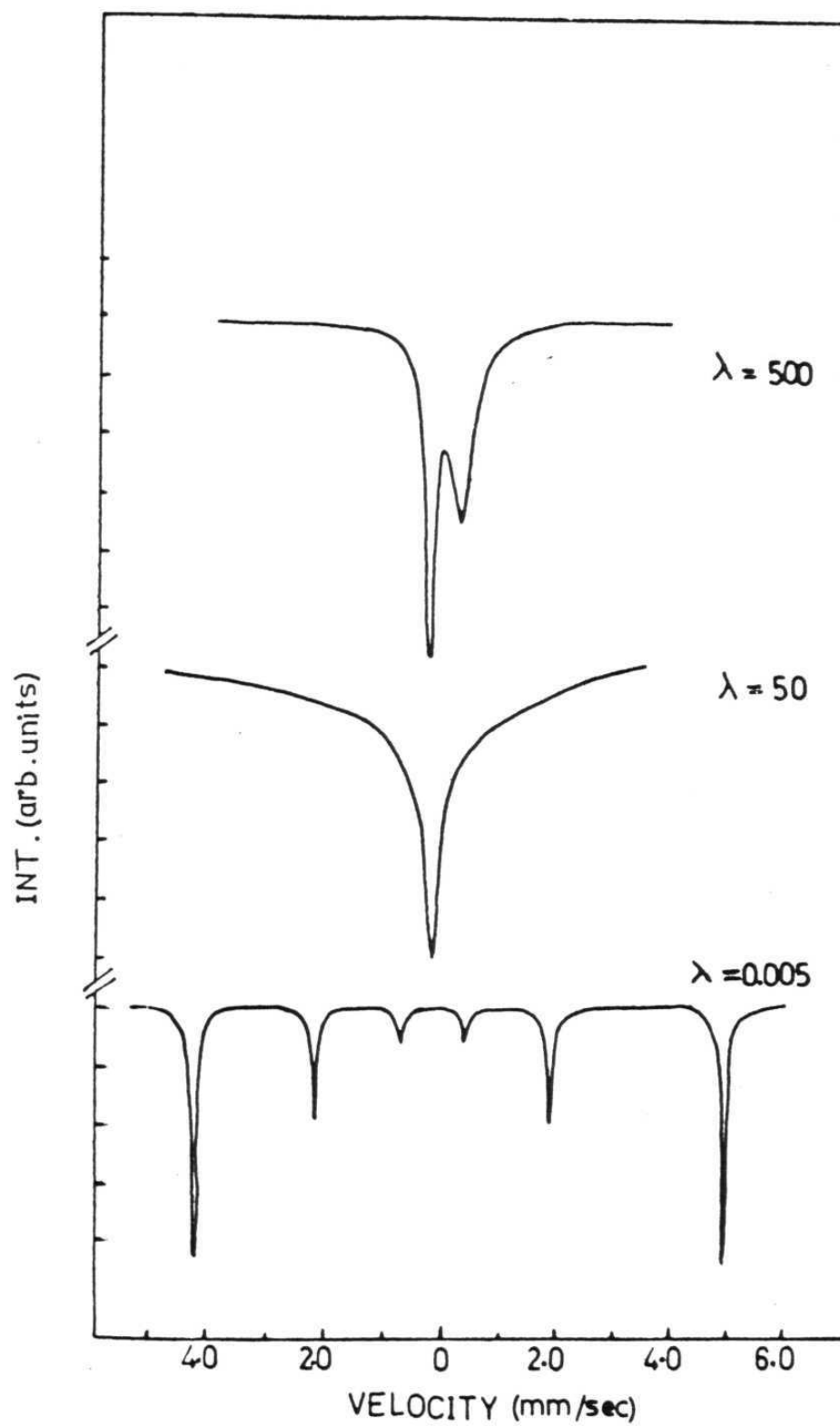


Fig.2.5 Representative spectra for different values of  $\lambda$ , the relaxation rate, in Eq.2.23.

$$\delta = (\omega_2 - \omega_1)/2$$

and  $\omega = 0$  at  $(\omega_1 + \omega_2)/2$ , the line shape expression can be written as

$$I(\omega) = \frac{2\Omega_s^2}{(1-\eta)} \times \frac{\delta^2 (\eta^2 - 1)}{(\omega^2 - \delta^2)^2 + \frac{4\Omega_s^2}{(1-\eta)^2} (\omega + \eta\delta)^2} \dots (2.25)$$

In the above expression the natural line width  $\Gamma$  which has been neglected, when taken into account, the line shape expression becomes

$$I(\omega) = \sum_{i=1}^6 \frac{\frac{2\Omega_s^2}{(1-\eta)} \delta_i^2 (\eta^2 - 1) - \Gamma[\delta_i^2 + \omega^2 + \frac{4\Omega_s^2}{(1-\eta)^2} - 2\omega\delta_i\eta]}{(\delta_i^2 - \omega^2)^2 + \frac{4\Omega_s^2}{(1-\eta)^2} (\omega + \eta\delta_i)^2 + \frac{4\Omega_s^2 \Gamma (\omega^2 + \delta_i^2 + 2\omega\delta_i\eta)}{(1-\eta)}} \dots (2.26)$$

A computer programme written using the above expression to simulate the experimental spectra is given in Appendix II. Representative spectra simulated using the above expression are shown in Figure 2.6. The relative intensities of the different lines in the hyperfine spectra are assumed to be that of the low temperature Zeeman spectra far away from  $T_c$  where the relaxation effects are insignificant. The effect of quadrupole interaction is not taken into account in the derivation of eq.(2.26).

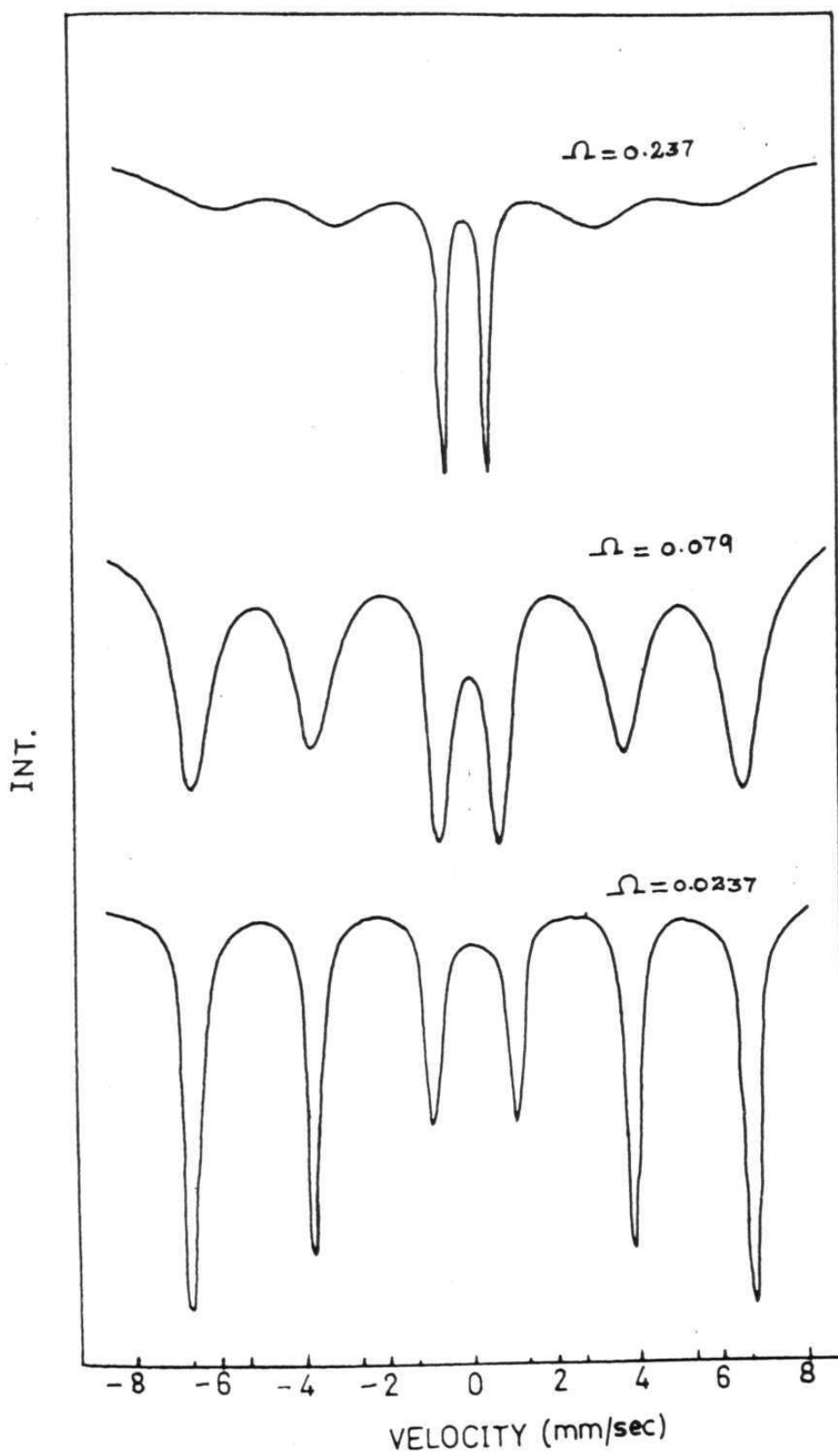


Fig.2.6 Representative spectra for different values of spin-flip frequency,  $\Omega$ , in Eq.2.26.

#### 2.2.4. Field distribution in model independent method [34].

In a substituted system such as  $\text{Fe}_{.9}\text{M}_{.1}\text{BO}_3$  reported in the present work a change in the local neighbourhood of iron atoms takes place. This results in a corresponding change in the hyperfine field and results in a distribution of the field. Instances where the models such as those due to Coey and others [12,13,33] do not explain the experimental observation imply that a model dependent approach is unsatisfactory. At the same time it is possible to directly obtain the field distribution by methods such as those due to Window where no assumptions are made with regard to distribution of the hyperfine field and only experimental data are relied upon [34,35]. The technique is based on a series expansion of the probability curve  $P(H)$  using trigonometric terms satisfying certain boundary conditions. In a magnetic material it is reasonable to assume that the probabilities of zero field and that of the fields higher than the experimentally observed field are zero, i.e.

$$\left(\frac{dP}{dH}\right)_{H=0} = 0 \quad \text{and} \quad \left(\frac{dP}{dH}\right)_{H=H_{\max}} = 0$$

The distribution of the observed field may then be taken to be

$$f_n(H) = \text{Cos} (n \pi H/H_{\max}) - (-1)^n \quad \dots (2.27)$$



where  $n = 1 \dots\dots\dots N$ . The coefficients in the series then satisfy

$$P(H) = \sum_{n=1}^H a_n W_i(H) \quad \dots (2.28)$$

where the  $W_i$  are 'elementary' functions of hyperfine field distributions between  $H = 0$  and  $H = H_{\max}$ . The distribution  $W_i$  may then be correlated with the spectral data in the form

$$S_i(v) = \int_0^{H_{\max}} W_i(H) L_6(H, v) dH \quad \dots (2.29)$$

The above expression can be written as follows to give the complete spectrum

$$S(v) = \sum_{i=1}^m a_i S_i(v) \quad \dots (2.30)$$

The unknown coefficients  $a_i$  are then evaluated directly using the least square condition

$$\sum [S(v) - S_m(v)]^2 = \text{minimum} \quad \dots (2.31)$$

The smoothness of the desired solution in this procedure depends on 'm' the number of 'elementary' hyperfine field distributions  $W_i(H)$  used in the calculation.

We have adopted this procedure in the next chapter to get insight into the distribution of the hyperfine field. In the method quadrupolar interaction is assumed to be negligible. The intensity ratio is not necessarily equal to 3:2:1:1:2:3 but modified to have a closer value to the intensity ratio obtained from the least square fit data to give a theoretically composed spectrum to fit well with the experimental data and  $\chi^2$  a minimum possible value.

References:

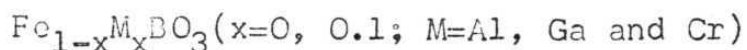
1. R.S. Preston, S.S. Hanna and J. Heberle, Phys. Rev. 128, 2207 (1962).
2. A.H. Muir Jr and H. Wiedersich. Bull, Am. Phys. Soc. 11, 770 (1966).
3. L. May, S.J. Druck and M.Sellers, U.S. Atomic Energy Comm. Rep. No. NYO 3798-2 (1968).
4. J.J. Spijkerman, J.R. De Voe and J.C. Travis, NBS Special Publication 260-20, Washington, D.C. (1970).
5. R.M. Sternheimer, Phys. Rev. 130, 1423 (1963).
6. R. Ingalls. Phys. Rev. 133, 787 (1964).
7. T.C. Gibb, J.Chem. Soc. (A) 1439 (1968).
8. H. Eicher, Z. Phys. 171, 582 (1963).
9. H.R. Leider and D.N. Pipkorn, Phys. Rev. 165, 494 (1968).
10. A.J. Freeman and R.E. Watson, Phys. Rev. 131, 2566 (1963).
11. N. Ravi, Ph.D. Thesis, University of Hyderabad, Hyderabad, 1981.
12. J.M.D. Coey, Phys. Rev. B6, 3240 (1972).
13. J.M.D. Coey, and G.A. Sawatzky, Phys. Status Solidi b44, 673 (1971).

14. M. Blume and J.A. Tjon, Phys. Rev. 165, 446 (1968).
15. J.A. Tjon and M. Blume, Phys. Rev. 165, 456 (1968).
16. M. Blume, Phys. Rev. 174, 351 (1968).
17. M. Blume, Phys. Rev. Lett. 14, 96 (1965).
18. M. Blume, Phys. Rev. Lett. 18, 305 (1967).
19. A.J. Dekker in Hyperfine Interactions, edited by  
A.J. Freeman and B.R. Frankel (Academic Press, New York,  
1967), p.679.
20. S. Morup and N. Thrane, Phys. Rev. B, 4, 2087 (1971).
21. A.J.F. Boyle and J.R. Gabriel, Phys. Lett. 19, 451 (1965).
22. J.K. Srivastava, Phys. Status Solidi (b), 97, K123 (1980).
23. J.K. Srivastava, Phys. Status Solidi (b), 55, K119 (1973).
24. S. Morup, Paramagnetic and Superparamagnetic Relaxation  
Phenomenon Studied by Mössbauer Spectroscopy, D.Sc. Thesis,  
Technical Univ. Denmark, 1981.
25. R. Nagarajan and J.K. Srivastava, Phys. Status Solidi (b)  
81, 107 (1977).
26. S. Dattagupta in Advance in Mössbauer Spectroscopy edited  
by B.V. Thosar, P.K. Iyengar S.C. Bhargava and J.K. Sri-  
vastava (Elsevier publishing co. 1983), p.586.

27. J.K. Srivastava, S.C. Bhargava, P.K. Iyengar and B.V. Thosar in Advances in Mössbauer Spectroscopy edited by B.V. Thosar P.K. Iyengar, S.C. Bhargava and J.K. Srivastava (Elsevier publishing co, 1983), p.1.
28. F. van der Woude, Ph.D. Thesis, Groningen, 1966. University of Groningen, Groningen, 1966.
29. H.H. Wickman, M.P. Klein and D.A. Shirley, Phys. Rev. 152, 345 (1966).
30. H.H. Wickman, in Mössbauer Effect Methodology, Vol. 2 edited by I. Gruverman (Plenum Press, New York, 1966), p.39.
31. H.H. Wickman and G.K. Wertheim in Chemical Applications of Mössbauer Spectroscopy, edited by V.I. Goldanskii and R.H. Herber, (Academic Press, New York, 1968), p.548.
32. M. Blume in Hyperfine Structure and Nuclear Radiations edited by E. Matthias and D. Shirley (North-Holland, Amsterdam, 1968), p.911.
33. J. Ray, T.S. Radhakrishnan, C. Bansal and G. Chandra, Phys. Status Solidi (b) 64, 335 (1974).
34. B. Window, J. Phys. E4, 401 (1971)
35. A Narayanasamy, T. Nagarajan, P. Muthukumarasamy and T.S. Radhakrishnan, J. Phys. F 9, 2261 (1979).

## CHAPTER 3

### MÖSSBAUER STUDIES OF



#### Abstract

The results of a Mössbauer study of the effect of substitution of  $\text{Al}^{3+}$ ,  $\text{Ga}^{3+}$  and  $\text{Cr}^{3+}$  in ferromagnetic  $\text{FeBO}_3$  close to  $T_c$  are presented. The Curie temperatures of  $\text{FeBO}_3$ ,  $\text{Fe}_{0.9}\text{Al}_{0.1}\text{BO}_3$ ,  $\text{Fe}_{0.9}\text{Ga}_{0.1}\text{BO}_3$  and  $\text{Fe}_{0.9}\text{Cr}_{0.1}\text{BO}_3$  have been determined to be 352, 317, 319 and 335 K respectively. The 'anomalous' spectra have been found to appear just  $1^\circ$  below  $T_c$  for  $\text{FeBO}_3$ , but even  $15^\circ$  below  $T_c$  for substituted borates. These spectra have been simulated using relaxation models and estimates of activation energy obtained for spin-flip processes. The results have been attributed to dominant superparamagnetic relaxation effects due to the presence of clusters. Evidence for the cluster formation in substituted borates is obtained by an analysis of hyperfine field distribution. The inadequacy of static models in explaining these spectra has been pointed out. The difference in the results of  $\text{Cr}^{3+}$  substituted borate from the rest of the solid solutions is brought out and the possible reasons stated.

### 3.1. Introduction

Room temperature ferromagnets, transparent in the visible or infrared are not common. Dillon has reviewed the potential applications of such materials in magneto-optic devices [1].  $\text{FeF}_3$  and  $\text{FeBO}_3$  are two such instances. For this reason attempts have been made to characterise well  $\text{FeBO}_3$ . The crystal structure has been studied by Bernal *et al* [2]. Joubert *et al* studied the intrinsic magnetic properties [3]. A magneto optical study on the flux grown single crystals of  $\text{FeBO}_3$  showed that it has a spontaneous magnetization  $4\pi M$  of 115 gauss at room temperature, Curie temperature ( $T_c$ ) of 343 K, a prominent absorption window in the green (5250 Å) region with  $\alpha = 39 \text{ cm}^{-1}$  and a large Faraday rotation of  $2300^\circ$  per centimeter at 5250 Å [4-6]. Other investigations on pure  $\text{FeBO}_3$  include crystal structure refinement by Diehl [7], neutron diffraction studies by Pernet *et al* [8] and investigations of hyperfine interactions by NMR and Mössbauer techniques [9-12]. Muller succeeded in developing easy methods of preparation of  $\text{FeBO}_3$  and its solid solutions and also reported susceptibility studies of the solid solutions [13]. In the course of our work a related study on  $\text{Fe}_{1-x}\text{Cr}_x\text{BO}_3$  ( $x = 0.11, 0.5$ ) has been reported by Ruckman *et al* [14]. In this chapter we present the results of our Mössbauer studies on  $\text{FeBO}_3$  and the solid

solutions  $\text{Fe}_{0.9} \text{M}_{0.1} \text{BO}_3$  ( $\text{M} = \text{Al}, \text{Ga}$  and  $\text{Cr}$ ) close to their Curie temperatures. An attempt is made to computer simulate the spectra employing (i) the static model of Coey [15,16] and (ii) relaxation models due to Blume and Tjon, Dattagupta and van der Woude and Dekker [17-19]. It is shown that the Coey's model is not satisfactory in accounting for the experimentally observed results. On the other hand, the relaxation models are shown to account well for the experimental observations. The results of the parent compound were compared with those of the solid solutions. The supporting evidences for electronic and/or superparamagnetic relaxations have been looked into. By way of looking at the possibility of the latter mechanism it is considered worthwhile to look at the hyperfine field distribution by a model independent approach assuming that the presence of clusters should be revealed by the nature of the distribution in the parent and the solid solutions. The method due to Window is employed for the purpose and the results presented [20, 21].

### 3.2. Experimental

$\text{FeBO}_3$  as well as the solid solutions,  $\text{Fe}_{0.9} \text{M}_{0.1} \text{BO}_3$  ( $\text{M} = \text{Al}, \text{Ga}$  and  $\text{Cr}$ ) were prepared according to the method of Muller et al [13]. Stoichiometric amounts of metal nitrates were



dissolved with a 400% excess  $\text{H}_3\text{BO}_3$  in hot deionised water. A small amount of  $\text{LiNO}_3$ , preferably 5 moles for every 50 moles of ferric nitrate, has been added to this solution. The solution was slowly evaporated to dryness. The resultant material was mixed thoroughly under acetone and heated in a platinum crucible at  $500^\circ\text{C}$  for 4 hours and at  $810^\circ\text{C}$  for 2 days. After cooling to room temperature the material was dissolved in de-ionised water to remove excess  $\text{B}_2\text{O}_3$ . The material was separated and dried under vacuum.

X-ray powder diffractograms of  $\text{FeBO}_3$  and its solid solutions confirmed the formation of these compounds and absence of starting materials as impurities [3]. The infrared and optical spectra of these samples were found to agree quite well with those reported [3,4]. Mössbauer spectra showed the absence of  $\text{Fe}_2\text{O}_3$ ,  $\text{Fe}_3\text{BO}_6$  or any other iron bearing materials.

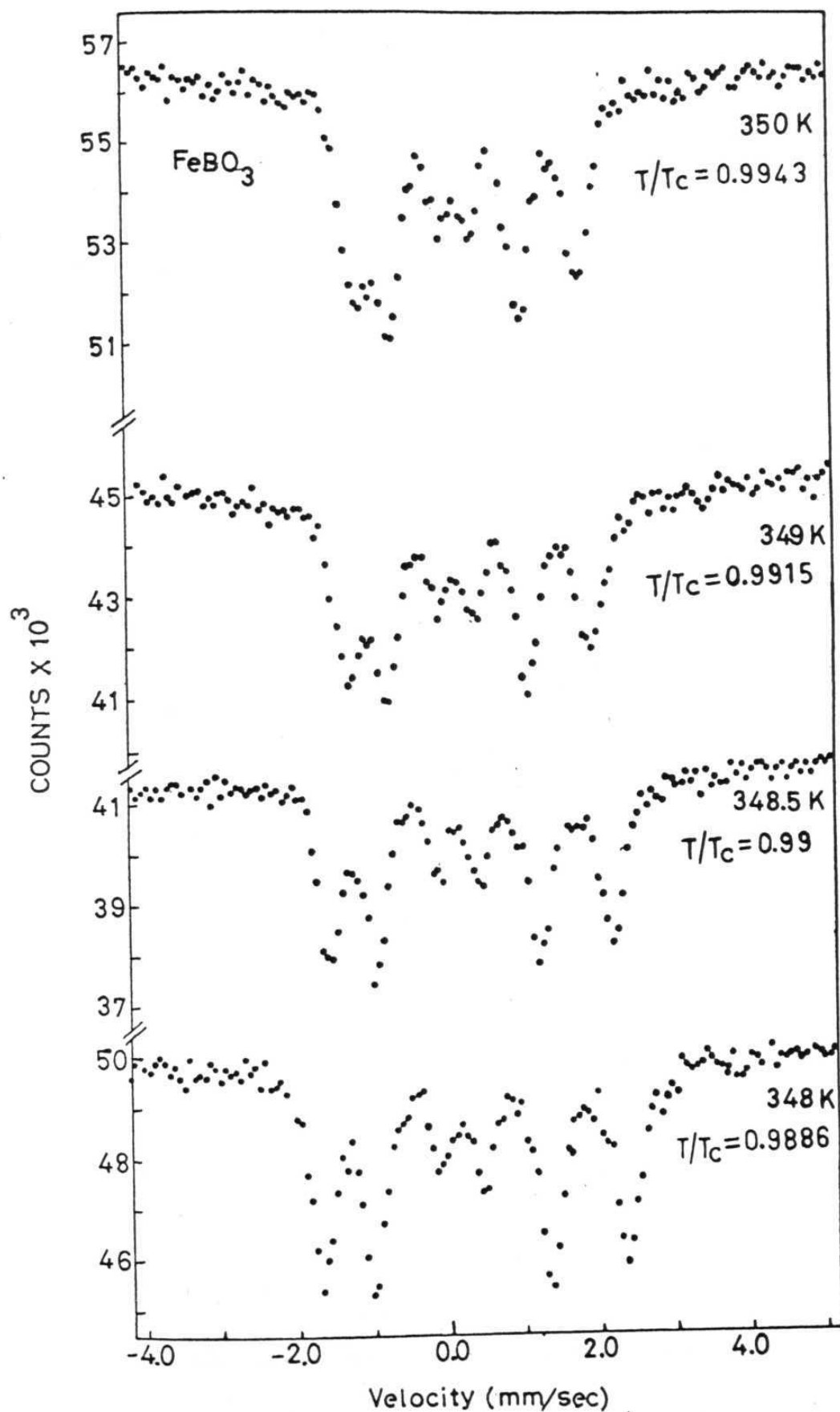
The Mössbauer measurements were carried out as described in section 2.1.1.

### 3.3. Results and Discussion

#### 1) $\text{FeBO}_3$

The Mössbauer spectra of  $\text{FeBO}_3$  close to  $T_c$  (352K) in the range  $348 < T < 352$  are given in Figures 3.1 and 3.2. The well resolved room temperature spectrum of the specimen is given in Figure 3.3 for comparison. The latter is found to be similar to the reported spectrum [22]. The powder spectrum gave relative intensities in the ratio 3:3:1:1:3:3 indicating strong anisotropy. At low temperatures the lines were sharp with linewidths of  $\sim 0.30$  mm/sec. By way of characterising the sample the optical spectrum which could be measured conveniently with the photoacoustic spectral technique is reproduced along with those of solid solutions in Figure 3.4. These spectra were identical to that of Kurtzig *et al* reported for  $\text{FeBO}_3$  [4]. Mössbauer spectra close to  $T_c$  exhibited significant differences in their profiles. For instance at 351 K a four finger pattern and at 351.5 K a spectrum with a doublet structure of unequal intensity superimposed on a broad background absorption characteristic of magnetic interaction were observed (Fig. 3.2). At 352 K a narrow doublet with line width typical of paramagnetic spectra was observed. This characteristic did not change even when the measurement was made even at

Fig.3.1 Mössbauer spectra of  $\text{FeBO}_3$  close to  $T_c$  from 348 to 350 K



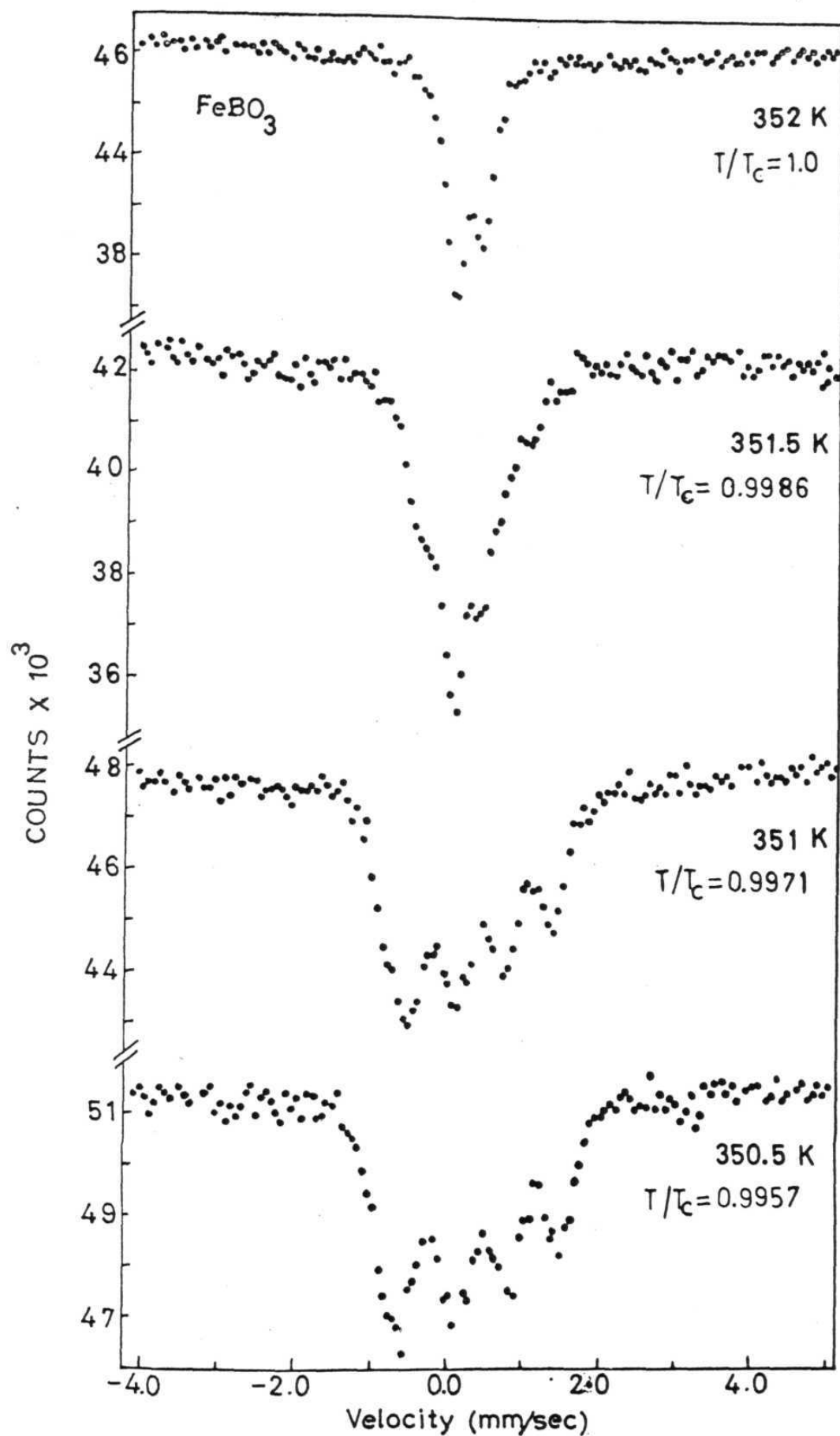


Fig.3.2 Mössbauer spectra of  $\text{FeBO}_3$  close to  $T_c$  from 350.5 to 352 K.

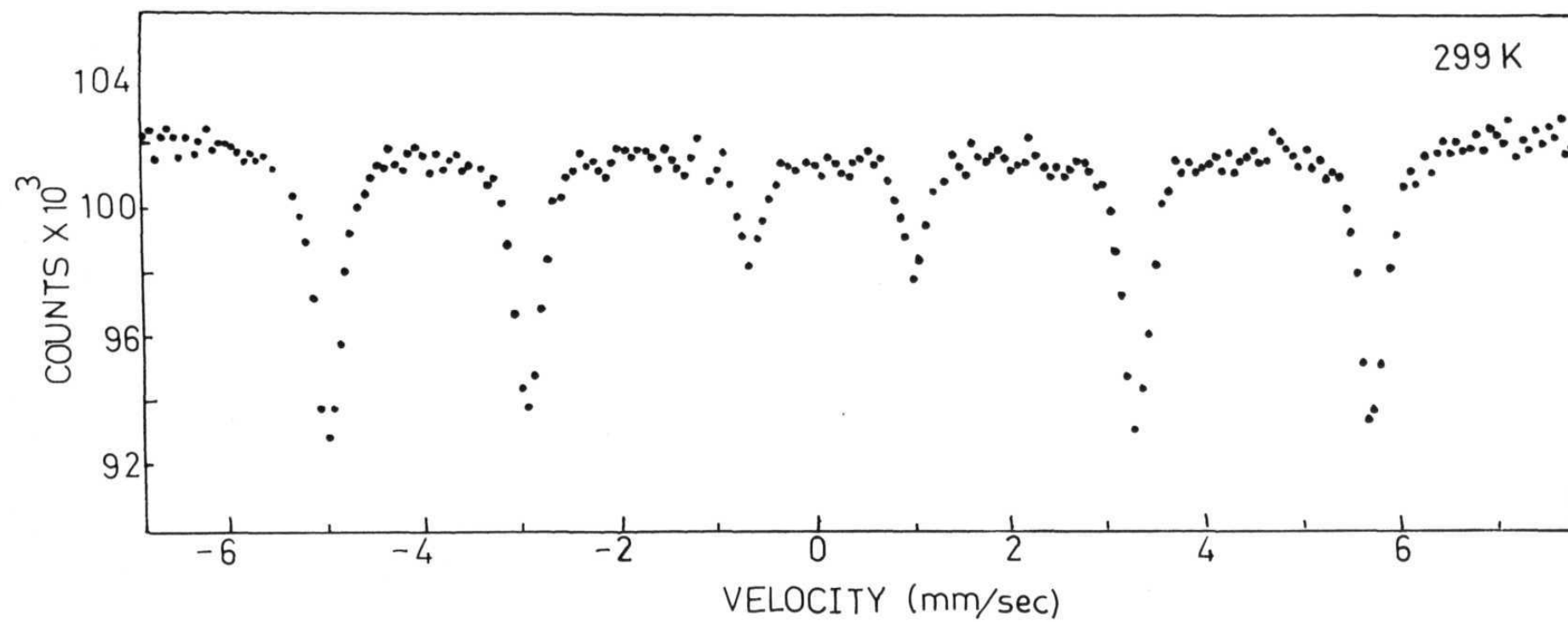


Fig.3.3 Room temperature Mössbauer spectrum of FeBO<sub>3</sub>

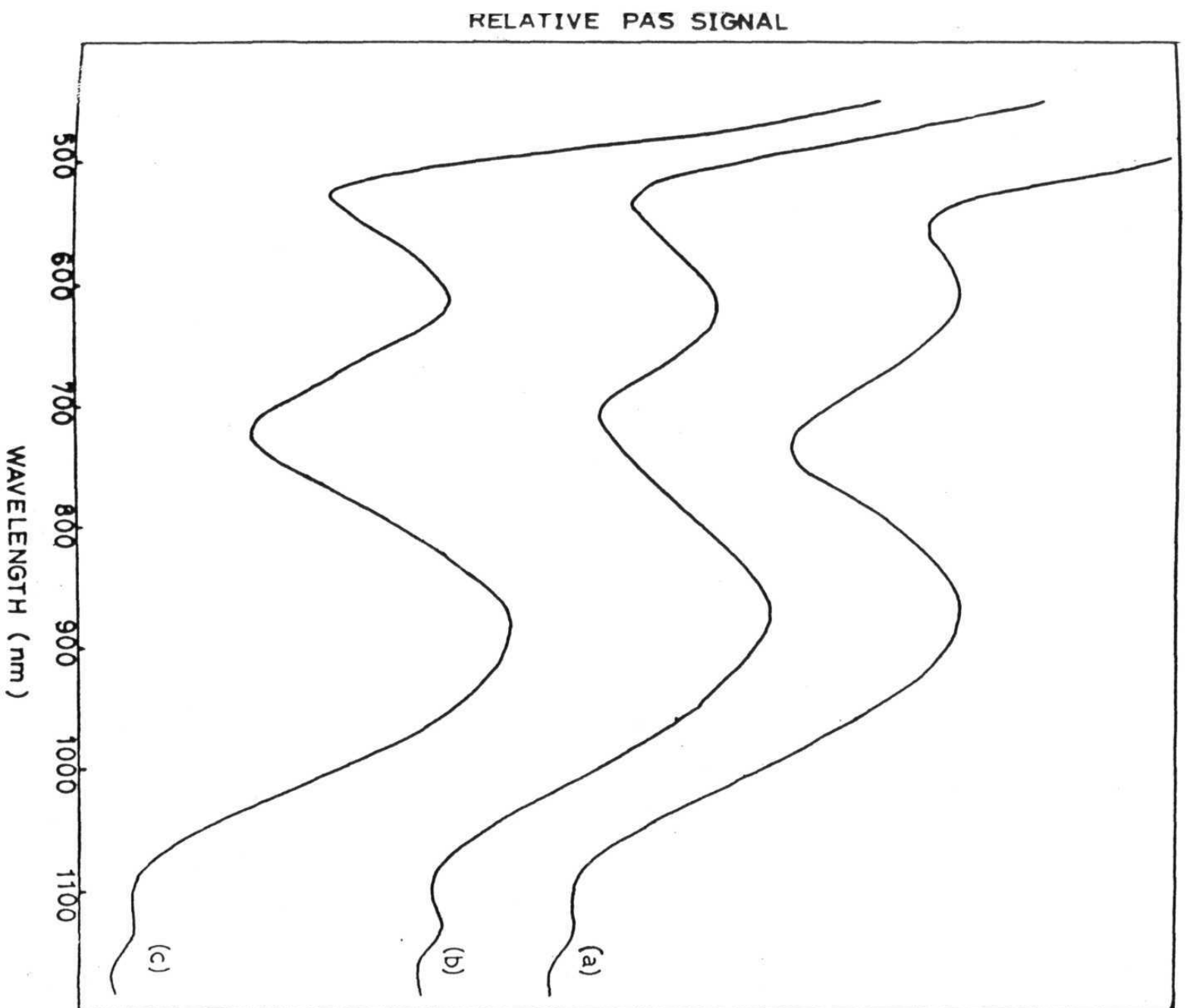


Fig. 4 Photoacoustic spectra of (a)  $\text{Fe}_{0.9}\text{Cr}_{0.1}\text{BO}_3$  (b)  $\text{FeBO}_3$  and (c)  $\text{Fe}_{0.9}\text{Ga}_{0.1}\text{BO}_3$  at room temperature

much higher temperatures. An attempt is made to least square fit the profiles of spectra close to  $T_c$  assuming a static magnetic field and relative intensities observed for the room temperature spectrum. The results of such a fit of Mössbauer spectra measured at 348.5 K and 351 K are reproduced in Figure 3.5. Further as relaxation effects are also known to lead to anomalous line shapes with an intense doublet superimposed on broad outer lines, the spectra were also analysed using Blume's relaxation model employing the equation 2.22 discussed in Chapter 2. The theoretical spectra thus obtained are compared with experimental spectra in Figure 3.6.

ii)  $\text{Fe}_{0.9}\text{Al}_{0.1}\text{BO}_3$

The Mössbauer spectra of 10%  $\text{Al}^{3+}$  substituted  $\text{FeBO}_3$  recorded close to  $T_c$  are reproduced in Figure 3.7. The low temperature spectra showed no anomalous features. However the spectra measured from 305.5 to 317 K clearly exhibited profiles typical of time dependent hyperfine field.

Unlike in the case of  $\text{FeBO}_3$ , the resultant spectra in the diamagnetically substituted system, as in the present case can also be accounted for, in the light of Coey's model which

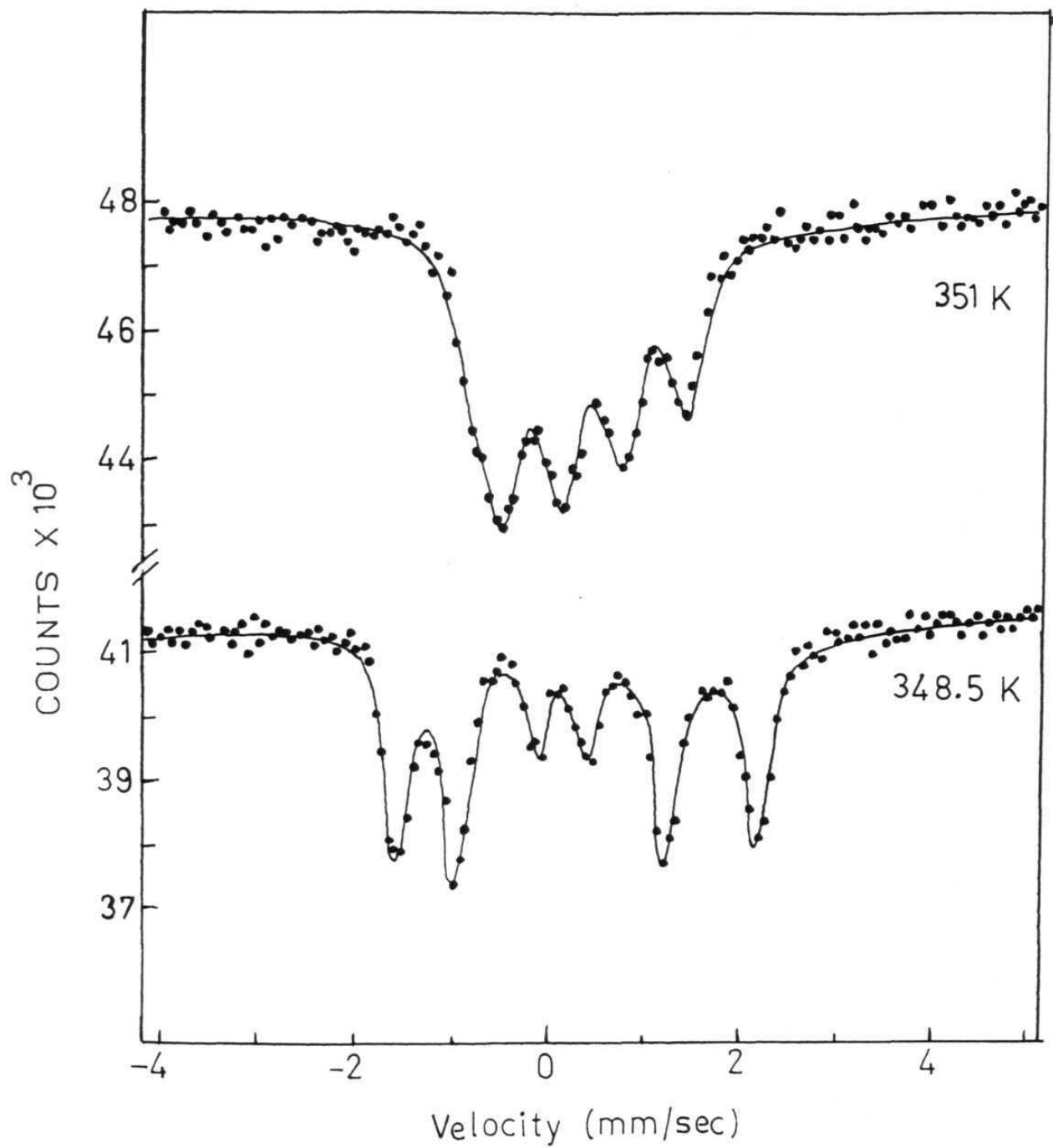


Fig.3.5 Mössbauer spectra of  $\text{FeBO}_3$  at 348.5 and 351 K; solid lines are calculated spectra with least square fit Mössbauer data



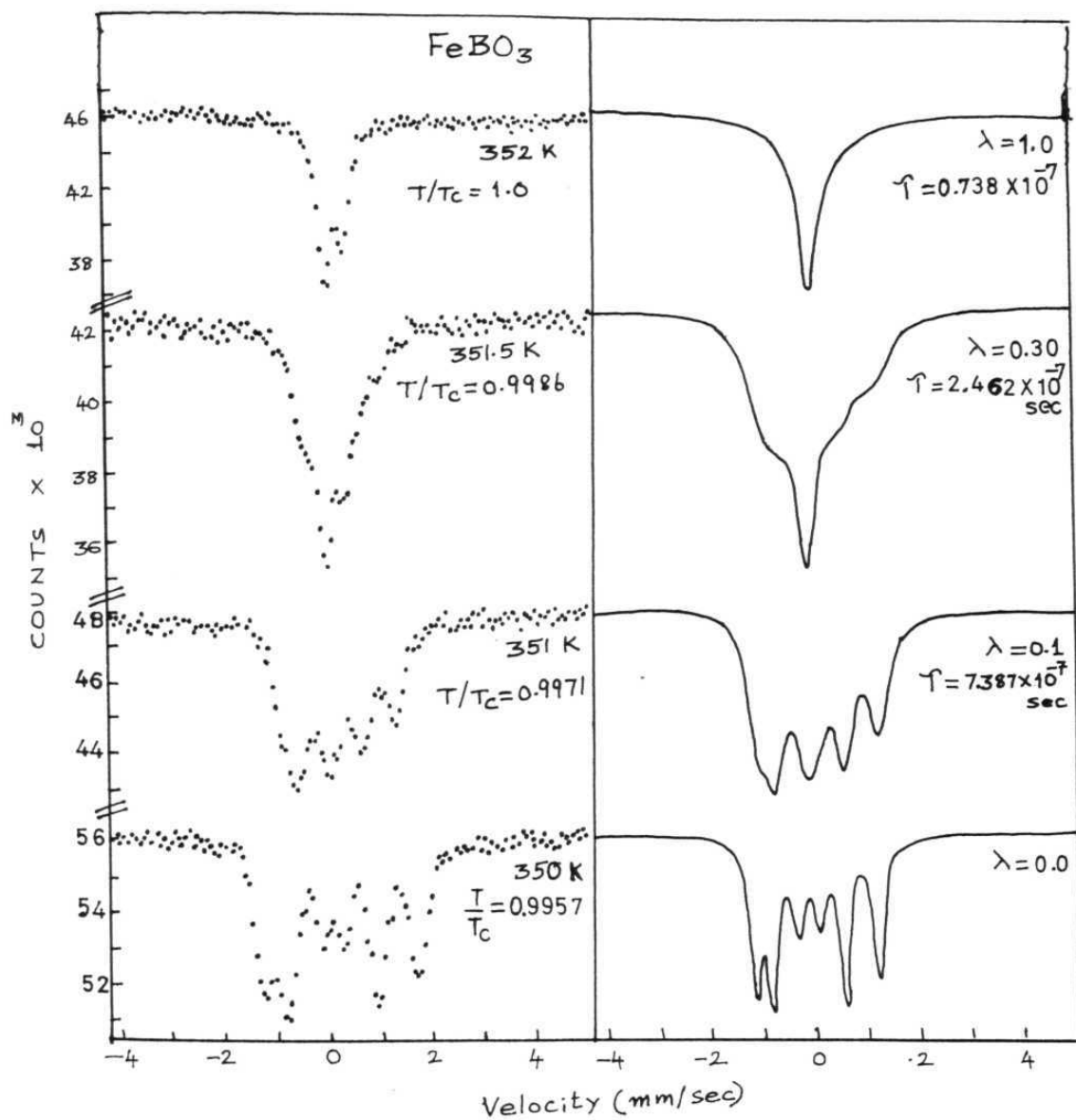


Fig.3.6 Comparison of experimental spectra of  $\text{FeBO}_3$  at different temperatures with theoretical Mössbauer spectra based on relaxation effects.

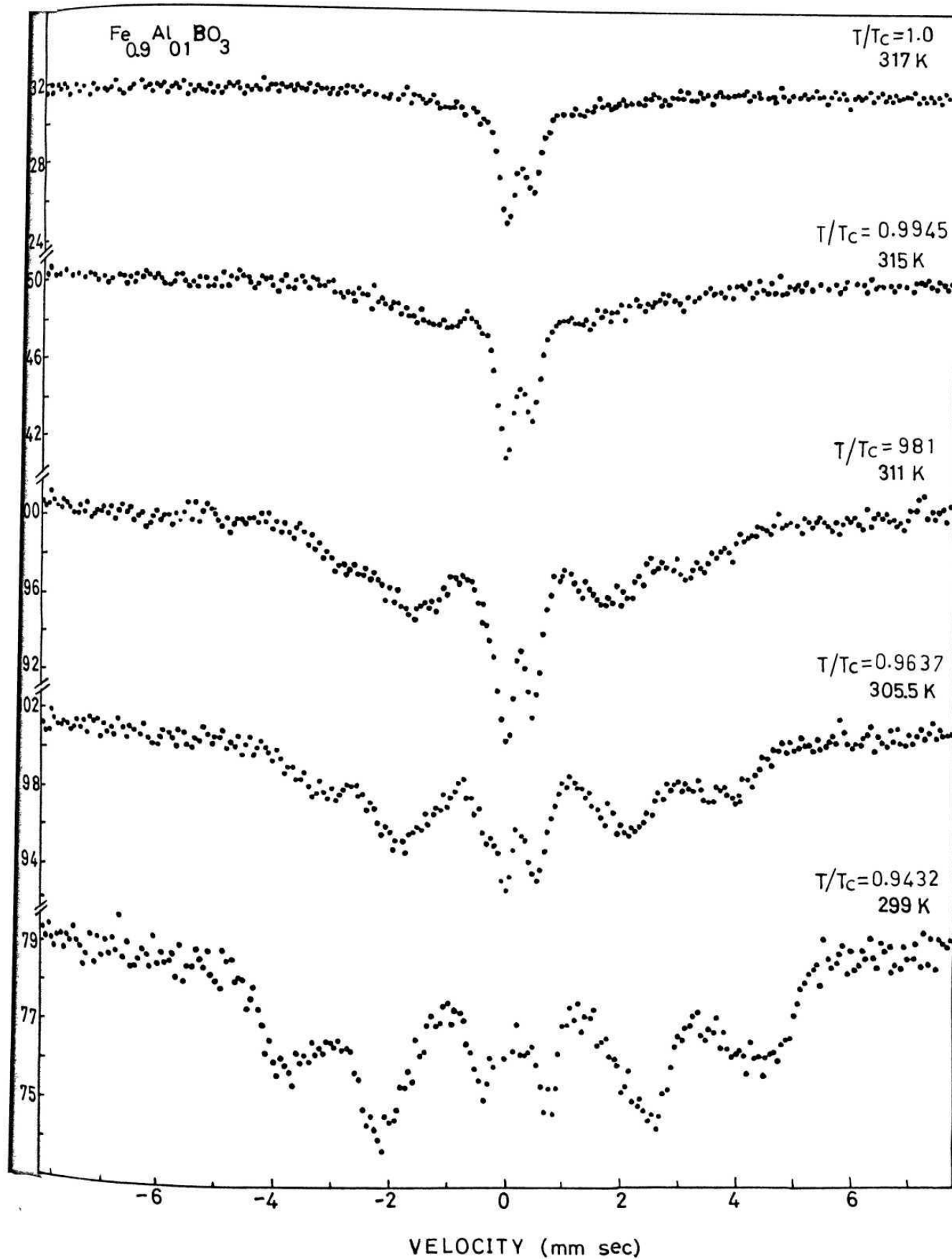


Fig.3.7 Mössbauer spectra of  $\text{Fe}_{0.9}\text{Al}_{0.1}\text{BO}_3$  measured between 299 to 317 K.

takes into account the probabilities of different coordinations due to substitution and the consequent distributions in the hyperfine field as discussed in section 2.2.2. With this view in mind, attempts were made in this case to simulate the spectra for 10% diamagnetic substitution by  $\text{Al}^{3+}$  in octahedral symmetry as discussed in the earlier chapter. It was found, however, the spectrum based on this model obtained for  $T/T_c = 0.99$  reproduced in Figure 3.8 showed poor agreement with the experimental spectrum shown in Figure 3.7, corresponding to 315 K.

Attempts to simulate the theoretical spectra employing expression 2.22 based on the relaxation model due to Blume also showed that unlike in the parent  $\text{FeBO}_3$  the profiles of the experimental spectra could not be reproduced in these cases. Hence the model of van der Woude which is basically the same as that of Blume's but includes an order parameter,  $\eta$ , which differentiates the probability of spins being present up or down was tried. The theoretical spectra obtained using the latter model with  $\omega_L$ , the spin-flip frequency in the range 0.113 to 0.303 and  $\eta = 0.45$  are compared with those of experimental spectra in Figure 3.9. The theoretical profiles show good agreement with the measured spectra. The spectra recorded at 317 K and above were found to be doublets with line widths

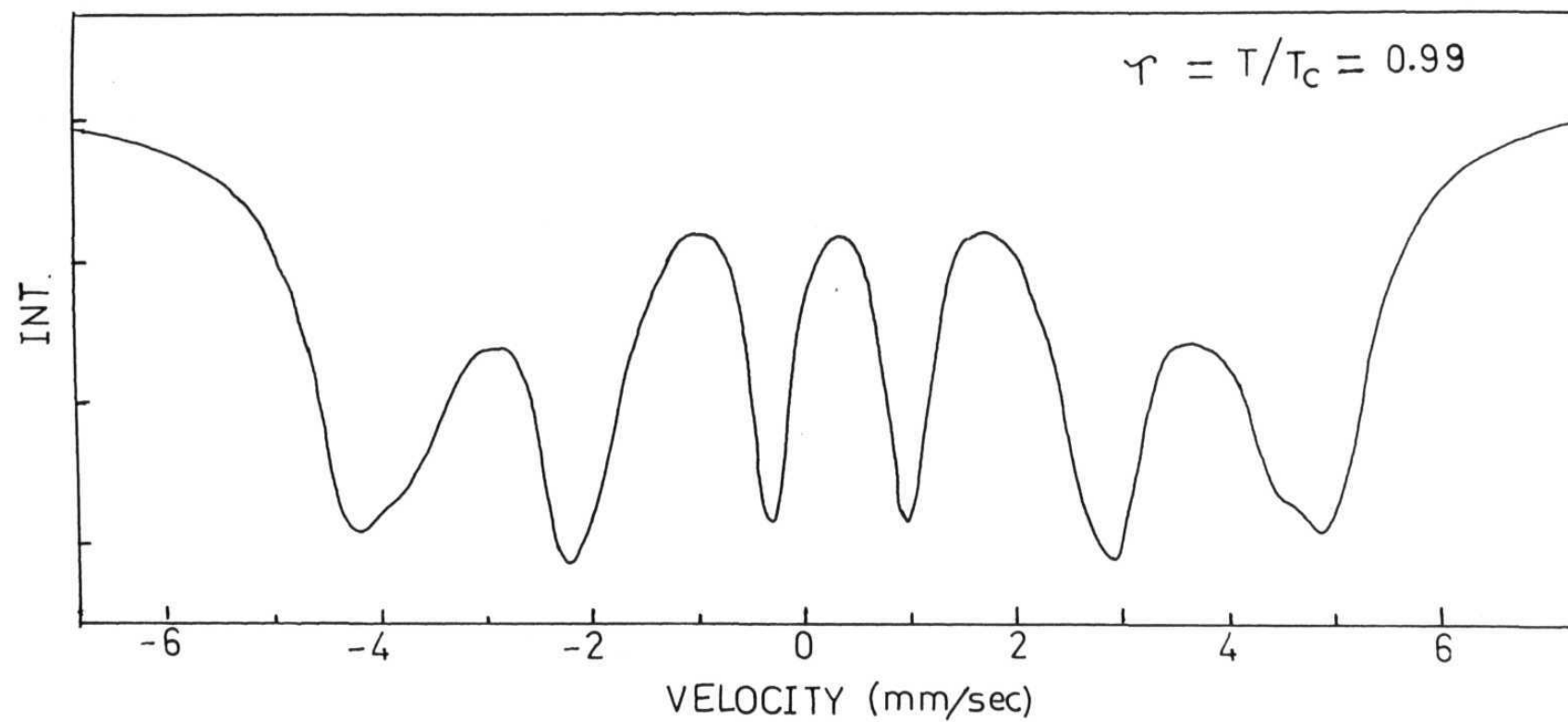


Fig.3.8 Theoretical Mössbauer spectrum simulated using the random distribution model (see text) for  $\tau = 0.99$

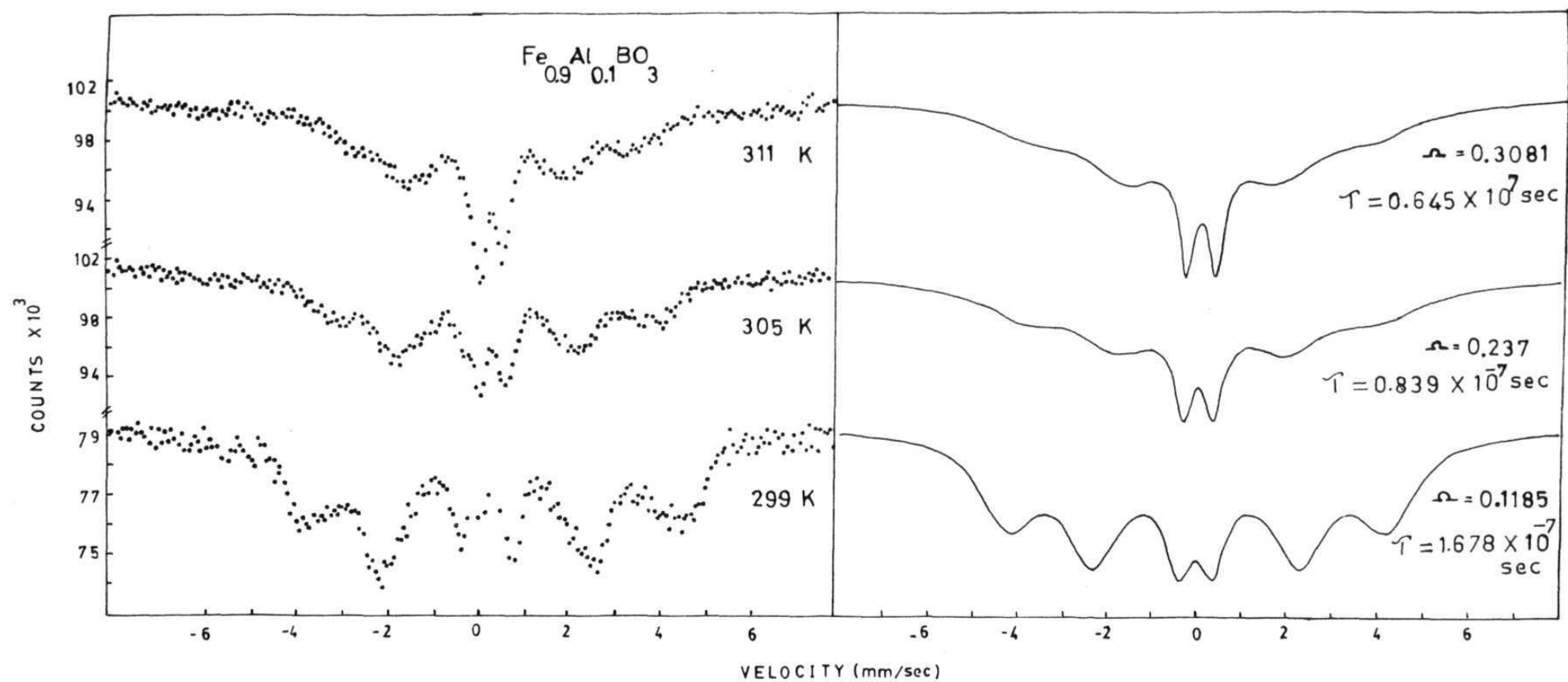


Fig.3.9 Comparison of experimental spectra of  $\text{Fe}_{0.9}\text{Al}_{0.1}\text{BO}_3$  at different temperatures with theoretical spectra based on relaxation effects.

typical of paramagnetic spectra. The spectra however showed unequal intensities for the doublet. In these cases an estimate of the activation energy of  $9.936 \times 10^{-13}$  erg. degrees<sup>-1</sup> is obtained using the expression

$$\Omega = \Omega_0 e^{-E_a/kT} \quad \dots (3.1)$$

where  $E_a$  is the activation energy for the spin-flip process.

iii)  $\text{Fe}_{0.9}\text{Ga}_{0.1}\text{BO}_3$

The Mössbauer spectra of 10%  $\text{Ga}^{3+}$  substituted  $\text{FeBO}_3$  recorded in the range 77-320 K showed features similar to those of  $\text{Fe}_{0.9}\text{Al}_{0.1}\text{BO}_3$ . Representative spectra measured between 299 and 317 K are reproduced in Figure 3.10. The spectra based on the relaxation model of van der Woude and Dekker with  $\Omega$ , the spin flip frequency lying in the range 0.166 to 0.379 and the order parameter  $\eta = 0.45$  were found to give rise to theoretical spectra close to experimental situations (Fig. 3.11). The line profiles of spectra recorded at and above 319 K indicated that  $T_c$  for this sample to be 319 K. An estimate of activation energy obtained for the spin flip process is found to be  $5.87 \times 10^{-13}$  erg.degree<sup>-1</sup> which is nearly the same as found for 10%  $\text{Al}^{3+}$  substituted  $\text{FeBO}_3$ .

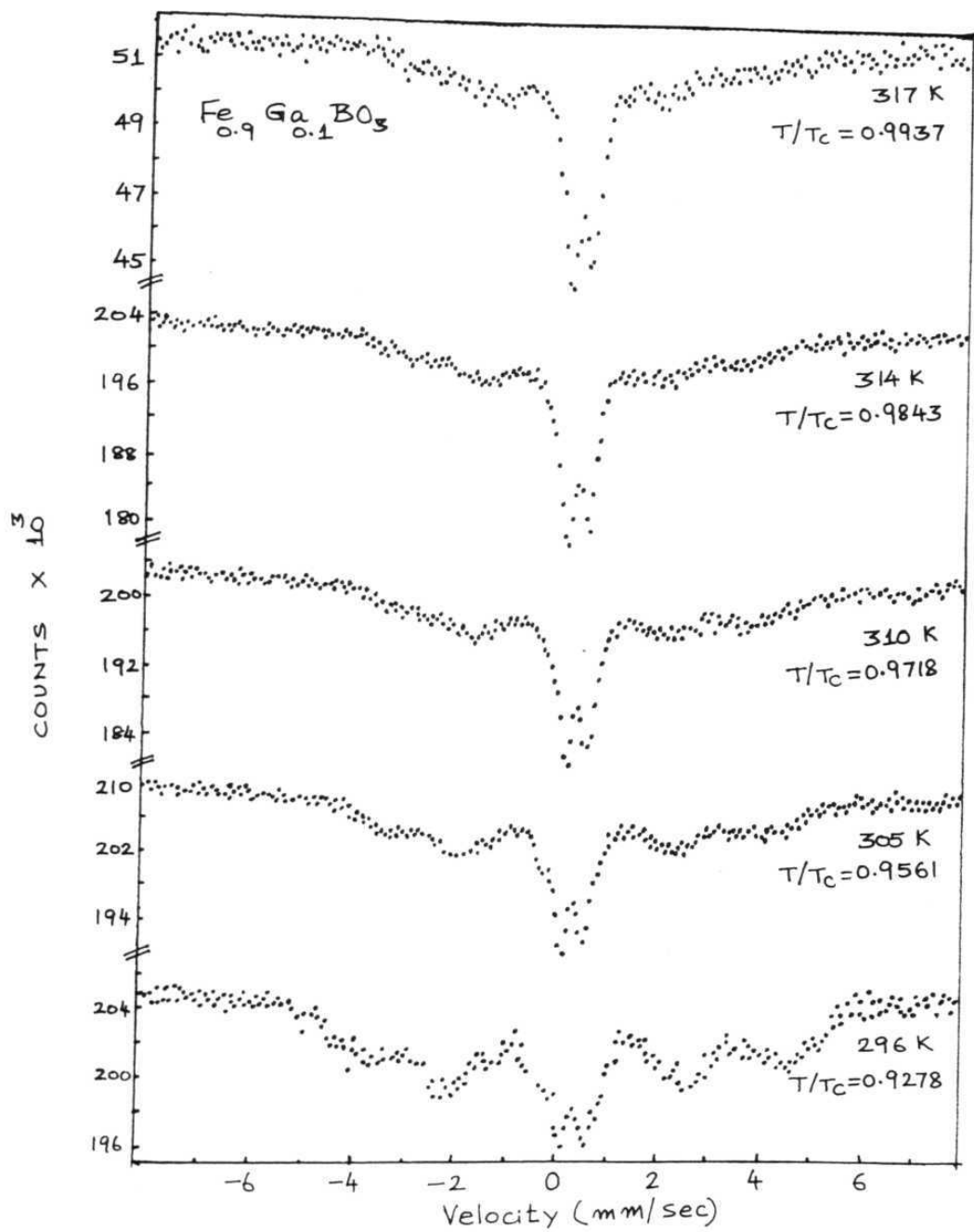


Fig.3.10 Mössbauer spectra of  $\text{Fe}_{0.9}\text{Ga}_{0.1}\text{BO}_3$  measured between 296-317 K.

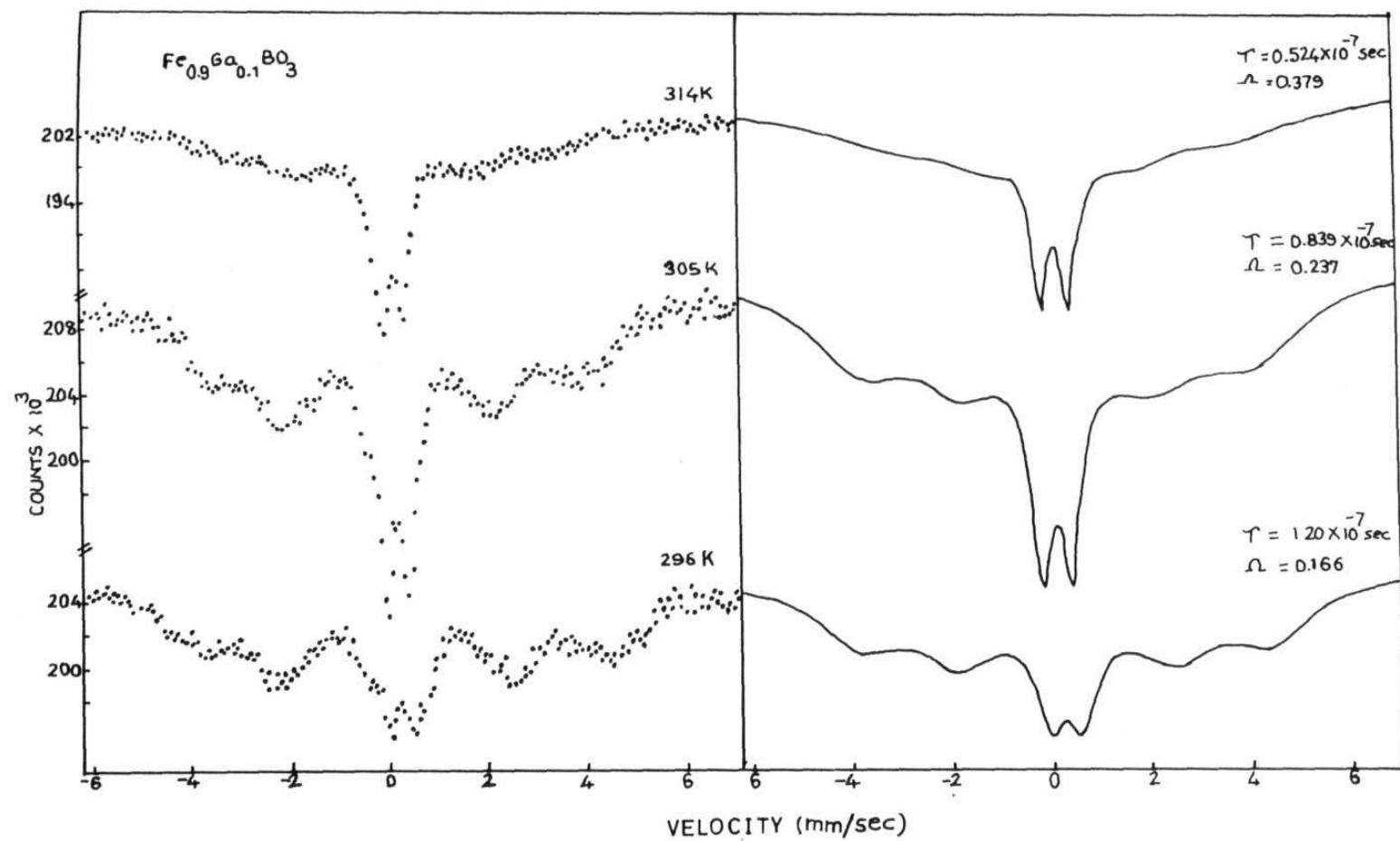


Fig.3.11 Comparison of experimental spectra of  $\text{Fe}_{0.9}\text{Ga}_{0.1}\text{BO}_3$  at different temperatures with theoretical spectra based on relaxation effects.



iv)  $\text{Fe}_{0.9}\text{Cr}_{0.1}\text{BO}_3$ 

The Mossbauer spectra of 10%  $\text{Cr}^{3+}$  substituted  $\text{FeBO}_3$  recorded far away from  $T_c$  were similar to those of the parent and other solid solutions. However, those recorded close to  $T_c$ , reproduced in Figure 3.12 showed significant differences both from those of the parent as well as the  $\text{Ga}^{3+}$  and  $\text{Al}^{3+}$  substituted systems particularly in the region  $-2$  to  $+2$  mm/sec. Attempts to simulate these experimental spectra using the relaxation models which successfully reproduced the spectra for other solid solutions gave unsatisfactory results, particularly in the above mentioned velocity region.

A plot of  $H_{\text{eff}}(T)/H_{\text{eff}}(0)$  vs  $T/T_c$  for  $\text{FeBO}_3$  and substituted  $\text{FeBO}_3$  is shown in Figure 3.13. It is found that all the data points closely follow the theoretical Brillouin curve for the  $S = 5/2$  case.

The values of  $\Omega$ , the spin flip frequency and  $\tau$ , the correlation time, and the activation energy obtained for the two substituted samples are given in Table 3.1. The hyperfine field at 80 K, the lowest temperature measured, the isomer-shifts and quadrupole splittings for the spectra measured in the paramagnetic states and the Curie temperatures for the

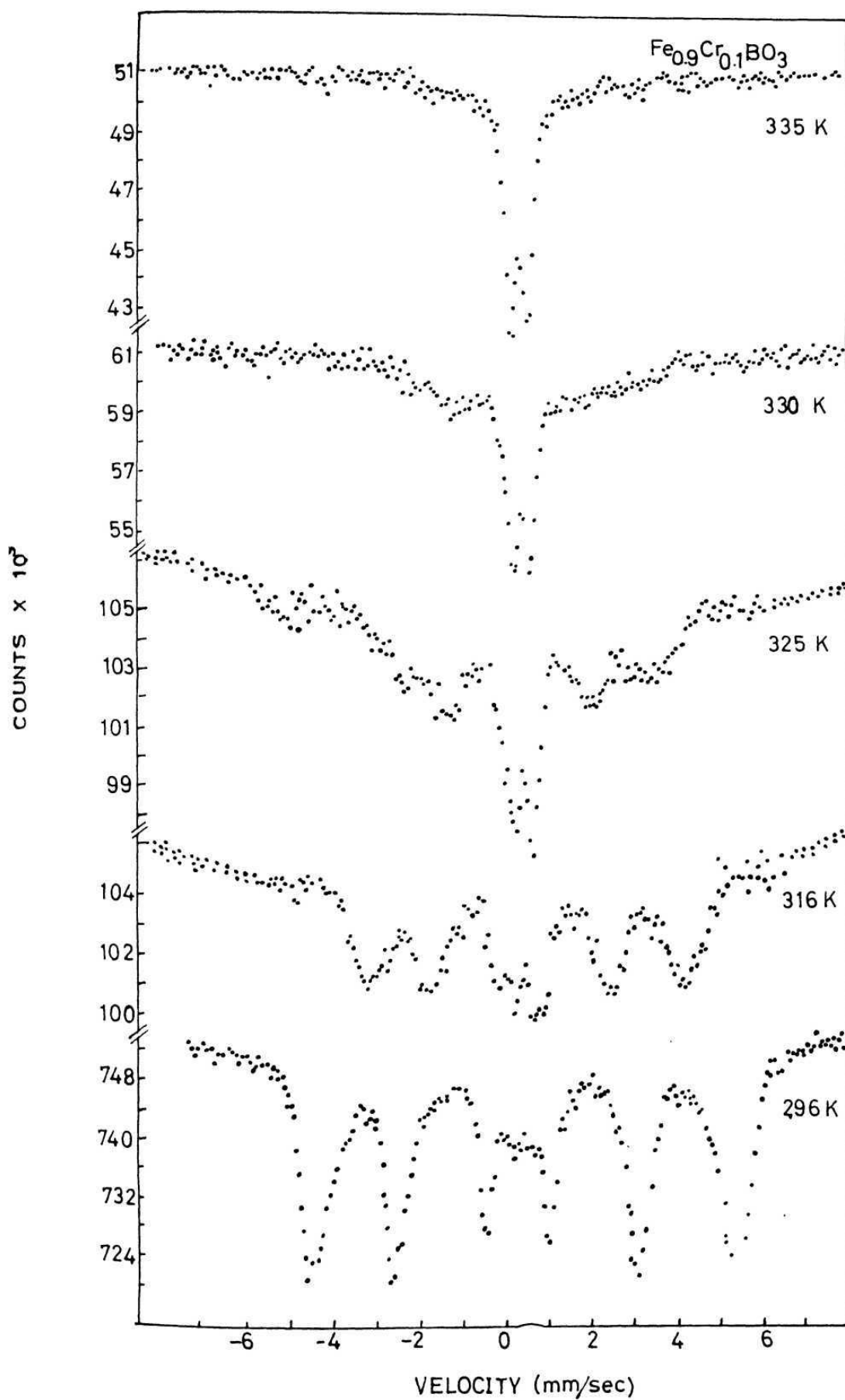


Fig.3.12 Mössbauer spectra of  $\text{Fe}_{0.9}\text{Cr}_{0.1}\text{BO}_3$  in the range 296-335 K.

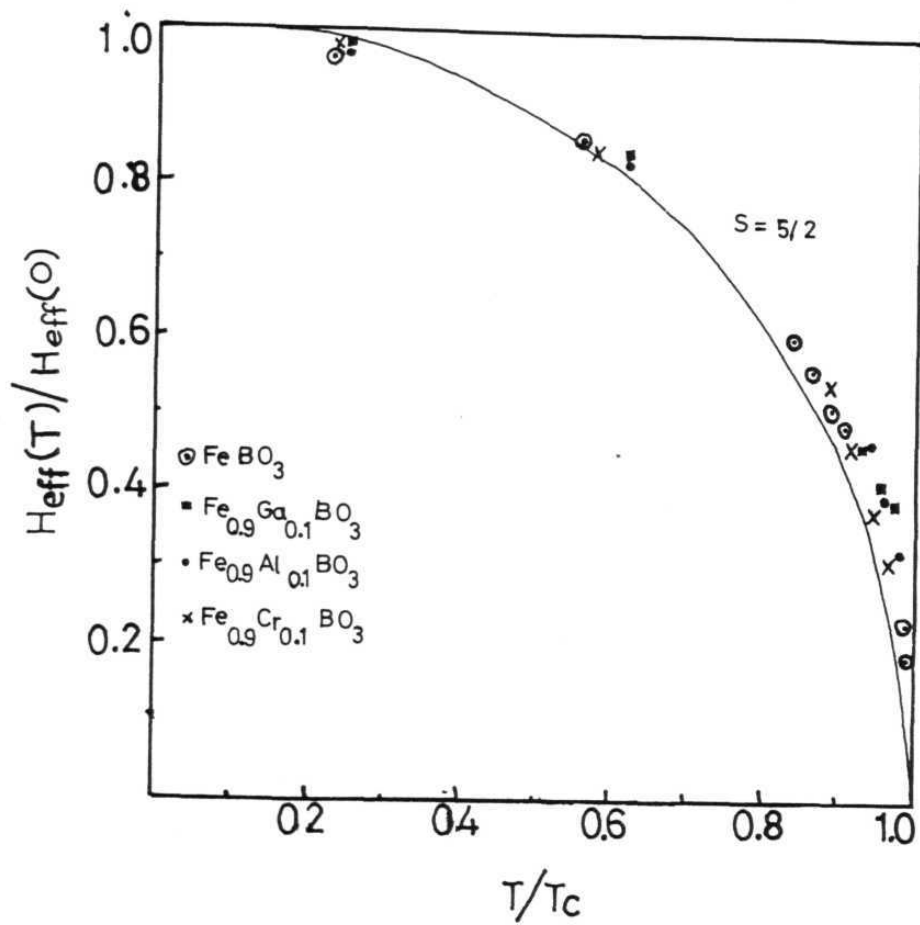


Fig.3.13 Plot of reduced hyperfine field vs reduced temperature for the case of  $\text{FeBO}_3$  and different solid solutions. The continuous line represents the Brillouin curve for  $S = 5/2$ .

Table 3.1. The spin-flip frequency ( $\Omega$ ) correlation time ( $\tau_s$ ) and the activation energy ( $E_a$ ) for spin-flipping process for 10%  $\text{Ga}^{3+}$  and  $\text{Al}^{3+}$  substituted  $\text{FeBO}_3$ .

Compound	Temp. (K) ( $\pm 1$ )	$\Omega$	$\tau_s (\text{sec}) \times 10^7$	$E_a \times 10^{13}$ (erg. degree $^{-1}$ )
$\text{Fe}_{0.9}\text{Ga}_{0.1}\text{BO}_3$	296	0.166	1.20	5.87
	305	0.237	0.84	
	314	0.379	0.52	
$\text{Fe}_{0.9}\text{Al}_{0.1}\text{BO}_3$	299	0.1185	1.678	9.93
	305.5	0.237	0.84	
	311	0.3081	0.64	

parent and the substituted systems are given in Table 3.2.

Attempts to understand situations giving rise to 'anomalous' Mössbauer spectra having superimposition of 'magnetic' and 'paramagnetic' profiles have been made both from theoretical [15-19, 23-28] as well as experimental points of view [29-37]. Detailed experimental investigations in these studies in magnetically ordered materials are to our knowledge confined to oxide systems such as the ferrites, where the preparatory techniques introduce non-stoichiometry and inhomogeneity. In that sense the data obtained in systems such as the present one where the crystalline materials were prepared from the flux techniques, should be more reliable. The anomalous spectra were obtained for  $\text{FeBO}_3$  just  $1^\circ$  below  $T_c$  where time dependent effects are unequivocal. In the case of the substituted borates they become evident even as far away as  $15^\circ$  below their respective Curie temperatures. Such situations can be explained on the basis of (i) electronic relaxation (ii) superparamagnetic relaxation effects or (iii) possible hyperfine field distribution particularly in the case of solid solutions. In the case of solid solutions different coordinations can be expected to give rise to a distribution in the hyperfine field as discussed by Coey and other workers leading to anomalous spectra [15,16,38]. It is found that such a model

Table 3.2. Quadrupole Splitting, Isomer Shift, Line width,  $H_{\text{eff}}(80 \text{ K})$  and  $T_c$  values for  $\text{FeBO}_3$  and  $\text{Fe}_{0.9}\text{M}_{0.1}\text{BO}_3$  (M = Ga, Al and Cr).

Compound	Q.S. at $T_c$ (mm/sec) $\pm 0.02$	I.S. <sup>†</sup> (mm/sec) $\pm 0.02$	FWHM at RT (mm/sec) $\pm 0.02$	$H_{\text{eff}}(80)$ $\pm 2 \text{ kOe}$	$T_c$ (K)
$\text{FeBO}_3$	0.36	0.30	0.33	545	352
$\text{Fe}_{0.9}\text{Al}_{0.1}\text{BO}_3$	0.45	0.28	0.38	533.5	317
$\text{Fe}_{0.9}\text{Ga}_{0.1}\text{BO}_3$	0.40	0.35	0.35	530.7	319
$\text{Fe}_{0.9}\text{Cr}_{0.1}\text{BO}_3$	0.38	0.32	0.34	539	335

<sup>†</sup> relative to Fe-foil.

does not reproduce the experimental results for 10% substitution in the said temperature range (Fig. 3.8), although it is found to be useful for accounting for observations away from  $T_c$  as discussed in the next chapter for  $\text{Fe}_3\text{BO}_6$  case. Thus the utility of such models seem to be limited to situations where time dependent effects are not important. This is understandable as mean field approximations are far from satisfactory when time dependent effects are dominant.

In the parent compound where the time dependent effects appear important only very close to  $T_c$  the line shape expression of Blume and Tjon successfully reproduces the experimental spectra without introducing weight factors for different spin levels unlike in the case of solid solutions. In the molecular field approximation due to van der Woude it is equivalent to the situation of order parameter  $\eta = 0$ . In solid solutions good match with experimental spectra are obtained only if  $\eta \neq 0$ . The correctness of our analysis is also shown by unresolved intense central absorption in the spectrum of  $\text{FeBO}_3$  at 351.5 K unlike in the solid solution spectra with resolved doublet structures. This trend is parallel to the trend shown by the theoretical spectra for  $\eta = 0$  and  $\eta \neq 0$  cases respectively [19]. The order parameter  $\eta$  is proportional to the magnetization. A finite value of  $\eta$  thus indicates polarisation of the

spin states implying that the collective behaviour of the spins has broken and partial order is present in the solid solutions.

Our results clearly show that relaxation effects are important. They occur only very close to  $T_c$  in the pure compound but could be easily observed over much wider ranges in solid solutions. Relaxation effects occur due to ionic spin fluctuations either due to the motion of the individual spins i.e., electronic relaxation effects or due to collective motion of large number of spins in a small region of the material i.e., superparamagnetic effects. The electronic relaxation effects may arise due to spin-lattice and spin-spin interactions.  $Fe^{3+}$  being an S state ion, the spin-spin relaxation mechanism is expected to be dominant. In this mechanism, the ion exchanges energy with another paramagnetic ion with which it is coupled through dipolar or exchange interactions. Relaxation effects arise as a result of the mutual spin-flip of one ion accompanied by that of another with identical Zeeman splitting so that the exchange is energy conserving. In this mechanism the population of the ionic levels vary with temperature resulting in temperature dependent lineshape.

Superparamagnetic effects in the Mössbauer spectra occur due to the presence of small regions, otherwise called clusters,



in a solid which are more magnetic than the rest of the solid and are magnetically decoupled from the rest of the solid, the cluster magnetisation fluctuating randomly among various easy directions of magnetisations due to thermal agitation. If  $V$  is the volume of the cluster, the relaxation time of the cluster magnetisation is given by [23, 39].

$$\tau_F = \tau_0 \exp(KV/k_B T) \quad \dots (3.2)$$

where  $K$  is the anisotropy energy per unit volume,  $V$  is the volume of the cluster and  $k_B$  the Boltzmann constant. Thus a plot of  $\log \tau_F$  vs.  $1/T$  should lead to an estimate of  $\tau_0$ . In the case of the solid solutions such a plot led to  $\tau_0 = 5.37 \times 10^{-8}$  sec. and  $\tau_0 = 5.01 \times 10^{-8}$  sec. for  $\text{Fe}_{.9}\text{Al}_{.1}\text{BO}_3$  and  $\text{Fe}_{.9}\text{Ga}_{.1}\text{BO}_3$  respectively, which is in the order expected for situations with superparamagnetic relaxation effects [19,23,39]. The superparamagnetic behaviour occurs for fine particles far below  $T_c$  as observed by the anomalous Mossbauer spectra. On the other hand, for large particle size this type of behaviour is observed as  $T \rightarrow T_c$  because then the anisotropy energy per unit volume and hence  $KV$  tends to zero. In a bulk material it is more appropriate to rewrite eq. (3.2) as

$$\tau_F = \tau_0 \exp(KV_{\text{eff}}/k_B T) \quad \dots (3.3)$$

where  $V_{\text{eff}}$  characterises a spread in effective volume due to the inhomogeneity intrinsic in the substituted materials. The inhomogeneity gives rise to large clusters of magnetically independent regions. If the inhomogeneity giving rise to clusters is important one would expect enhancement of relaxation region in magnetically diluted systems. In the parent  $\text{FeBO}_3$  any such inhomogeneities may be expected to be minimal resulting in a very small distribution of  $V_{\text{eff}}$  leading to the so called critical superparamagnetism with the relaxation effects becoming observable only very close to  $T_c$ . On the other hand substitution by nonmagnetic ion such as  $\text{Al}^{3+}$  or  $\text{Ga}^{3+}$  causes a significant change giving rise to clusters with a wider distribution in the value of  $V_{\text{eff}}$ . The collective motions of spins in the substituted systems are therefore highly damped affecting the relaxation processes. The large relaxation region with the effects seen even upto  $(T_c - 15)$  in solid solutions thus arises predominantly due to superparamagnetic relaxation. It may be emphasised at this point that such an observation of the anomalous spectra over a wide range of temperature does not imply a distribution of  $T_c$  but signifies a range over which size effects become important [30]. Further, according to the super exchange relaxation model the spin-flip time,  $\tau_F$  has been shown to decrease with increase in temperature which is found to be the case in our own observations in the systems under investigation [30] (Table 3.1).

It is suggested above that substitution of a non-magnetic ion should cause significant change in the nature of the clusters of magnetically independent regions present in the sample as shown in particular by the extension of observation of relaxation phenomena as far as  $15^{\circ}$  below  $T_c$ . It should be possible to get an estimate of the change brought about in the magnetic interaction by the substitution, provided a model independent method of obtaining the distribution of hyperfine fields discussed in section 2.2.4. is used. With this point of view a representative analysis of the hyperfine field distribution was carried out for both  $\text{FeBO}_3$  as well as  $\text{Fe}_{.9}\text{Ga}_{.1}\text{BO}_3$  close to  $T_c$ . Figures 3.14 and 3.15 show the Mössbauer spectra of  $\text{FeBO}_3$  at 348.5 K and  $\text{Fe}_{.9}\text{Ga}_{.1}\text{BO}_3$  at 296 K respectively along with the theoretical spectra simulated based on this approach. The plots of  $P(H)$ , the probability of given hyperfine field vs  $H$  are shown in Figure 3.16. The widths of the distribution curves for  $\text{FeBO}_3$  and  $\text{Fe}_{.9}\text{Ga}_{.1}\text{BO}_3$  were found to be  $\sim 35$  gauss and  $\sim 135$  gauss respectively. The large width found for the latter clearly shows large distribution of magnetic fields present in the system. Thus 10%  $\text{Ga}^{3+}$  substitution brings about a large number of different near neighbours or clusters and hence a large field distributions in the substituted sample, in contrast to that of the parent material viz.,  $\text{FeBO}_3$ . Further, attempts to reproduce the anomalous spectra close to

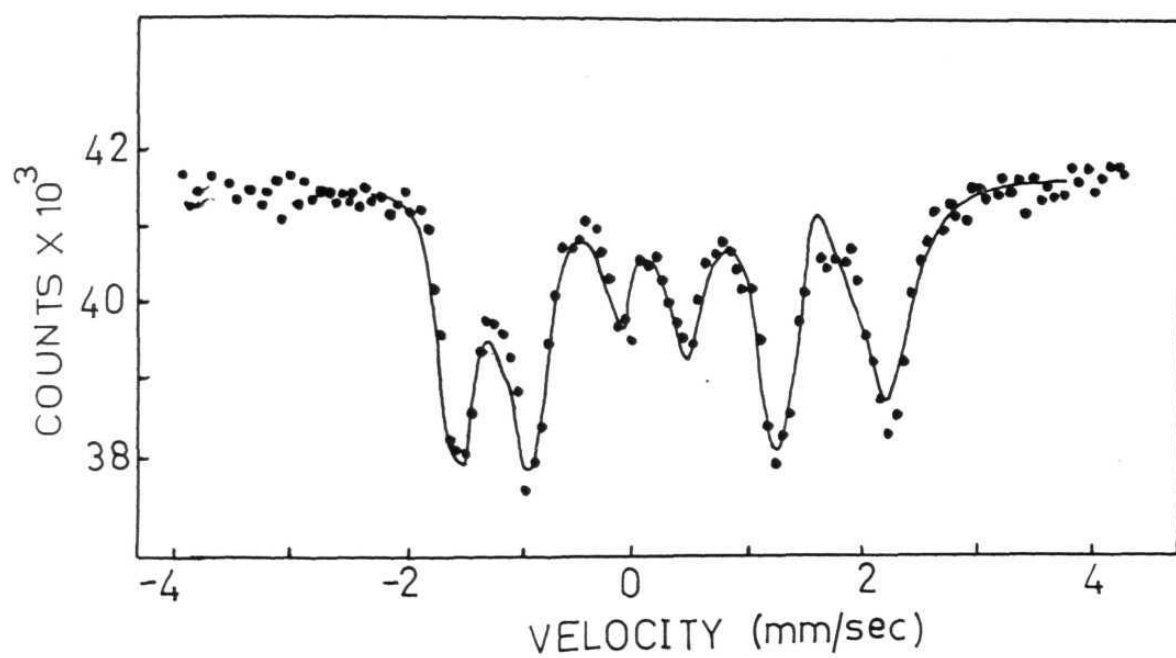


Fig.3.14 Mössbauer spectrum of  $\text{FeBO}_3$  at 348.5 K. The solid line is the composite theoretical spectrum based on the field distribution using Window's method [20].

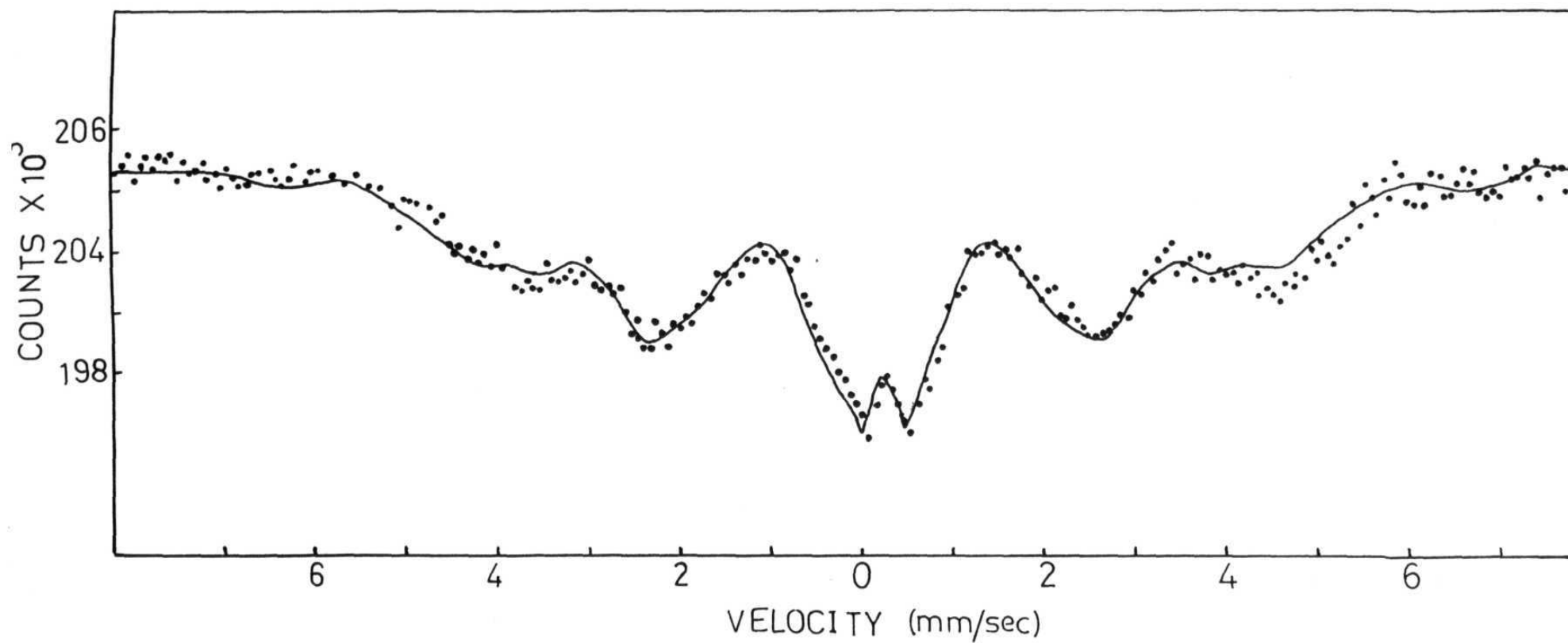


Fig.3.15 Mössbauer spectrum of  $\text{Fe}_{0.9}\text{Ga}_{0.1}\text{BO}_3$  at 296 K. The solid line is the composite theoretical spectrum using Window's method [20].

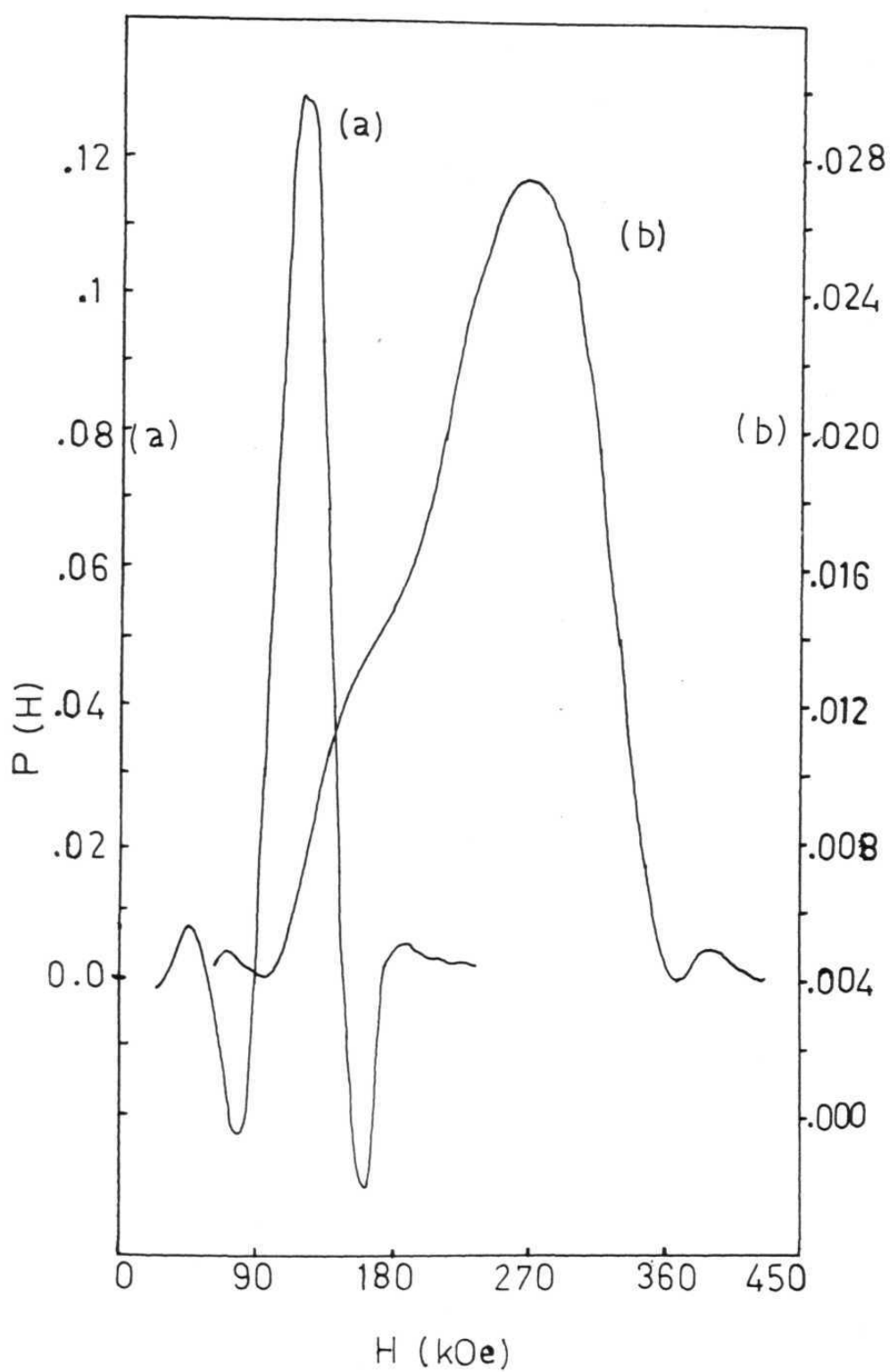


Fig.3.16 Hyperfine-field distribution  $P(H)$  of  
 (a)  $\text{FeBO}_3$  at 348.5 K and  
 (b)  $\text{Fe}_{0.9}\text{Ga}_{0.1}\text{BO}_3$  at 296 K.

$T_c$  using this method of analysis were not successful indicating cluster formation leads to superparamagnetism and hence time dependent relaxation phenomena become important close to  $T_c$ .

It was found that the line profiles of the solid solution  $Fe_{.9}Cr_{.1}BO_3$  could not be closely reproduced particularly in the central portion of the spectrum using either of the expressions based on the relaxation mechanisms viz., eqs. 2.22 or 2.26. The influence of substitution by another magnetic ion with a different spin state such as  $Cr^{3+}$  has always resulted in observations not well accounted. For instance (i) partial  $Cr^{3+}$  substitution of  $Fe^{3+}$  in  $CaFe_2O_4$  led to several magnetic phases in equilibrium with each other [40], (ii)  $Cr^{3+}$  substituted  $LiFeO_2$  shows anomalous susceptibility behaviour [41], (iii) a theoretical analysis predicts a sign reversal for the superexchange interaction parameters  $I(Fe, Cr)$  as a function of  $\theta$  the super exchange angle [42], (iv) for certain compositions of  $(Fe_{1-x}Cr_x)_2O_3$ , the reduced field vs reduced temperature plots show quite unexpected results [43], (v) the anomalous spectra showing relaxation effects in the  $(Cr_2O_3/Fe_2O_3)$  in  $Al_2O_3$  showed the existence of cross-spin relaxation [44].

Compositional dependence studies in the solid solution of  $FeBO_3$ - $CrBO_3$  shows competition between the two related

structures resulting in a weakly ferromagnetic to antiferromagnetic interaction as one goes from iron rich to chromium rich composition. Although the overall profiles for the  $\text{Cr}^{3+}$  substituted  $\text{FeBO}_3$  could be simulated with similar relaxation times, agreement in the central portions of the spectra were found to be poor. It may also be mentioned here that the results of the Mössbauer measurement, are treated here assuming a two level problem with regard to the spin states although for  $\text{Fe}^{3+}$ ,  $S = 5/2$ . But the observed anomaly cannot be ascribed simply to this approximation only as the line profiles obtained in this two cases are closely similar [36,45].

### 3.4. Conclusions

Mössbauer study of  $\text{FeBO}_3$  and the solid solutions  $\text{Fe}_{0.9}\text{Ga}_{0.1}\text{BO}_3$ ,  $\text{Fe}_{0.9}\text{Al}_{0.1}\text{BO}_3$  and  $\text{Fe}_{0.9}\text{Cr}_{0.1}\text{BO}_3$  shows that their Curie temperatures are 352, 319, 317 and 335 K respectively. The reduced hyperfine field follows the Brillouin behaviour for  $S = 5/2$  when plotted against reduced temperature. A static model assuming hyperfine field distribution due to different coordinations such as the one put forward by Coey [16] is found to be inadequate in explaining the spectra measured close to  $T_c$  in these cases. It is found that the relaxation models well account for the profiles close to  $T_c$ .



Estimates of activation energies for the spin-flip have been found to be  $9.93 \times 10^{-13}$  erg/degree and  $5.87 \times 10^{-13}$  erg/degree for  $\text{Fe}_{0.9}\text{Al}_{0.1}\text{BO}_3$  and  $\text{Fe}_{0.9}\text{Ga}_{0.1}\text{BO}_3$  respectively. In the parent material viz.,  $\text{FeBO}_3$  relaxation effects are important only very close to  $T_c$  i.e  $1^\circ$  below  $T_c$ . In the solid solutions relaxation effects dominate even  $15^\circ$  below  $T_c$ . It is found necessary to include  $\eta$  the order parameter signifying a differentiation in the probabilities of different spin states and a partial order, in the line-shape expression for simulating spectra close to experimentally observed results. The results show that the superparamagnetic relaxation effects due to the presence of clusters produced by substitution of magnetic by non-magnetic ions are important. Evidence for the presence of clusters is obtained by obtaining a distribution in the hyperfine field by a model independent approach due to Window [20] in analysing the spectra. Simple relaxation models have been found to be inadequate in fully reproducing the experimental spectra close to  $T_c$  for  $\text{Fe}_{0.9}\text{Cr}_{0.1}\text{BO}_3$ . The possible reasons for this have been pointed out in the light of experimental and theoretical observations in  $\text{Cr}^{3+}$  substituted systems in literature.

# References::

1. J.F. Dillon Jr, J. Appl, Phys. 39, 922 (1968).
2. I. Bernal, C.W. Struck and J.G. White, Acta. Crystallogr. 16, 849 (1963).
3. J.C. Joubert, T. Shirk, J.B. White and R. Roy, Mater. Res. Bull. 3, 671 (1968).
4. A.J. Kurtzig, R. Wolfe, R.C. LeCraw and J.W. Nielsen, Appl. Phys. Lett. 14, 350 (1969).
5. R.C. LeCraw, R. Wolfe and J.W. Nielsen, Appl. Phys. Lett. 14, 352 (1969).
6. R. Wolfe, A.J. Kurtzig and R.C. LeCraw, J. Appl. Phys. 41, 1218 (1970).
7. R. Diehl, Solid State Commun. 17, 743 (1975).
8. M. Pernet, D. Elmalesh and J.C. Joubert, Solid State Commun. 8, 1583 (1970).
9. M.P. Petrov, G.A. Smoleusky, A.P. Paugurt, and S.A. Kizhaev, AIP. Conf. Proc. 5, 379 (1971), Amer. Inst. of Physics.
10. N.M. Salanskii, Z.A. Glozman and V.N. Seleznev, Sov. Phys. JETP. 41, 704 (1975).
11. N.M. Salanskii, E.A. Glozman and V.N. Seleznev, Phys. Status Solidi a36, 779 (1976).

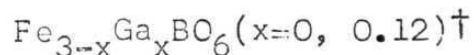
12. M. Eibschutz, L. Pfeiffer and J.W. Nielsen, J. Appl. Phys. 41, 1276 (1970).
13. O. Muller, M.P.O'Horo and J.F.O'Neill, J. Solid State Chem. 23, 115 (1978).
14. M.W. Ruckman, R.A. Levy and R. Chennette, J. Appl. Phys. 53, 1694 (1982).
15. J.M.D. Coey and G.A. Sawatzky, Phys. Status Solidi b44, 673 (1971).
16. J.M.D. Coey, Phys. Rev. B6, 3240 (1972).
17. M. Blume and J.A. Tjon, Phys. Rev. 165, 446 (1968).
18. S. Dattagupta in Advances in Mössbauer Spectroscopy edited by B.V. Thosar, P.K. Iyengar, J.K. Srivastava and S.C. Bhargava. (Elsevier, New York, 1983), p.586.
19. F. van der Woude and A.J. Dekker, Phys. Status Solidi 9, 775 (1965).
20. B. Window, J. Phys. E4, 401 (1971).
21. A. Narayanasamy, T. Nagarajan, P. Muthukumarasamy and T.S. Radhakrishnan, J. Phys. F9, 2261 (1979).
22. M. Eibschutz and M.E. Lines, Phys. Rev. B7, 4907 (1973).
23. J.K. Srivastava, S.C. Bhargava, P.K. Iyengar and B.V. Thosar in 'Advance In Mössbauer Spectroscopy' edited by B.V. Thosar P.K. Iyengar, J.K. Srivastava and S.C. Bhargava, (Elsevier, New York, 1983), p.1.

24. H. Gabriel, J. Besse and K. Rander, Phys. Status Solidi. 27, 301 (1968).
25. H.H. Wickman in Mössbauer Effect Methodology edited by I. Gruverman (Plenum Press, New York, 1966). Vol. 2 p, 39.
26. Yu. Kagan and A.M. Afanas'ev, Sov. Phys. JETP, 20, 743 (1965).
27. H. Wegener, Z. Physik 186, 498 (1967).
28. L.M. Levinson and M. Luban, Phys. Rev. 172, 268 (1968).
29. V.U.S. Rao, F.E. Huggins and G.P. Huffman, J. Appl. Phys. 50, 2408 (1979).
30. L.M. Levinson, M.Luban and S. Shtrikman, Phys. Rev. 177, 864 (1969).
31. F. van der Woude and A.J. Dekker, Phys. Status Solidi 13, 181 (1966).
32. D.E. Cox, G. Shirane, P.A. Flinn, S.L. Ruby and W.J. Takei, Phys. Rev. 132, 1547 (1963).
33. M. Eibschutz, S. Shtrikman and D. Treves, Phys. Rev. 156, 562 (1967).
34. I. Deszi and M. Foder, Phys. Status Solidi 15, 247 (1966).
35. H. Yamamoto, T. Okada, H. Watanabe and M. Fukase, J. Phys. Soc. Jpn. 24, 275 (1968).

36. R. Nagarajan and J.K. Srivastava, Phys. Status Solidi b81, 107 (1977).
37. C.M. Srivastava, S.N. Shringi and R.G. Srivastava, Phys. Rev. B 14, 2041 (1976).
38. J.M. Trooster, Phys. Lett. 16, 21 (1965).
39. H.H. Wickman, in Hyperfine Structure and Nuclear Radiations edited by E. Matthias and D.A. Shirley (North Holland, Amsterdam, 1968), p.930.
40. L.M. Corliss, J.M. Hastings and W. Kunmann, Phys. Rev. 160, 408 (1967).
41. A. Tauber, W.M. Moller and E. Banks, J. Solid State Chem. 4, 138 (1972).
42. A.S. Moskvina, N.S. Ovanesyan and V.A. Trukhtanov, Hyp. Inter. 1, 265 (1975).
43. T. Birchall and A.F. Reid., J. Solid State Chem, 13, 351 (1975).
44. J.K. Srivastava and B.W.Dale, Phys. Status Solid: b90, 391 (1978).
5. Ref. 23, p.68.

## CHAPTER 4

### A MÖSSBAUER STUDY OF HYPERFINE INTERACTIONS IN THE BOROFERRITE



#### Abstract

$\text{Fe}_3\text{BO}_6$  and 4%  $\text{Ga}^{3+}$  substituted  $\text{Fe}_3\text{BO}_6$  have been found to undergo spin-reorientation at 418 and 403 K respectively. The hyperfine field in the vicinity of spin-reorientation temperature ( $T_{\text{SR}}$ ) shows no hysteresis effects either in  $\text{Fe}_3\text{BO}_6$  or in  $\text{Fe}_{2.88}\text{Ga}_{0.12}\text{BO}_6$  inspite of being a first order phase transition as shown by the change in the quadrupole splitting. A comparison of our results has been made with those reported for  $\alpha\text{-Fe}_2\text{O}_3$ . The reduced hyperfine field vs reduced temperature in the case of  $\text{Fe}_3\text{BO}_6$  and  $\text{Fe}_{2.88}\text{Ga}_{0.12}\text{BO}_6$  shows that 8d site follows the Brillouin curve for  $S = 5/2$  closely unlike the 4c site which shows consistently higher values than expected for  $S = 5/2$  and requires inclusion of the biquadratic exchange term  $j/J = 0.015$ . The critical exponent  $\beta$ , for the two sites show a 'splitting'. The Mössbauer spectrum of  $\text{Fe}_{2.88}\text{Ga}_{0.12}\text{BO}_6$  far away from  $T_c$  is simulated using Coey's model and an exchange constant  $J \sim 10 \text{ cm}^{-1}$  has been evaluated.

---

<sup>†</sup>Part of this work is published in Bull. Mater. Sci. 6, 33 (1984).

#### 4.1. Introduction

Study of magnetic interactions of the order-disorder type where one magnetic structure loses its stability and a new structure with a different magnetic symmetry becomes stable is of considerable theoretical and experimental interest [1-3]. Among the borates  $\text{Fe}_3\text{BO}_6$  happens to be the only system exhibiting spin-reorientation and has been studied in some detail both by magnetic as well as Mössbauer measurements [4-6]. However these studies show differences in their observations and conclusions [5-7]. Further, two aspects, (i) the possible hysteresis effects suggested on the strength of microscopic models to explain spin-reorientation and (ii) the effect of substitution have not been so far investigated in this system. We report here the Mössbauer measurements on  $\text{Fe}_3\text{BO}_6$  and  $\text{Fe}_{2.88}\text{Ga}_{0.12}\text{BO}_6$  in the temperature range 77-518 K and compare our results with those of different workers on related systems such as  $\alpha\text{-Fe}_2\text{O}_3$  where results of parallel studies are available. An attempt is made to explain the differences in the hyperfine fields at the inequivalent sites on the basis of structural factors and account for the deviation from the Weiss molecular field theory by considering the biquadratic exchange interaction terms. Employing Coey's model for simulating Mössbauer

spectra of diamagnetically substituted systems information on coordination sites, associated hyperfine fields and exchange interaction are derived.

#### 4.2. Experimental procedure and analysis of data

The reported preparation of  $\text{Fe}_3\text{BO}_6$  uses  $\text{Bi}_2\text{O}_3$  flux or the ceramic technique [4,8]. Muller has reported the formation of  $\text{Fe}_3\text{BO}_6$  as a stable intermediate in a slow formation of  $\text{FeBO}_3$  from  $\text{B}_2\text{O}_3$  flux [9]. This procedure is adapted for the preparation of  $\text{Fe}_3\text{BO}_6$  as follows. Ferric nitrate (B.D.H) and boric acid (B.D.H) were used as the starting materials. Stoichiometric mixture of boric acid and ferric nitrate is dissolved in warm deionised water with a 400% excess of boric acid. The solution is slowly evaporated to dryness. The dried material is mixed thoroughly with acetone and loaded into a platinum crucible. The mixture is heated slowly at  $500^\circ\text{C}$  and kept at that temperature for 12 hrs. and finally at  $800^\circ\text{C}$  for 2 days. After cooling to room temperature the product is dissolved in hot water to remove excess  $\text{B}_2\text{O}_3$ . After filtration the product is dried under vacuum. For the substituted compound, required amount of gallium was taken as  $\text{Ga}_2\text{O}_3$  (Koch-Light Labs) and was converted to the nitrate by dissolving in nitric acid and subsequently the ferric



nitrate and boric acid solutions were added. The subsequent steps were the same as described above. The ir spectra of both the compounds were found to agree well with the spectrum reported for  $\text{Fe}_3\text{BO}_6$  [8]. Mössbauer spectra showed no contribution due to iron oxide or any other species. The powder X-ray diffractograms confirmed the formation of the compounds and absence of impurities. Mössbauer spectra were recorded as described earlier (section 2.1.1).

An estimate of  $\eta$ , the asymmetry parameter,  $\theta$  and  $\phi$  the Euler angles giving the orientation of the electric field gradient (e.f.g) relative to the  $H_{\text{eff}}$ , the hyperfine field and  $R = \text{e.f.g}/H_{\text{eff}}$  were obtained by comparing the experimental line positions with the theoretical plots similar to those described by Kundig [10a]. A computer programme based on this method is used for the purpose of analysing the line positions [10b].  $R$  was then varied to get the theoretical line positions that matched with experimental within  $\pm 0.04$  mm/sec. Knowing  $H_{\text{eff}}$  from experimental positions e.f.g. was calculated from the value of  $R$ .

#### 4.3. Results and discussion

The Mössbauer spectra of  $\text{Fe}_3\text{BO}_6$  were recorded in the temperature range 77–520 K. The spectra recorded at 77K and room temperature show close similarity with those reported for the single crystal [4].  $\text{Fe}_3\text{BO}_6$  is known to have iron in two inequivalent sites in an orthorhombic unit cell [11]. In the low temperature spectrum the two hyperfine spectra arising due to the inequivalent sites overlap considerably unlike in the case of spectra measured at room temperature and above as shown in Figure 4.1. The higher temperature spectra show good resolution enabling easy identification of the two sextets with relative intensities in the ratio 2:1. The spectra recorded close to the spin reorientation temperature ( $T_{\text{SR}}$ ) both above as well as below are reproduced in Figure 4.2 for comparison. The spin reorientation could be identified by the change in the splitting of the first and the last pairs of lines for both the sites and is found to occur at 418 K. The transition is found to be abrupt and takes place within  $1^\circ$  range. The  $T_{\text{SR}}$  value obtained is slightly higher than the value reported by susceptibility measurements viz., 415 K [4,12]. These spectra were analysed for hyperfine parameters viz., isomer-shift, quadrupole split and hyperfine field for the two sites from the line

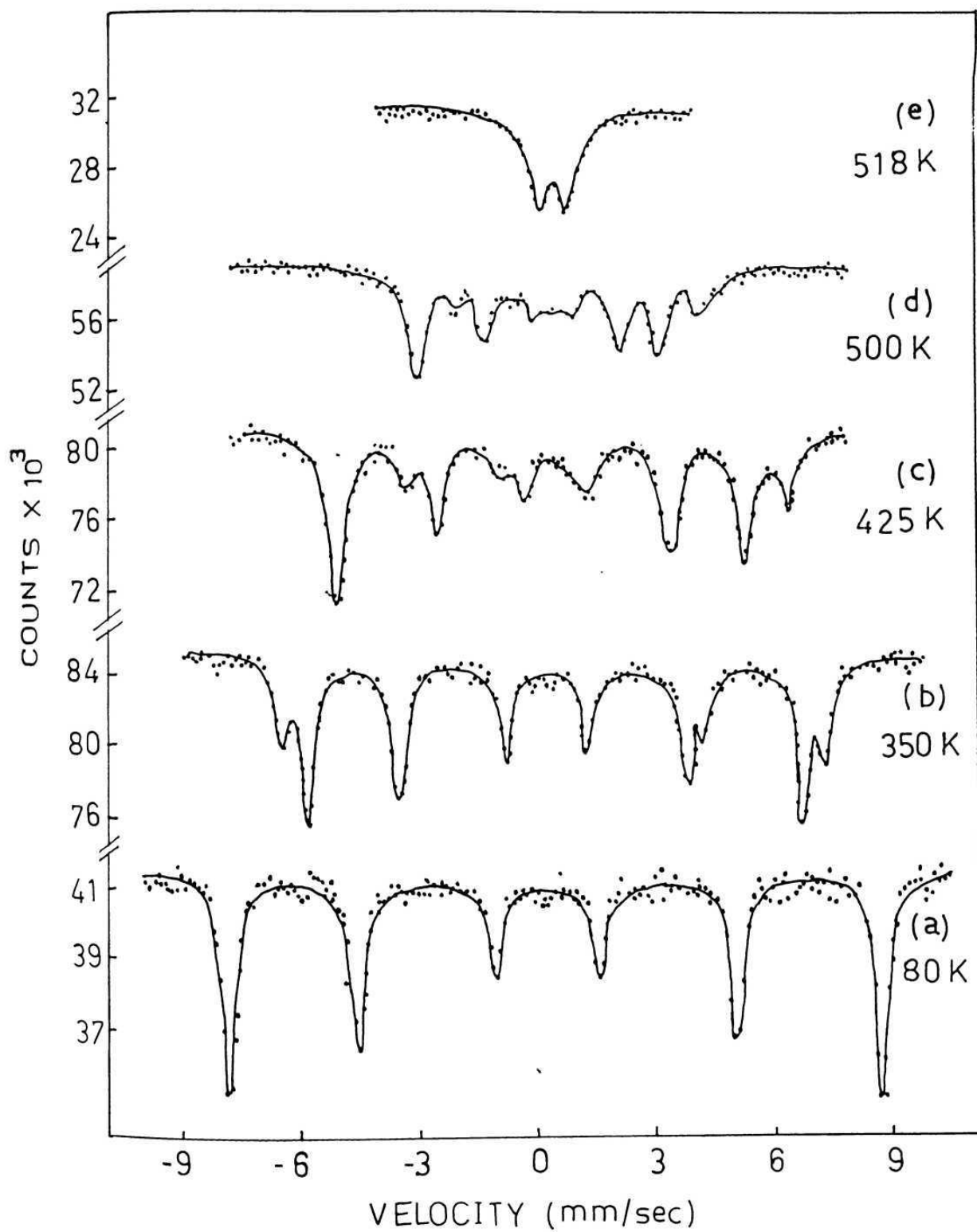


Fig.4.1 Mössbauer spectra of  $\text{Fe}_3\text{BO}_6$  from 80 to 518 K.

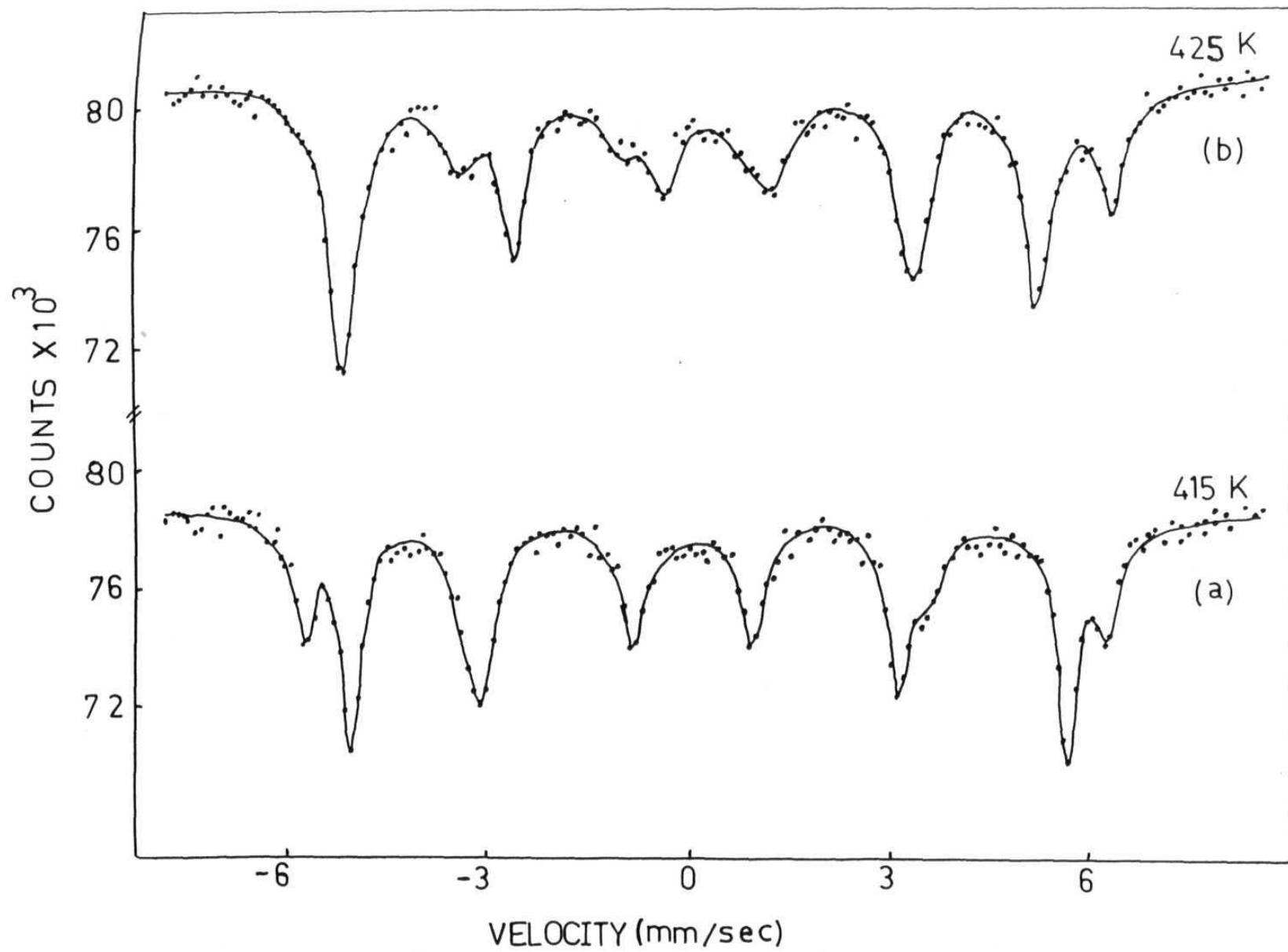


Fig.4.2 Mössbauer spectra of  $\text{Fe}_3\text{BO}_6$  (a) below and (b) above  $T_{\text{SR}}$ .

positions as described in the experimental section and are given in Table 4.1. Further, the spectra were recorded below and above  $T_{SR}$  by heating and cooling the sample in a cyclic manner. It was found that the spectra could be fully reproduced for a given temperature irrespective of the heat treatment. This observation shows that  $Fe_3BO_6$ , unlike  $\alpha-Fe_2O_3$  [2,13] does not show any thermal hysteresis behaviour. The variation in the isomer shift, quadrupols splitting and the hyperfine field as a function of temperature in the vicinity of  $T_{SR}$  are shown in Figure 4.3. The variation of  $H_{eff}(T)$  vs  $T$  when extrapolated to  $H_{eff}(T) = 0$  gave a Curie temperature of 518 K. This value is verified by the observation of a paramagnetic spectrum resulting from the collapse of the hyperfine spectrum at this temperature (Fig. 4.1). The Curie temperature thus determined is found to be significantly higher than 508 K reported from susceptibility measurements [4].

The plot of reduced hyperfine fields  $H_{eff}(T)/H_{eff}(0)$  for the two sites as a function of reduced temperature is given in Figure 4.4. It is found that one of the two sites viz., (8d) followed a behaviour close to that predicted by the Brillouin function based on Weiss molecular field theory [14]. On the other hand the 4c site showed consistently higher values of  $H_{eff}(T)/H_{eff}(0)$  for the reduced hyperfine

Table 4.1. Experimental values of  $\epsilon$  and q.s. obtained from line positions below and above  $T_{SR}$ .

Site	T(K) ( $\pm 0.5$ )	$\theta$	$\epsilon$ (mm/sec)* ( $\pm 0.04$ )	Q.S (mm/sec) ( $\pm 0.04$ )
8d	350	90	-0.53	-0.53
	425	0	+0.79	-0.42
4c	350	90	-0.35	-0.35
	425	0	-0.98	+0.49

\*  $\epsilon = \Delta_{12} - \Delta_{56}$  where  $\Delta_{12}$  and  $\Delta_{56}$  are the splittings between lines 1, 2 and 5, 6 respectively.

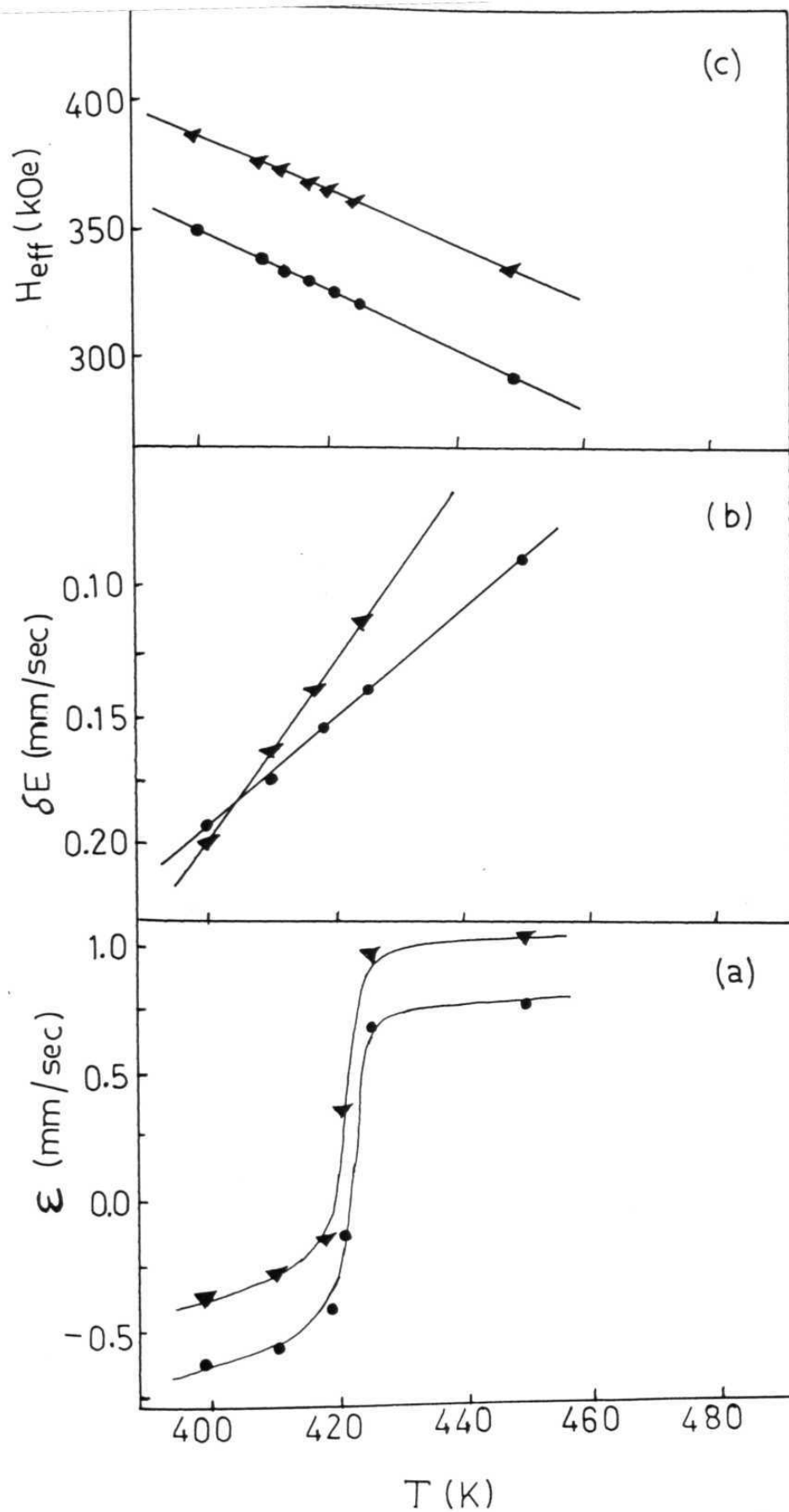


Fig.4.3 Plots of (a)  $\epsilon$  (where  $\epsilon = \Delta_{12} - \Delta_{56}$ ) (b) Isomer-shift relative to  $^{57}\text{Co/Rh}$  and (c) Effective magnetic field ( $H_{eff}$ ) vs temperature in the vicinity of  $T_{SR}$ . • and ▼ are the experimental points for the 8d and 4c sites respectively.

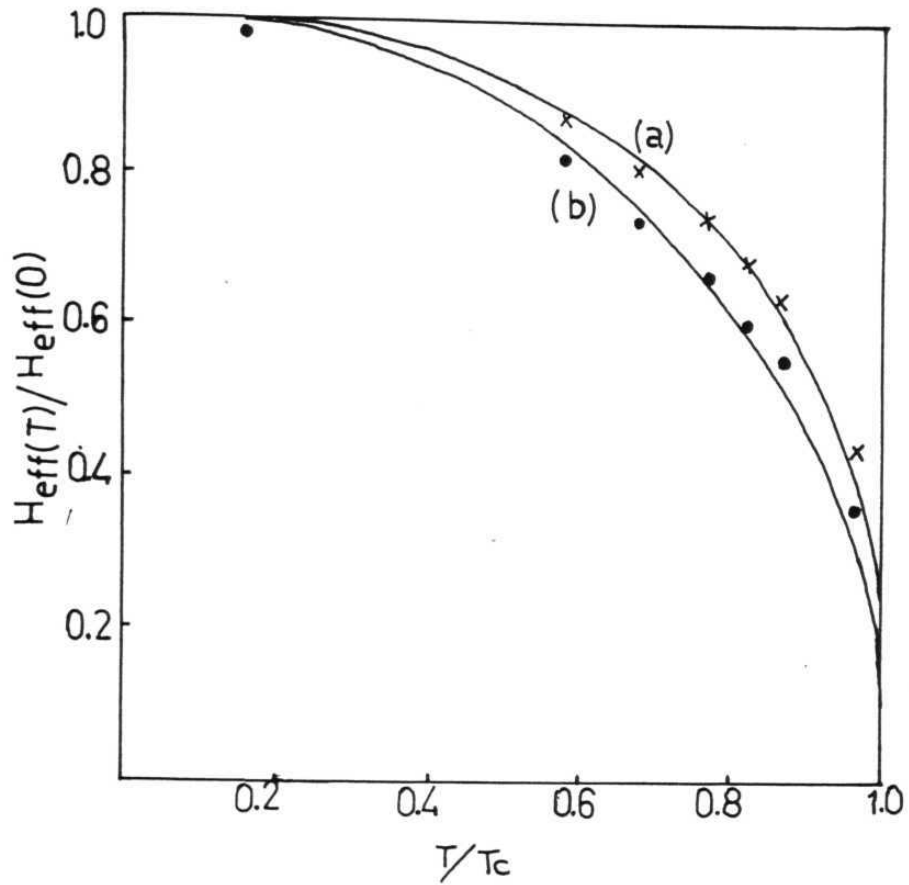


Fig.4.4 Reduced hyperfine field vs reduced temperature in the case of  $\text{Fe}_3\text{BO}_6$ . Solid spheres and crosses are experimental points for the 8d and 4c sites respectively. Solid line (a) is the theoretical Brillouin curve for  $S = 5/2$  and (b) for  $S = 5/2$  including biquadratic exchange  $j/J = 0.015$ .



field with a significant deviation from the Brillouin curve as shown in Figure 4.4. Such a deviation can be explained on the basis of a biquadratic contribution to the linear isotropic exchange interaction as suggested by Rodbell et al [15]. The theoretical Brillouin Curve including the biquadratic exchange term with a  $j/J$  value of 0.015 is found to show close agreement with experimental data (Fig. 4.4).

An analysis of the temperature dependence of the hyperfine field can give information about the behaviour of the system at the critical temperature  $T_c$ . At temperatures close to  $T_c$ ,  $H_{\text{eff}}(T)/H_{\text{eff}}(0)$  will follow the power law  $H_{\text{eff}}(T)/H_{\text{eff}}(0) = D(1-T/T_c)^\beta$  and thus one can get the critical exponent  $\beta$  for the two sites. The double log plots of  $H_{\text{eff}}(T)/H_{\text{eff}}(0)$  vs  $(1-T/T_c)$  are given in Figure 4.5. The values of  $\beta$  obtained from the slopes of the plots were found to be 0.27 and 0.31 for the 4c and 8d sites respectively.

The Mössbauer spectra for the substituted sample  $\text{Fe}_{2.88}\text{Ga}_{0.12}\text{BO}_6$  were recorded from 77 to 494 K. Representative spectra are shown in Figure 4.6. The lines of the two hyperfine spectra observed for the solid solution were more broad and as a result showed less resolution of the sextets. This sample is also found to show spin reorientation

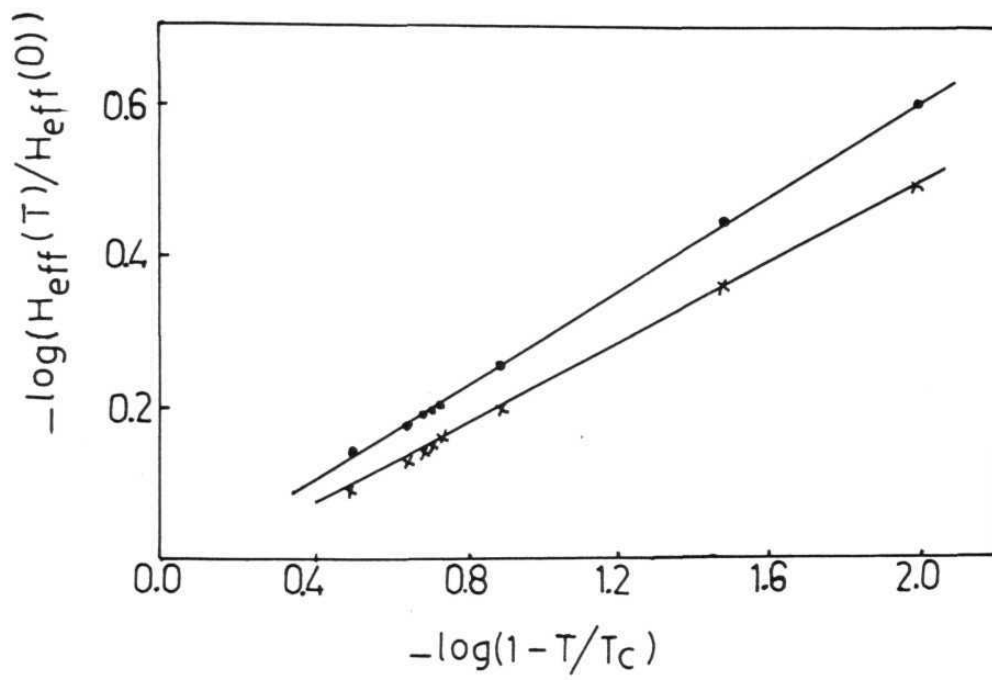


Fig.4.5 Double log plots of  $H_{\text{eff}}(T)/H_{\text{eff}}(0)$  vs  $(1-T/T_c)$  for  $\text{Fe}_3\text{BO}_6$ . Solid spheres and crosses are experimental points for 8d and 4c sites respectively.

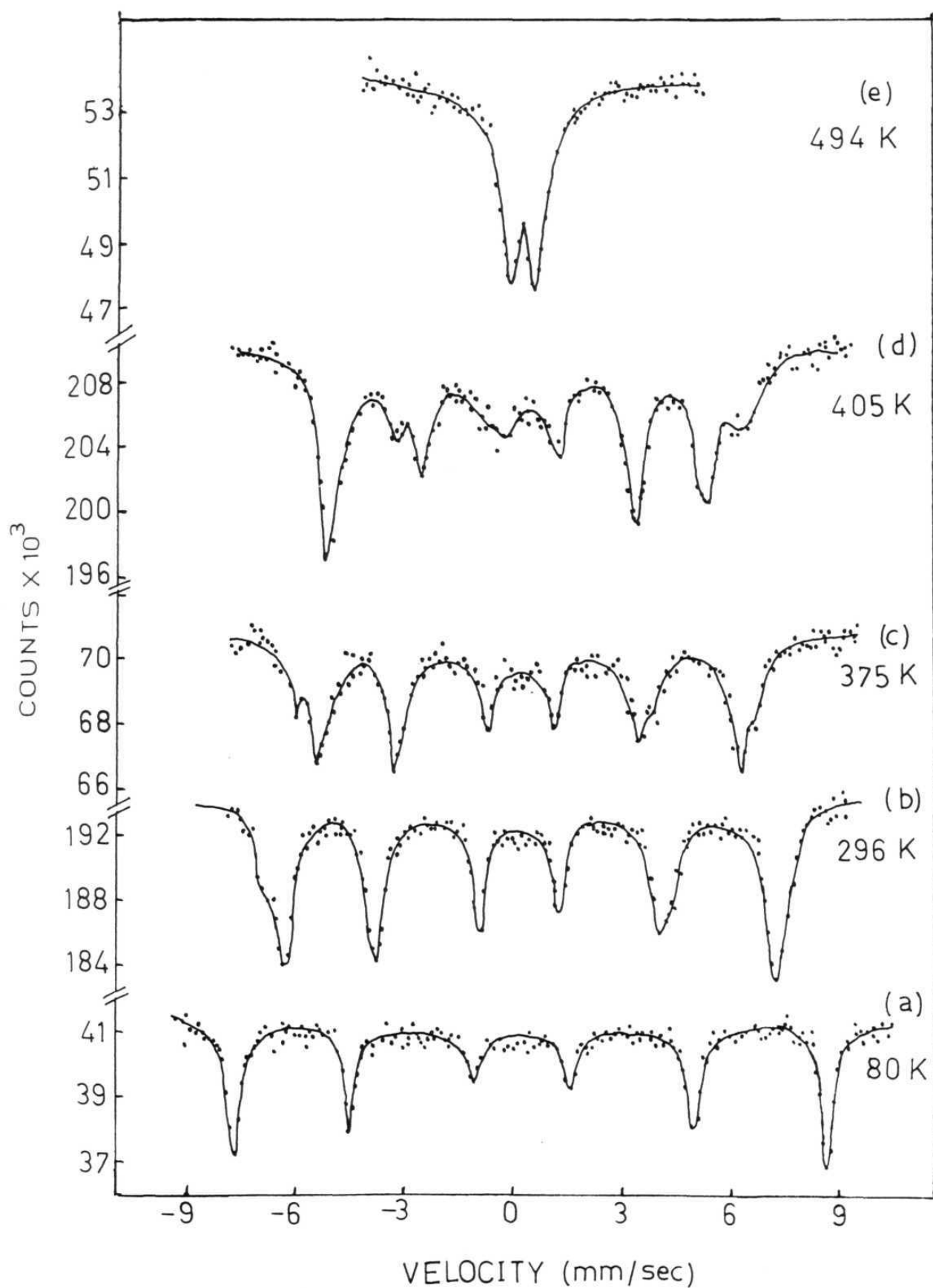


Fig.4.6 Mössbauer spectra of  $\text{Fe}_{2.88}\text{Ga}_{0.12}\text{BO}_6$  from 80 to 494 K.

at 403 K as shown by significant changes in the  $\Delta_{12}$  and  $\Delta_{56}$  values for the two sites. The temperature dependence of the hyperfine parameters showed a trend similar to that exhibited by the parent material (Fig. 4.3).  $H_{\text{eff}}(T)$  vs  $T$  is found to lead to a Curie temperature of 494 K for the substituted sample compared to 518 K for the parent material. Further a plot of reduced magnetic field vs reduced temperature showed that the nature of the Brillouin plots did not significantly alter compared to the plots for the parent material and required inclusion of biquadratic exchange term with a  $j/J$  value of 0.015 for the 4c site.

#### 4.3.1. Nature of spin-transition

The phenomena of spin reorientation can proceed in two ways. (a) The magnetic moment vector may rotate continuously and coherently from the x-axis to the z-axis. (b) The magnetic moment vector jumps discontinuously from x-axis to the z-axis. The former is explained by the Landau's theory of second order phase transition. On the other hand, process (b) arises from the local first order phase transition.

Kamzin and Bokov carried out detailed single crystal Mössbauer studies of  $\text{Fe}_3\text{BO}_6$  in the temperature range 395–416 K in the presence of applied magnetic field and established

first order phase transformation for spin reorientation on the observation of coexistence of the two magnetic phases [16]. Consequently it is quite interesting to compare the behaviour for  $\text{Fe}_3\text{BO}_6$  with that of  $\alpha\text{-Fe}_2\text{O}_3$  as they show several differences in spite of both being shown to follow a first order transformation. For example in  $\alpha\text{-Fe}_2\text{O}_3$ , spin reorientation is accompanied by a break in the plots of isomer shift and hyperfine field vs temperature [17]. Further a thermal hysteresis behaviour is observed over a temperature range of  $15^\circ$  around  $T_{\text{SR}}$  and was explained on the basis of first order transition accompanied by a phase transformation [2]. Our results on  $\text{Fe}_3\text{BO}_6$  show neither a break in the hyperfine field, isomer-shift vs temperature plots (Fig. 4.3) nor a thermal hysteresis behaviour and the transition occurs within  $1^\circ$ .

It is found that the line positions of the Mossbauer spectra recorded below and above  $T_{\text{SR}}$  could be reproduced using the Hamiltonian which includes the magnetic and quadrupolar interactions [10a, 10b] only if it is assumed that the magnetic field lies perpendicular and parallel to the principal axis of the electric field gradient tensor respectively (Table 4.1). Earlier studies show that the easy axis is parallel to 100 and 001 axis respectively below and

and above  $T_{SR}$  [4]. These results are consistent with our analysis if it is assumed that the principal e.f.g. axis lies along the z-axis. Table 4.1 shows that the  $\mathcal{E}$  value corresponding to  $\Delta_{12} - \Delta_{56}$  does not change to simply  $-2\mathcal{E}$  which happens to be the case for example in  $\alpha\text{-Fe}_2\text{O}_3$  implying only an orientation change in the latter. This clearly indicates a change in the quadrupole splitting (Table 1) during spin reorientation. Further, for the 4c site it is also found that a change in the sign of e.f.g. is required to reproduce the line positions of the hyperfine split spectrum. Our own results in this regard are in general agreement with the preliminary report of Bayukov *et al* but the signs in all the cases are just the reverse [18]. These results clearly show that spin reorientation is accompanied by structural change. However as isomershift is not a sensitive parameter for  $3d^5$  systems the structural change is not shown up in isomer-shift vs temperature plot. The non-observance of a break in the hyperfine field vs temperature may be explained on the basis of relative contributions to the hyperfine field from different sources. The effective field at the nucleus is given by

$$H_{\text{eff}} = H_C + H_D + H_L \quad \dots (4.1)$$

where  $H_C$  is the contact field,  $H_D$ , the dipolar field and  $H_L$

arises due to the orbital magnetic moment of the 3d electrons.  $H_C$  the contact field is the largest contribution and arises from spin density at the nucleus ( $\sim -500$  kOe). An estimate of the dipolar field may be obtained from the relationship

$$H_D = -2\mu_B q \left\langle \sum_S \frac{3\cos^2\theta - 1}{r^3} \right\rangle$$

$$= -\mu_B q \quad \dots (4.2a)$$

for the case when the magnetization is along C axis and

$$H_D = \frac{1}{2} \mu_B q \quad \dots (4.2b)$$

when the magnetization is perpendicular to the C-axis [17].  $q$  in (4.2) may be obtained from quadrupole splitting as the values of the quadrupole moment is known. Thus using  $Q = 0.3 \times 10^{-24} \text{ cm}^2$  [17] the values of  $H_D$  obtained for the two sites below and above  $T_{SR}$  are given in Table 4.2. Thus spin reorientation involves a change in the hyperfine field equal to 13.7 kOe and 14.1 kOe for the 4c and 8d sites respectively. In the case of  $\alpha\text{-Fe}_2\text{O}_3$  a change in the hyperfine field during spin transition is attributed to the dipolar field assuming the field due to spin-orbit coupling ( $H_L$ ) to be negligible [13]. The absence of any such change in the field at  $T_{SR}$  in the present system thus implies that there is

Table 4.2. Estimates of dipolar contributions  
for the 4c and 8d sites below and  
above  $T_{SR}$ .

Site	$T(K)$ ( $\pm 0.5$ )	$H_D(kOe)$ ( $\pm 0.4$ )
8d	350	+5.4
	425	-8.6
4c	350	+3.6
	425	-10.1



a significant orbital contribution which cancels the contribution due to the dipolar term.

The microscopic models put forward for explaining reorientation of the easy axis of magnetization are based on the dependence of the thermodynamic free energy ( $F$ ), on  $\theta$ , the angle between  $\langle S \rangle$  and the Z-axis which is of the form [1].

$$F = F_0 + A_0(T) + A_2(T)\sin^2\theta + A_4(T)\sin^4\theta \quad \dots (4.3)$$

where  $A_2(T)$  and  $A_4(T)$  represent the second and fourth order single ion anisotropy contributions respectively. It is shown that in the case of spin jump mechanism,  $A_4(T) < 0$  and associated hysteresis effects are observable. To our knowledge the only attempt of correlation of the hysteresis width to any measurable parameter is due to Thomas and Staveland who pointed out that the loop area is related to the difference in the molar volumes of the two phases [19]. This has also been substantiated by experimental observations [20]. Thus the non-observance of hysteresis in our case despite the transformation being first order may be attributed to small changes in the molar volume during the transformation.

#### 4.3.2. Temperature dependence of hyperfine field

The magnetic inequivalence of the 4c and 8d sites can be understood in terms of the stronger metal-metal interaction of the 8d iron sites where the concerned octahedra are edge-sharing compared to the 4c iron sites in which the octahedra are only corner sharing (Fig. 4.7). The deviations from the Weiss molecular field theory can be successfully accounted for by including a biquadratic contribution to the linear isotropic exchange interaction of the form

$$J \cdot S_a \cdot S_b - j(S_a \cdot S_b)^2$$

where  $J > 0$  and the magnitude of  $j$  can differ depending upon the superexchange interaction [21]. The theoretical curve including such an interaction is found to give close agreement with experimental data for 4c site for  $j/J$  value of 0.015. Similar values have been obtained for other systems with  $S = 5/2$  [21,22].

#### 4.3.3. The critical exponents

Our values of  $\beta$ , the critical exponents for the two sites are close to those of Kamzin et al who also observe a 'splitting' in the  $\beta$  values [23]. Irshinskii and Cherepanov have stated that after applying correction to the field,

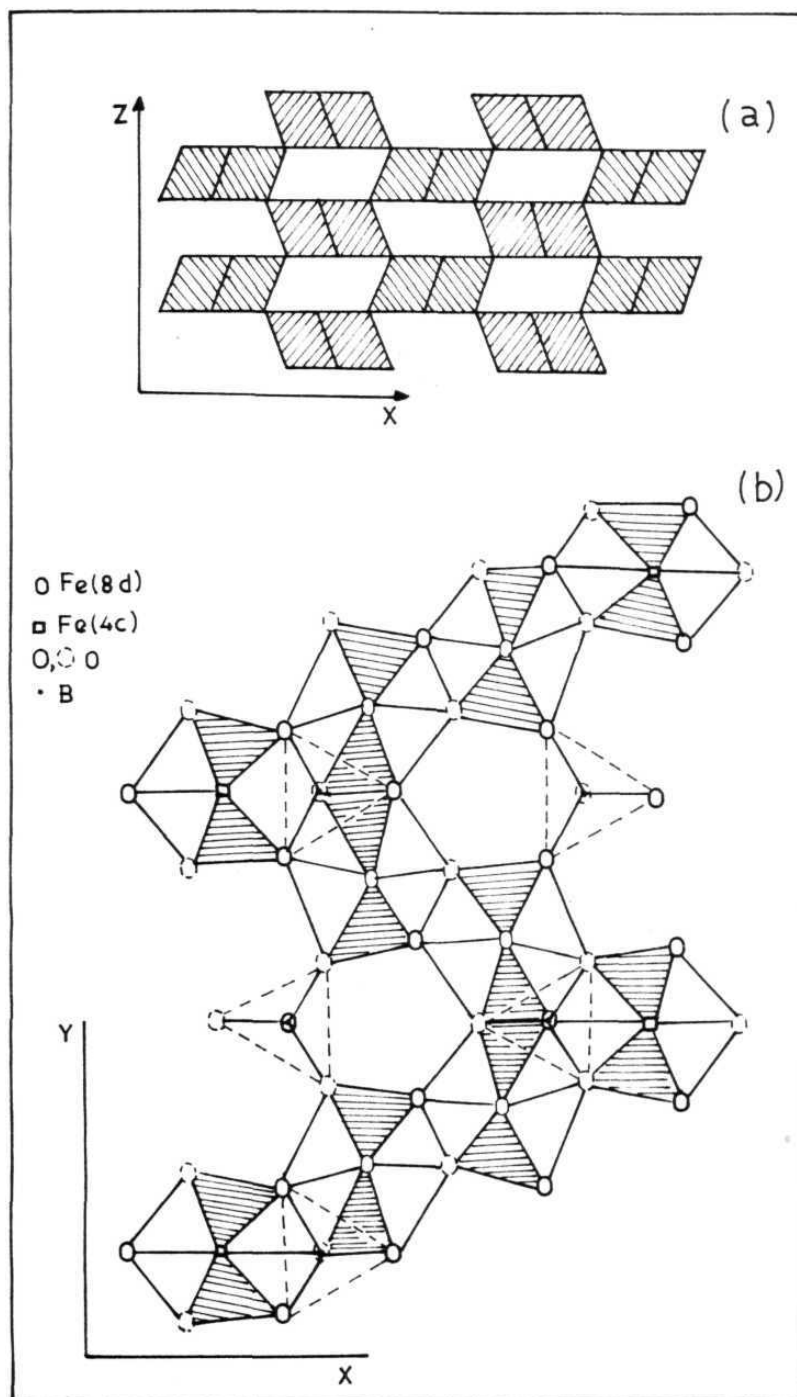
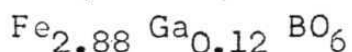


Fig.4.7 Schematic diagram of (a)  $\text{FeO}_6$  octahedra in  $\text{Fe}_3\text{BO}_6$  viewed along the y-axis contributing to interactions in the xz-plane; all the iron atoms occupy 8d sites and (b) viewed along z-axis; hatched portions depict planar ligands in the octahedra. ○ and • represent  $\text{O}^{2-}$  ions above and below xy-plane respectively.

a single  $\beta$  value agreeing with that of Voigt and Ross based on magnetic measurements is obtained [7, 24]. It may be stated that although the line positions get shifted due to quadrupole interaction the splitting between the first and the last transitions is not influenced and needs no correction for obtaining the internal magnetic field [2,17,24]. The 'split' in the  $\beta$ -values is not unreasonable in the case of  $\text{Fe}_3\text{BO}_6$  as the extent to which the interaction of the two sites with the near neighbours are weakened by the linking non metal atoms differ significantly, resulting in a corresponding change in  $\beta$  which is known to depend on the dimensionality in the magnetic interaction.

#### 4.3.4. Mössbauer studies of the substituted compound



The temperature dependence of isomershift, quadrupole splitting and hyperfine field for the substituted system  $\text{Fe}_{2.88} \text{Ga}_{0.12} \text{BO}_6$  is found to follow closely the behaviour of the parent material. Our results show that 4% substitution by the diamagnetic  $\text{Ga}^{3+}$  ion in  $\text{Fe}_3\text{BO}_6$  leads to a decrease in the  $T_{\text{SR}}$  which is found to occur at 403 K compared to that of the parent occurring at 418 K. On the other hand the Curie temperature decreases as expected as the magnetic

interaction will be weakened by the presence of the non-magnetic ion. Different substituents are known to influence the  $T_{SR}$  differently as illustrated by the reported observations presented in Table 4.3 [3,25-29]. To our knowledge the only attempt at rationalisation of the effect of substituent on  $T_{SR}$  is due to Gratz and Nowotny [3]. These authors show that an enhancement or decrease in  $T_{SR}$ , can be explained in cases where a detailed knowledge of the crystalline electric field and molecular field parameters are available [3].

The Mössbauer spectra of 4% substituted sample show the following features. The room temperature spectrum, for example shows less resolved profile (Fig. 4.6). The spectra near the Curie temperature showed in contrast with that of parent material the simultaneous presence of paramagnetic with magnetic spectra as shown in Figure 4.8. The latter situation is complex for analysis for both the effects of hyperfine field distribution due to magnetic dilution as well as relaxation play a role. However considerable information can be elicited from the Mössbauer spectra of mixed crystals recorded away from  $T_C$  employing the model of Coey [30-32]. In this model a binomial distribution is assumed for calculating the probability of the possible near neighbour environments for a given coordination around the iron site, for a given

Table 4.3. Effect of substitution on spin reorientation behaviour in systems containing Fe/R.E.

System	Effect of dopant on $T_{SR}$	Ref.
$(Ho_{1-x}Y_x)Co_2$	$T_{SR}$ increases	3
$(Nd_{1-x}Y_x)Co_2$	$T_{SR}$ decreases	3
$\alpha-(Fe_{1-x}Cr_x)_2O_3$ ( $0.005 < x < 0.02$ )	$T_{SR}$ decreases	25
$Er(Fe_{1-x}Co_x)_3$ ( $0 < x < 0.4$ )	almost same	26
	$T_{SR}$ increases	
$\alpha-(Fe_{1-x}Al_x)_2O_3$ ( $x = 0.048$ )	$T_{SR}$ decreases	27
$\alpha-(Fe_{1-x}Rh_x)_2O_3$	$T_{SR}$ increases	28
$\alpha-(Fe_{1-x}Sn_x)_2O_3$	$T_{SR}$ decreases	29

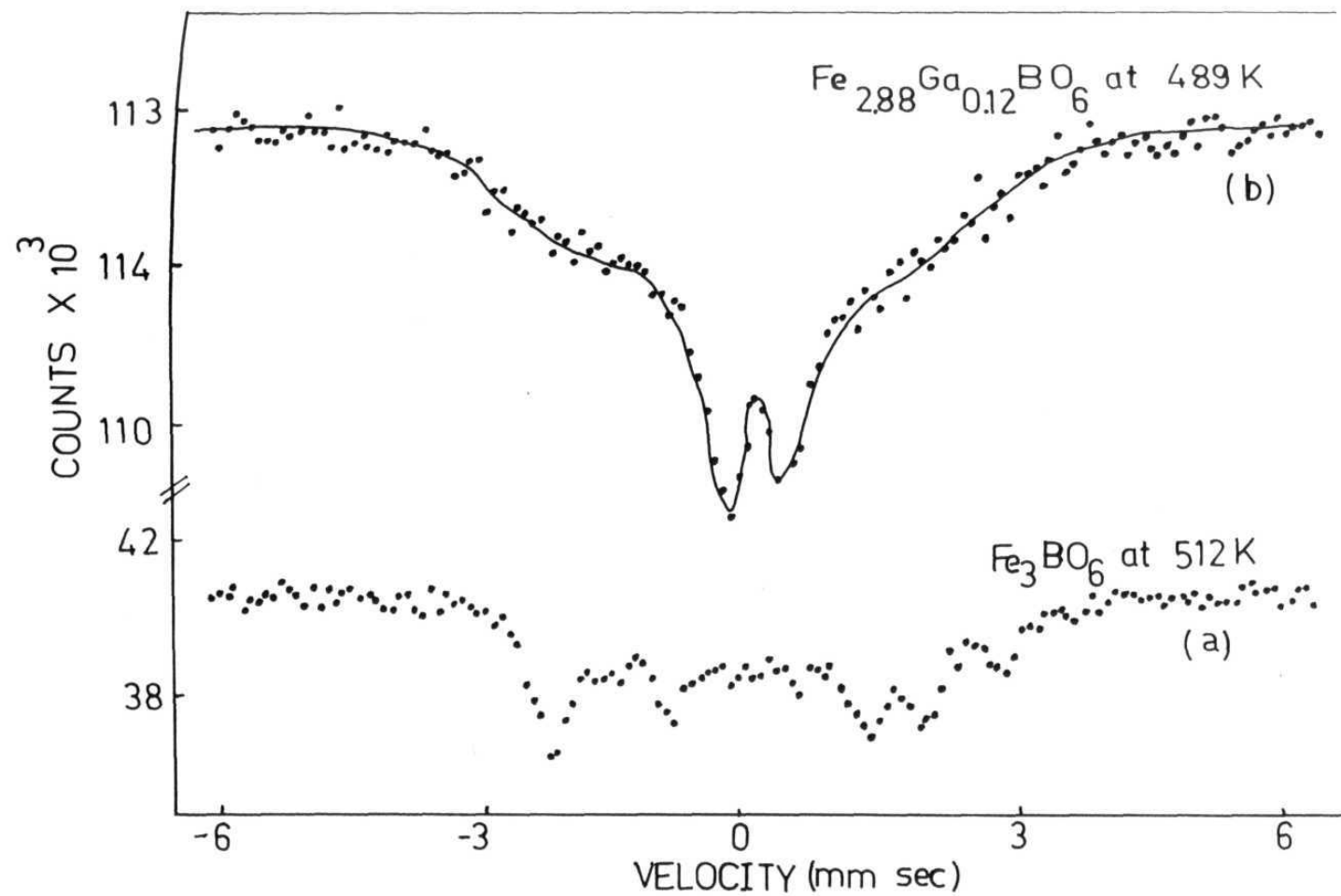


Fig.4.8 Mössbauer spectra of (a) Fe<sub>3</sub>BO<sub>6</sub> and (b) Fe<sub>2.88</sub>Ga<sub>0.12</sub>BO<sub>6</sub> close to their Curie temperatures, 518 and 494 K respectively.

concentration of the non magnetic ion. The further details of analysing the spectra on the basis of this model are given in section 2.2.2. In the present case the Mössbauer site is assumed to be surrounded by  $Z \text{ Fe}^{3+}$  ions and  $(N-Z) \text{ Ga}^{3+}$  ions where  $N = 6$ . The original model does not take into account quadrupole interaction which can be introduced in the following manner. Line positions were first calculated assuming no quadrupole interaction. Subsequently the positions were shifted such that the resultant splittings of the lines will correspond with the observed orientation of the electric field gradient with respect to the magnetic field. The quadrupole splitting is then varied to get the best match. It is found that the spectrum simulated as discussed in section 2.2.2. for  $T=0.7$  for  $x = 0.04$  agreed quite well with the measured room temperature spectrum as shown in Figure 4.9. The match also explains the large line broadening due to different coordination sites brought about by substitution. The line widths for the substituted specimen for the outermost lines were found to be  $\sim 0.65$  mm/sec compared to  $\sim 0.35$  mm/sec for the parent material supporting the applicability of the model for the present case. The probabilities of different coordinations and their resultant hyperfine fields are given in Table 4.4. The model assumes a random distribution of non-magnetic ions in the place of magnetic ions.



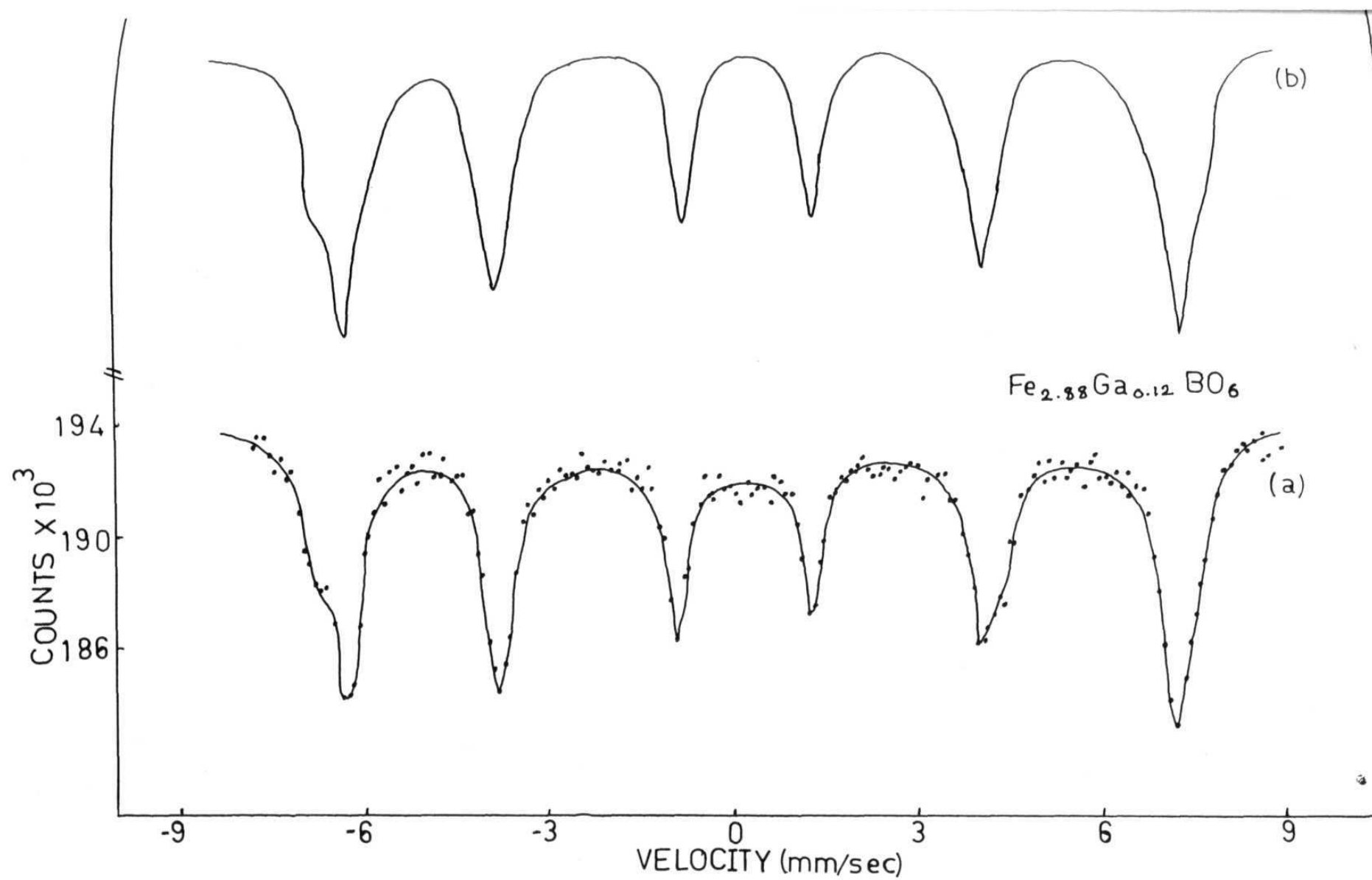


Fig.4.9 Comparison of (a) experimental Mössbauer spectrum at 296 K with (b) theoretical spectrum based on the random substitution model.

Table 4.4. Nearest neighbour probabilities and the corresponding fields for a random distribution of two types of atoms in a lattice with six nearest neighbours for  $x = 0.04$ .

Number of magnetic neighbours	Probability (%)	$H_{\text{eff}}$ (kOe)	
		4c	8d
1	< 0.1	130.0	121.5
2	< 0.1	196.6	186.8
3	0.11	252.0	239.2
4	2.04	294.4	279.6
5	19.57	326.3	310.0
6	78.27	350.2	332.6

Thus agreement with theoretical spectrum also implies that  $\text{Ga}^{3+}$  ions show no preference between 4c and 8d sites. The value for which the theoretical fit gave a good match with experiment is found to be 0.7 and corresponds to an average  $J$  value of  $\sim 10 \text{ cm}^{-1}$ .

For materials with  $x < 0.5$ , the  $\langle Z \rangle_{av}$ , the average over different coordinations is given by  $\langle Z \rangle_{av} = 6(1-x)$  for octahedral systems [27].  $T_c$  for the solid solution is proportional to  $\langle Z \rangle_{av}$  and the value thus obtained for  $x = 0.04$  would correspond to 496 K. This is in good agreement with the experimentally determined value viz., 494 K.

#### 4.4. Conclusions

Mössbauer measurements of hyperfine parameters close to  $T_{SR}$  shows no hysteresis effects unlike in the case of  $\alpha\text{-Fe}_2\text{O}_3$  although in both cases the spin-reorientation has been shown to follow first order. Thus, measurement of hysteresis effects alone cannot be considered conclusive in stating whether the reorientation takes place by first or second order mechanism. However, as is characteristic of first-order change, significant change in structure is indicated by the changes in the quadrupole interactions.

The temperature dependence of hyperfine field for the 8d site follows closely the Brillouin function for  $S = 5/2$ . The deviation of the 4c site from the Brillouin curve has been explained by including the biquadratic exchange interaction giving rise to  $j/J = 0.015$ . 4% substitution of  $\text{Fe}^{3+}$  by  $\text{Ga}^{3+}$  brings down  $T_{\text{SR}}$  from 418 to 403 K. It is found that  $\text{Ga}^{3+}$  has no site preference. Unlike in the case of experimental spectra close to  $T_c$  it is found that static model such as that of Coey can be employed for simulating the experimental spectra at temperatures far away from  $T_c$ . An exchange constant  $J \sim 10 \text{ cm}^{-1}$  has been obtained on the basis of this model.

References:

1. L.M. Levinson, M. Luban and S. Shtrikman, Phys. Rev. 187, 715 (1969) and references therein.
2. R.C. Nininger Jr. and D. Schroeder, J. Phys. Chem. Solids, 39, 137 (1978).
3. E. Gratz and H. Nowotny, J. Mag. Mag. Mater. 29, 127 (1982).
4. R. Wolfe, R.D. Pierce, M. Eibschutz and J.L. Nielsen, Solid state Comm. 7, 949 (1969).
5. C. Voigt, Phys. Lett. 53A, 223 (1975).
6. A.S. Kamzin and V.A. Bokov, Sov. Phys. Solid State, 19, 1247 (1977).
7. A.L. Irshinskii and V.M. Cherepanov, Sov. Phys. JETP. 52, 714 (1980).
8. J.C. Joubert, T. Shirk, W.B. White and R. Roy, Mat. Res. Bull. 3, 671 (1968).
9. O. Muller, M.P. O'Horo and J.F. O'Neill, J. Solid State Chem. 23, 115 (1978).
10. (a) W. Kundig, Nucl. Instr. Methods, 40, 219 (1967).  
(b) N. Ravi, Ph.D. Thesis, University of Hyderabad, Hyderabad.

11. R. Diehl and G. Brandt, Acta Crystallogr. B31, 1662 (1975).
12. E.V. Bonnenberg, Physica B+C 80, 439 (1975).
13. L. Tobler, W. Kundig and I. Savic, Exp. Int. 10, 1017 (1981).
14. F. Weiss, J. Phys. and Radium 4, 661 (1907).
15. D.S. Rodbell, I.S. Jacobs, J. Owens and E.A. Harris, Phys. Rev. Lett. 11, 10 (1963).
16. A.S. Kamzin and V.A. Bokov, Sov. Phys. Solid State, 19, 1187 (1977).
17. F. van der Woude, Phys. Stat. Sol. 17, 417 (1966).
18. O.A. Bayukov, V.P. Ikonnikov, M.I. Petrov, V.N. Seleznev, R.P. Smolin and V.V. Uskov, JETP Lett. 14, 32 (1971).
19. D.C. Thomas and L.A.K. Staveley, J. Chem. Soc. 1420 (1951).
20. K.J. Rao and C.N.R. Rao, J. Mater. Sci., 1, 238 (1966).
21. V.G. Bhide and G.K. Shenoy, Phys. Rev. 143, 309 (1966).
22. D.E. Cox, G. Shirane, P.A. Flinn, S.L. Ruby and W.J. Takei, Phys. Rev. 132, 1547 (1963).
23. A.S. Kamzin, V.A. Bokov and G.A. Smolenskii, JETP Lett. 27, 477 (1978).

24. C. Voigt and W. Ross, J. Phys. C9, L-469 (1976).
25. V.A. Povitskii, A.N. Salugin, E.F. Makarov and Yu.V. Baldokhin, Sov. Phys. Solid State, 18, 958 (1976).
26. P.C.M. Gubbens, A.M. van der Kraan and K.H.J. Buschow, J. Phys. Colloq(France), 40, p.C5/200 (1979).
27. E. De Grave, D. Chambaere and L.H. Bowen, J. Mag. Mag. Mater. 30, 349 (1983).
28. I. Dezsi, G. Erlaki and L. Keszthelyi, Phys. Status Solidi, 21, K121 (1967).
29. P.B. Fabritchnyi, E.V. Lamykin, A.M. Babechkin and A.N. Nesmeianov, Solid State Commun. 11, 343 (1972).
30. J.M.D. Coey and G.A. Sawatzky, Phys. Status Solidi, b44, 673 (1971).
31. J.M.D. Coey, Phys. Rev. B6, 3240 (1972).
32. J.M.D. Coey and G.A. Sawatzky, J. Phys. C4, 2386 (1971).

## PART - B



### 5.1. Introduction

Organic acids complex with transition metals and the rare earths with ease. Despite their long history significant amount of work on this subject appear even in current literature. The reasons are not far to seek. As for example, the carboxylic acids lend themselves to a comparative study of complexes of the same carboxylic acid with different metal ions, of different carboxylic acids with the same metal ion and of the transition metal ions with the rare earths in analogous situations[1,2]. Such a comparative study shows several revealing features. By way of illustration, we may cite examples mainly from the simple mono and dicarboxylic acids such as formic, acetic, malonic and maleic acids and transition metal ions such as  $\text{Fe}^{2+}$ ,  $\text{Mn}^{2+}$ ,  $\text{Cu}^{2+}$  and  $\text{Zn}^{2+}$  as some of our own studies pertain to systems closely related to these.

### 5.2. Structural features

Some of the distinguishing structural features in the transition metal complexes with organic acids are (1) one or more of the oxygen atoms, even in the case of mono carboxylic acids can coordinate to the metal ion, (2) depending on the

structure both intermolecular and intramolecular hydrogen bonding can occur which are revealed in the study of their crystal structures. In copper formate tetrahydrate (CuFTH), for instance, each copper atom is surrounded by four oxygen atoms of four different formate ions in an approximately square planar configuration at a distance of  $2.0 \text{ \AA}$ , with two water molecules above and below at  $2.36 \text{ \AA}$  (Fig. 5.1(a)). The remaining water molecules are hydrogen bonded either to the coordinated water molecule ( $O_{III}$ ) or to the oxygen atom ( $O_{II}$ ) of the  $\text{COO}^-$  group [3]. On the other hand Fe(II), Zn(II) and Mn(II) give rise to isomorphous formates with structural features strikingly different from that of CuFTH (Fig. 5.1(b)) [4,5]. In these systems the metal ion occupies two crystallographically inequivalent sites, one coordinated to six carboxylic oxygens (site I) and the other by two carboxylic oxygens in trans position and four water molecules in a plane (site II) [4].

In the case of the next higher monocarboxylic acid in the homologous series viz., acetic acid, the transition metal ion  $\text{Co}^{2+}$  forms a simple acetate wherein the metal ion is coordinated to two  $\text{-COO}^-$  groups and four water molecules with intermolecular hydrogen bonding between them (Fig. 5.2(a)) [6]. On the other hand in  $\text{Cu}^{2+}$  acetate monohydrate one

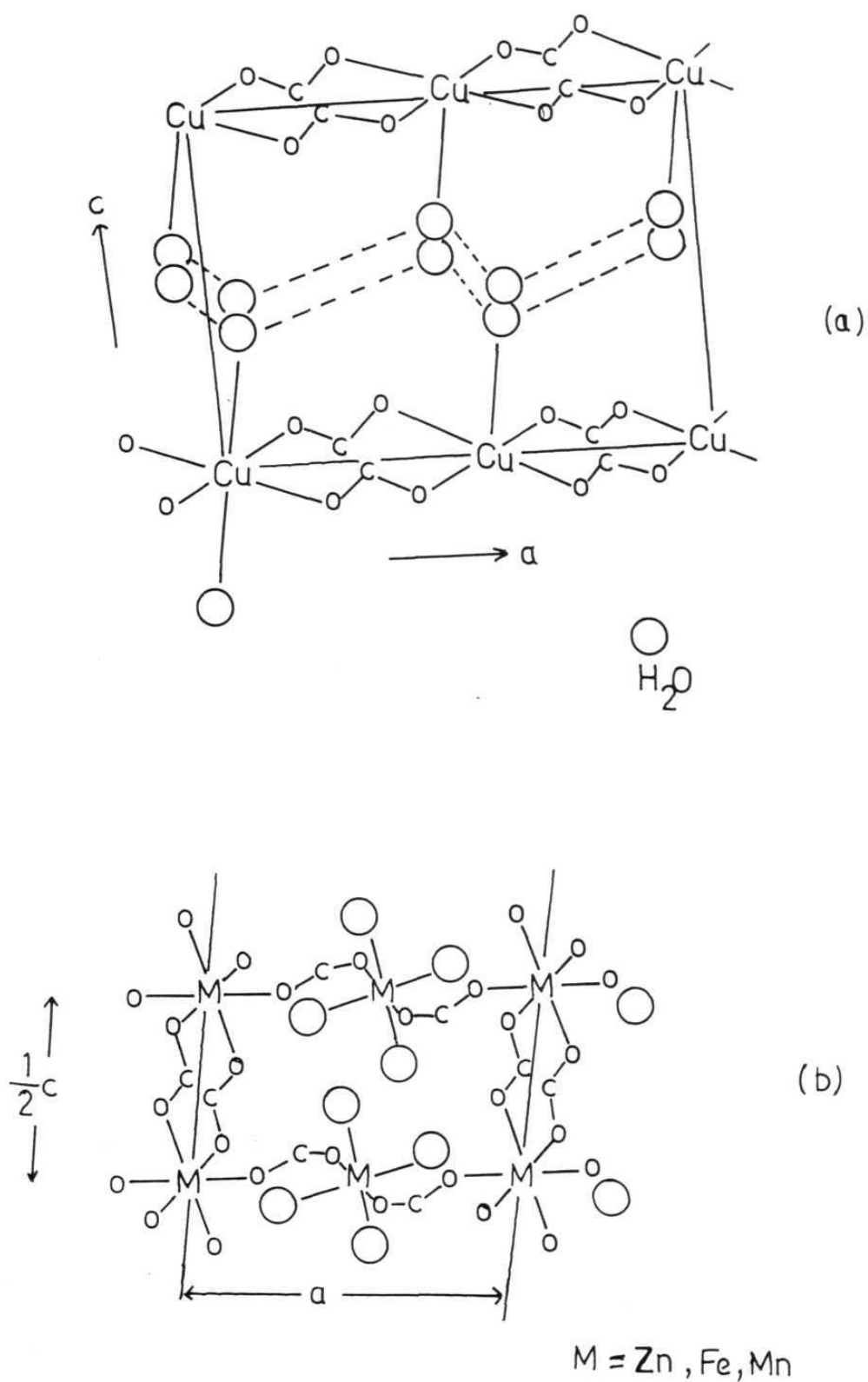


Fig.5.1 Crystal structures of (a) Cu(II) formate tetrahydrate and (b) M(II) formate (M = Fe, Zn and Mn) dihydrate.

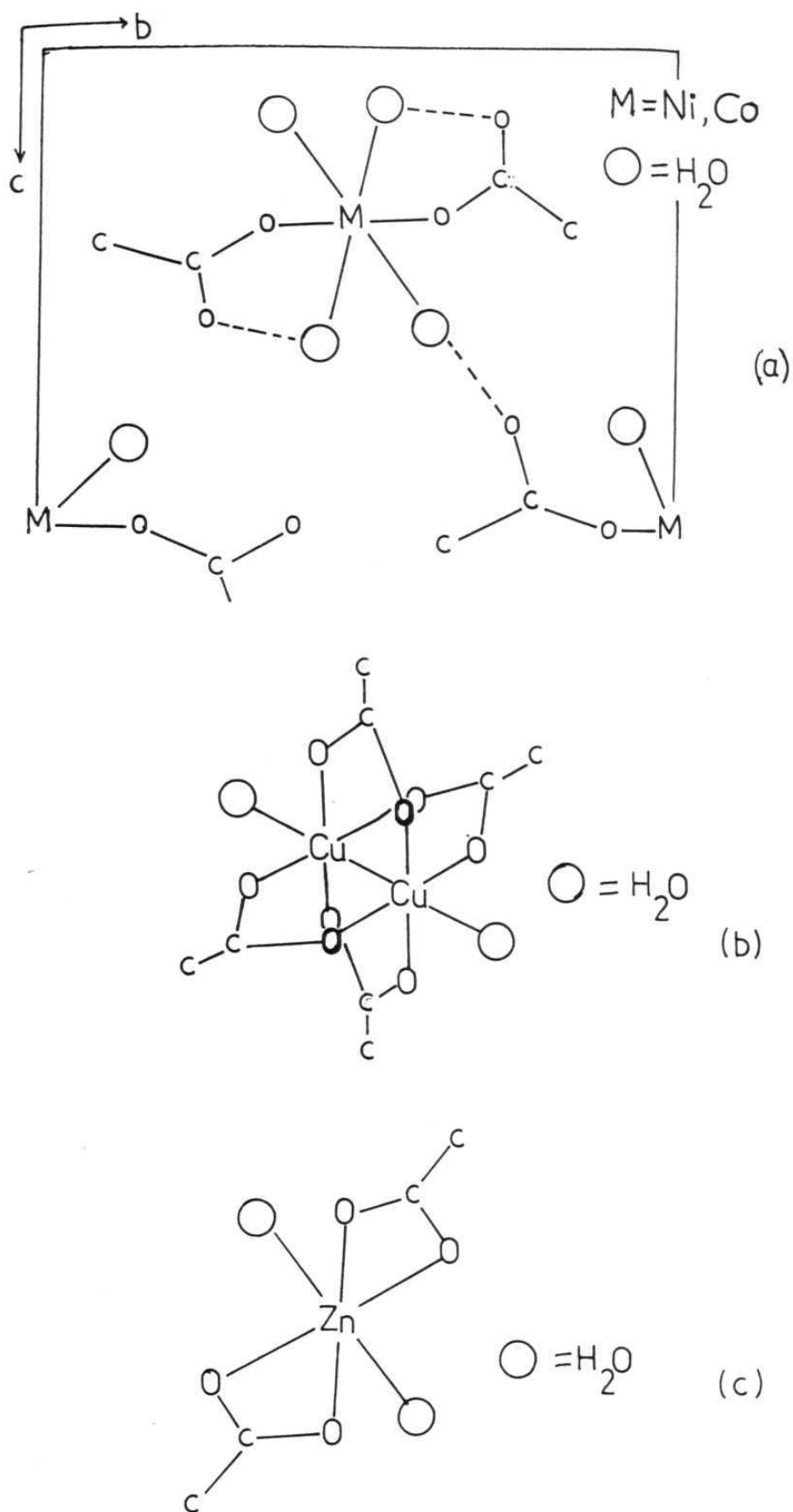


Fig.5.2 Crystal structures of (a) Co(II) acetate tetrahydrate (b) Cu(II) acetate monohydrate and (c) Zn(II) acetate dihydrate.

carboxylic acid group is coordinated to two metal ions [Fig. 5.2(b)] [7]. Yet in another instance viz., zinc acetate dihydrate, the  $\text{-COO}^-$  group chelates with the metal ion forming a four membered ring as shown in Figure 5.2(c). [8]. Similar features have been observed in the higher members of the monocarboxylic acid series [2].

The di and poly carboxylic acids exhibit additional interesting features stemming from the fact that their dissociation constants  $\text{pK}_a$  for the acid groups in the case of higher members differ significantly, unlike the first dicarboxylic acid viz., oxalic acid, enabling formation of both acid as well as normal complexes. For instance in the case of Cu(II) oxalate two types of structures have been proposed on the basis of magnetic studies (Fig. 5.3(a,b)). In both the cases, both the carboxylic acid groups are coordinated to the metal ion [9].  $\text{Fe}^{2+}$ ,  $\text{Co}^{2+}$  and  $\text{Ni}^{2+}$  also form oxalates with a structure analogous to the polymeric copper oxalate dihydrate [10,11]. Ferrous oxalate dihydrate has been reported to exist in two allotropic modifications,  $\alpha$  and  $\beta$  forms, which show difference in the X-ray and infrared data but are indistinguishable by Mössbauer spectra [10,12-14]. A dibasic acid higher up in the series such as malonic acid however behaves differently from oxalic acid on account of steric considerations

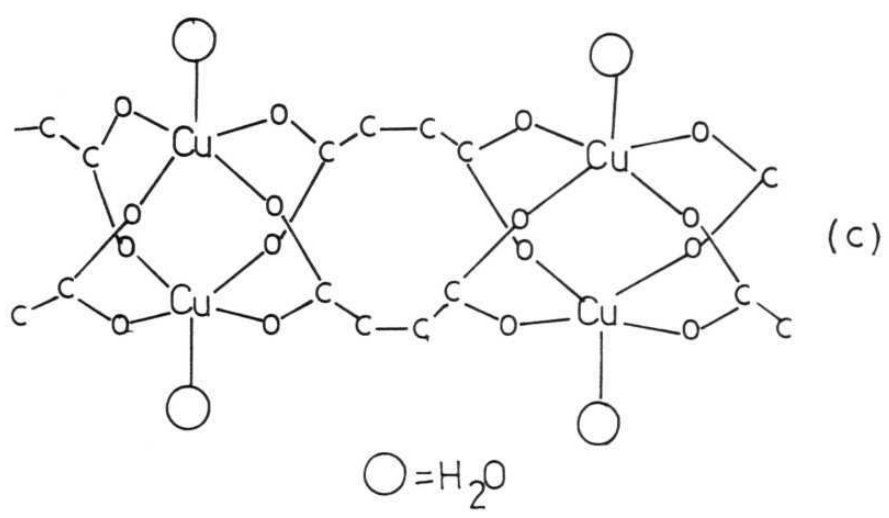
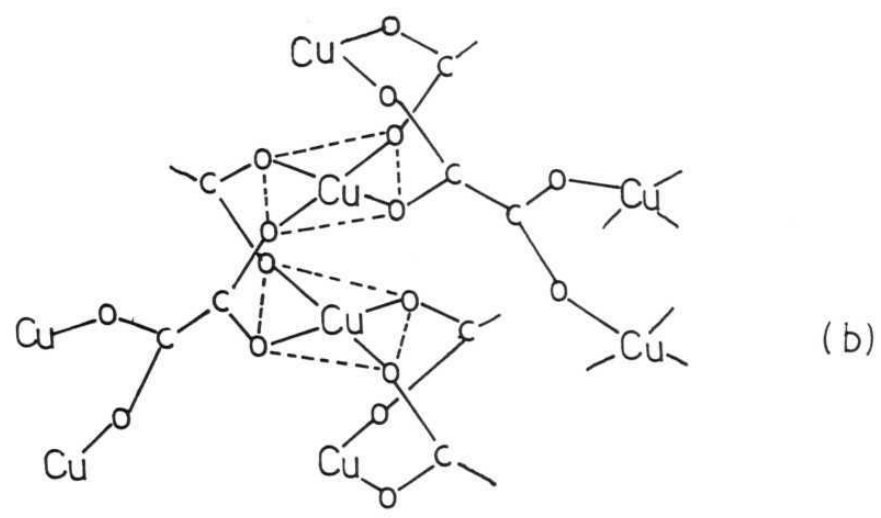
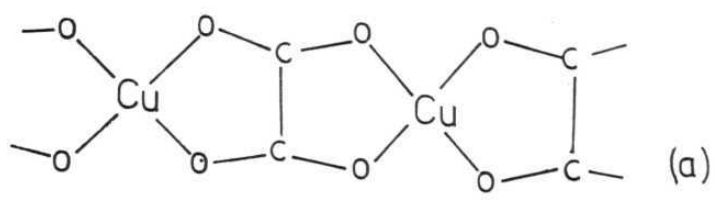


Fig.5.3 (a), (b) proposed structures for Cu(II) oxalate and (c) Cu(II) succinate [9].

arising due to the separation of the two carboxylic acid groups by a  $-\text{CH}_2-$  group reducing the spatial restriction in bonding and a significant difference in the  $\text{pK}_1$  and  $\text{pK}_2$  values ( $\text{pK}_1 = 2.83$ ,  $\text{pK}_2 = 5.69$ ). In these cases one of the carboxylic acid groups is deprotonated and the oxygen atom of the  $\text{OH}^-$  group is coordinated to the metal ion. The other  $-\text{COOH}$  group also is coordinated but through the oxygen of the  $-\text{C=O}$  group with hydroxyl ion remaining intact [15]. Detailed crystal structure work on malonates of  $\text{Ca}^{2+}$  and  $\text{Mg}^{2+}$  have been reported and are typically different due to the difference in their coordination behaviour [16,17].  $\text{Fe}^{2+}$  has been shown to form an octahedral compound isomorphous with  $\text{Mg}^{2+}$  where malonic acid acts as a bidentate ligand forming an acid complex in profound contrast to the ferrous oxalate dihydrate which exists in polymeric form as discussed earlier. Very little is known about the other transition metal malonates. The crystal structure data also provide evidence for considerable inter and intramolecular hydrogen bondings in the malonates [17]. The next higher acid viz., succinic acid forms a dimer with  $\text{Cu}^{2+}$  and the individual dimeric units are joined by two  $-\text{CH}_2-\text{CH}_2-$  bridges from opposite corners [18] (Fig 5.3(c)). The Cu-Cu separation within the dimeric unit is 2.61 Å. The Cu-Cu separation between nearest copper atoms in adjacent dimers in the chain is 6.44 Å. Our own work pertains to a

Mössbauer study of iron maleate tetrahydrate and electron spin resonance studies of  $\text{Cu}^{2+}$  and  $\text{Mn}^{2+}$  doped in zinc maleate tetrahydrate. References to crystal structures of the related maleates are included at the appropriate place in the course of discussion of our results.

### 5.3. Mössbauer studies

Mössbauer studies of simple carboxylic acid complexes of iron, tin and the rare-earths, europium and dysprosium provide illustrations how informations both on structure as well as hyperfine interactions can be obtained by this spectroscopic technique [15,19-26]. A survey of the study of iron(III) carboxylates by this technique is included by Catterick and Thornton in their review on polynuclear carboxylates [2]. An account of preliminary Mössbauer data on some of organic acid salts of both iron(II) and iron(III) is reported by Y. Takashima and Y. Tateishi [27]. The method has also been exploited in the study of decomposition products of carboxylates in particular, which reveal several interesting features. For instance, the decomposition study of strontium tris oxalato iron(III) in the absence of air shows that at  $300^{\circ}\text{C}$ , the oxidation state of the iron changes to +2 completely, and reverts to +3 by  $400^{\circ}\text{C}$ . At  $700^{\circ}\text{C}$



a significant percentage is present as +4, which is gradually reduced to +3 with increasing temperature [28]. As our own study pertains to a Fe(II) compounds we shall briefly survey here related Mössbauer studies. The study of iron(II) formate dihydrate by Hoy and deBarros is remarkable for being able to distinguish the two inequivalent sites discussed in the earlier section (p.129), by the difference in their quadrupole splittings. Lowering of temperature even upto 6K does not show any metal-metal interaction [19].

A number of investigations have been reported on ferrous oxalate dihydrate, including one from our own laboratory [14,20,21,29]. The interest in the system arises from the hyperfine split spectrum below 15 K giving rise to a significant combined quadrupole and Zeeman interaction effect resulting in forbidden transitions. The metal-metal interaction below 15 K has been explained on the basis of superexchange mechanism via oxalate ions. The inability to distinguish by Mössbauer spectra the two forms reported on the basis of X-ray data and the effect of replacing H<sub>2</sub>O by D<sub>2</sub>O in the dihydrate also have been investigated in detail [20,29]. Further, some reports are available on the decomposition products of ferrous oxalate dihydrate which indicates the intermediate formation of  $\gamma$ -Fe<sub>2</sub>O<sub>3</sub> [14,30-32]. The preliminary X-ray

data and detailed Mössbauer studies on iron(II) malonate dihydrate revealed the presence of discrete octahedra with monomeric structure and the absence of metal-metal interaction down to 1.2 K. This study is an illustration of the formation of a monomer in the higher dicarboxylic acid in view of the large difference in the  $pK_1$  and  $pK_2$  values and separation of the metal ions for steric reasons. A combined study of Mössbauer and differential thermal analysis (DTA) showed that ferrous malonate dihydrate when heated in the range 120-210°C becomes anhydrous, with the microsymmetry of the central metal ion changing from octahedral to tetrahedral coordination. Further heating showed the intermediate formation of  $\gamma\text{-Fe}_2\text{O}_3$  as in the case of the oxalate [15]. In the present work, by way of extension of these studies we report the preparation, structural and decomposition studies of iron(II) maleate tetrahydrate by Mössbauer, optical, DTA and thermogravimetric studies.

#### 5.4. Electron spin resonance studies.

Electron spin resonance (ESR) studies of carboxylic acid complexes have been an attractive area in the application of the technique for the study of microsymmetry, metal-metal interaction and hyperfine interaction studies on transition

metal ions and rare-earth ions. It has been gainfully employed particularly in the study of  $\text{Cu}^{2+}$  and  $\text{Mn}^{2+}$  carboxylic acid complexes in the pure form, in powder or in single crystals and in isomorphous lattices doped with the transition metal ions as well. In the last mentioned cases detailed informations can be obtained. We present here an account of  $\text{Cu}^{2+}$  and  $\text{Mn}^{2+}$  ESR studies in simple monocarboxylic and dicarboxylic acid complexes, related to our own studies of  $\text{Cu}^{2+}$  and  $\text{Mn}^{2+}$  ions doped in zinc maleate tetrahydrate. In the case of  $\text{Cu}^{2+}$  and  $\text{Mn}^{2+}$  complexes ESR studies have been reported for formate, acetate and propionate both in their pure forms as well as on  $\text{Cu}^{2+}$  and  $\text{Mn}^{2+}$  doped in the respective diamagnetic zinc lattices [33-46]. In the case of  $\text{Cu}^{2+}$  doped in  $\text{Zn}(\text{HCOO})_2 \cdot 2\text{H}_2\text{O}$ ,  $\text{Cu}^{2+}$  shows preferential substitution of site-I of the two sites available (Fig. 1b) in which the metal ion is coordinated to six formate groups in a distorted octahedron [37]. Further, the  $\text{Cu}^{2+}$  ions in this site exhibit exchange coupling when the concentration of the dopant is increased. Temperature dependence studies give  $|J| = 33 \pm 1 \text{ cm}^{-1}$  [37]. At higher concentrations copper ions go to the second site as well. The spin-Hamiltonian parameters have been deduced to be  $g_{||} = 2.416$ ,  $g_{\perp} = 2.077$  for site I and  $g_{||} = 2.42$  and  $g_{\perp} = 2.066$  for site II. Billing and Hathaway investigated the ESR and optical spectra of pure  $\text{Cu}(\text{HCOO})_2 \cdot 4\text{H}_2\text{O}$  in single

crystals and deduced  $g_{||} = 2.35$  and  $g_{\perp} = 2.06$  with the metal ion situated in  $D_{4h}$  symmetry with  $d_{x^2-y^2}$  ground state [34]. For  $Mn^{2+}$  doped in  $Zn(HCOO)_2 \cdot 2H_2O$ , Morigaki and Abe deduced from single crystal ESR studies that there is no site preference unlike in the case of  $Cu^{2+}$  [38]. They obtained the ESR parameters  $g_1 = 2.005$ ,  $D_1 = 295$ ,  $E_1 = 30$ ,  $A_1 = -92$  for site I and  $g_2 = 1.993$ ,  $D_2 = 455$ ,  $E_2 = 28$  and  $A_2 = -91$  G for site II. The normal ESR and half field resonance of  $Mn(HCOO)_2 \cdot 2H_2O$  have been studied by Karra and Kemmerer [36]. Of the two sites present in  $Mn(HCOO)_2 \cdot 2H_2O$ , the resonances due to site II were too broad to observe. From the normal ESR and half field measurements of site I it was concluded that the above material is a quasi-two dimensional magnet.

$Cu(II)$  acetate monohydrate happens to be one of the earliest instances studied by Bleaney and Bowers where the measurements were accounted in terms of a singlet ground state with an excited triplet state, whose population varied with temperature [39]. This observation gave an impetus to investigate a number of copper(II) carboxylates with copper-copper interactions culminating in a review by M. Kato et al [47]. Paramagnetic resonance in single crystals of

$\text{Mn}(\text{CH}_3\text{COO})_2 \cdot 4\text{H}_2\text{O}$  was studied down to 1.3 K [41]. An interesting observation in this case is a shift of the resonance field at  $< 3$  K which has been attributed to ferromagnetic character below  $T_c = 3$  K [41]. The ESR studies of zinc doped  $\text{Cu}(\text{CH}_3\text{COO})_2 \cdot \text{H}_2\text{O}$  have been studied by Kokoszka *et al* [42], and Kawamori *et al* [43]. These authors investigated the effects of dipolar and exchange interactions and from dilution studies derived the relationship between the hyperfine tensor components for the doublet and the triplet species and compared their results with the predictions of Slichter [48]. A set of 30 allowed ESR transitions arising from a single type of  $\text{Mn}^{2+}$  ions has been reported for  $\text{Mn}^{2+}/\text{Zn}(\text{CH}_3\text{COO})_2 \cdot 2\text{H}_2\text{O}$  and analysed to give the spin-Hamiltonian parameters  $g_z = 2.0013$ ,  $g_x = 2.0014$  and  $g_y = 2.004$ ,  $D = 248$ ,  $E = -25.3$ ,  $A_z = -89.6$ ,  $A_x = -89.9$  and  $A_y = -89.3$  G. The observation of the forbidden transitions have been reported and the values  $Q' = 0.402$  G and  $Q'' = 4.7$  G have been deduced for the axial and rhombic components of quadrupole interaction terms for the  $^{55}\text{Mn}$  nucleus respectively [45]. The single crystal ESR studies of zinc doped copper propionate monohydrate by Fujiwara indicate that there exists super-exchange interaction via the bridging carboxyl groups similar to that of copper acetate monohydrate [46].

A number of ESR studies have been reported where the transition metal ion is doped in organic acid complexes of non-transition metal ions such as  $\text{Ca}^{2+}$ ,  $\text{Sr}^{2+}$  and  $\text{Cd}^{2+}$ . The results in such studies are of interest as they provide a non-isomorphous host lattice and the doped  $\text{Cu}^{2+}$  or  $\text{Mn}^{2+}$  can occupy substitutional or interstitial sites. From the angular variation studies of  $\text{Mn}^{2+}$  and  $\text{Cu}^{2+}$  doped in  $\text{Sr}(\text{CH}_3\text{COO})_2 \cdot 0.5\text{H}_2\text{O}$ , Jain and Upreti concluded that the unit cell symmetry of the parent lattice is triclinic in contrast to the X-ray report suggesting monoclinic symmetry [49]. Further, these authors showed that  $\text{Cu}^{2+}$  and  $\text{Mn}^{2+}$  occupy different sites.

Although considerable work has been reported on monocarboxylic acid complexes, ESR studies of transition metal ions in polycarboxylic acid complexes is relatively meagre. Recently Karmakaz et al reported a  $\text{Cu}^{2+}$  doped cadmium oxalate trihydrate single crystal ESR study [50]. In yet another recent work, an ESR study of  $\text{Mn}^{2+}$  in cadmium oxalate trihydrate has been reported by the same authors analysing the allowed and forbidden transitions in terms of the spin-Hamiltonian including a rhombic crystalline electric field.  $\text{Mn}^{2+}$  substitutionally replaces  $\text{Cd}^{2+}$  in this case and gives a g-value slightly anisotropic [51]. The ESR studies of  $\text{Mn}^{2+}$

and  $\text{VO}^{2+}$  doped in  $\text{K}_2\text{C}_2\text{O}_4 \cdot \text{H}_2\text{O}$  single crystals have been reported by Jain [52]. The dopants have been found to go into interstitial sites. The doublet separation of forbidden hyperfine transitions corresponding to  $m = \pm 1$  for  $\text{Mn}^{2+}$  have been observed and analysed. A value of 0.44 G for  $Q'$  and 0.09 G for  $Q''$  have been obtained.

## References:

1. C. Oldham, in Progress in Inorganic Chemistry, edited by F.A. Cotton (Interscience Publishers, New York, 1968), Vol.10, p 223.
2. J. Catterick and P. Thornton, in Advances in Inorganic Chemistry and Radiochemistry, edited by Emeleus and Sharpe (Academic Press, New York, 1977), Vol.20, p 291.
3. R. Kiriyama, H. Ibamoto and K. Matsuo, Acta. Crystallogr. 7, 482 (1954).
4. K. Osaki, Y. Nakai and T. Watanabe, J. Phys. Soc. Jpn. 19, 717 (1964).
5. K. Osaki, Y. Nakai and T. Watanabe, J. Phys. Soc. Jpn. 18, 919 (1963).
6. J.N. Van Niekerk and F.R.L. Schoening, Acta. Crystallogr. 6, 609 (1953).
7. J.N. Van Niekerk and F.R.L. Schoening, Acta. Crystallogr. 6, 223 (1953).
8. J.N. Van Niekerk, F.R.L. Schoening and J.H. Tablot, Acta Crystallogr. 6, 720 (1953).
9. L. Dubicki, C.M. Haris, E. Kokot and R.L. Martin, Inorg. Chem. 5, 93 (1966).



10. R. Deyrieux and A. Peneloux, Bull. Soc. Chim. France, 8, 2676 (1969).
11. H. Pezert, J. Pubernat and J. Pierre Lagier, Compt. Rend. Acad. Sci., Ser C., 226, 1357 (1968).
12. D. Vigouroux, M.M. Clande, Carel and P. Vellet, Compt. Rend. 265, 451 (1967).
13. F. Aramu, V. Maxia and C. Muntoni, Lettere Al Nuovo Cimento 12, 225 (1975).
14. N. Ravi, Ph.D. Thesis, University of Hyderabad, Hyderabad.
15. N. Ravi, R. Jagannathan, B. Rama Rao and Raza Hussain, Inorg. Chem. 21, 1019 (1982).
16. B. Briggman and A. Oskarsson, Acta Crystallogr. B33, 1900 (1977).
17. B. Briggman and A. Oskarsson, Acta Crystallogr. B34, 3357 (1978).
18. B.N. Figgis and D.J. Martin, Inorg. Chem. 5, 100 (1966).
19. G.R. Hoy and F. de S. Barros, Phys. Rev. A139, 929 (1965).
20. N. Ravi and R. Jagannathan, Hyp. Inter. 12, 167 (1982).
21. F. de S. Barros, P.S. Zory and L.E. Campbell, Phys. Lett. 7, 135 (1963).

22. T.C. Gibb, B.A. Goodman and N.N. Greenwood, J. Chem. Soc., Chem. Commun. 774 (1970).
23. J.D. Donaldson, E.J. Filmore and M.J. Tricker, J. Chem. Soc.(A), 1109 (1971).
24. G.J. Ehnholm, T.E. Katila, O.V. Lounasmaa, P. Rieväri, G.M. Kalvius and G.K. Shenoy, Z. Physik. 235, 289 (1970).
25. P.K. Gallagher, F. Schrey and B. Prescott, Inorg. Chem. 9, 215 (1970).
26. H.H. Wickman and I. Nowick, J. Phys. Chem. Solids, 28, 2099 (1967).
27. Y. Takashima and Y. Tateishi, Bull. Chem. Soc. Jpn., 38, 1688 (1965).
28. P.K. Gallagher and C.R. Kurkjian, Inorg. Chem. 5, 214 (1966).
29. B. Brunot, Chem. Phys. Lett. 29, 368 (1974).
30. R.A. Robin and S.C. Bevan, J. Inorg. Nucl. Chem., 28, 387 (1966).
31. P.L. Gunther and H. Rehaag, Z. anorg. Chem., 243, 60 (1939).
32. A.B. Biswas, J. Mater. Sci. 9, 430 (1974).
33. Y. Morimoto and M. Date, J. Phys. Soc. Jpn. 29, 1093 (1970).
34. D.E. Billing and B.J. Hathaway, J. Chem. Soc., A1516 (1968).

35. H. Abe, H. Morigaki, M. Matsuura, K. Torii and K. Yamagata, J. Phys. Soc. Jpn. 19, 775 (1964).
36. J.S. Karra and G.E. Kemmerer, Solid State Commun. 40, 53 (1981).
37. G.R. Wagner, R.T. Schumacher and S.A. Friedberg, Phys. Rev. 150, 226 (1966).
38. H. Morigaki and H. Abe, J. Phys. Soc. Jpn. 23, 462 (1967).
39. B. Bleaney and K.D. Bowers, Phil. Mag. 43, 372 (1952).
40. H. Kumugai, H. Abe and J. Shimada, Phys. Rev. 87, 385(1952).
41. H. Abe and H. Morigaki in Paramagnetic Resonance, edited by W. Low (Academic Press, New York, 1963), Vol. 2, p.567.
42. G.F. Kokoszka, H.C. Allen Jr. and G. Gordon, J. Chem. Phys. 42, 3693 (1965).
43. A. Kawamori, S. Matsuura and H. Abe, J. Phys. Soc., Jpn. 29, 1170 (1970).
44. S.K. Misra and M. Kahrizi, Phys. Rev. B30, 2920 (1984).
45. R. Janakiraman and G.C. Upreti, J. Phys. Chem. Solids, 31, 1419 (1970).
46. Fujiwara, J. Mag. Resonance, 10, 139 (1973).

47. M. Kato, H.B. Jonassen and J.C. Fanning, Chem. Rev. 64, 99 (1964).
48. C.P. Slichter, Phys. Rev. 99, 479 (1955).
49. A.K. Jain and G.C. Upreti, J. Chem. Phys. 71, 4752 (1979).
50. M. Korkmaz and B. Aktas, J. Phys. Chem. Solids, 45, 259 (1984).
51. M. Korkmaz, M. Dupont and B. Aktas, J. Phys. Chem. Solids, 45, 465 (1984).
52. V.K. Jain, Phys. Status. Solidi, B97, 337 (1980).

## CHAPTER 6

### EXPERIMENTAL METHODS AND METHODOLOGY

#### Abstract

The experimental details pertaining to ESR spectral measurements of single crystals, differential thermal analysis, thermogravimetric analysis and optical spectral measurements are presented. A description of the appropriate spin Hamiltonian for the case of  $\text{Cu}^{2+}$  and  $\text{Mn}^{2+}$  ESR spectral analysis is given. The steps involved in the derivation of the  $g$  and  $A$  tensors for the  $\text{Cu}^{2+}$  case are also presented. The various expressions required for the analysis of allowed and forbidden ESR transitions for the case of  $\text{Mn}^{2+}$  leading to evaluation of the spin-Hamiltonian parameters are also given.

## 6.1. Experimental measurements

### 6.1.1. Electron spin resonance (ESR) measurements

First derivative ESR spectra were recorded in JEOL-FE-3X X-band spectrometer employing 100 KHz modulation. For angular variation study the sample was mounted on a Teflon sample holder and rotated about three mutually perpendicular axes. The Z-axis was found by recording in a plane which gives the maximum spread in the spectrum and designated as X'Z-plane. Spectra are recorded in two other planes Y'Z and X'Y' chosen such that the three planes are mutually perpendicular. Each of the three crystal planes were explored at  $10^\circ$  interval. The spectrometer settings were optimised to record intense, resolved hyperfine lines. DPPH was used as field marker.

The g value of a peak in an ESR spectrum can be calculated using the relationship

$$gH = 2.0023 H_{\text{DPPH}}$$

where H is the magnetic field at the ESR peak of the sample and  $H_{\text{DPPH}}$  is the field of DPPH resonance. The ESR positions could be measured to 0.1 mm on the 40 cm wide chart paper which

corresponds to an accuracy of  $\pm 5\text{G}$  for magnetic field scans of 2500 G. This gives an accuracy of  $\pm 0.003$  in the  $g$  values.

#### 6.1.2. Differential thermal analysis (DTA)

The DTA measurements were made on a unit fabricated in our laboratory. The block diagram of the same is given Figure 6.1. The unit consists of (i) a furnace (ii) specimen holder made up of nickel (iii) ceramic support for keeping the holder in position (iv) a light spot galvanometer for measuring the differential thermocouple output (v) Keithley digital multimeter (model 174) for measuring the e.m.f output of the thermocouple measuring the temperature of the nickel block and (vi) chromel-alumel (25 s.w.g) thermocouples. The heating rate of the furnace was controlled manually using a variac. In all the measurements a heating rate of  $4\text{--}5^\circ/\text{min}$  was employed. Initial standardisation of the set up was carried out by recording the DTA of ammonium nitrate [1].

#### 6.1.3. Thermogravimetric measurements

The thermogravimetric analysis (TGA) was carried out on a home made unit. The unit consists of (i) a balance (ii) a furnace (iii) sample holder made up of Corning glass and

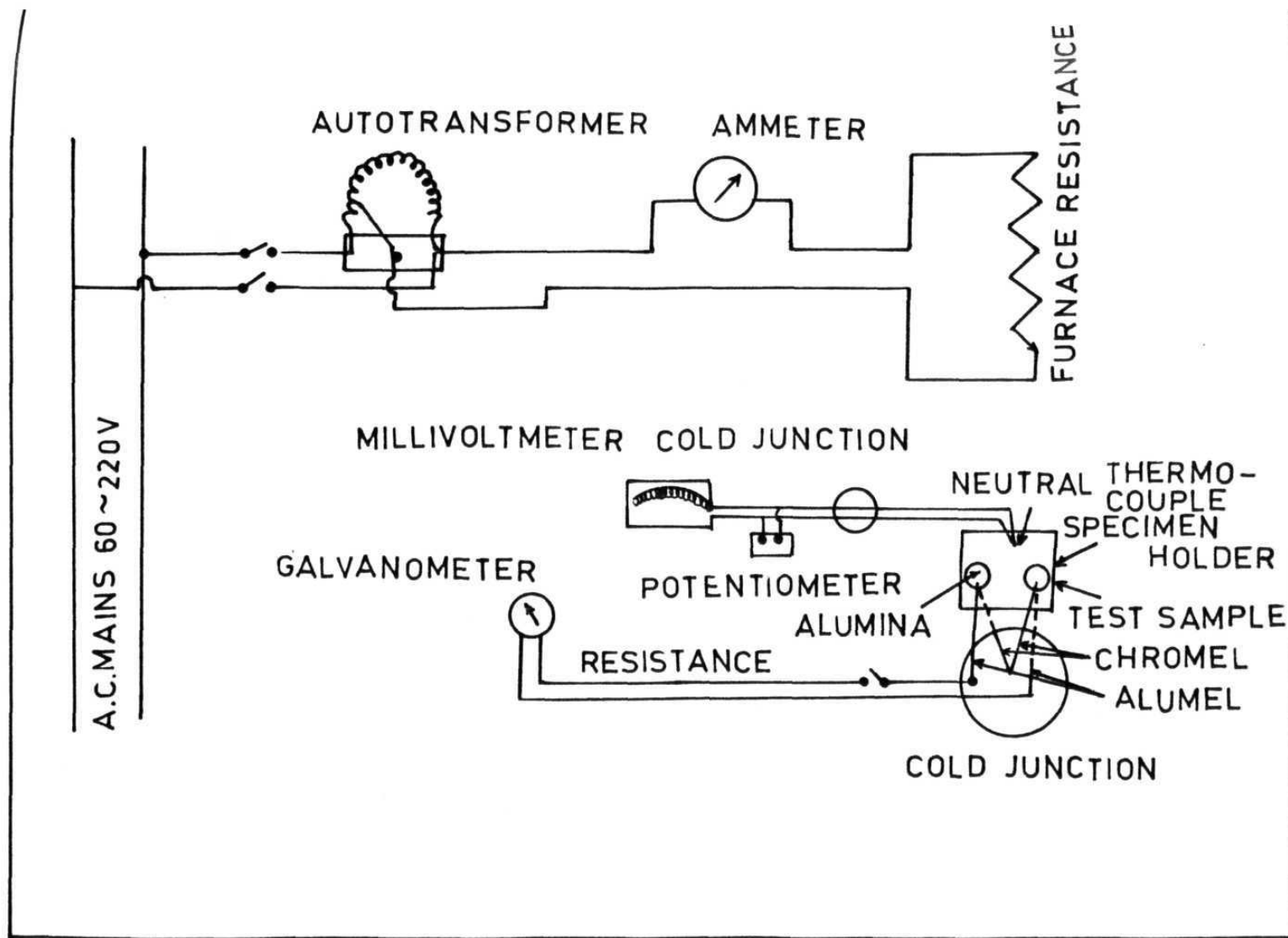


Fig.6.1 Experimental set up used for differential thermal analysis (DTA)



(iv) a digital multimeter (Keithley model 174). The heating rate of the furnace was controlled manually using a variac. A heating rate of  $4-5^{\circ}/\text{min}$  was employed. The sample was placed in the sample holder hanging at the centre of tubular furnace with the help of an insulated copper wire attached to a single pan balance. The weight loss was monitored by the balance and the corresponding temperature was noted by measuring the e.m.f of a thermocouple placed near the sample holder.

## 6.2. Methodology

This part of the thesis concerns with a Mössbauer study of iron maleate tetrahydrate and its decomposition products and single crystal ESR studies of  $\text{Cu}^{2+}$  and  $\text{Mn}^{2+}$  doped zinc maleate tetrahydrate (ZnMTH). The methodology employed for the Mössbauer studies has been presented earlier in chapter 2. Here we confine to a brief discussion of (i) the spin-Hamiltonian (ii) the splitting of the energy levels for the  $\text{Cu}^{2+}$  and  $\text{Mn}^{2+}$  cases and (iii) the formalisms used for obtaining the g-tensor and the ground state in the case of  $\text{Cu}^{2+}/\text{ZnMTH}$  and hyperfine constants from an analysis of the allowed and forbidden transitions of  $\text{Mn}^{2+}/\text{ZnMTH}$  from the experimental spectra.

### 6.2.1. Total Hamiltonian and the effective spin-Hamiltonian

The total Hamiltonian for an ion in a crystalline electric field with an applied magnetic field may be written as

$$H_{\text{total}} = H_V + H_{\text{LF}} + H_{\text{LS}} + H_{\text{SS}} + H_{\text{HI}} + H_Q + H_{\text{SH}} + H_{\text{SI}} + H_{\text{II}} \dots (6.1)$$

where the significance of the different terms of the total Hamiltonian and the order of magnitude of each term are given in Table 6.1 [2].

The effective spin-Hamiltonian contains those parts of the total Hamiltonian which are relevant for the purpose of ESR i.e., the spin vectors only. The energy levels of the paramagnetic ion can be represented by this Hamiltonian using the fictitious or effective spin  $S$ . This is given by

$$H_{\text{spin}} = \beta_e (g_x S_x H_x + g_y S_y H_y + g_z S_z H_z) + D[S_z^2 - \frac{1}{3}S(S+1)] + \\ E(S_x^2 - S_y^2) + (A_x S_x I_x + A_y S_y I_y + A_z S_z I_z) - \beta_N g_N H \cdot I + \\ \frac{e^2 q Q}{8I(2I-1)} (3\cos^2\theta - 1) [I_z^2 - \frac{1}{3}I(I+1)] \dots (6.2)$$

Table 6.1. Hamiltonian operators in order of approximate decreasing magnitude[2].

Hamiltonian	Interaction	Magnitude( $\text{cm}^{-1}$ )	Expanded form.
V	Electron-Electron	$10^5$	$\sum_{k>j=1}^n \frac{e^2}{r_{kj}}$
LF	Ligand Field	$10^4$	$\sum_k -eV(x_k, y_k, z_k)$
LS	Spin-Orbit	$10^2-10^3$	$\lambda \cdot \hat{L} \cdot \hat{S}$
SS	Electron-Electron dipole	$10^{-1}-1$	$\beta e^2 r_{12}^{-3} [\hat{S}_1 \cdot \hat{S}_2 - \frac{3(\hat{S}_1 \cdot \hat{r}_{12})(\hat{S}_2 \cdot \hat{r}_{12})}{r_{12}^2}]$
HI	Nuclear Zeeman	$10^{-1}-10^{-3}$	$-g_N \beta_N \hat{H} \cdot \mathbf{I}$
Q	Nuclear Quadrupole	$10^{-3}$	$Q' [I_z^2 - \frac{1}{3} I(I+1)]$ where $Q' = \frac{3eQ}{4I(2I-1)} \frac{\partial^2 V}{\partial Z^2}$
SH	Electron Zeeman	-	$\beta_e (\hat{L} \cdot g\hat{S}) \cdot \mathbf{H}$
SI	Electron spin-Nuclear Spin	$10^{-2}-10^{-4}$	$A \cdot \hat{I} \cdot \hat{S}$
II	Nuclear Spin-Spin	-	$\sum_{i>j} I_i J_{ij} I_j$

where  $g_x, g_y$  and  $g_z$  are the principal components of the  $g$  tensor,  $A_x, A_y$  and  $A_z$  are the principal components of the hyperfine coupling tensor,  $D$  and  $E$  are the axial and rhombic components of zero field splitting respectively, and the significance of the other terms have been pointed out earlier (Table 6.1.) The importance of the various terms relevant to our studies with  $\text{Cu}^{2+}(3d^9)$  and  $\text{Mn}^{2+}(3d^5)$  are given below.

#### 6.2.2. $\text{Cu}^{2+}(3d^9)$ Case

The ground state of  $\text{Cu}^{2+}$  with a  $d^9$  configuration is  $^2D$  with  $S = 1/2$ . The orbital splittings for the different stereochemistries are shown in Figure 6.2. The magnetic properties of the lowest orbital singlet are modified by an admixture of the excited states through spin-orbit interaction resulting in anisotropic  $g$ -values. Figure 6.3 shows the splitting of the  $^2D$  state in the presence of crystalline fields, spin-orbit coupling and magnetic field. In the case of trigonal symmetry with an orbital doublet ground state, the structure will distort itself so as to resolve the degeneracy by Jahn-Teller effect. In either case the ground state is a Kramer's doublet and ESR spectra are readily observed at room temperature.

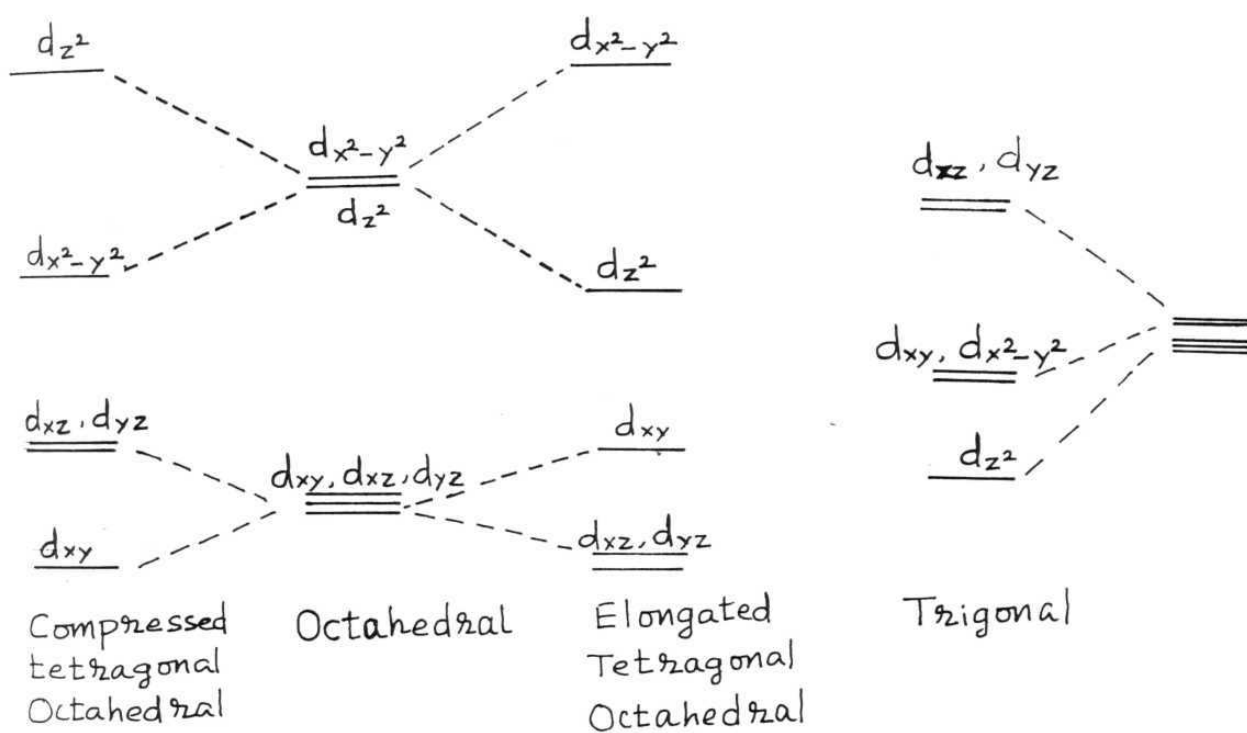


Fig.6.2 The d-orbital splittings for different geometries in  $\text{Cu}^{2+}(d)^9$

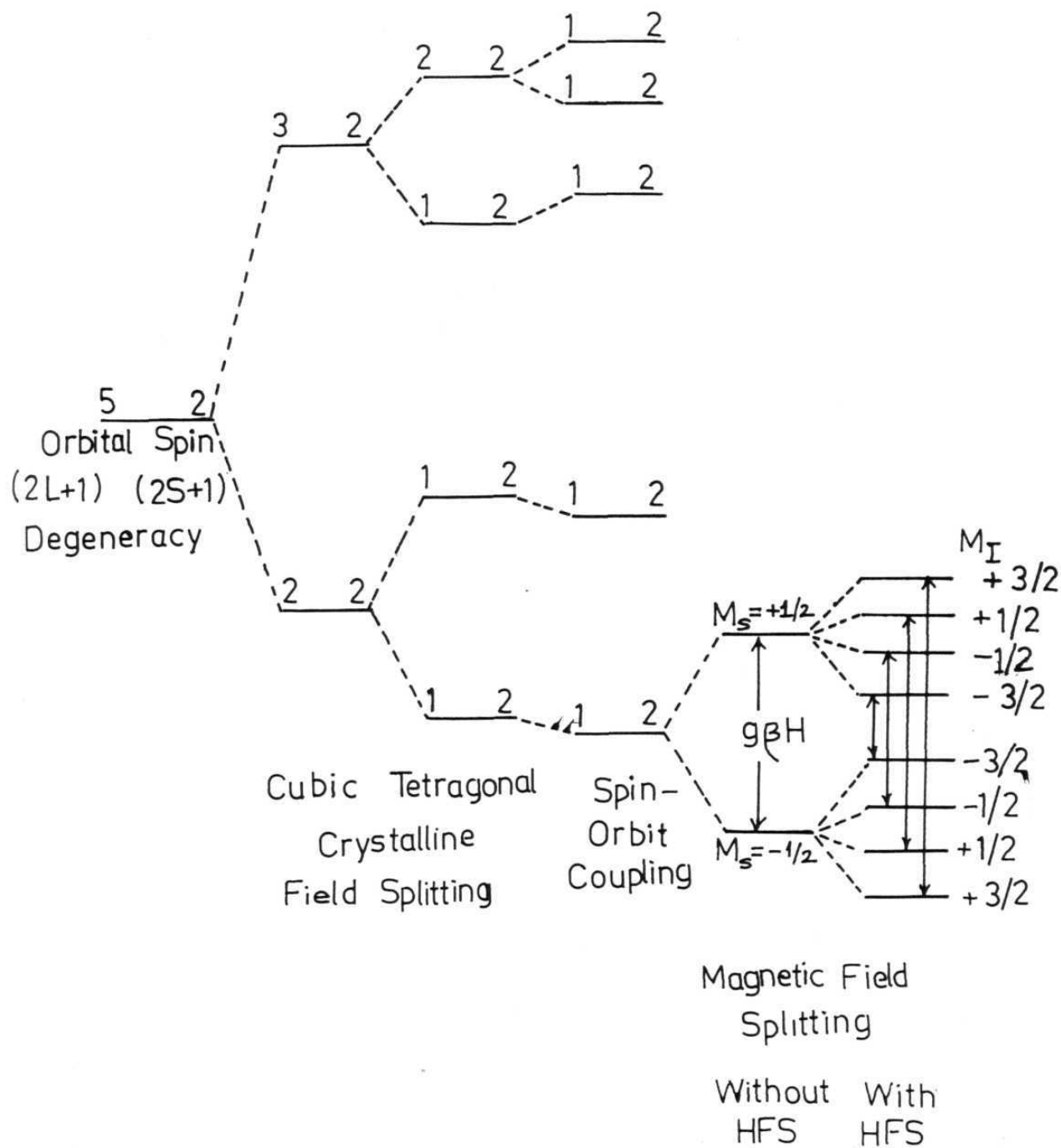


Fig.6.3 Splitting of the  $^2D$  state of  $\text{Cu}^{2+}$  under the action of crystalline fields, spin-orbit coupling and Magnetic field.

For  $\text{Cu}^{2+}$  ion the Eq. 6.2 may be written as

$$\begin{aligned}
 H_{\text{spin}} = & \beta_e (g_x H_x S_x + g_y H_y S_y + g_z H_z S_z) + \\
 & (S_x A_x I_x + S_y A_y I_y + S_z A_z I_z) - \beta_N g_N H \cdot I + \\
 & Q' [I_z^2 - \frac{1}{3} I(I+1)] \quad \dots (6.3)
 \end{aligned}$$

The D and E terms are not included since for  $S = 1/2$ , the zero field terms do not exist. Determination of the g-tensor in the case of copper is helpful in fixing the ground state and understanding the stereochemistry. One method of determining the g and A tensors from experimental measurements on single crystals is due to Schonland [3], the details of which are given in section 6.2.4.

### 6.2.3. $\text{Mn}^{2+}(3d^5)$ Case

The ground state of high spin  $\text{Mn}^{2+}(3d^5)$  is  ${}^6\text{A}$ .

The presence of crystalline electric field does not split this orbital singlet ground state as the ion is spherically symmetric. There are no other sextuplet terms and the next higher state is  ${}^4\text{G}$ . Since there is no other sextuplet term of the  $3d^5$  configuration, the ground state cannot mix with any other by spin-orbit coupling and so there is no

zero field splitting. However if there is an axial distortion, the zero field splitting does occur and three Kramers doublets appear. It has been shown by Van Vleck and Penney that this splitting comes in due to higher order admixtures involving the spin-orbit coupling and the axial field [4]. Further it is shown that the contribution to zero field splitting from spin-spin interaction also is significant. The contribution due to spin-spin interaction and the spin-orbit coupling have been calculated by Watanabe [5]. However, the results calculated by Watanabe appeared to be smaller than the values measured experimentally. Yet another mechanism suggested which contributes to zero field splitting through axial splitting is due to Blume and Orbach [6]. These authors showed that the  ${}^6\overline{1}_1$  term of the ground state  ${}^6A$  has the right symmetry to mix with the linear combinations ( ${}^4_1\overline{1}_4$ ) of the excited states  ${}^4G$ ,  ${}^4P$  and  ${}^4F$  through spin-orbit coupling generating the axial field responsible for zero field splitting.

In the absence of a magnetic field the axial crystal-line field splits the  ${}^6S_{5/2}$  state as discussed above into three Kramer's doublets viz.,  $\pm 5/2$ ,  $\pm 3/2$  and  $\pm 1/2$ , each being 2-fold spin degenerate. The separations between the  $\pm 5/2$  and  $\pm 3/2$ ,  $\pm 3/2$  and  $\pm 1/2$  states are  $4D$  and  $2D$  respectively,



where  $D$  is the zero field splitting (Figure 6.4). When the magnetic field is applied the spin degeneracy is lifted giving six electronic levels with  $-5/2$  lying lowest. Since the nuclear spin of  $^{55}\text{Mn}$  with natural abundance of 100%, is  $5/2$ , each electronic level is further split into six levels. The splitting between the hyperfine components is given by the term  $A \cdot M_S \cdot M_I$ . Thus the separation between the hyperfine components will be five times as large in the case of the outer electronic levels as for the central levels. Since the electronic spin magnetic quantum number  $M_S(\text{max})$  corresponds to the case in which the magnetic moment of the electron is parallel with the external magnetic field, it represents the lowest energy for the electron spin, and hence the largest negative electronic quantum number ( $M_S$ ) will be lowest. Considering the nuclear magnetic quantum numbers associated with the electronic levels the nuclear levels  $+M_I$  will lie lowest in energy for the above case. This results from the fact that the hyperfine coupling constant  $A$  is usually positive so that the net hyperfine interaction contribution will be negative for the case of  $-M_S$  and  $+M_I$ . For the higher electronic levels reverse will be the case because for a positive  $M_S$  value, a negative  $M_I$  value gives negative contribution due to the hyperfine interaction. Thus applying the selection rules viz.,  $\Delta M_S = \pm 1$  and  $\Delta M_I = 0$  for the allowed transitions,

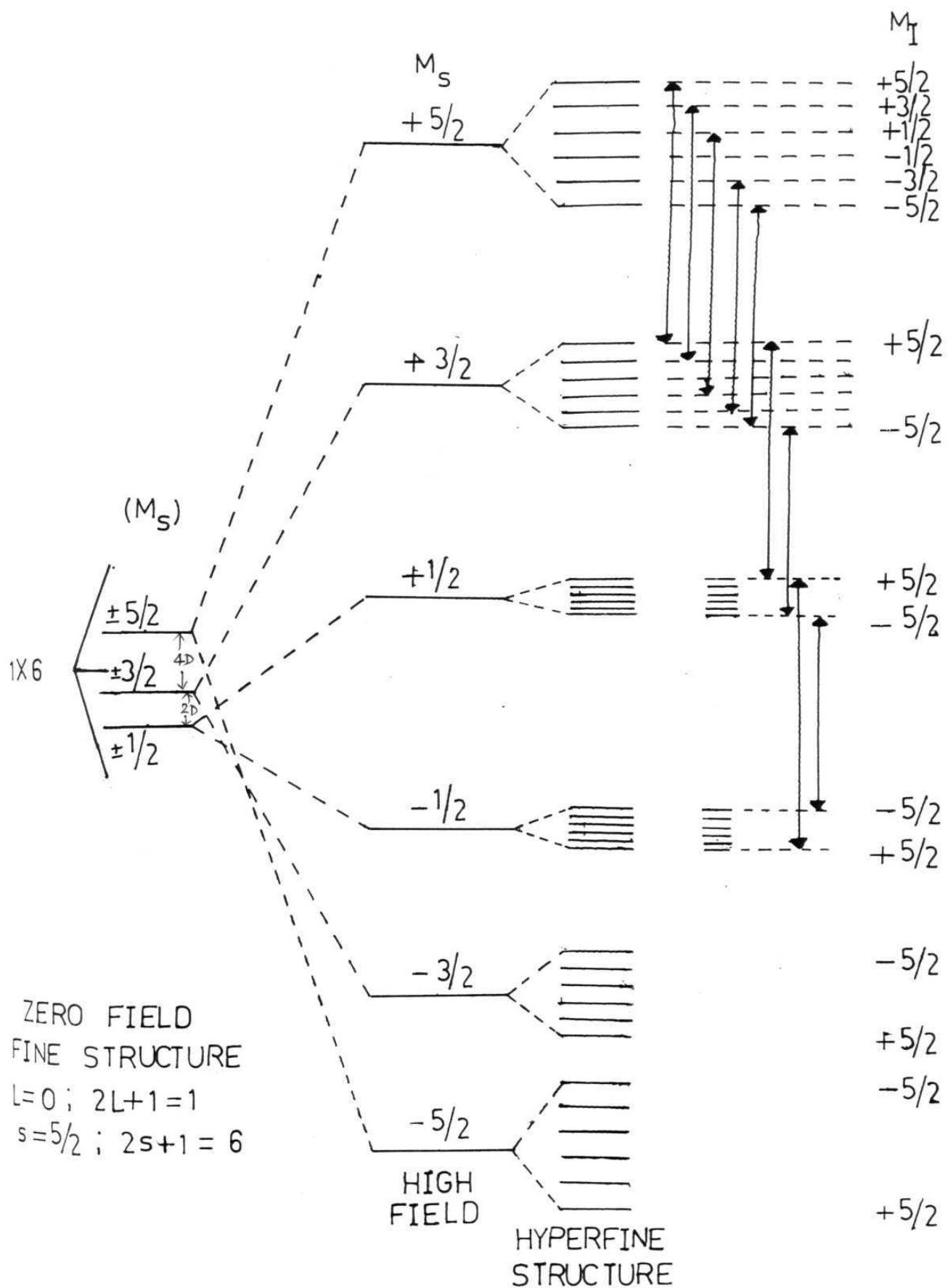


Fig. 6.4 Splitting of the  $6S$  state of  $Mn^{2+}$  under the action of crystalline field, magnetic field and hyperfine interactions.

a 30 line spectra will be obtained for  $Mn^{2+}$  ion in axial crystalline fields as designated in Figure 6.4.

The effective spin Hamiltonian viz., (6.2) for  $Mn^{2+}$  ( $3d^5$ ) may be written as

$$\begin{aligned}
 H = g\beta HS + D'[S_z^2 - \frac{1}{3} S(S+1)] + E'[S_x^2 - S_y^2] \\
 + \frac{a'}{6} [S_x^4 + S_y^4 + S_z^4 - \frac{1}{5} S(S+1) (3S^2 + 3S - 1)] + SA'I \\
 \dots (6.4)
 \end{aligned}$$

where the first term represents the Zeeman splitting energy, second and third terms represent the axial and rhombic zero field splittings respectively. The fourth term is the cubic field part while the last term represents the hyperfine interaction. The constants  $D'$ ,  $E'$ ,  $a'$  and  $A'$  are related to  $D$ ,  $E$ ,  $a$  and  $A$  through a multiplication factor of  $g\beta$  (viz.,  $D' = g\beta D$  etc).

The above spin-Hamiltonian can also be written in the form of crystal field parameters as follows for  $Mn^{2+}$  in orthorhombic (or lower) symmetry [7]

$$\begin{aligned}
H = & \beta [S_z g_z B_z + g_x (S_x B_x + S_y B_y) + \frac{1}{3} b_2^0 O_2^0 + \\
& \frac{1}{3} b_2^2 O_2^2 + \frac{1}{60} (b_4^0 O_4^0 + b_4^2 O_4^2 + b_4^4 O_4^4) + \\
& [S_z A_z I_z + A_x (S_x I_x + S_y I_y)] \quad \dots (6.5)
\end{aligned}$$

where  $O_n^m$  is an operator function having the same transformation properties as the corresponding spherical harmonics  $Y_n^m$  and the coefficients  $b_n^m$  are parameters to be determined by experiment. The relationship between the  $b_n^m$  and D, E, a are

$$a = 120 b_4^0$$

$$D = 3b_2^0$$

$$F = 180 b_4^0$$

We have retained the terms a, D and E corresponding to expression (6.4), for our discussion.

The spin Hamiltonian given above is derived from zero order wavefunctions  $|M, m_I\rangle$ , which would be appropriate to an ion in a very large magnetic field, are admixed by the off diagonal terms in this Hamiltonian. If we consider the second order admixtures arising from the cross products of the terms in D and A of the type

$$(S_z S_+) (S_- I_+), (S_z S_-) (S_+ I_-)$$

then a nuclear state  $|m_I\rangle$  becomes admixed with states  $|m_I \pm 1\rangle$  by amounts of order  $3D \sin 2\theta / 4g\beta H$  and forbidden transitions of the type  $\Delta M_S = \pm 1, \Delta m_I = \pm 1$ , occur [8]. They have intensities of the order of the square of the respective admixture coefficients relative to the intensities of the allowed transitions in which  $m$  does not change. The expressions derived from this Hamiltonian using which the forbidden transitions are analysed are given at the end of this chapter.

#### 6.2.4. Analysis of angular variation data for the case of $\text{Cu}^{2+}$ .

##### (a) Evaluation of $g$ and $A$ tensors.

The  $g$  value of a hyperfine pattern is determined by measuring the magnetic field at the centre of the hyperfine pattern. The hyperfine coupling constant ( $A$ ) is given by the field separation between adjacent hyperfine components. However if the spacings between consecutive peaks are unequal, then the average of all such spacings is taken to be the value of  $A$ . This has been adopted in the cases of  $\text{Mn}^{2+}/(\text{ZnMTH})$  and  $\text{Cu}^{2+}/(\text{ZnMTH})$ , in evaluating the value of  $A$ , as the adjacent spacings were unequal.

(b) Least square fit.

In an angular variation experiment the ESR spectra are recorded for rotations of the single crystal about any three mutually perpendicular (but not necessarily crystallographic) axes, at intervals of  $5^\circ$  or  $10^\circ$ , depending upon the amount of information present in the spectra. We have recorded the ESR spectra at  $10^\circ$  intervals as this was sufficient to get the angular variation of  $g$  and  $A$ . The  $g^2$  values thus obtained are plotted against  $\theta$ , the angle which the d.c. magnetic field makes with one of the reference axes, for rotations about the Z or Y axes. Each of the three plots obtained is fitted, by the method of least squares to the relationship,

$$g_{xy}^2(\theta) = g_{xx}^2 \cos^2\theta + g_{yy}^2 \sin^2\theta + 2g_{xy}^2 \sin\theta \cos\theta \quad \dots (6.6)$$

with similar equations for  $g_{yz}^2(\theta)$  and  $g_{zx}^2(\theta)$ . As  $g_{xx}^2$ ,  $g_{yy}^2$  and  $g_{zz}^2$  occur twice during the three rotations, they serve as checks on the correct mounting of the crystal for the rotations (for example see Table 7.1 for these values in the case of  $\text{Cu}^{2+}/\text{ZnMTH}$ ).

Equation (6.6) could be rewritten as

$$g^2(\theta) = U + V \cos 2\theta + W \sin 2\theta \quad \dots (6.7)$$

where  $U = (g_{xx}^2 + g_{yy}^2)/2$ ,  $V = (g_{xx}^2 - g_{yy}^2)/2$  and  $W = g_{xy}^2$ . Equation (6.7) could also be used for fitting experimental  $g^2$  values. Then the maximum and minimum  $g^2$  values are determined using the  $\theta$  values given by

$$\tan 2\theta = W/V$$

Appendix III gives the listings of a HI-BASIC programme for DCM Spectrum-7 to least square fit the measured  $g$  values to eq.(6.7) to get the values of  $U$ ,  $V$ ,  $W$ ,  $g_{\max}^2$  and  $g_{\min}^2$ .

(c) Diagonalization of  $g$  and  $A$  tensors.

The  $g^2$  matrix to be diagonalized is

$$\{g^2\} = G = \begin{bmatrix} g_{xx}^2 & g_{xy}^2 & g_{xz}^2 \\ g_{yx}^2 & g_{yy}^2 & g_{yz}^2 \\ g_{zx}^2 & g_{zy}^2 & g_{zz}^2 \end{bmatrix} \quad \dots (6.8)$$

The various elements of  $G$  are obtained from a least square fit of the experimental data to the relations of the type given in eq.(6.7). The eigen value problem

$$|G - \lambda I| = 0$$

is solved to get the principal g-values, which occur as the positive square roots of  $\lambda_1, \lambda_2, \lambda_3$  which are the roots of the equation

$$\lambda^3 + p^2\lambda + q\lambda + r = 0 \quad \dots (6.9)$$

where  $p = -(g_{xx}^2 + g_{yy}^2 + g_{zz}^2)$ ,

$$q = [(g_{xx}^2 g_{yy}^2 + g_{yy}^2 g_{zz}^2 + g_{zz}^2 g_{xx}^2) - (g_{xy}^2 + g_{yz}^2 + g_{zx}^2)]$$

and

$$r = (g_{xx} g_{yz}^2)^2 + (g_{yy} g_{zx}^2)^2 + (g_{zz} g_{xy}^2)^2 - g_{xx}^2 g_{yy}^2 g_{zz}^2 - 2g_{xy}^2 g_{yz}^2 g_{zx}^2$$

Schonland has developed a method to obtain the  $g^2$  matrix [6.8] by just knowing accurately the  $g_{\max}^2$  and  $g_{\min}^2$  for crystal rotations about three mutually perpendicular axes [3]. In this procedure the full angular variation curve fitted by the least square method to eq.(6.7) can be used to obtain accurate values for  $g_{\max}^2$  and  $g_{\min}^2$  for each rotation. If the axis of rotation is  $i$  ( $i = x, y$  or  $z$ ), the parameters  $\alpha$  and  $\delta$  may be defined as



$$\alpha_i = (g_{\max}^2(i) + g_{\min}^2(i))/2$$

$$\partial_i = (g_{\max}^2(i) + g_{\min}^2(i))/2 \quad \dots (6.10)$$

we thus get  $\alpha_x, \alpha_y, \alpha_z$  and  $\partial_x, \partial_y, \partial_z$ . After computing  $\alpha$  and  $\partial$  values, the matrix elements of  $g$  tensor can be set up as follows.

$$g_{xx} = \alpha_y + \alpha_z - \alpha_x$$

$$g_{yy} = \alpha_z + \alpha_x - \alpha_y$$

$$g_{zz} = \alpha_x + \alpha_y - \alpha_z$$

$$g_{zy} = g_{yz} = \pm \sqrt{(\partial_x + \alpha_y - \alpha_z)(\partial_x - \alpha_y + \alpha_z)}$$

$$g_{xz} = g_{zx} = \pm \sqrt{(\partial_y + \alpha_z - \alpha_x)(\partial_y - \alpha_z + \alpha_x)}$$

$$g_{xy} = g_{yx} = \pm \sqrt{(\partial_z + \alpha_x - \alpha_y)(\partial_z - \alpha_x + \alpha_y)} \quad \dots (6.11)$$

The  $G$  matrix is then diagonalized by the Jacobi method [9].

The matrix elements which are found to be imaginary are rejected and their values are taken as zeros. The diagonalization of the  $G$ -matrix (6.8) gives the principal  $g$  values.

The principal A values can also be computed using the same procedure. Initially  $g^2 A^2$  values for all the three axes are calculated and least square fit using the eq.(6.7) to give  $g^2 A_{\max}^2$  and  $g^2 A_{\min}^2$  values. These  $g^2 A_{\max}^2$  and  $g^2 A_{\min}^2$  values are then used to calculate  $\alpha$  and  $\delta$  defined in a similar manner as in 6.11 which are used to set up the matrix elements of the form  $g_{ij}^2 A_{ij}^2$ . The diagonalisation of the corresponding matrix gives the principal  $g^2 A^2$  values from which the principal A values can be computed.

#### 6.2.5. Analysis of angular variation data for the case of $Mn^{2+}$ .

##### (a) Allowed transitions

Equation 6.4 may be written in the form

$$H = g\beta HS + D' [S_z^2 - \frac{1}{3} S(S+1)] + E' [S_x^2 - S_y^2] + \frac{a'}{6} [S_x^4 + S_y^4 + S_z^4 - \frac{1}{5} S(S+1) (3S^2 + 3S - 1)] + SA'I \dots (6.12)$$

neglecting the other terms which do not undergo any change during the transition. For the case of axial symmetry, it has been shown that the line-positions in terms of magnetic fields exhibit a variation given by  $(3\cos^2\theta - 1)$  [10].

However, the effect of diagonal terms results in a deviation in the experimental situation from strict adherence to such a variation. The analysis of the line-positions for obtaining the hyperfine parameters,  $D$ ,  $E$ ,  $a$  and  $A$  are fairly simplified by locating the spectrum corresponding to  $H \parallel Z$  as shown by the largest split of the external lines and the absence of forbidden transitions [10]. In such a case the hyperfine terms are related as follows [11].

(a) for fine structure ( $H \parallel Z$ )

$$H(M = \pm 5/2 \rightarrow \pm 3/2) = H_0 \mp 4D + \frac{9E^2}{(H+D)} - \frac{5E^2}{(H \pm 3D)} \mp 2a$$

$$H(M = \pm 3/2 \rightarrow \pm 1/2) = H_0 \mp 2D \mp \frac{9E^2}{(H+D)} \pm \frac{9E^2}{(H-D)} -$$

$$\frac{5E^2}{(H \pm 3D)} \pm \frac{5}{2} a$$

$$H(M = + 1/2 \rightarrow - 1/2) = H_0 - \frac{9E^2}{(H-D)} + \frac{5E^2}{(H+3D)} + \frac{5E^2}{(H-3D)} \dots (6.13)$$

(b) for hyperfine structure ( $H \parallel Z$ )

$$H(m \rightarrow m) = H - Am - \frac{A^2}{2H} [I(I+1) - m^2 + (2M-1)m] \dots (6.14)$$

The parameters D, E, a and A are calculated using the above expressions in an iterative manner till a good match between  $H_{cal}$  and  $H_{obs}$  are obtained. The computer programme to calculate self consistently the D, E, a and A using the above expressions is given in appendix IV. The values D, E, a and A thus obtained are used in analysis of the forbidden transitions described below.

(b) Forbidden transitions.

The spin Hamiltonian used in the analysis of forbidden transitions is derived from the perturbation approach and is of the form

$$\begin{aligned}
 H = & \beta \tilde{g} \cdot H \cdot S + D[S_z^2 - \frac{1}{3} S(S+1)] + E[S_x^2 - S_y^2] + S \cdot \tilde{A} \cdot I - \\
 & \gamma \beta_N H \cdot I + Q'[I_z^2 - \frac{1}{3} I(I+1)] + Q''(I_x^2 - I_y^2) \\
 & \dots (6.15)
 \end{aligned}$$

where  $Q'$  and  $Q''$  represent respectively the axial and rhombic components of the quadrupole coupling constants of  $^{55}\text{Mn}$  nucleus. The significance of the other terms have been discussed earlier.

The above Hamiltonian is applicable only when the applied magnetic field is along Z-axis of the crystal.

However, if the magnetic field is not along the Z-axis but makes an angle  $\theta$  to Z-axis and  $\phi$  to X-axis in the XY-plane, equation (6.15), takes the form [12],

$$\begin{aligned}
 H = & g\beta HS'_Z + \sigma \left[ S_Z^2 - \frac{1}{3} S(S+1) \right] + P S_+^2 + P^* S_-^2 + \\
 & \frac{\lambda}{2} (S_Z S_+ + S_+ S_Z) + \frac{\lambda^*}{2} (S_Z S_- + S_- S_Z) + A S_Z I_Z + \\
 & \frac{A}{2} (S_+ I_- + S_- I_+) - \gamma \beta_N H I_Z + P \left[ I_Z^2 - \frac{1}{3} I(I+1) \right] \\
 & \dots (6.16)
 \end{aligned}$$

taking the Z' axis along H. Here

$$\begin{aligned}
 S_+ &= S_{x'} + i S_{y'} \quad ; \quad S_- = S_{x'} - i S_{y'} \\
 \sigma &= \frac{1}{2} [D(3\cos^2\theta - 1) + 3E\sin^2\theta \cos 2\phi], \\
 P &= \frac{1}{4} [D\sin^2\theta + E(\cos^2\theta \cos 2\phi - \sin^2\phi) + 2iE\cos\theta \sin 2\phi], \\
 \lambda &= \sin\theta [(D-E \cos 2\phi) \cos\theta + iE \sin 2\phi], \\
 P &= \frac{1}{2} [Q'(3\cos^2\theta - 1) + 3Q'' \sin^2\theta \cos 2\phi]
 \end{aligned}$$

In the above expression the small anisotropy in the hyper-fine constant and g value are neglected for simplicity.

In the perturbation approach we approximate  $g\beta H \gg |D|$ ,  $|E|$ ,  $|A|$  and the eigen values of the above Hamiltonian to

a third order are

$$\begin{aligned}
 E_{|M,m\rangle} = & g\beta H M + \sigma[M^2 - \frac{1}{3} S(S+1)] + AMm + \\
 & \frac{A^2}{2g\beta H} [m\{M^2 - S(S+1)\} + M\{I(I+1) - m^2\}] - \\
 & \gamma\beta_N H m + P[m^2 - \frac{1}{3} I(I+1)] + \frac{|A|^2}{(2g\beta H)^2} \cdot \frac{2Am}{M} [\{M^2 - \\
 & S(S+1)\}^2 - M^2] + \frac{|P|^2}{(g\beta H)^2} 2AMm[2M^2 + 1 - 2S(S+1)] \\
 & + \frac{A^2\sigma}{(2g\beta H)^2} [\{S(S+1) - M(M+1)\}\{I(I+1) - \\
 & m(m-1)\} (2M+1) - \{S(S+1) - M(M-1)\}\{I(I+1) - \\
 & m(m+1)\} (2M-1) + \frac{A^3}{(2g\beta H)^2} [\{S(S+1) - \\
 & M(M+1)\}\{I(I+1) - m(m-1)\} (m-M-1) + \\
 & \{S(S+1) - M(M-1)\}\{I(I+1) - m(m+1)\} (M-m-1)] \\
 & \dots (6.17)
 \end{aligned}$$

The energy levels of allowed and forbidden hyperfine lines can be obtained by substituting the appropriate M and m values and applying the selection rules viz.,  $\Delta M = \pm 1$ ,  $\Delta m_I = 0$  for allowed lines and  $\Delta M = \pm 1$ ,  $\Delta m_I = \pm 1$  or  $\pm 2$  for forbidden lines. The forbidden lines are analysed in pairs to simplify the

calculations. The distance between two forbidden transitions viz.,  $\Delta H$  (in gauss) can be obtained by substituting the  $M$  and  $m$  values. Thus we get for  $M = +1/2 \longrightarrow -1/2$  sextet

$\Delta m = \pm 1$  Transitions

$$\begin{aligned}\Delta H &= H|1/2, m+1\rangle \longrightarrow |-1/2, m\rangle - H|1/2, m\rangle \longrightarrow |-1/2, m+1\rangle \\ &= (17A^2/2H_0) + 2(\gamma\beta_N/g\beta)H_0 - (2m+1)[2P - (8A^2\sigma/H_0^2) + \\ &\quad (25A^3/3H_0^2) + (\gamma\beta_N/g\beta)A]\end{aligned}$$

$\Delta m = \pm 2$  transitions

$$\begin{aligned}\Delta H &= H|1/2, m+1\rangle \longrightarrow |-1/2, m-1\rangle - H|1/2, m-1\rangle \longrightarrow |-1/2, m+1\rangle \\ &= (17A^2/H_0) + 4(\gamma\beta_N/g\beta)H_0 - 2m[4P + (16A^2\sigma/H_0^2) + \\ &\quad (25A^3/H_0^2) + 2(\gamma\beta_N/g\beta)A]\end{aligned}$$

$M = +3/2 \longrightarrow +1/2$  sextet

$\Delta m = \pm 1$  transitions

$$\begin{aligned}\Delta H &= H|3/2, m+1\rangle \longrightarrow |1/2, m\rangle - H|3/2, m\rangle \longrightarrow |1/2, m+1\rangle \\ &= -2A + 2(\gamma\beta_N/g\beta)H_0 - 2P(2m+1) - (|\lambda|^2 256A/3H_0^2) + \\ &\quad (|\rho|^2 52A/H_0^2) + (A^2/H_0)(2m+8.5) + (A^2\sigma/H_0^2)(14m+9) - \\ &\quad (A^3/H_0^2)(m^2 + 19m - 51/4)\end{aligned}$$

$$M = +5/2 \longrightarrow +3/2 \text{ sextet}$$

$$\Delta m = \pm 1 \text{ transitions}$$

$$\begin{aligned} \Delta H &= H |5/2, m+1\rangle \longrightarrow |3/2, m\rangle - H |5/2, m\rangle \longrightarrow |3/2, m+1\rangle \\ &= -4A + 2(\gamma\beta_N/g\beta)H_0 - 2P(2m+1) - (40A|\lambda|^2/3H_0^2) + \\ &\quad (56A|\rho|^2/H_0^2) + (A^2/H_0)(4m+6.5) + (A^2\sigma/H_0^2)(18m+8) - \\ &\quad (A^3/H_0^2)(2m^2-m-33) \end{aligned}$$

$$M = -3/2 \longrightarrow -1/2 \text{ sextet}$$

$$\Delta m = \pm 1 \text{ transitions}$$

$$\begin{aligned} \Delta H &= H |-1/2, m+1\rangle \longrightarrow |-3/2, m\rangle - H |-1/2, m\rangle \longrightarrow |-3/2, m+1\rangle \\ &= -2A - 2(\gamma\beta_N/g\beta)H_0 + 2P(2m+1) - (256A|\lambda|^2/H_0^2) + \\ &\quad (52A|\rho|^2/H_0^2) + (A^2/H_0)(2m-6.5) - (A^2\sigma/H_0^2)(4m+5) - \\ &\quad (A^3/H_0^2)(m^2-17m - (123/4)) \end{aligned}$$

$$M = -5/2 \longrightarrow -3/2 \text{ sextet}$$

$$\Delta m = \pm 1 \text{ transitions}$$

$$\begin{aligned} \Delta H &= H |-3/2, m+1\rangle \longrightarrow |-5/2, m\rangle - H |-3/2, m\rangle \longrightarrow |-5/2, m+1\rangle \\ &= -4A - 2(\gamma\beta_N/g\beta)H_0 + 2P(2m+1) - (40A|\lambda|^2/3H_0^2) + (56A|\rho|^2/H_0^2) \\ &\quad + (A^2/H_0)(4m-2.5) - (18mA^2\sigma/H_0^2) - (A^3/H_0^2)(2m^2+5m-30) \\ &\quad \dots (6.18) \end{aligned}$$



Using the above equations for  $H_{cal}$ , trial values of  $Q'$  and  $Q''$  are given as input parameters and the calculations are done in an iterative manner. The iteration is continued till a good fit is obtained between  $H_{cal}$  and  $H_{obs}$ . A computer programme used for this purpose is given in the appendix V.

The intensities of ESR hyperfine lines (both allowed as well as forbidden) of ions in sufficiently strong crystalline fields exhibit strong angular variations when the static magnetic field direction is varied with respect to the crystal field directions. The intensities of the forbidden lines will follow the expression

$$\left( \frac{3D \sin^2 \theta}{4g\beta H} \right)^2 \left\{ 1 + \frac{S(S+1)}{3M(M-1)} \right\}^2 \left\{ I(I+1) - m^2 + m \right\} \dots (6.19)$$

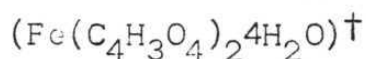
It is evident from the above expression that the intensities of forbidden lines will be zero at  $\theta = 0^\circ$  and maximum at  $\theta = 45^\circ$ .

References:

1. W.W. Wendlandt in Techniques of Inorganic Chemistry edited by H.B. Jonassen and A. Weissberger (Interscience, London 19), vol. 1 p.
2. B.A. Goodman and J.E. Raynor in 'Advances in Inorganic Chemistry and Radiochemistry' edited by H.J. Emeleus and A.G. Sharpe (Academic Press, New York, 1970), vol 13, p.147.
3. D.S. Schonland, Proc. Phys. Soc. 73, 788 (1959).
4. J.H. Van Vleck and W.G. Penney, Phil. Mag. 17 961 (1939).
5. H. Watanabe, Prog, Theoret. Phys. (Kyota). 18, 405 (1957).
6. M. Blume and R. Orbach. Phys. Rev. 127, 1587 (1962).
7. V.M. Vinukurov, M.M. Zaripov and V.G. Stepanov, Sov. Phys. Solid State (U.S.A). 6, 870 (1964).
8. Abragam and B. Bleaney, 'Electron Paramagnetic Resonance of transition ions', (Clarendon Press, Oxford, 1970), p.187.
9. S.S. Kuo, 'Computer Applications of Numerical Methods', (Addison-Wesley, 1972), Massachusetts.
10. Ref. 8. p.158.
11. B.V.R. Chowdari and P. Venkateshwarlu, J. Chem. Phys. 48, 318 (1968).
12. G.C. Upreti, J. Mag. Resonance 13, 336 (1974).

## CHAPTER 7

### PREPARATION AND MÖSSBAUER STUDIES OF FERROUS MALEATE TETRAHYDRATE



#### Abstract

$\text{Fe}(\text{C}_4\text{H}_3\text{O}_4)_2 \cdot 4\text{H}_2\text{O}$  is shown to be monomeric with a structure isomorphous with the  $\text{Mn}(\text{II})$  analogue and the unit cell dimensions are determined to be  $a = 7.27$ ,  $b = 9.60$  and  $c = 5.24 \text{ \AA}$ ,  $\alpha = 105.9$ ,  $\beta = 87.8$  and  $\gamma = 115.6^\circ$ . The temperature dependence of quadrupole splitting and optical spectral data give  $\sim 10,000 \text{ cm}^{-1}$ ,  $\sim 650 \text{ cm}^{-1}$ ,  $\sim 190 \text{ cm}^{-1}$  and  $\sim 1400 \text{ cm}^{-1}$  for the  $10 Dq$ , tetragonal field, rhombic field and the splitting of the  $e_g$  level respectively. The quadrupole splitting data indicate that the distortion from cubic symmetry increases in the following order, oxalate < malonate < maleate. DTA, TGA and Mössbauer studies indicate elimination of one molecule of maleic acid at  $235^\circ\text{C}$ . The resulting intermediate product is found to be a stable divalent compound with less distortion and is attributed to the formation of maleato (2-) iron (II).

---

<sup>†</sup>Part of this work is published in Trans. Metal Chem.

### 7.1. Introduction:

In this and the next two chapters we report the studies of ferrous maleate tetrahydrate (hereafter FeMTH),  $\text{Cu}^{2+}$  doped zinc maleate tetrahydrate (hereafter  $\text{Cu}^{2+}/\text{ZnMTH}$ ) and  $\text{Mn}^{2+}$  doped zinc maleate tetrahydrate (hereafter  $\text{Mn}^{2+}/\text{ZnMTH}$ ), as part of a programme of detailed investigations of hyperfine interactions and decomposition behaviour of organic acid complexes which give rise to situations of interest presented earlier. In the case of the first candidate viz., FeMTH Mössbauer spectroscopy provides a suitable technique to study structure and related properties. The latter two systems can be best studied by electron spin resonance technique. In this chapter we give an account of preparation and Mössbauer studies of FeMTH and its decomposition products. X-ray data establishing the octahedral structure isomorphous with the  $\text{Mn}^{2+}$  analogue are also presented. Crystal-field parameters have been derived from an analysis of temperature dependence of quadrupole splitting for the  $d^6$  case and optical spectral data conveniently obtained in the solid state using the photoacoustic spectral technique. The results of differential thermal analysis and thermogravimetric studies carried out to facilitate Mössbauer studies of decomposition products are also presented. A brief note on the Mössbauer spectrum of the single crystal,

originally taken up for an e.f.g. tensor analysis but yet to be completed is also included.

## 7.2. Experimental

FeMTH was prepared by dissolving iron powder (500 mg) (electrolytic grade, Sarabhai Chemicals) in a hot aqueous solution containing a 100% excess of maleic acid (Reidel), concentrating the resultant solution to half the original volume and cooling to room temperature. For the manganese analogue, the stoichiometric amount of manganese chloride (BDH) was converted into hydroxide by adding ammonia. The excess of ammonia was eliminated by slow heating and the resultant solution was dissolved in aqueous solution containing a 100% excess maleic acid. The crystals obtained were separated and dried in vacuum. Light yellow and colourless crystals were obtained for the iron and manganese salts, respectively.

The Mössbauer spectra were recorded as discussed in section 2.1.1. DTA and TGA were recorded on home made units, details of which are given in sections 6.1.2. and 6.1.3. Details of X-ray measurements also are given earlier in Section 2.1.4.

### 7.3. Results and Discussion

#### 7.3.1. X-ray studies

FeMTH is found to be highly soluble in water. Its solubility in water and the similarity of the molecular formula with that of MnMTH, CoMTH, ZnMTH, NiMTH and CuMTH suggest a monomeric structure. Of these the crystal structures of CuMTH and MnMTH have been reported [1,2]. For the maleates CoMTH, ZnMTH and NiMTH preliminary crystal structure data are available [3,4]. We prepared these maleates to investigate whether FeMTH is isomorphous with any one of them. Figure 7.1 shows the X-ray powder diffractograms of FeMTH and MnMTH in the form of histograms. The d-values and the intensities of the respective lines of FeMTH were found to be close to that of MnMTH (Table 7.1). A comparison of the d-values of the two maleates show them to be isomorphous. MnMTH crystallizes in the triclinic unit cell with  $P\bar{1}$  space group. The cell parameters are reported to be  $a = 7.35$ ,  $b = 9.77$ ,  $c = 5.18$  Å and  $\alpha = 106.9$ ,  $\beta = 94.6$  and  $\gamma = 116.6^\circ$  [2]. The unit cell contains one molecule of MnMTH and the central metal ion is situated at (000) position in an octahedral geometry. The metal ion is coordinated to four water molecules and two maleate groups as shown in Figure 7.2. An analysis of X-ray

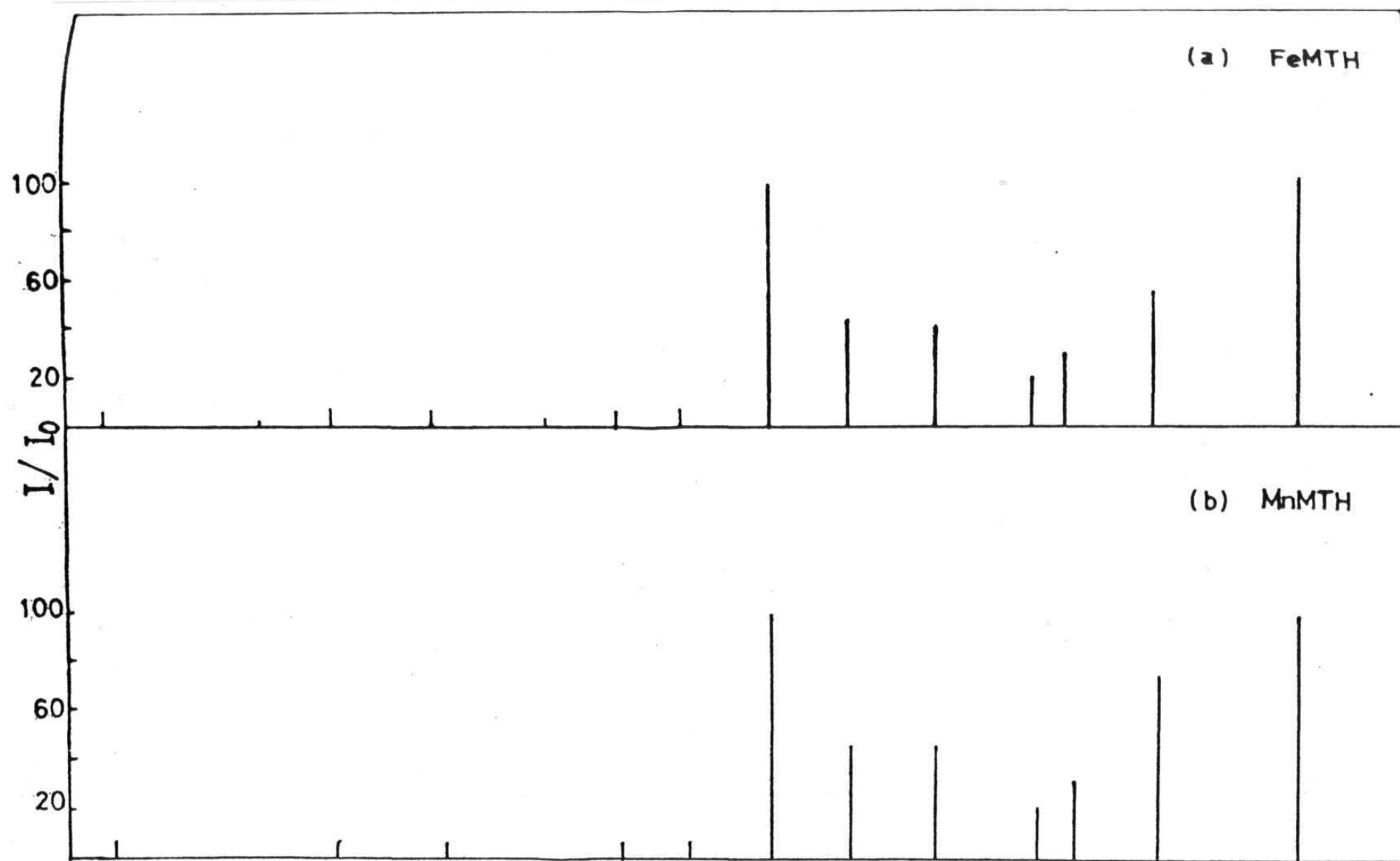


Fig.7.1 X-ray diffractograms of (a) Ferrous Maleate Tetrahydrate and (b) Manganese Maleate Tetrahydrate.

Table 7.1. X-ray data of tetraquabis [Maleato(-1) iron(II) and manganese(II)].

FeMTH $d_{\text{obs}}$	Relative intensity	MnMTH $d_{\text{obs}}$	Relative intensity
6.56	100	6.69	100
5.02	75	5.06	80
4.40	30	4.41	30
4.15	20	4.18	20
3.68	40	3.71	45
3.30	45	3.34	45
3.02	100	3.07	100
2.86	5	2.85	5
2.66	5	2.70	5
2.65	3	2.67	3
2.29	5	2.32	5
2.28	3	2.26	5
2.11	5	2.13	8
1.75	5	1.75	5





data of FeMTH complex using a least square fit programme for the refinement of cell parameters lead to  $a = 7.27$ ,  $b = 9.60$ ,  $c = 5.24 \text{ \AA}$  and  $\alpha = 105.9^\circ$ ,  $\beta = 87.8^\circ$  and  $\gamma = 115.6^\circ$ .

### 7.3.2. Mössbauer studies

The Mössbauer spectra of FeMTH were recorded in the range 15–320 K. Figure 7.3 shows a representative Mössbauer spectrum recorded at 15.5 K. All the spectra show large quadrupole splitting with sharp line widths of  $\sim 0.30 \text{ mm/sec}$ . Table 7.2 gives the Mössbauer parameters for these spectra. The isomer shifts, quadrupole splits and the line width values are typical of  $\text{Fe}^{2+}$  in high spin state with only one type of iron present. The increase in isomer shift with decrease in temperature is in accordance with the theoretical prediction for the second order doppler shift [5]. The absence of magnetically split spectra up to 15 K shows the absence of any strong metal-metal interactions either directly or indirectly through the ligand atoms unlike in the case of ferrous oxalate dihydrate [6]. The significantly large quadrupole splitting of  $3.15 \pm 0.02 \text{ mm/sec}$  for this compound is in accordance with the crystal structure for the isomorphous manganese complex which shows the metal ion to be in a considerably distorted octahedral environment [2]. The quadrupole

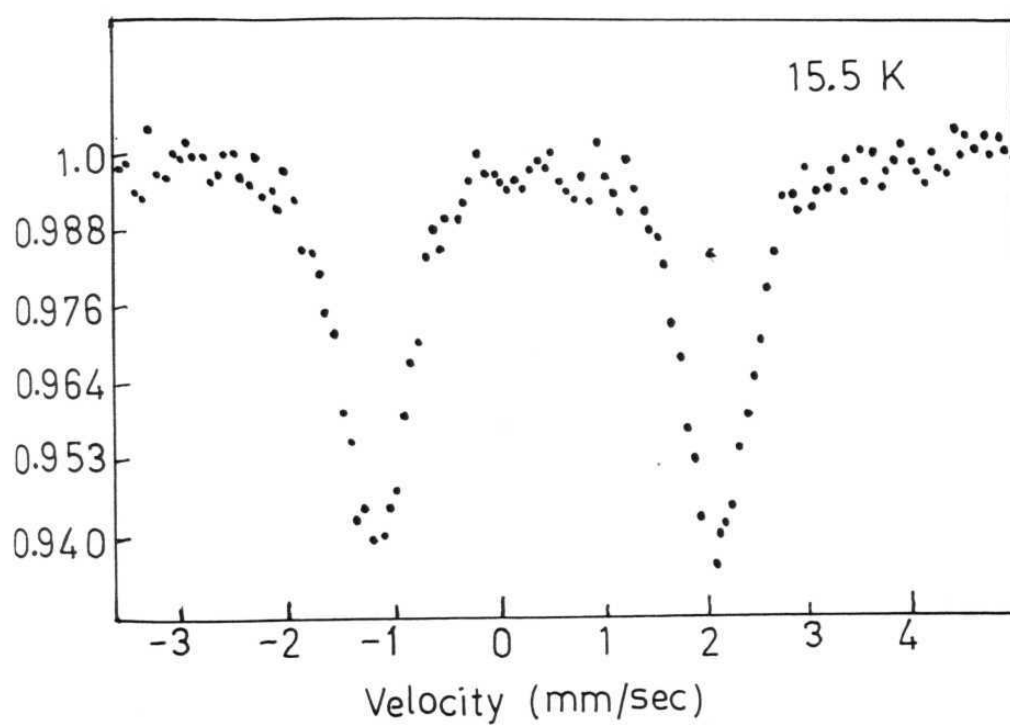


Fig.7.3 Mössbauer spectrum of Ferrous Maleate Tetrahydrate at 15.5 K.

Table 7.2. Mössbauer parameters of Iron(II) maleate tetrahydrate between 15.5 and 323 K.

Temp (K)	I.S. <sup>†</sup> . (mm/sec) ( $\pm 0.02$ )	Q.S. (mm/sec) ( $\pm 0.02$ )	(mm/sec) (0.015)
323	1.23	2.99	0.34
303	1.26	3.15	0.31
196	1.26	3.29	0.26
80	1.37	3.51	0.29
15.5	--	3.24	0.28

<sup>†</sup>w.r.t Fe-foil.

splitting for the FeMTH is found to be significantly larger than that of iron(II) oxalate dihydrate and iron(II) malonate dihydrate [6,7]. Although one would expect less distortion in complex formation with monodentate ligands, the quadrupole splitting at any given temperature in these systems show that the distortion from cubic symmetry at the metal site is in the order: oxalate < malonate < maleate. Thus the differences in the bonding of the anions with the transition metal ions mentioned above, the size of the anions and possibly hydrogen bonding in these systems discussed in detail in literature play a significant role in deciding the crystal symmetry and the local symmetry at the metal site [2,8,9].

The variation of quadrupole splitting with temperature in the range 15-320 K is given in Figure 7.4. The data were fitted to a theoretical curve by diagonalising a  $15 \times 15$  matrix to obtain the energy levels arising from the  $^5T_{2g}$  level of  $Fe^{2+}$  ( $^5D$ ) state. The terms corresponding to tetragonal ( $\delta$ ) and rhombic ( $\epsilon$ ) distortions were included in the calculations of the electric field gradient (e.f.g) as discussed in section 2.2.1. The contributions to the e.f.g from the  $^5E_g$  levels were ignored. The matrix elements and the computer programme developed earlier in this laboratory for the purpose of such an analysis were made use of for

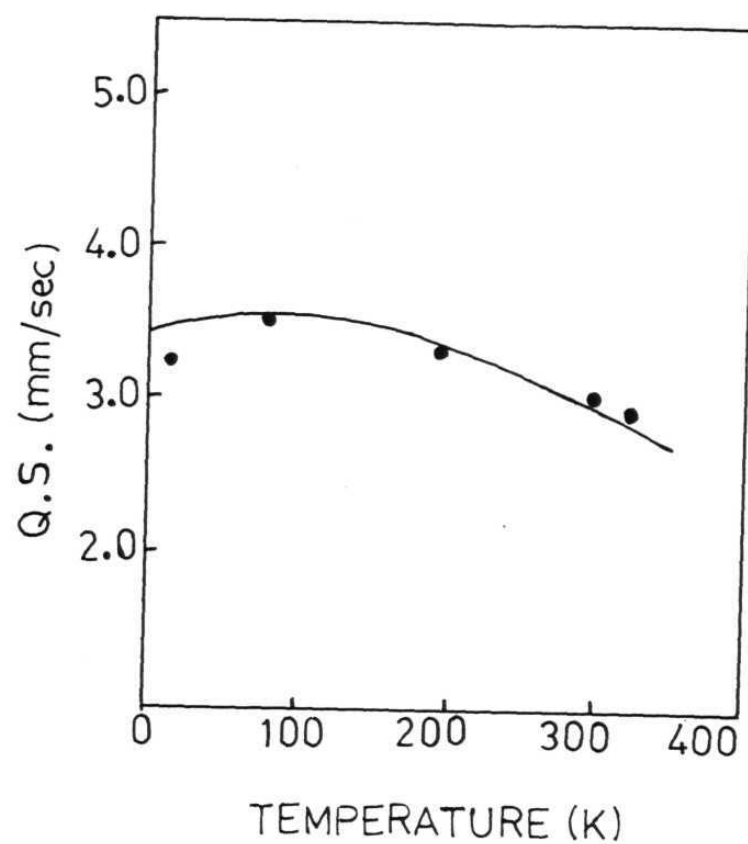


Fig.7.4 Plot of  $q.s.$  vs  $T$ . Experimental data are given as points and the continuous line reproduces the theoretical curve.

obtaining the crystal field parameters for the present case. The theoretical curve giving close agreement with experimental points thus obtained is also reproduced in Figure 7.4. A value of  $\lambda = -80 \text{ cm}^{-1}$  was employed for spin-orbit coupling constant [10]. The closest agreement is found to correspond to a tetragonal field ( $\delta$ ) of  $\sim 650 \text{ cm}^{-1}$  and a rhombic field ( $\epsilon$ ) of  $\sim 190 \text{ cm}^{-1}$  with an orbital singlet ( $d_{xy}$ ) lying lowest. The theoretical prediction of a decrease in the quadrupole splitting at low temperature was substantiated by experiment. Any deviations between the theoretical curve and the experimental points may be attributed to the approximation employed by way of the crystal field approach.

A single crystal Mössbauer spectrum recorded at room temperature for an arbitrary orientation is reproduced in Figure 7.5 for a comparison with that of the powder spectrum. This shows significantly unequal intensities for the quadrupole split spectrum compared to the powder spectrum (Fig. 7.3) and arises due to the difference in the dependence of intensities for the lower and higher  $\gamma$ -rays to the angle between the direction of emission and the axis of symmetry [11-13]. Further Mössbauer and X-ray work to determine the e.f.g. tensor relative to the crystal axes are under progress.

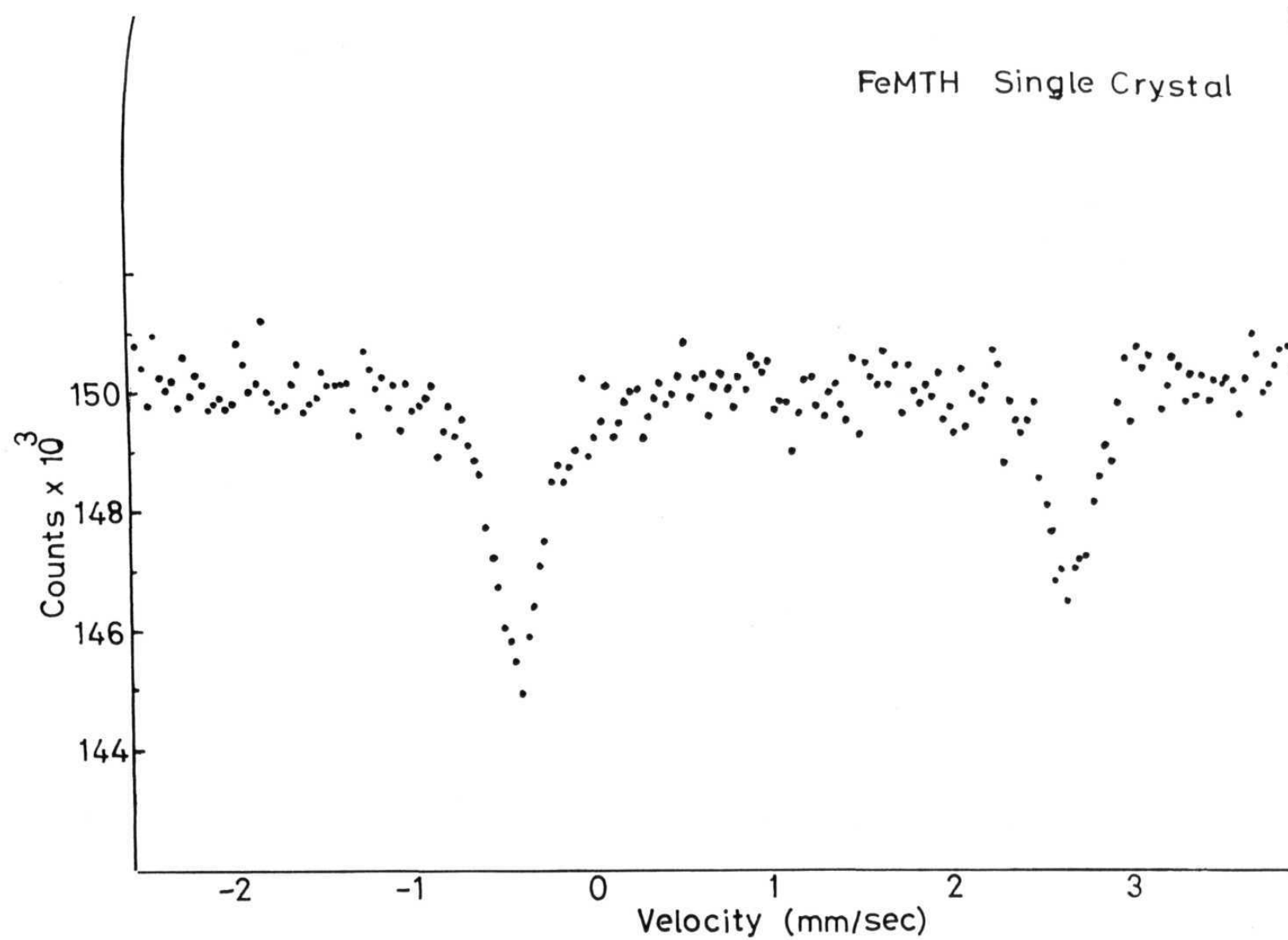


Fig.7.5 Single crystal Mössbauer spectrum of Ferrous Maleate Tetrahydrate at an arbitrary orientation.



### 7.3.3. Optical spectra

Optical spectra can give complementary information on the lower ligand fields. The solution spectrum of FeMTH gives a broad symmetric maximum around  $10,000\text{ cm}^{-1}$  with an extinction coefficient of 1.8 due to d-d transition (Fig. 7.6) [14]. The photoacoustic spectrum (PAS) of solid FeMTH gives an asymmetric band with shoulders, the centre of gravity of which was found to be at  $9800\text{ cm}^{-1}$  (Fig. 7.7). The band has a definite doublet structure with a peak separation of  $1400\text{ cm}^{-1}$ . The optical spectrum is very similar to those reported for high-spin  $\text{Fe}^{2+}$  and arises from the  ${}^5\text{T}_{2g} \longrightarrow {}^5\text{E}_g$  transition [15]. The splitting of the band can be ascribed to the splitting of the excited state in a permanently distorted ligand field as in the case of  $\text{Fe}(\text{NH}_4)_2(\text{SO}_4)_2 \cdot 6\text{H}_2\text{O}$  or to dynamic Jahn-Teller effects [15,16]. We prefer the former reason in the present case in view of the large quadrupole splitting, indicative of large distortion from cubic symmetry at the iron site. A large distortion from cubic symmetry in this case could arise both from the electronic and lattice contributions. Evidence for a strongly distorted lattice symmetry at the metal site was also obtained from the ESR measurements on the manganese analogue [17].

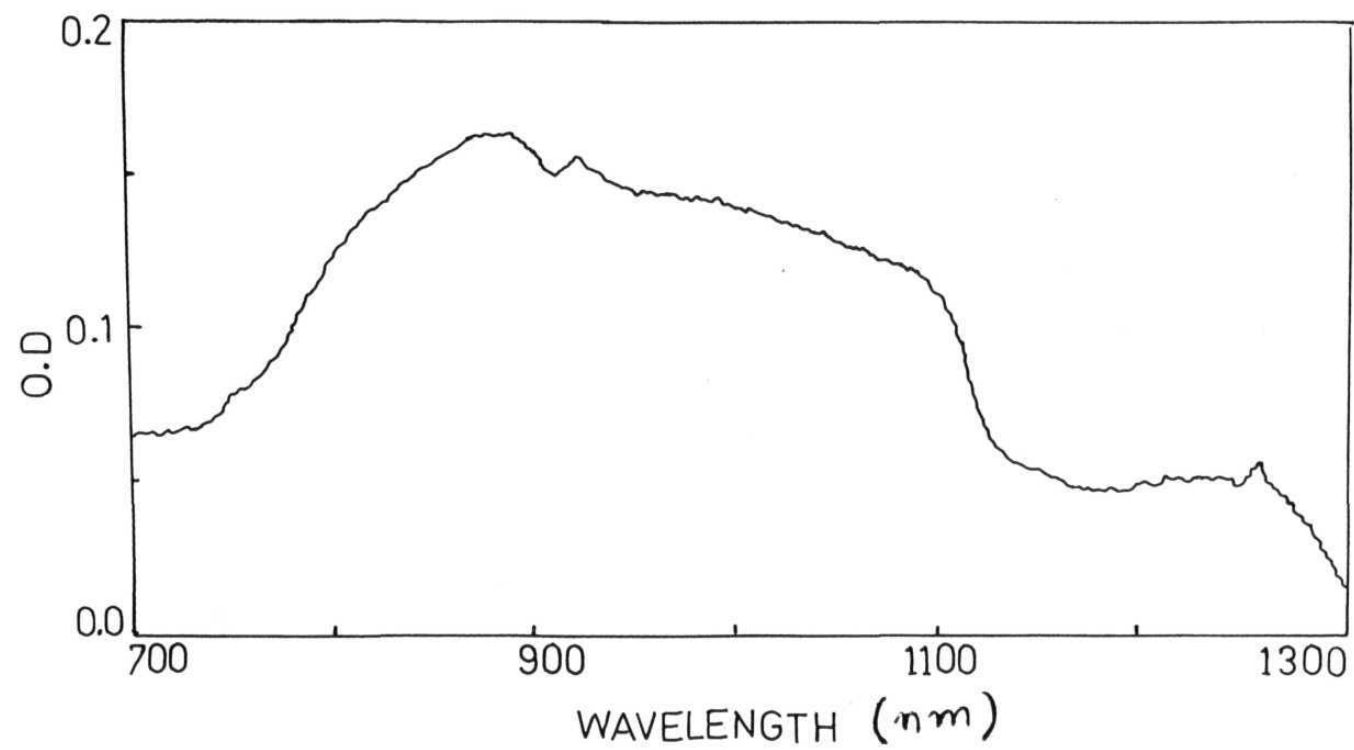


Fig.7.6 Optical spectrum of Ferrous Maleate Tetrahydrate.

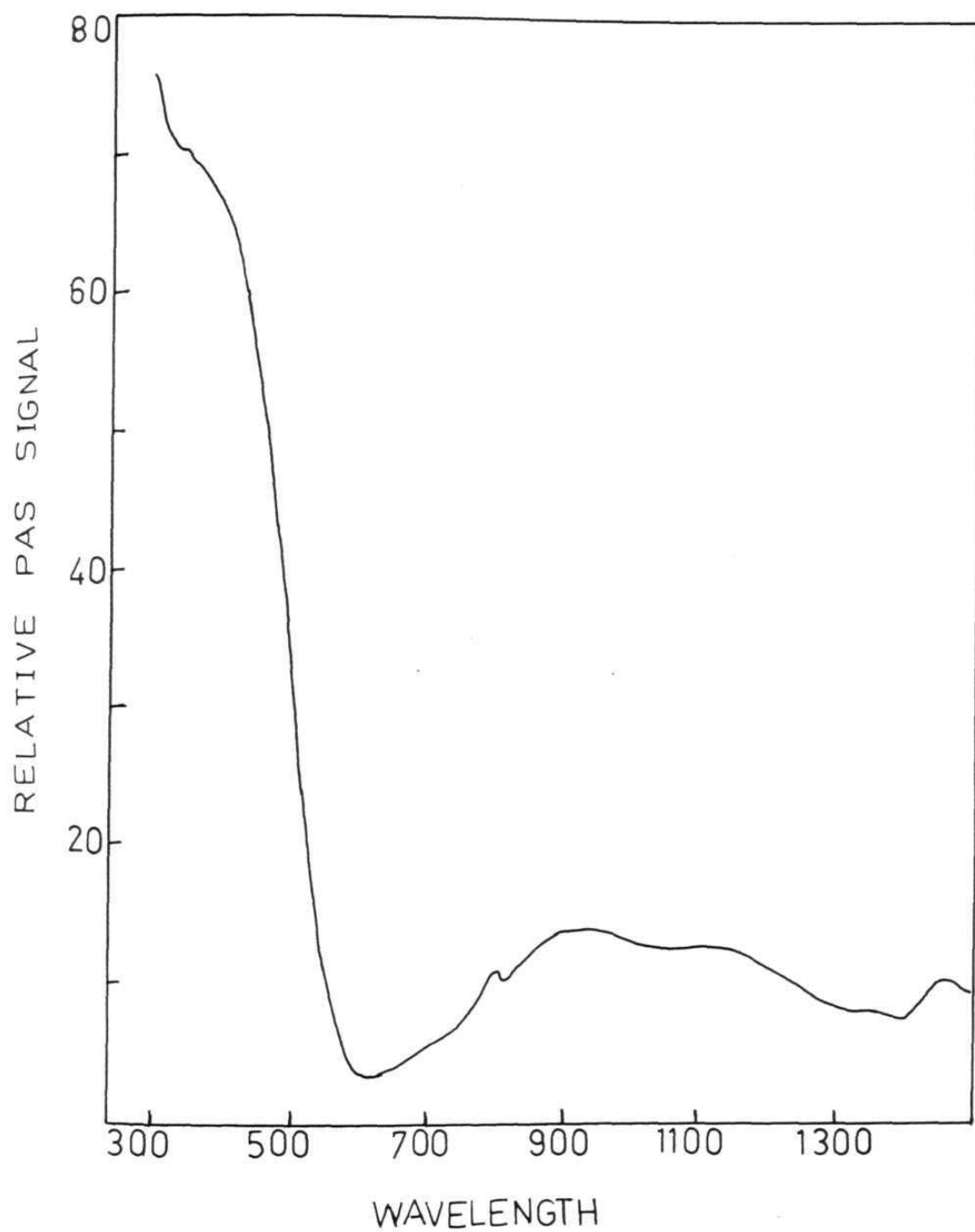


Fig.7.7 Photoacoustic spectrum of Ferrous Maleate Tetrahydrate (wavelength in nm).

#### 7.3.4. Decomposition studies

The differential thermal analysis (DTA) and thermogravimetric analysis (TGA) curves obtained for FeMTH are given in Figure 7.8. The compound starts decomposing at 140°C and gives rise to an endothermic peak in the region 140–240°C. Further decomposition of the resultant material occurs exothermally at 270–500°C. Both the TGA results corresponding to weight loss at 230°C and independent decomposition studies at this temperature showed weight loss corresponding to the loss of 32.1% which is quite close to 32.4% corresponding to the loss of one molecule of maleic acid. The TGA curve also shows the decomposition product formed at ~230°C to be fairly stable up to ~260°C. The room temperature Mössbauer spectra of the original compound and those of the decomposition products obtained at 235 and 275°C are compared in Figure 7.9. The product obtained by heating the complex at 235°C gave rise to a spectrum with an isomer shift of  $1.20 \pm 0.02$  mm/sec relative to iron and a quadrupole splitting of  $2.5 \pm 0.02$  mm/sec providing evidence for  $\text{Fe}^{2+}$  in octahedral symmetry. Further, the smaller quadrupole splitting of the product compared to that in the parent material indicates a structure with a significantly less distortion from cubic symmetry. The iron(II) product thus obtained is also

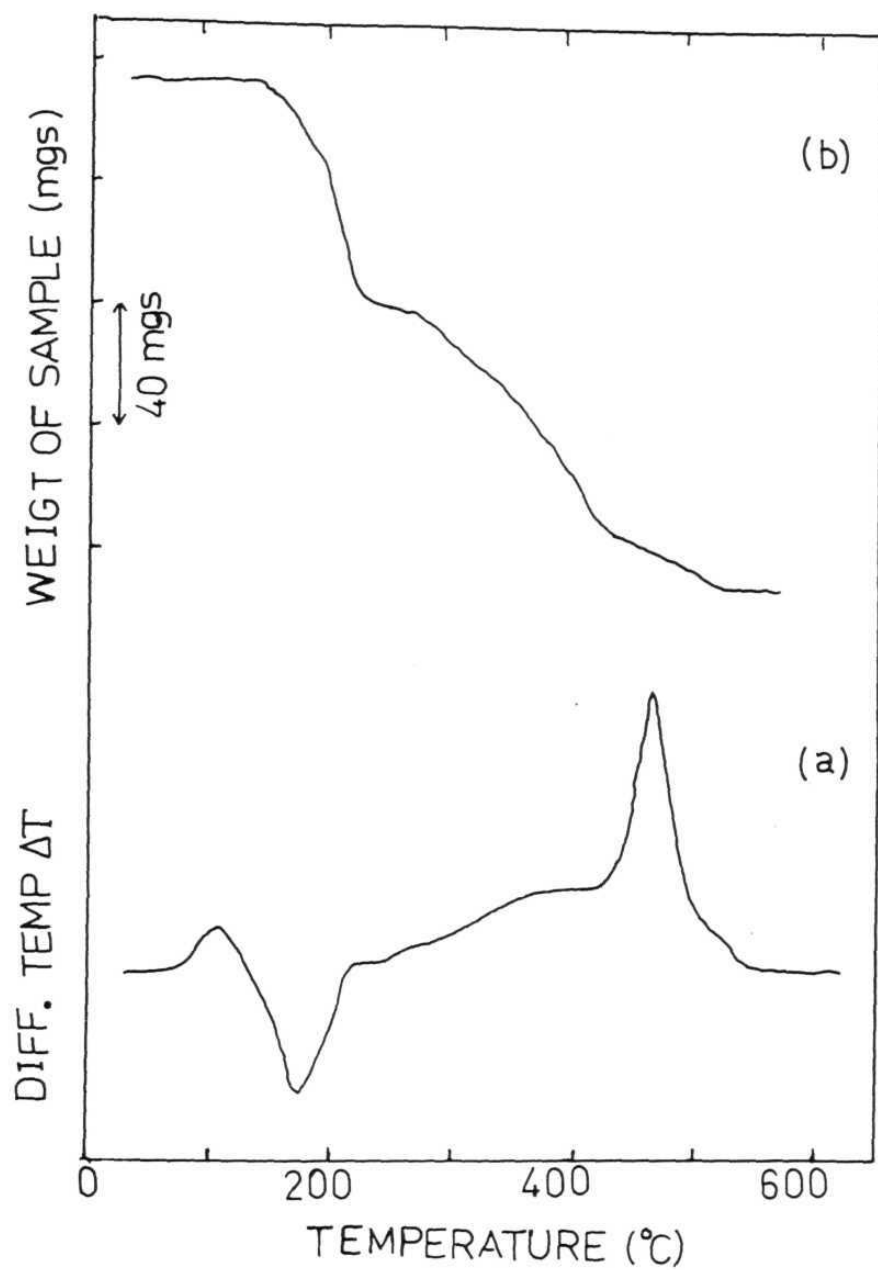


Fig.7.8 (a) DTA and (b) TGA curves for Ferrous Maleate Tetrahydrate.

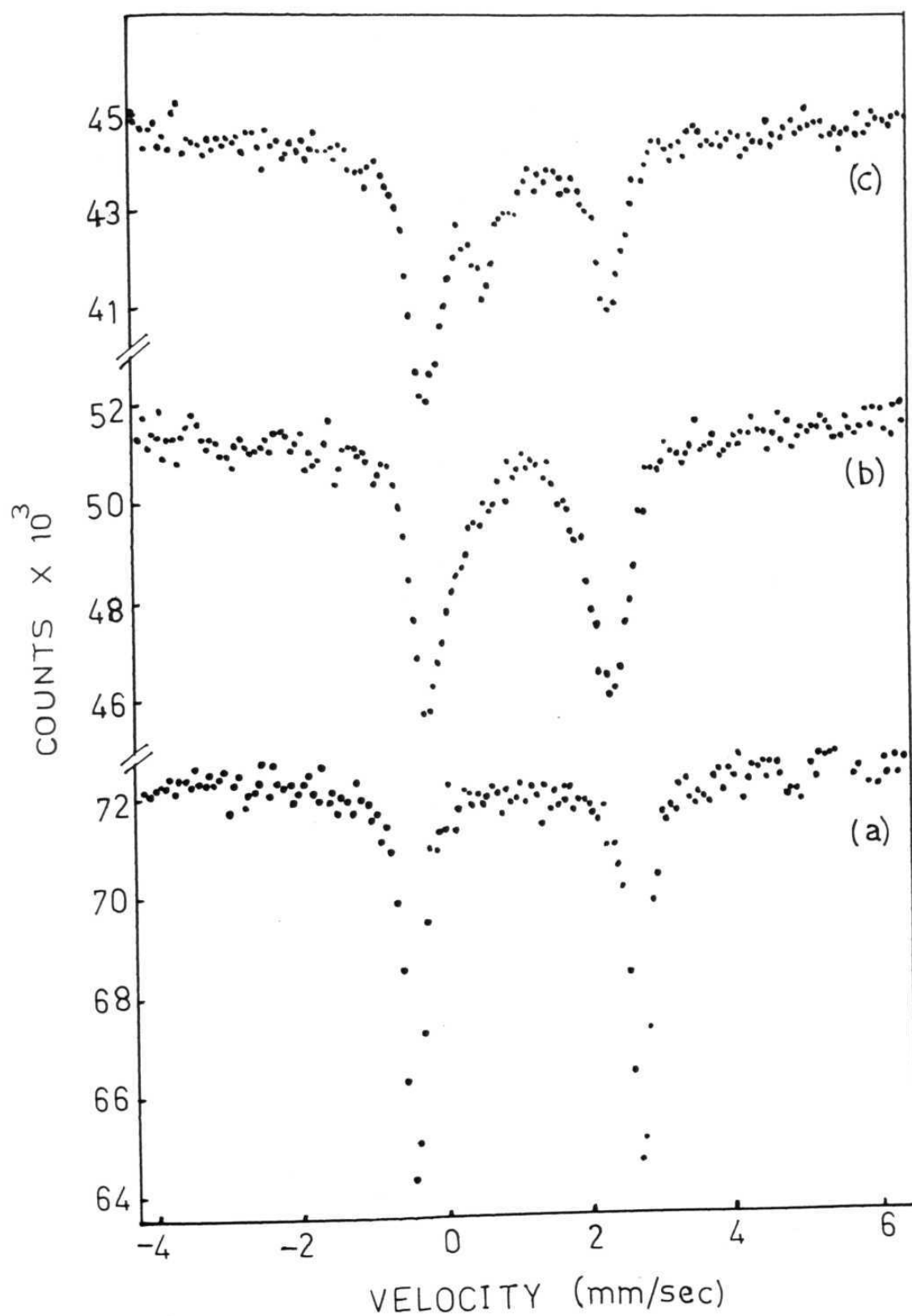
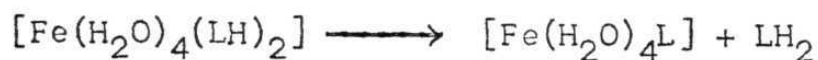


Fig.7.9 Room temperature Mössbauer spectra of (a) Ferrous Maleate Tetrahydrate (b) the product obtained after heating to 235°C and (c) after heating to 280°C.

resistant to air oxidation. Any heating carried out at higher temperatures give rise to products with Mössbauer spectra with components corresponding to iron(III) (Fig. 7.9c). The intermediate product is tentatively identified as an iron(II) maleate formed from the complex FeMTH by a reaction of the type shown



where  $\text{LH}_2$  is maleic acid.

#### 7.4. Conclusions

FeMTH contains maleate (1-) and is isomorphous with the manganese(II) analogue. Mössbauer studies show the structure to be highly distorted from cubic symmetry compared to the ferrous oxalate dihydrate and ferrous malonate dihydrate. The temperature dependence of quadrupole splitting in the range from 320 down to 15 K shows the absence of any metal-metal interactions. Mössbauer data and optical spectra allow estimates of 10 Dq, the tetragonal field, rhombic field and  $E_g$  level splitting to be 10,000, ~650, ~190 and ~1400  $\text{cm}^{-1}$ , respectively. DTA and TGA studies indicate elimination of one molecule of maleic acid at 235°C. Mössbauer

studies of the decomposition products show formation of a stable compound with octahedral geometry and less distorted than the parent material. Further heating shows appearance of an iron (III) species which subsequently decomposes into oxide.



References

1. C.K. Prout, J.R. Carruthers and F.J.C. Rossetti, J. Chem. Soc.(A), 3342 (1971).
2. M.P. Gupta and B. Mahanta, Cryst. Struct. Commun. 7, 179 (1978).
3. K. Saroja and S.V. Raman, Current Science 41, 599 (1972).
4. A.S. Antsyshkina, M.A. Porai-Koshits and M.G. Guseinov. Izv. Akad. Nauk. SSSR, Ser Khim, 237 (1974).
5. G.K. Wertheim, D.N.E. Buchanan and H.J. Guggenheim, Phys. Rev. B2, 1392 (1970).
6. F.de Barros, P.S.Zory and L.E. Cambell Phys. Lett. 7, 135 (1963).
7. N. Ravi, R. Jagannathan, B. Rama Rao and Raza Hussain, Inorg. Chem. 21, 1019 (1982).
8. F. Mazzi and C. Garavelli, Periodico Mineral (Rome), 26, 269 (1975).
9. B. Briggman and A. Oskarsson, Acta. Crystallogr, B34, 3357 (1978).
10. T.C. Gibb, J. Chem. Soc. A, 1439 (1968).
11. P.Zory, Phys. Rev. 140, A1401 (1965).

12. C.E. Johnson, Proc. Phys. Soc. 88, 943 (1966).
13. K. Chandra and S.P. Puri, Phys. Rev. 169, 272 (1968).
14. B.N. Figgis, Introduction to Ligand Fields (Interscience, New York, 1971), p.209.
15. F.A. Cotton and M.D. Meyers, J. Am. Chem. Soc. 82, 5023 (1960).
16. K.D. Bowers and J. Owens, Rep. Prog. Phys., 18, 304 (1955).
17. M. Vithal and R. Jagannathan, Unpublished results.

## CHAPTER 8

### ESR STUDY OF $\text{Cu}^{2+}$ DOPED IN ZINC MALEATE TETRAHYDRATE†

#### Abstract

An ESR study of 1%  $\text{Cu}^{2+}$  doped in zinc maleate tetrahydrate single crystal is found to give rise to  $g_1 = 2.374$ ,  $g_2 = 2.257$  and  $g_3 = 2.043$ . These values are quite different from the  $g$  values for the pure copper(II) compound, copper maleate tetrahydrate, viz.,  $g_{\parallel} = 2.172$  and  $g_{\perp} = 2.095$  indicating that in  $\text{Cu}^{2+}/\text{ZnMTH}$ ,  $\text{Cu}^{2+}$  occupies a compressed octahedral, substitutional site. The ground state is determined to be  $0.724|3z^2-r^2\rangle + 0.173|x^2-y^2\rangle$ . In this case  $\text{Cu}^{2+}$  is coordinated to two maleate groups and four water molecules unlike in the parent copper compound where coordination takes place only with water molecules. The photoacoustic spectrum of copper maleate tetrahydrate gives rise to a charge-transfer band at  $\sim 37,000 \text{ cm}^{-1}$  and d-d transition at  $\sim 15,000 \text{ cm}^{-1}$  with a shoulder at  $\sim 12,000 \text{ cm}^{-1}$ .

---

†Part of this work is published in Spectro.Chim.Acta 41A, 000 (1985).

### 8.1. Introduction

An electron spin resonance (ESR) study of  $\text{Cu}^{2+}$  doped in zinc maleate tetrahydrate (hereafter ZnMTH) is of interest as the crystal structures of copper maleate tetrahydrate (hereafter CuMTH) and ZnMTH are different and  $\text{Cu}^{2+}$  can retain its original structure or it can assume a structure dictated by the parent lattice [1-3]. In ZnMTH the metal ion is coordinated to two maleate groups and four water molecules as in the case of MnMTH, the structure of which is reproduced in chapter 7 (Fig. 7.2). On the otherhand, in CuMTH the maleate groups are not coordinated but only hydrogen bonded to water molecules (Fig. 8.1). A third possibility is the occupation of an interstitial site by  $\text{Cu}^{2+}$  as found in cadmium maleate dihydrate [4]. In this chapter we present the results of an ESR single crystal study of  $\text{Cu}^{2+}/\text{ZnMTH}$ . The informations regarding the g and A tensors, the ground state and the extent of mixing with higher orbitals are obtained. A brief discussion of the powder ESR spectrum and the photoacoustic spectrum giving the d-d transitions of the parent copper compound, viz., CuMTH are also included to bring out the differentiating features in the microsymmetries.

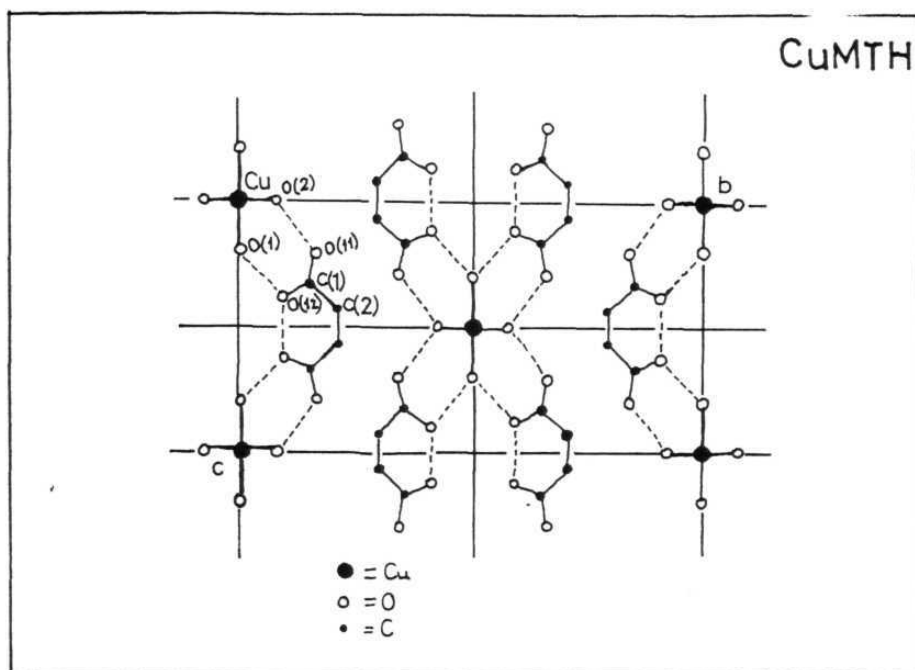


Fig.8.1 Crystal structure of Copper Maleate Tetrahydrate

## 8.2. Experimental

Stoichiometric amounts of  $\text{Cu}^{2+}$  or  $\text{Zn}^{2+}$  metal ions are taken in the form of sulphates (Analar. BDH) and precipitated as hydroxides using ammonium hydroxide. After eliminating excess ammonia by warming the solution the resultant hydroxide is treated with 100% excess hot maleic acid (SD chemical). Upon concentrating the solution deep blue crystals of CuMTH and colourless crystals of ZnMTH separated out. The ZnMTH crystals were doped with 1%  $\text{Cu}^{2+}$  at the starting point.  $\text{Cu}^{2+}$  and  $\text{Zn}^{2+}$  in the pure compounds were estimated as oxides. (Cald. for  $\text{C}_8\text{H}_{14}\text{O}_{12}\text{M}^{\text{II}}$ , ( $\text{M} = \text{Cu}^{2+}$ ,  $\text{Zn}^{2+}$ ):  $\text{Cu}^{2+} = 17.38\%$ ,  $\text{Zn}^{2+} = 17.79\%$ , observed:  $\text{Cu}^{2+} = 17.05\%$ ,  $\text{Zn}^{2+} = 17.06\%$ ).

The ESR spectra have been recorded on three mutually perpendicular laboratory planes (hereafter plane  $\text{YZ}$ ,  $\text{XZ}$  and  $\text{XY}$ ) at an interval of  $10^\circ$ .

The  $g$  values corresponding to equivalent positions achieved in rotating the crystal along the three mutually perpendicular axes were found to agree within experimental error confirming proper mounting of the crystal for different orientations. The values thus obtained for the equivalent positions are presented in Table 8.1.

Table 8.1. Comparison of g-values corresponding to identical orientations when the crystal is rotated in different planes.

Plane    H	g ( $\pm 0.003$ )		
	X'	Y'	Z
X'Y'	2.270	2.176	-
Y'Z	-	2.172	2.168
X'Z	2.262	-	2.167

### 8.3. Results and Discussion

The ESR spectra  $\text{Cu}^{2+}/\text{ZnMTH}$  consists of four lines for an arbitrary orientation of the crystal in the static magnetic field with adjacent lines separated by  $\sim 40$  gauss (Fig. 8.2). The linewidth of the individual lines is found to be  $\sim 40$  gauss. The results of an angular variation study carried out for crystal rotations in three mutually perpendicular planes are reproduced as  $g^2$  vs  $\theta$  and  $g^2 A^2$  vs  $\theta$  plots in Figures 8.3 and 8.4, where  $\theta$  is the angle between the dc magnetic field and the reference axis. These plots were analysed according to the method of Schonland [5] by least square fitting the experimental data to the expression

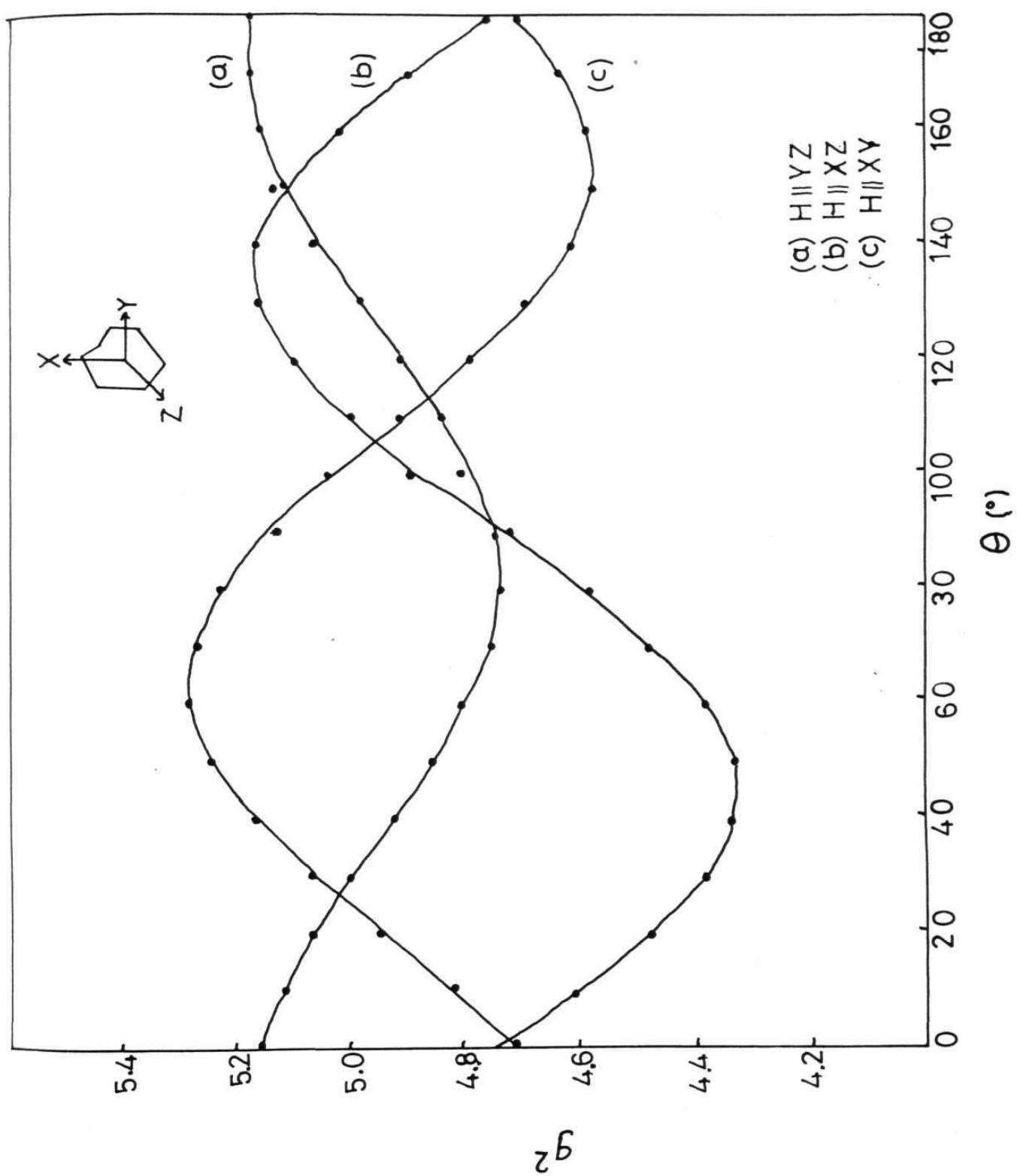
$$g(\theta) = U + V\cos 2\theta + W\sin 2\theta \quad \dots (6.7)$$

as discussed in section 6.2.4. The solid lines in the figure correspond to the least square fit expression of the experimental points. Using the  $g_{\max}^2$ ,  $g_{\min}^2$ ,  $g_{\max}^2 A_{\max}^2$  and  $g_{\min}^2 A_{\min}^2$  the  $g$  and  $A$  matrices were set up and diagonalised to give the  $g$  and  $A$  values in the principal axes system. The values thus obtained are given in Table 8.2. Figures 8.5 and 8.6 show the powder ESR spectra of  $\text{CuMTH}$  and  $\text{Cu}^{2+}/\text{ZnMTH}$  respectively. The  $g$  values evaluated from these powder spectra are also included in Table 8.2.





Fig.8.2 Room temperature ESR spectrum of Cu-doped ZnMTH for crystal rotation about Y' axis.



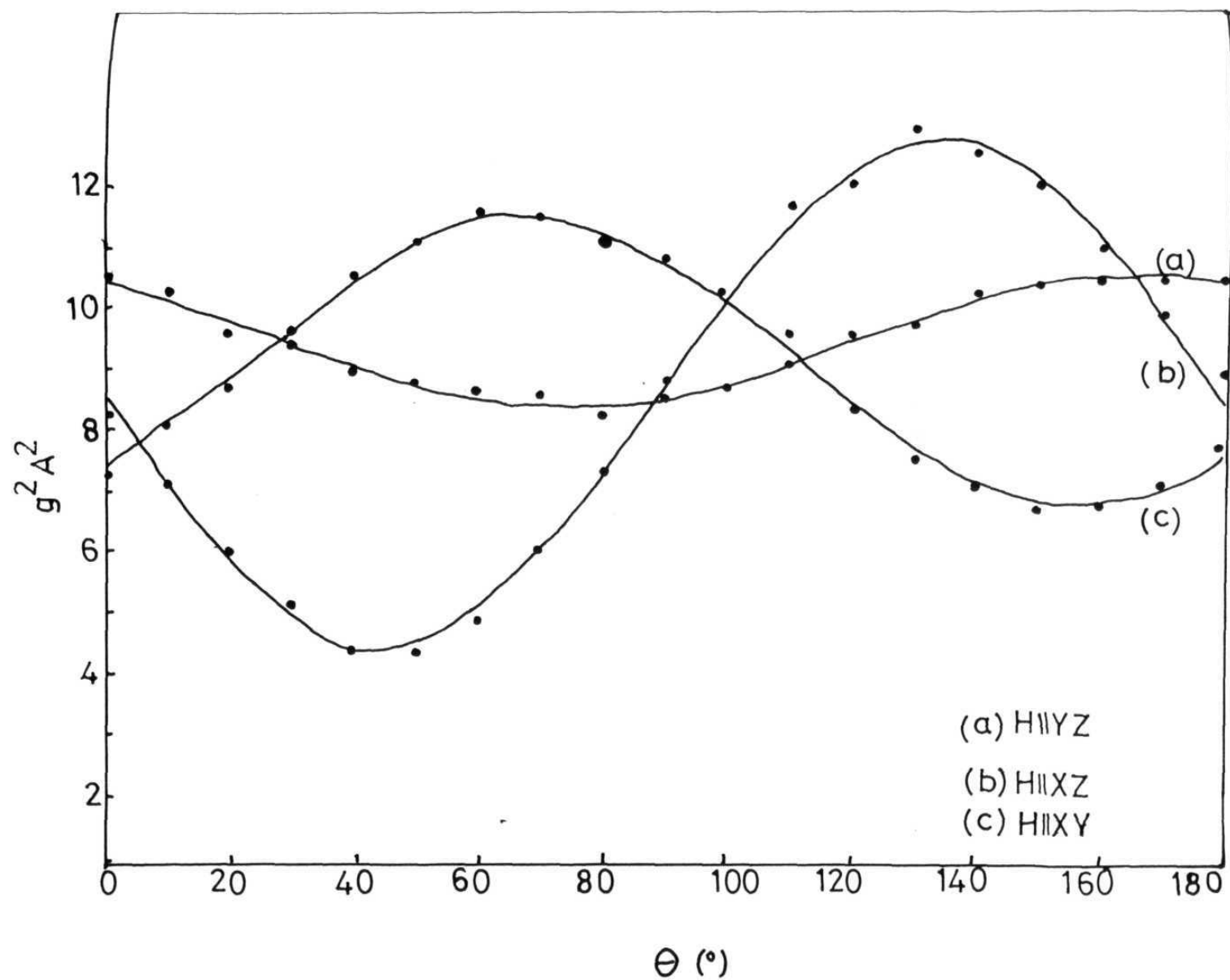


Fig.8.4 Angular variation of Cu-hyperfine structure ( $g^2 A^2$ ) in the ESR spectra of Cu-doped ZnMTH for crystal rotations about (a) X' axis, (b) Y' axis and (c) Z axis.

Table 8.2. Comparison of  $g$ ,  $A$ ,  $\alpha$ ,  $\beta$  values in Cu-doped ZnMTH and related systems

(  $A$  values are in units of  $10^{-4} \text{ cm}^{-1}$  ).

Host lattice	$g_{xx}$	$g_{yy}$	$g_{zz}$	$A_{xx}$	$A_{yy}$	$A_{zz}$	$\alpha$	$\beta$	ground state	Remarks	Ref.
$\text{Zn}(\text{HCOO})_2 \cdot 2\text{H}_2\text{O}$	2.077	2.077	2.416	23	23	124			$d_{x^2-y^2}$	2 sites Substitutional	13
ZnMTH* (Single crystal)	2.374	2.207	2.043	46.8	39.7	29.5	0.724	0.173	$d_z^2$	Substitution	Present work
ZnMTH (powder)	2.33	2.21	2.06	-	-	-	-	-	-	-	Present work
CuMTH (powder)	2.095	2.095	2.172	-	-	-	-	-	-	-	Present work
Cadmium maleate dihydrate	2.091	2.091	2.409	11	11	126	0.895	0.104	$d_{x^2-y^2}$	Interstitial	4
Zn(II) (pyridine-3-sulphonate)	2.283	2.221	2.055	63	42	77	-	-	$d_z^2$	Substitutional	10

\* $g$  values are accurate to  $\pm 0.003$ .

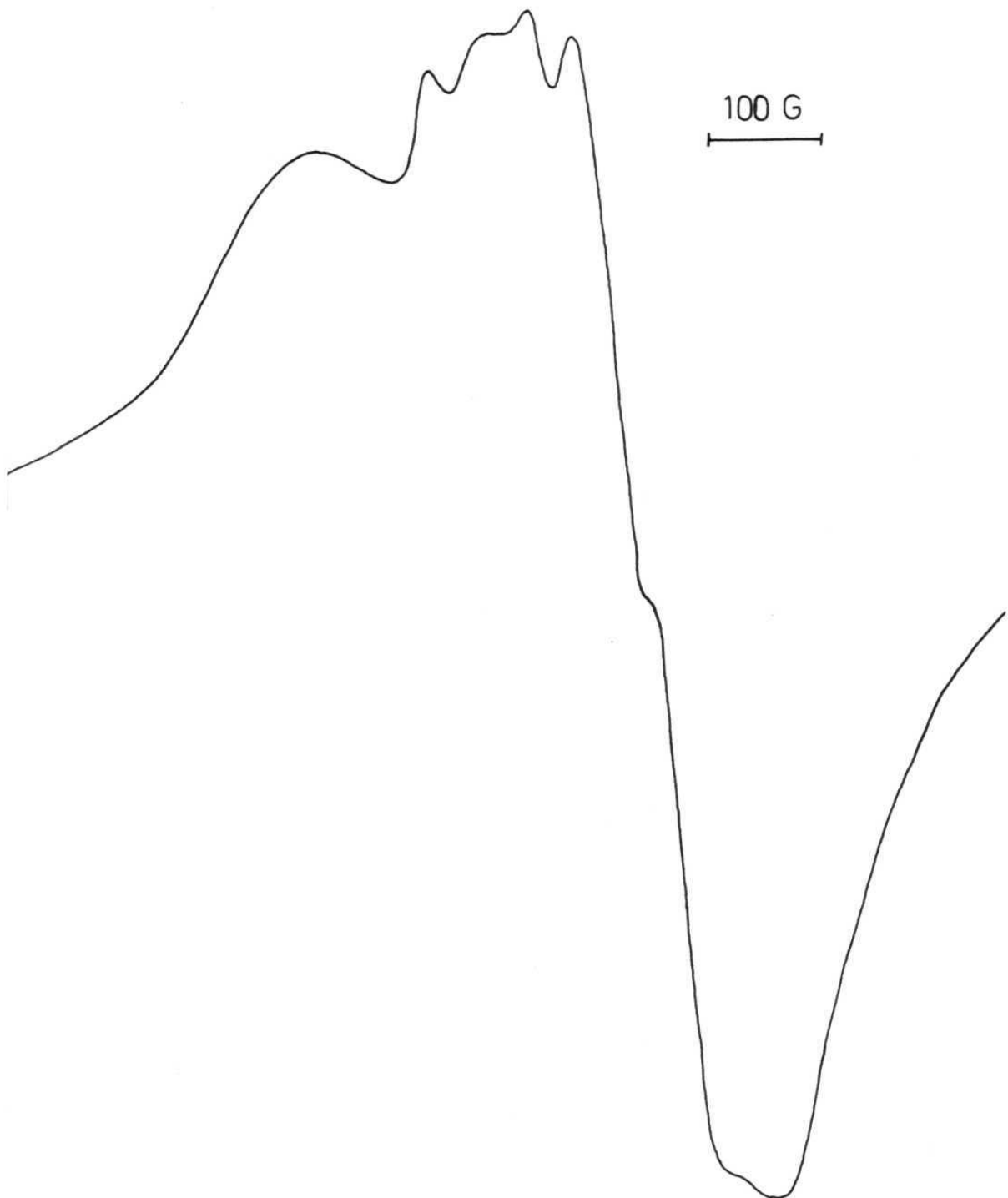


Fig.8.5 Room temperature powder ESR spectrum of Copper Maleate Tetrahydrate.

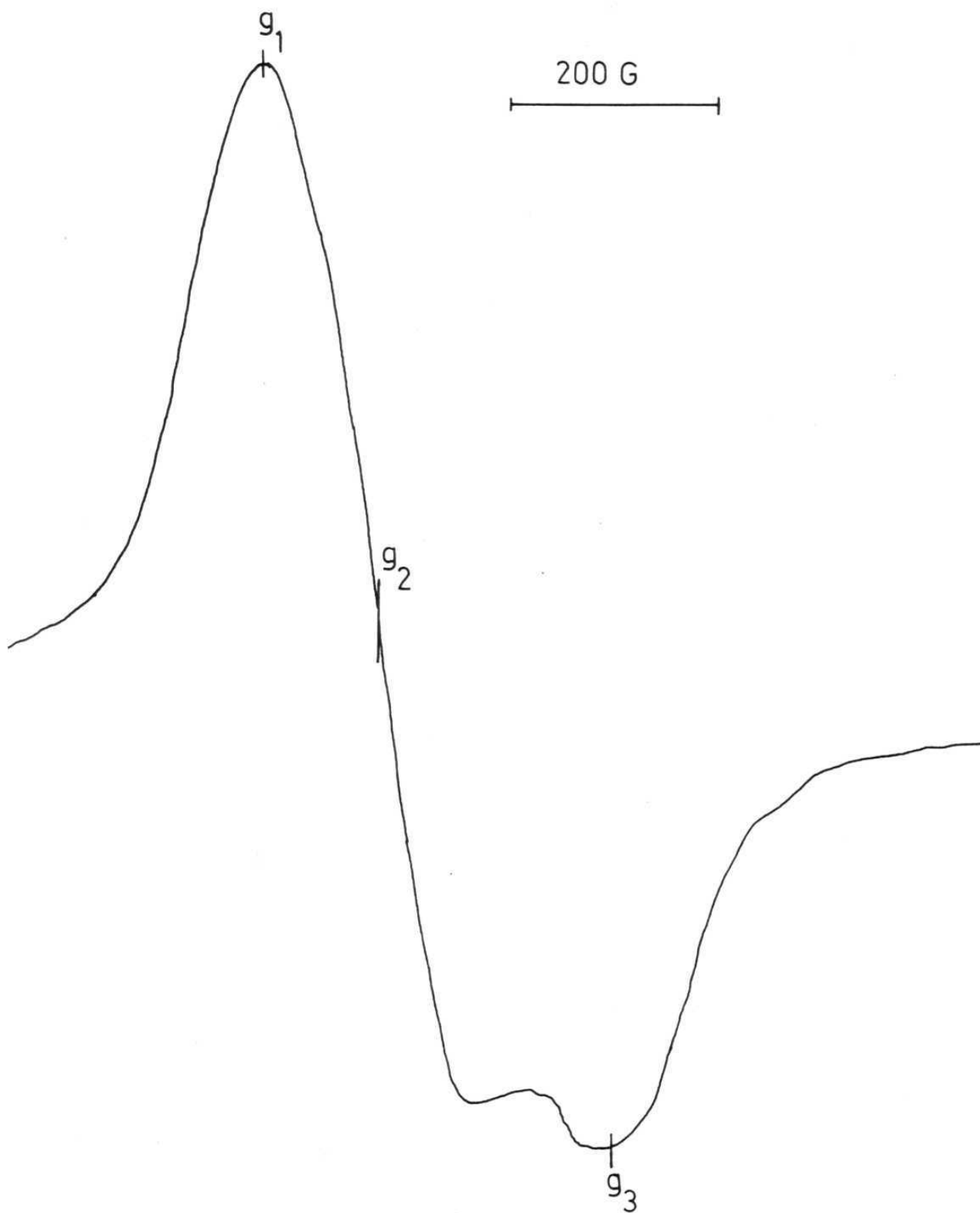


Fig.8.6 Room temperature powder ESR spectrum of Cu-doped ZnMTH.

The observed four line spectra (Fig. 8.2) is typical of  $\text{Cu}^{2+}$  resonance arising from single site. The linewidth of the individual lines which is  $\sim 40$  gauss is of the order of hyperfine coupling constant. The present system being paramagnetically dilute, the observed linewidth could arise from (i) spin lattice relaxation (ii) unresolved isotopic resonances ( $^{63}\text{Cu}$  and  $^{65}\text{Cu}$ ) and (iii) possible unresolved super hyperfine interaction with nearby protons. Furthermore, the lines are fairly symmetric and there are only four peaks for all crystal orientations. The crystal structure of the host lattice being of such low symmetry, any physical or chemical inequivalence in the occupancy of  $\text{Cu}^{2+}$  would easily manifest in the ESR spectra [6]. Interstitial insertion may also be ruled out in view of the fact that in analogous systems it is found to give rise to poorly resolved broad lines in all orientations in the room temperature measurements [4]. A comparison of the unit-cell dimensions of the isomorphous triclinic systems  $\text{M}^{\text{'}}\text{MTH}$  ( $\text{M}^{\text{'}} = \text{Co}^{2+}$ ,  $\text{Ni}^{2+}$  and  $\text{Zn}^{2+}$ ) with the reported detailed crystal structure data for  $\text{MnMTH}$ , according to which  $\text{Mn}^{2+}$  ions occupy special positions (000) in the triclinic unit cell, and our own observation by ESR that  $\text{Mn}^{2+}$  goes into substitutional site in  $\text{ZnMTH}$ , support the view that the transition metal ion in  $\text{ZnMTH}$  and  $\text{MnMTH}$  have closely similar micro-symmetry with only type of site occupancy [1,2,7,8]. In

such a case,  $\text{Cu}^{2+}$  occupying only one type of site substitutionally, should also give rise to ESR spectrum due to only one type of  $\text{Cu}^{2+}$  ion as observed.

The  $^2\text{D} (d^9)$  ground state of  $\text{Cu}^{2+}$  splits into five non-degenerate orbitals if the symmetry of the crystalline electric field is lower than axial. Taking  $d_{z^2}$  as the ground state for reasons discussed later, and  $d_{x^2-y^2}$  as the close by, higher state, the ground state wavefunction may be written as  $\alpha|3z^2-r^2\rangle + \beta|x^2-y^2\rangle$  where  $\alpha$  and  $\beta$  are the mixing coefficients arising from spin-orbit interaction. The departure ( $\Delta g_i$ ) of each of the three principal g-values,  $g_i$  from the free spin value 2.0023, and the principal A values are substituted in the simultaneous equations developed by Sroubeck and Zdansky [9] and solved to obtain the values of  $\alpha$  and  $\beta$ . As the signs of  $A_1, A_2$  and  $A_3$  are not known, trial combinations were used in the above equations. Only when  $A_1$  and  $A_2$  were chosen positive and  $A_3$  negative, the conditions  $\alpha \approx 1$  and  $\beta \ll 1$  could be met and the values were found to be  $\alpha = 0.724$  and  $\beta = 0.173$ . The other parameters obtained are  $P_{\text{exptl}} = \alpha^2 P_{\text{freeion}} = \alpha^2 g\beta_N \beta_N \langle r^{-3} \rangle = 0.019 \text{ cm}^{-1}$  using the value  $0.036 \text{ cm}^{-1}$  for  $P_{\text{freeion}}$  in the case of  $\text{Cu}^{2+}$  and  $k = 0.353$  which represents the admixture of configurations with s electrons caused by spin exchange polarisation.



To facilitate discussion we have included the  $g$  and  $A$  values of related systems along with those of  $\text{Cu}^{2+}/\text{ZnMTH}$  in Table 8.2. The lowest  $g$  value obtained for  $\text{Cu}^{2+}/\text{ZnMTH}$  viz., 2.043 is rather high to correspond to a pure  $d_z^2$  ground state and suggests extensive mixing of the  $d_z^2$  and the  $d_{x^2-y^2}$  in the ground state [10]. This is well in accord with the  $\alpha$  and  $\beta$  values obtained. Two other noteworthy features are (i) the comparable magnitude of the  $A$  values and (ii) the association of the largest  $g$ -value with the largest  $A$ -value. Attempts to explain these features pointing out the importance of temperature dependence of the hyperfine parameters in such cases have been made by Walsh and Hathaway [10].

A comparison of the  $g$ -value for the  $\text{Cu}^{2+}/\text{ZnMTH}$  in single crystal and powder form of  $\text{Cu}^{2+}/\text{ZnMTH}$  and that of pure copper compound in the powder form show that  $\text{Cu}^{2+}$  is in different microsymmetries in ZnMTH and CuMTH. The  $g$ -values for the  $\text{Cu}^{2+}$  doped ZnMTH powder are close to those obtained for the single crystal (Table 8.2). On the other hand the pure copper compound, gives  $g_{\parallel} = 2.172 \pm 0.002$ ,  $g_{\perp} = 2.095 \pm 0.002$  indicating axial symmetry with  $\text{Cu}^{2+}$  in elongated octahedron ( $g_{\parallel} > g_{\perp}$ ) with  $d_{x^2-y^2}$  as the ground state [1]. For the doped system  $g_3 > g_2 > g_1 > 2.0$  signifies a distorted octahedron [11]. A survey of literature shows that in

parent zinc host lattices  $\text{Cu}^{2+}$  invariably goes into  $\text{Zn}^{2+}$  site, unlike in the case of  $\text{Cd}^{2+}$ ,  $\text{Sr}^{2+}$  host lattices, where  $\text{Cu}^{2+}$  can also occupy interstitial sites. This may be attributed to comparable ionic radii for  $\text{Cu}^{2+}$  and  $\text{Zn}^{2+}$  ( $\text{Cu}^{2+} = 0.73 \text{ \AA}$ ,  $\text{Zn}^{2+} = 0.75 \text{ \AA}$ ) unlike in the case of  $\text{Cu}^{2+}$  and  $\text{Cd}^{2+}$  or  $\text{Sr}^{2+}$  ( $\text{Cd}^{2+} = 0.95 \text{ \AA}$ ,  $\text{Sr}^{2+} = 1.16 \text{ \AA}$ ). This is found to be true in the case of complexes of organic acids as well [4,12,13]. It is therefore reasonable to attribute the above g-values as due to substituted  $\text{Cu}^{2+}$ . The space group, unit cell dimensions and coordinations reported for the host lattice suggest a close similarity with that of manganese maleate tetrahydrate [2,3,7]. Assuming similar microsymmetry for the  $\text{Cu}^{2+}$  environment would imply that the g-values correspond to a compressed octahedron with  $d_{z^2}$  ground state. Such a conclusion would mean that Zn-lattice dictates both coordination and microsymmetry to the  $\text{Cu}^{2+}$  ion. Similar situations have been reported in cases like Zn(II) bis(pyridine-3-Sulphonate) [10,14]. Thus unlike in the CuMTH where copper ion is coordinated to six water molecules, in 1%  $\text{Cu}^{2+}$ /ZnMTH it will be bound to two maleate groups and four water molecules. Further confirmation of this conclusion can be obtained by determining the direction cosines provided the detailed crystal structure data for ZnMTH are available.

The photoacoustic spectrum of CuMTH is reproduced in Figure 8.7. An intense band at  $\sim 37,000 \text{ cm}^{-1}$  and a relatively less intense and broad band at  $\sim 15,000 \text{ cm}^{-1}$  with a shoulder at  $\sim 12,000 \text{ cm}^{-1}$  are observed. The intense band at  $\sim 37,000 \text{ cm}^{-1}$  arises due to charge transfer [15]. The broad bands at  $\sim 15,000 \text{ cm}^{-1}$  arise from d-d transitions. For the present case where  $\text{Cu}^{2+}$  is situated in an octahedron with four oxygen atoms in the plane at  $1.95 \text{ \AA}$  and two oxygen atoms at  $2.68 \text{ \AA}$  with  $d_{x^2-y^2}$  as the ground state, the transitions would correspond to  $d_z^2 \rightarrow d_{x^2-y^2}$ ,  $d_{xy} \rightarrow d_{x^2-y^2}$  and  $d_{xz,yz} \rightarrow d_{x^2-y^2}$ . However, only two bands are observed due to poor resolution in a powder spectrum [15,16].

#### 8.4. Conclusions

An ESR study of  $1\% \text{ Cu}^{2+}$  doped in ZnMTH single crystal gives rise to  $g_1 = 2.374$ ,  $g_2 = 2.257$  and  $g_3 = 2.043$ . These values are quite different from the g-values for the pure copper compound viz.,  $g_{\parallel} = 2.172$  and  $g_{\perp} = 2.095$ , indicating that in  $\text{Cu}^{2+}/\text{ZnMTH}$ ,  $\text{Cu}^{2+}$  occupies a compressed octahedral, substitutional site with the ground state  $0.724|3z^2-r^2\rangle + 0.173|x^2-y^2\rangle$ , coordinated to two maleate groups and four water molecules, the microsymmetry being dictated by the host lattice, unlike in the copper compound

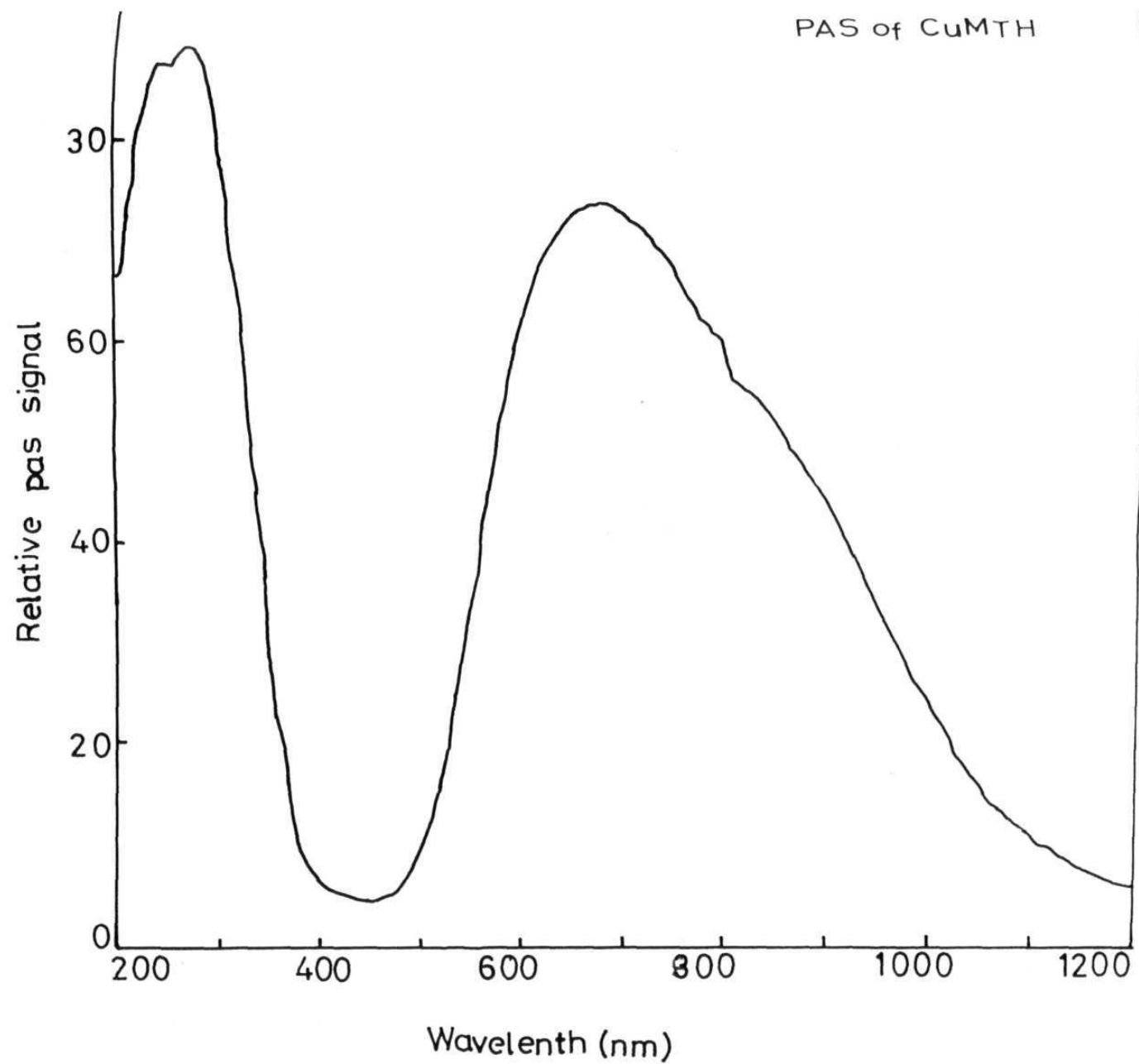


Fig.8.7 Photoacoustic spectrum of solid Copper Maleate Tetrahydrate.

where coordination takes place only with water molecules. The photoacoustic spectrum of CuMTH gives rise to a charge transfer band at  $\sim 37,000 \text{ cm}^{-1}$  and d-d transitions at  $\sim 15,000 \text{ cm}^{-1}$  with a shoulder at  $\sim 12,000 \text{ cm}^{-1}$ .

References:

1. C.K. Prout, J.R. Carruthers and F.J.C. Rossetti, J. Chem. Soc. (A) 3342 (1971).
2. A.S. Antsyshkina, M.A. Porai-Koshits and M.G. Guseinov, Izv. Akad. Nauk. SSSR, Ser Khim, 237 (1974).
3. K. Saroja and S.V. Raman, Current Science 41, 599 (1972).
4. V. Chandra Mouli and G. Sivarama Sastry, Pramana 12, 165 (1979).
5. D.S. Schonland, Proc. Phys. Soc. 73, 788 (1959).
6. S.K. Yadav, V.P. Seth and R.K. Malhotra, Ind. J. Pure and Appl. Phys. 21, 631 (1983).
7. M.P. Gupta and B. Mahanta, Cryst. Struct. Commun. 7, 179 (1978).
8. M. Vithal and R. Jagannathan, Unpublished results.
9. Z. Sroubeck and K. Zdansky, J. Chem. Phys. 44, 3078 (1966).
10. B.J. Hathaway and B. Walsch, J. Chem. Soc., Dalton Trans. 681 (1980).
11. B.J. Hathaway, M. Duggan, A. Murphy, J. Mullane, C. Power, A. Walsh and B. Walsh, Coord. Chem. Rev. 36, 267 (1981).

12. M. Narayana, S.G. Satyanarayana and G. Sivaramasastry, Ind. J. Pure. Appl. Phys. 14, 741 (1976).
13. G.R. Wagner, R.T. Schumacher and S.A. Friedberg, Phys. Rev. 150, 226 (1966).
14. Ref. 11, p.308.
15. B.J. Hathaway and D.E. Billing, Coord. Chem. Rev. 5, 143 (1970) and references therein.
16. B.J. Hathaway, Coord, Chem. Rev. 52, 87 (1983).

## CHAPTER 9

### AN ESR STUDY OF $Mn^{2+}$ DOPED ZINC MALEATE TETRAHYDRATE

#### Abstract

The ESR study of 1%  $Mn^{2+}$  doped in ZnMTH single crystal gives rise to the spin-Hamiltonian parameters  $D = 385.6$ ,  $E = 71.5$ ,  $a = -9.5$  and  $A = -93$  gauss from an analysis of the allowed hyperfine transitions corresponding to the orientation of the principal axis parallel to the magnetic field as shown by the absence of forbidden transitions. The large  $g$  value viz., 2.035 observed for this system has been attributed to a highly distorted cubic environment. An ionicity of 96.5% is deduced for the metal-ligand bonding from a plot of  $A$  vs the Pauling's covalency parameter. The analysis of forbidden hyperfine transitions is shown to lead to  $Q' = 1.69$  and  $Q'' = 0.304$  for the axial and rhombic components of the quadrupole coupling constants respectively of the  $^{55}Mn$  nucleus.



### 9.1. Introduction

Electron spin resonance studies in organic acid complexes show that the dopant can go into substitutional or interstitial sites [1-5]. In addition, ESR studies throw light on the nature of the microsymmetry of the dopant [6]. A more interesting feature in such studies in the case of  $\text{Mn}^{2+}$  systems is the observation of forbidden transitions which arise due to the admixture of the off diagonal terms of the type,

$$(S_z S_+) (S_- I_+), (S_z S_-) (S_+ I_-)$$

in the spin Hamiltonian [section 6.2.3]. However in most cases, where such forbidden transitions are observed, detailed analysis are precluded due to large line widths or presence of more than one inequivalent site. Consequently analyses of forbidden transitions have been reported only in few cases [7-9]. Wherever the analysis is possible one gets the Spin-Hamiltonian subjected to a more extensive analysis of the ESR spectra and additional hyperfine parameters relating to the quadrupole moment. In this chapter we present the results of a single crystal ESR study of  $\text{Mn}^{2+}$  ions doped in zinc maleate tetrahydrate (hereafter ZnMTH). Rotation of the

single crystal along mutually perpendicular axes is shown to lead to variations in the intensities of allowed and forbidden transitions as predicted by theory including total absence of the forbidden transitions corresponding to  $H||Z$ . The line positions in the case of  $H||Z$  have been analysed to give the spin Hamiltonian parameters. From the zero field splitting, information on the microsymmetry of  $Mn^{2+}$  is obtained. From the value of  $A$ , the percentage ionicity in the metal-ligand bonding is estimated. Using the spin-Hamiltonian parameters, the line positions of the forbidden transitions also have been analysed as discussed in section 6.2.5, and the values of  $Q'$  and  $Q''$ , the axial and rhombic components of the quadrupole coupling moment of  $^{55}Mn$  respectively, are derived.

## 9.2. Experimental section

Stoichiometric amount of  $Zn^{2+}$  is taken in the form of sulphate (Analar. BDH) and precipitated as hydroxides using ammonium hydroxide. After eliminating excess ammonia by warming the solution, the resultant hydroxide is treated with 100% excess hot maleic acid (SD Chemical). Upon concentrating the solution colourless crystals separated out. The  $ZnMTH$  was doped with 1%  $Mn^{2+}$  at the starting point.  $Zn^{2+}$  in the

pure compound viz., ZnMTH was estimated as oxide. (Cald. for  $C_8H_{14}O_{12}Zn$ ,  $Zn^{2+} = 17.79\%$ , observed:  $Zn^{2+} = 17.14\%$ ).

The detailed crystal structure of ZnMTH is not yet available. However, as per the preliminary reports, ZnMTH forms a triclinic system with space group  $P1$ . There is slight difference in the unit-cell dimensions reported by the two groups. Antsyshkina et al have reported  $a = 7.30$ ,  $b = 9.82$  and  $c = 5.28 \text{ \AA}$  and  $\alpha = 110.2^\circ$ ,  $\beta = 77.1^\circ$  and  $\gamma = 117.0^\circ$  which may be compared with  $a = 7.29$ ,  $b = 9.73$ ,  $c = 5.36 \text{ \AA}$  and  $\alpha = 110^\circ 48'$ ,  $\beta = 63^\circ.18'$  and  $\gamma = 63^\circ.18'$  reported by Saroja and Raman [10,11]. There is one molecule of ZnMTH per unit cell. Experimentally the principal axis is located by observing the spectra at different orientations and achieving that orientation which gives rise to only allowed transitions with intensities free from forbidden transitions which corresponds to  $H||Z$ . Figure 9.1(inset) shows the morphology of the crystal and the plane (marked with crosses) which gives rise to 30 ESR transitions free from forbidden lines. The spectra were subsequently recorded by rotating in two other axes choosing these axes such that they form a mutually perpendicular system with respect to the principal axis. The spectra have been recorded at an interval of  $10^\circ$ . Other details of ESR measurements are already given in 2.1.

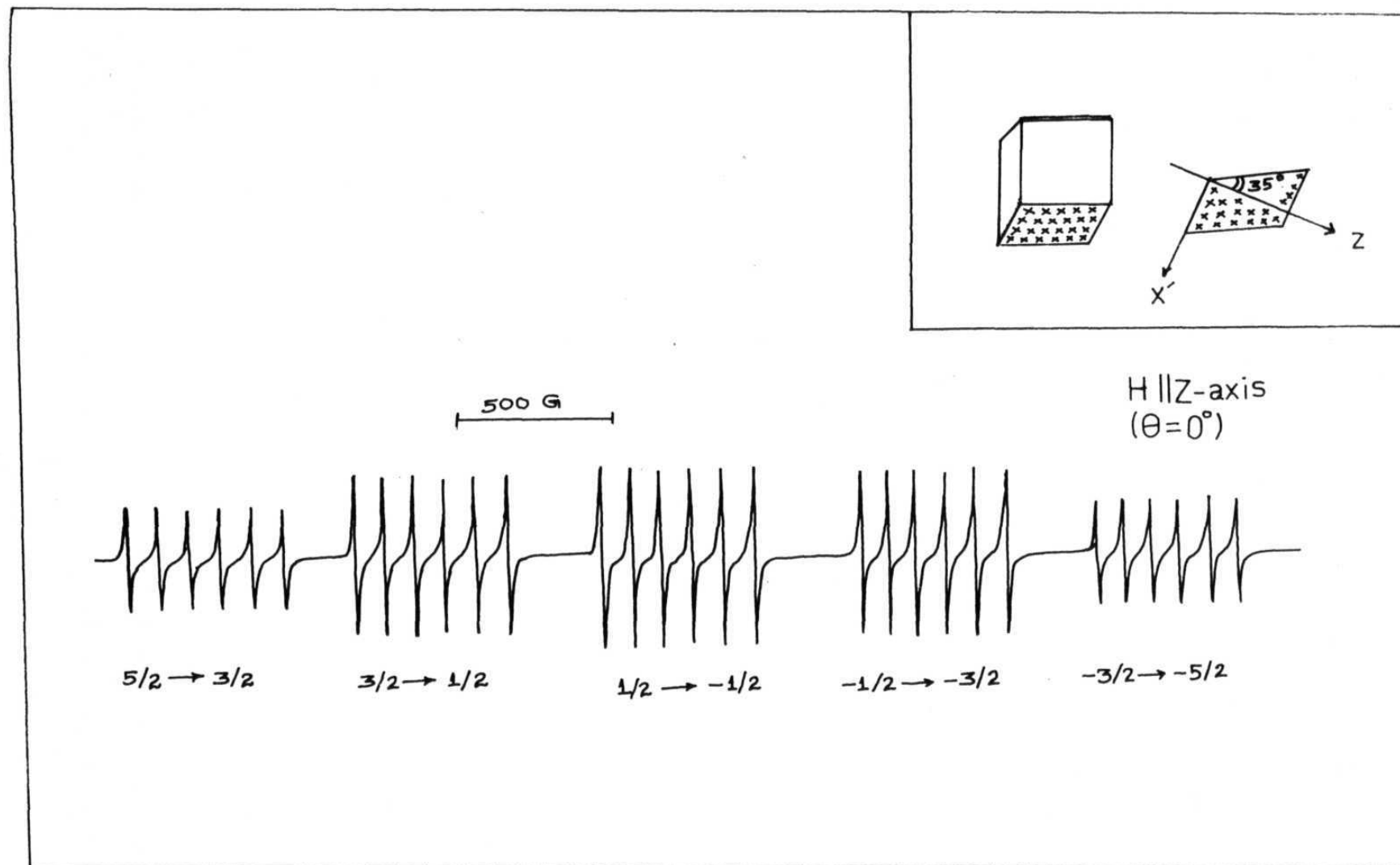


Fig.9.1 Room temperature ESR spectrum of  $\text{Mn}^{2+}/\text{ZnMTH}$  in the  $X'Z$  plane at  $\Theta = 0^\circ$

### 9.3. Results and discussion

A thirty line spectra is typically observed for ESR of  $\text{Mn}^{2+}$  in orthorhombic symmetry when no forbidden lines are present as shown in Figure 9.1. The ground state of  $\text{Mn}^{2+}$  with  $d^5$  configuration is unique among  $d^n$  configurations in that there is only one state with maximum spin multiplicity ( $^6S_{5/2}$ ). This state splits into three Kramers doublets ( $\pm 5/2$ ,  $\pm 3/2$  and  $\pm 1/2$ ) in an orthorhombic crystalline field which are further split in the presence of applied magnetic field. These six levels will give rise to five fine structure transitions. Each fine structure transition will be further split into six hyperfine components due to nuclear spin of  $5/2$  of  $^{55}\text{Mn}$  isotope. Figure 9.2 shows the ESR spectra recorded in the  $X'Z$ -plane making an angle of  $5^\circ$  and  $7^\circ$  with  $Z$ -axis respectively. A neat thirty line spectrum indicates that there is only one type of site in the lattice. Even a small rotation of about  $5^\circ$  around the principal axis makes the presence of forbidden transitions conspicuous as shown in Figure 9.2 compared to Figure 9.1. When the principal axis is parallel to the magnetic field the separation in energy levels and hence the separation between the  $M = 5/2 \rightarrow -3/2$  and  $M = +3/2 \rightarrow +5/2$  will be maximum [12]. The ratio of the

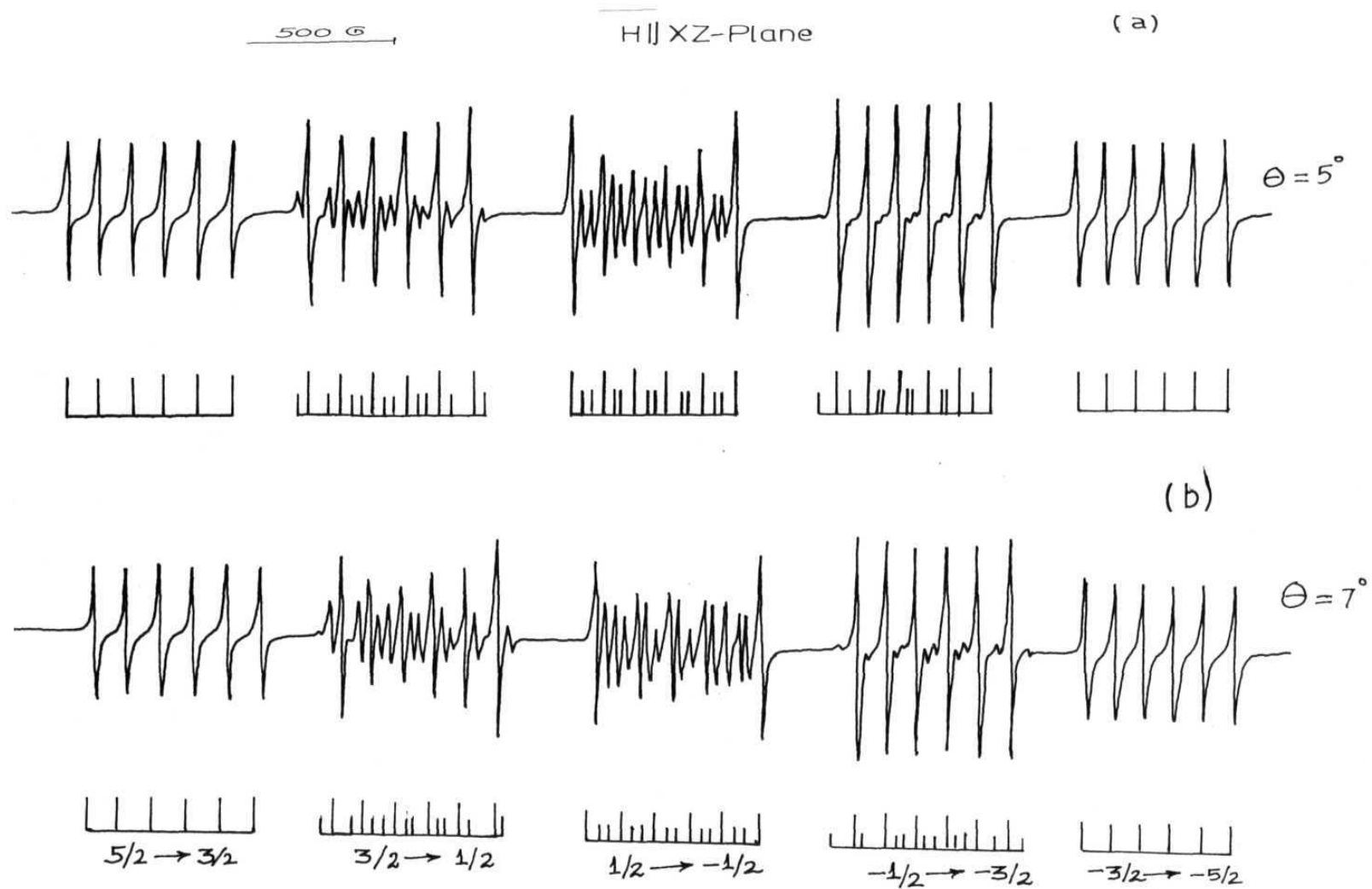


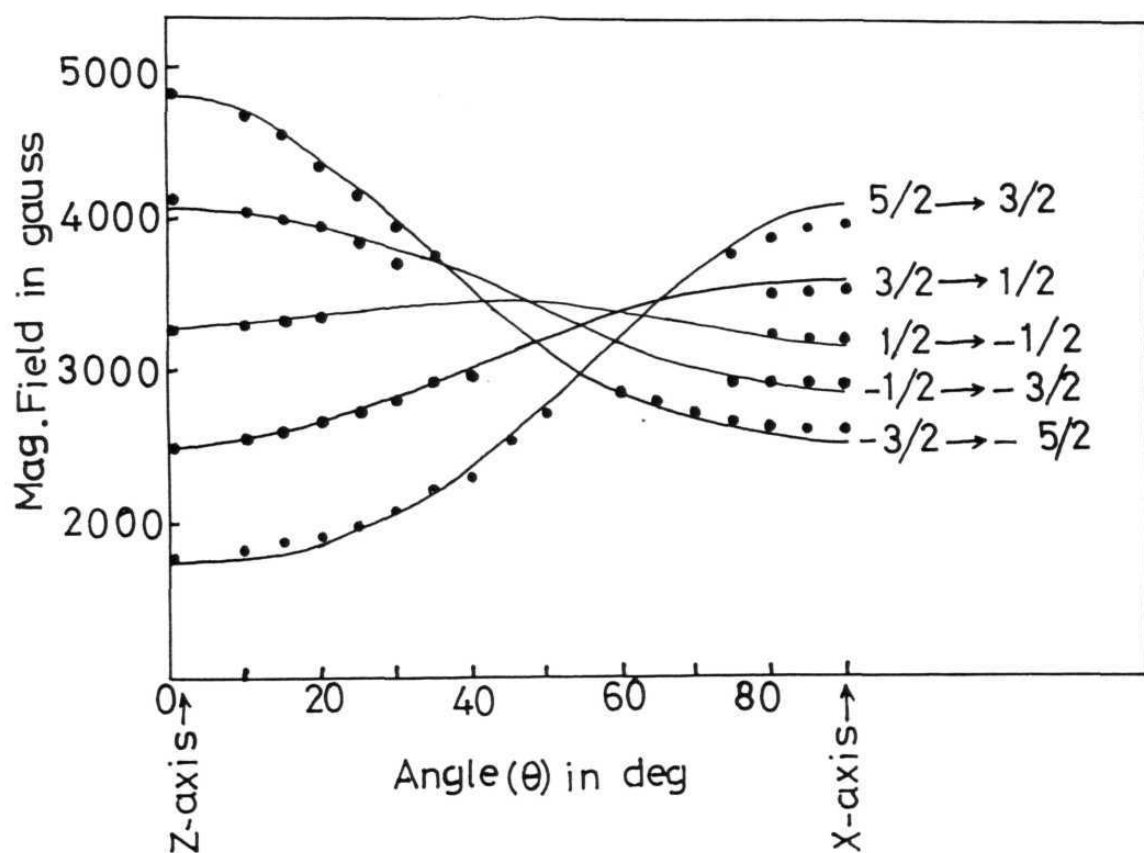
Fig.9.2 Room temperature ESR spectra of  $\text{Mn}^{2+}/\text{ZnMTH}$  in the  $X'Z$  plane at (a)  $\theta = 5^\circ$  and (b)  $\theta = 7^\circ$ ; longer vertical lines correspond to  $\Delta m = 0$  transitions and small vertical lines corresponding to  $\Delta m = \pm 1$  transitions.

relative intensities are proportional to  $(J+M)(J-M+1)$ . These therefore occur in the ratios 5:8:9:8:5 as observed.

The angular variation of the fine structure transitions corresponding to  $M \rightarrow M_{\pm 1}$ , depends on the term  $(3\cos^2\theta - 1)$ , when the higher order terms are neglected [13]. The field for all the sextets will be same at the magic angle. However, if the higher order terms are also included, all the five curves corresponding to the five sextets may not meet at the same point. Figure 9.3 shows the angular variations of these transitions in the  $X'Z$  plane. The theoretical curves corresponding to each sextet is found to overlap closely with experimental points.

The line positions of the spectrum corresponding to  $H||Z$  are given by a set of five simultaneous equations in terms of spin Hamiltonian parameters, as discussed in section 6.2.5. The spin-Hamiltonian parameters  $D$ ,  $E$ , ' $a$ ' whose significances have been discussed earlier (Section 6.2.3, p.162) are obtained using a computer programme based on these equations (appendix IV). The value of  $A$  is then calculated from the line positions in each sextet and the error given viz.,  $\pm 1$  G corresponds to the  $A$  value obtained from the different sextets. Expression 6.14 provides a check on the value of  $A$  obtained. The calculated field position of the sextets,

Fig.9.3 Angular variation in X'Z plane of the allowed transitions in the ESR spectrum of  $\text{Mn}^{2+}/\text{ZnMTH}$  at RT. Full curves: theoretical; circles: experimental.





$H_1$ , and the experimental  $H$  values are given in Table 9.1. along with the  $D, E, 'a'$  and  $A$  values. An indirect check on the relative sign of  $D$  is as follows. If the separations of these sextets decreases on the high field side when the direction of the magnetic field is parallel to  $Z$ -axis,  $D/A$  will be positive. In all the systems so far studied  $A$  is negative [14]. In the present case the separation of the sextets increase towards the high field side and hence  $D/A$  is negative which implies  $D$  is positive if we take a negative sign for  $A$  for the present system as well. The sign and magnitude of  $D$  gives information regarding the microsymmetry of the metal ion. A positive  $D$  is associated with a tetragonal compression or trigonal elongation [15]. In the present case the positive  $D$  corresponds to tetragonal compression. Such a conclusion is in accordance with the known crystal structure of  $MnMTH$  if we assume that a similar symmetry is obtained when  $Mn^{2+}$  goes substitutionally into  $ZnMTH$ . A comparison of the unit cell dimensions of  $MnMTH$  and  $ZnMTH$  suggests that these two systems are likely to be closely similar if not isomorphous, facilitating the above described situation [10,11,16]. However a definite conclusion regarding whether the microsymmetry is governed purely by the guest ion or dictated both by the guest ion as well as the parent diamagnetic zinc lattice can be drawn only when

Table 9.1. Observed and calculated  $H_i$  values for  $H||Z$  axis in  $Mn^{2+}/ZnMTH$  along with D, E, a and A values.

	Cald.	Obs ( $\pm 3$ gauss)	D ( $\pm 1$ gauss)	E ( $\pm 1$ gauss)	a ( $\pm 1$ gauss)	A ( $\pm 1$ gauss)
$H_1$	1785	1780	385.6	71.5	-9.5	-93
$H_2$	2493	2495				
$H_3$	3290	3275				
$H_4$	4070	4075				
$H_5$	4815	4818				

a knowledge of a detailed crystal structure for the ZnMTH becomes available.

The  $g$  value (viz., 2.035) shows large anisotropy. Most of the  $Mn^{2+}$  systems reported in literature show  $g$  values close to free spin value of 2.0023. However deviation from this value has been observed in highly distorted systems such as  $Mn^{2+}$  doped tris ethylene diamine Zinc(II),  $Mn^{2+}$  doped lithium ammonium tartrate monohydrate [17,18]. Two mechanisms have been suggested for the enhancement of  $g$ -value. The spin-orbit coupling produces a slight breakdown of LS coupling introducing an admixture of the excited state  $^4P_{1/2}$  but the expected deviation in this case is small. A more dominant contribution comes due to covalent bonding excited states of symmetry  $^6T_{1g}$  whose single electron states will tend to be full or empty depending upon the nature of the metal-ligand bondings [19,20]. The  $D$  value of  $0.0358\text{ cm}^{-1}$  does indicate a significantly large distortion from cubic symmetry for  $Mn^{2+}/ZnMTH$  [15]. An estimate of the covalency in the present case may be obtained from the hyperfine splitting constant  $A$ . The relation between  $A$  and the local bonding of the  $Mn^{2+}$  and the nearest neighbour ligands has been derived phenomenologically on a more quantitative basis by plotting  $A$  versus the Pauling covalency parameter [21,22].

From this curve we obtain, for  $A = -93$  gauss, an ionicity of 96.5% for  $\text{Mn}^{2+}/\text{ZnMTH}$ . Similar values have been found for  $\text{Mn}^{2+}$  doped  $(\text{NH}_4)_2(\text{COO})_2\text{H}_2\text{O}$ [23],  $\text{K}_2(\text{COO})_2\cdot\text{H}_2\text{O}$ [24] and  $\text{Cd}(\text{COO})_2\cdot 3\text{H}_2\text{O}$ [9] single crystals.

Figure 9.2 shows the appearance of forbidden transitions when the crystal is rotated by  $5^\circ$  and  $7^\circ$  respectively, the intensities becoming larger with increasing rotation. The increase in intensity with angular variation is illustrated for the first sextet in Figure 9.4. Theoretically intensities for forbidden transitions vary as  $\sin 2\theta$  (eq. 6.19) and the observed spectral behaviour is in agreement with the expected trend. These forbidden transitions occur in pairs corresponding to  $\Delta m_I = \pm 1$  (see section 6.2.5). The relationship for the positions of the different forbidden transitions and the hyperfine parameters are presented in section 6.2.5 and the computer programmes based on these expressions are given in appendices Va and Vb. Using these programmes the line positions for the forbidden transitions have been analysed. For all the sextets the doublet separations have been calculated and are given in Table 9.2 along with the experimental doublet separations. A good fit is obtained for  $Q' = 1.69$  and  $Q'' = 0.304$ , which are the axial and rhombic components of the quadrupole coupling constant of the  $^{55}\text{Mn}$  nucleus

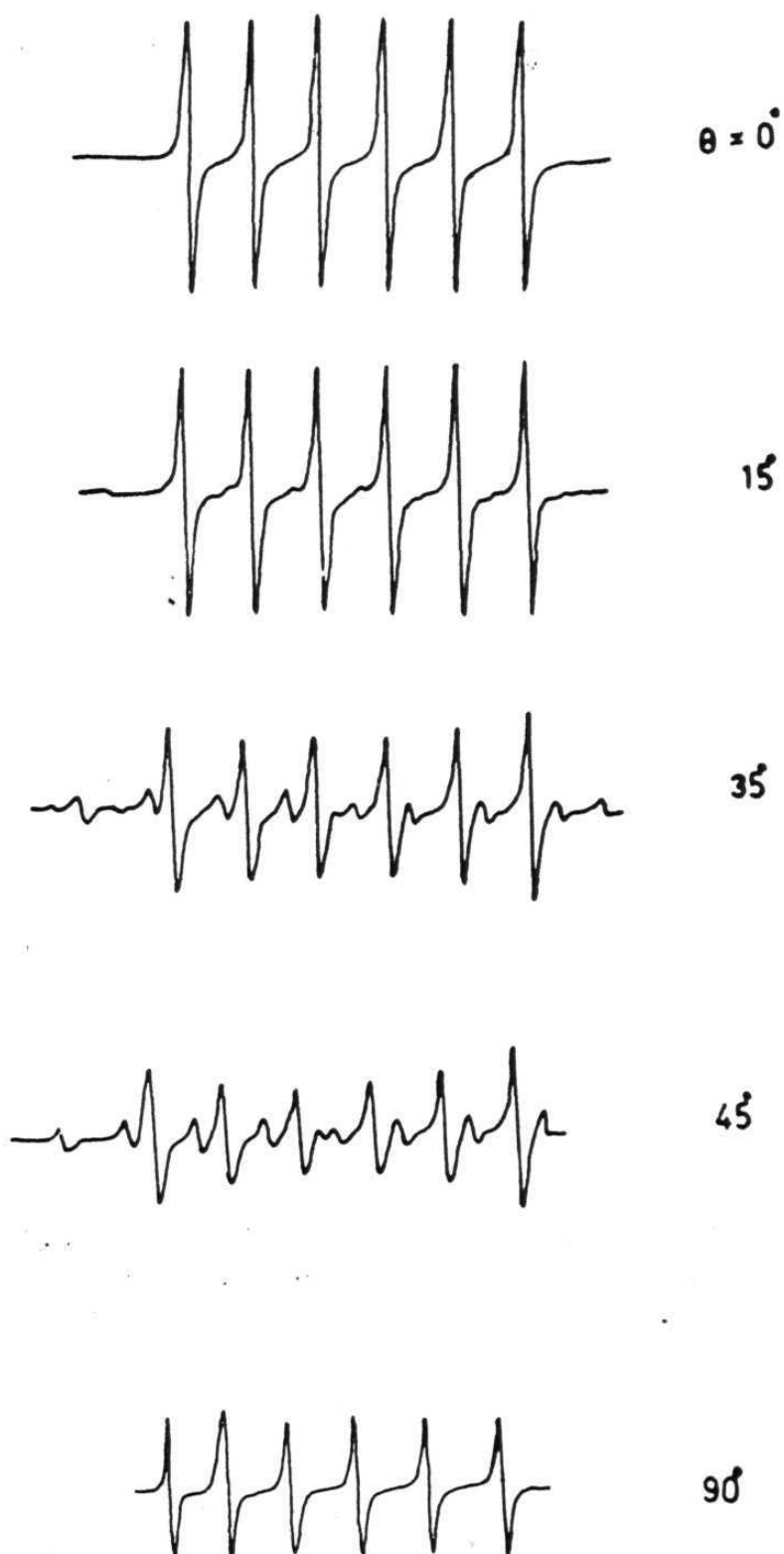


Fig.9.4 Angular variation of ESR spectra of  $\text{Mn}^{2+}/\text{ZnMTH}$  in X'Z plane. The first sextet is given to illustrate the variation of intensities of forbidden transitions.

Table 9.2. Observed and calculated doublet separations  $\Delta H$  (in G) of the forbidden hyperfine transitions ( $\Delta m = \pm 1$ ) for various transitions ( $\Delta M = \pm 1$ ) in the X'Z-plane ( $\phi = 0^\circ$ ,  $\theta = \text{Variable}$ ) of the complex  $\text{Mn}^{2+}$ /zinc maleate tetrahydrate single crystals at 298 K.

m	Doublet separation ( H)									
	$M = \frac{1}{2} \rightarrow -\frac{1}{2}$		$M = \frac{3}{2} \rightarrow \frac{1}{2}$		$M = -\frac{1}{2} \rightarrow -\frac{3}{2}$		$M = -\frac{5}{2} \rightarrow \frac{3}{2}$		$M = -\frac{3}{2} \rightarrow -\frac{5}{2}$	
	$m = \pm 1$		$m = \pm 1$		$m = \pm 1$		$m = \pm 1$		$m = \pm 1$	
	$\theta = 5^\circ$		$\theta = 10^\circ$		$\theta = 5^\circ$		$\theta = 15^\circ$		$\theta = 25^\circ$	
	obs	cal	obs	cal	obs	cal	obs	cal	obs	cal
- 5/2	23.8	24.7	201.6	202.8	149.2	152.5	369.2	377.0	330.1	339.4
- 3/2	24.5	25.0	205.8	207.1	155.8	158.5	372.3	383.2	341.3	350.2
- 1/2	24.9	25.3	210.8	211.5	163.1	164.8	379.2	389.7	350.9	362.4
+ 1/2	25.0	25.5	215.8	216.0	168.3	171.2	388.3	396.4	362.3	374.4
+ 3/2	25.1	25.8	217.5	220.8	174.2	177.7	395.5	403.5	377.0	386.7

respectively. The relatively large deviation between the observed and calculated doublet separations in  $M = +5/2 \rightarrow +3/2$  and  $M = -5/2 \rightarrow -3/2$  sextets may be attributed to the large angle ( $\theta = 15$  and  $25$ ) at which the comparison is made. The perturbation theory gives quantitatively unsatisfactory results at large angles and a considerable deviation of the direction of the nuclear magnetic moment from that of H has to be taken into account [25]. For these sextets the forbidden transitions were observable only at large angles i.e., away from the principal axis and hence a comparison at smaller angles was not possible.

#### 9.4. Conclusions.

$Mn^{2+}$  when doped in zinc maleate tetrahydrate is found to occupy a compressed octahedral site, substitutionally replacing the  $Zn^{2+}$  ion. The spin-Hamiltonian parameters have been determined to be  $D = 385.6$ ,  $E = 71.5$ ,  $a = -9.5$  and  $A = -93$  gauss, where  $D, E, a$  and  $A$  are the axial component of zero field splitting, the rhombic component of zero field splitting, the cubic field term and the hyperfine coupling constant respectively. The unusually large anisotropy in the  $g$  value viz., 2.035 has been ascribed to a highly distorted cubic environment. An ionicity of 96.5% is deduced for the

metal-ligand bonding from a plot of A vs the Pauling's covalency parameter [22]. The analysis of forbidden ESR transitions which give good agreement between calculated and observed  $\Delta H$ , the splitting of the lines leading to  $Q = 1.69$  and  $Q'' = 0.304$  which are the axial and rhombic components of the quadrupole coupling constants of the  $^{55}\text{Mn}$  nucleus respectively.



References:

1. G.R. Wagner, Schumacher and S.A. Friedberg, Phys. Rev. 150, 226 (1966).
2. H. Morigoki and H. Abe, J. Phys. Soc. Jpn. 23, 462 (1967).
3. R. Janakiraman and G.C. Upreti, J. Phys. Chem. Solids 31, 1419 (1970).
4. V. Chandra Mouli and G. Sivarama Sastry, Pramana 12, 165 (1979).
5. V.K. Jain, Phys. Status Solidi B97, 337 (1980).
6. R. Debuyst, F. Dejehet, C. Gorller-Walrand and L.G. Vanguickenborne, Inorg. Chimica Acta. 51, 117 (1981).
7. G.C. Upreti, J. Mag. Resonance 13, 336 (1974).
8. T. Takeda, J. Phys. Soc. Jpn. 23, 1314 (1967).
9. M. Korkmaz, M. Dupont and B. Atkas, J. Phys. Chem. Solids 45, 465 (1984).
10. A.S. Antsyshkina, M.A. Porai-Koshits and M.G. Guseinov, Izv. Akad. Nauk. SSSR, Ser Khim 237 (1974).
11. K. Saroja and S.V. Raman, Current Science 41, 599 (1972).
12. A. Abragam and B. Bleaney, 'Electron Paramagnetic Resonance of Transition Ions' (Clarendon Press, Oxford, (1970) p.158.

13. Ref 12, p.437.
14. Ref 12, p.439.
15. J.C. Hempel, J. Chem. Phys. 64, 4307 (1976).
16. M.P. Gupta and B. Mahanta, Cryst. Struct. Common. 7, 179 (1978).
17. R.A. Palmer, M. Chin-Lam Yang and J.C. Hempel, Inorg. Chem. 17, 1200 (1978).
18. A.K. Jain and G.C. Upreti, J. Chem. Phys. 75, 1623 (1981).
19. Fidone and K.W.H. Stevens, Proc. Phys. Soc. 73, 116 (1959).
20. Watanabe, J. Phys. Chem. Solids 25, 1471 (1964).
21. O. Matumura, J. Phys. Soc. Jpn. 14, 108 (1959).
22. E. Simaneck and K.A. Muller, J. Phys. Chem. Solids 31, 1027 (1970).
23. S. Radhakrishna and B.V.R. Chowdari, Crystal lattice Defects 8, 1 (1978).
24. M. Kormaz, Rev. Fac. Sci. Univ. Istanbul, Ser C44, 147 (1979).
25. D.H. Lyons and R.W. Kedzie, Phys. Rev. 145, 148 (1966).

APPENDIX I

Computer programme for simulation of relaxation spectra employing Eq.2.23:

The following computer programme is written in HI-BASIC to evaluate the Mössbauer spectrum based on the relaxation model due to Blume and Tjon discussed in Chapter 2. To evaluate the expression

$$F(\omega) = \sum_{i=1}^6 \frac{(\frac{\Gamma}{2} + 2\lambda) [\frac{\Gamma^2}{4} + \lambda\Gamma - (\alpha - \omega)^2 + \beta^2] + (\alpha - \omega)^2(\Gamma + 2\lambda)}{(\frac{\Gamma^2}{4} + \Gamma\lambda - (\alpha - \omega)^2 + \beta^2)^2 + (\alpha - \omega)^2(2\lambda + \Gamma)^2} \dots (2.23)$$

$\lambda$  and  $\Gamma$  (mm/sec) are given as input parameters. In addition 'HZERO' and 'HONE' which define line positions are also given as input parameters. The output 'SUM' plotted against  $\omega$  (JA) gives the required spectrum. The representative spectra simulated using the above equation are reproduced in Figure 2.5 for different values of  $\lambda$ .

LPRINTER WIDTH 130

REM THIS PROGRAMME CALCULATES THE LINE PROFILES USING  
 REM L. DATTA GUPTA'S EXPRESSION FOR VALUES OF  $\lambda$ , THE  
 REM RELAXATION RATE 'NLW' IS LINE WIDTH, 'QUAD' IS QUADRUPOLE  
 REM SPLITTING, 'GNOT' AND 'GONE' ARE THE 'g' VALUES FOR  
 REM GROUND AND EXCITED STATE OF  $^{57}\text{Fe}$  NUCLEUS. HZERO AND HONE  
 REM ARE THE INPUT PARAMETERS. 'CGRC' IS CLEBSH - GORDON  
 REM COEFFICIENT.

DIM BETA(8), MEX(4), MGR(2), ALP(8), CGRC(8), W(300)

PP = 10.657/160

PPA = (256\*PP)/2

PP1 = (20\*PP)-PPA

PP2 = (40\*PP)-PPA

PP3 = (60\*PP)-PPA

PP4 = (80\*PP)-PPA

PP5 = (100\*PP)-PPA

PRINT TAB(10); PP; TAB(25); PP1; TAB(40); PP2; TAB(55); PP3;  
 TAB(70); PP4; TAB(85); PP5.

PAP = 0.1\*PP

INPUT 'HZERO ='; HZERO

INPUT 'HONE ='; HONE

INPUT 'NLW ='; NLW

```

GNOT = 0.181208
GONE = -0.1036
INPUT 'LAMDA = '; LAMDA
INPUT 'QUAD = '; QUAD
FOR I = 1 TO 4
  INPUT 'MEX(I) = '; MEX(I)
NEXT I
FOR JP = 1 TO 8
  INPUT 'CGRC(JP)= '; CGRC(JP)
NEXT JP
INPUT AMGR1, AMGR2
FOR IA = 1 TO 4
  BETA(IA) = ((AMGR1*HZERO) - (MEX(IA)*HONE))
NEXT IA
FOR IB = 1 TO 4
  BETA(9-IB) = -BETA(IB)
NEXT IB
FOR IC = 1 TO 8
  PRINT 'BETA(IC) = ', BETA(IC)
NEXT IC
FOR IA = 1 TO 4
  ALP(IA) = QUAD*(3*MEX(IA)*MEX(IA) - 3.75)
  PRINT 'ALP(IA) = ', ALP(IA)
NEXT IA

```

```

FOR ID = 1 TO 4
ALP(ID+4) = ALP(ID)
NEXT ID

INCRM = PP

INPUT 'W(1) = '; W(1)

PRINT TAB(15); 'SUM'; TAB(35); 'W'; TAB(70); 'CHA'

FOR JA = 1 TO 300

SUM = 0.0

FOR JB = 1 TO 8

ALPS = ALP(JB)*ALP(JB)
BETAS = BETA(JB)*BETA(JB)
AA = (NLW*0.5) + (2*LAMDA)
ALPOME = (ALP(JB) -W(JA))*(ALP(JB)-W(JA))
BB = (NLW*NLW*0.25) + (NLW*LAMDA)-ALPOME +BETAS
BBB = BB * BB
CC = NLW+(2*LAMDA)
CCS = CC*CC
DD = ALPOME*CC
ANUME = (AA*BB)+DD
ADENQM = BBB+(ALPOME*CCS)
EQAV = (ANUME)/(ADENQM)
MASTEQ = EQAV*CGRC(JB)
SUM = SUM+MASTEQ
NEXT JB

```

```
CHA = W(JA)/PP  
PRINT TAB(10); SUM; TAB(25); W(JA); TAB(10); CHA  
W(JA + 1) = W(JA) + INCRM  
NEXT JA  
STOP  
END
```

APPENDIX II

Computer programme for the simulation of relaxation spectra  
employing Eq. 2.26:

The following computer programme is written in FORTRAN IV to evaluate the Mössbauer spectrum based on the relaxation model due to van der Woude and Dekker discussed in Chapter 2. To evaluate the expression

$$I(\omega) = \sum_{i=1}^6 \frac{\frac{2f_L s}{(1-\eta)} \delta_i^2 (\eta^2 - 1) - \sqrt{\left[ \delta_i^2 + \omega^2 + \frac{\Omega_s}{(1-\eta)^2} - 2\omega\delta_i\eta \right]}}{(\delta_i^2 - \omega^2)^2 + \frac{4f_L s}{(1-\eta)^2} (\omega + \eta\delta_i)^2 + \frac{4f_L s}{(1-\eta)^2} \sqrt{(\omega^2 + \delta_i^2 + 2\omega\delta_i\eta)}} \dots (2.26)$$

$\Omega$ ,  $\delta_i$  and  $\eta$  are given as input parameters. The output 'ANINTE' plotted against 'CHA(J)' gives the required spectrum. The representative spectra simulated using the above equation are reproduced in Figure 2.6.



```
C   THIS IS A MODIFIED EXP. OF VANDER WOUDE INCLUDING NATURAL
C   LINE WIDTH. NLW SHOULD BE IN UNITS OF DELTA. 'DELTA' IS LINE
C   POSITION. 'N' IS NO. OF LORENTZIAN.
C   PCVEL IS PER CHANNEL VELOCITY
      DIMENSION WATT(8),DELTA(8),OMEGA(8),SOME(256),AKONST(8),
      CHA(250)
      READ 9,NSET
9    FORMAT(13)
      DO 16 IB=1,NSET
      N=6
      ANLW=0.064
      ETA=0.4
      PRINT 20,N,ANLW,NSET
20   FORMAT(10X,'N=',13,5X,'ANLW=',F6.4,'NSET=',13)
      YSCAL=5.0
      YSCAL1=6.0
      YSCAL2=7.0
      WAIT(1)=3.0
      WAIT(2)=3.0
      WAIT(3)=1.0
      WAIT(4)=1.0
      WAIT(5)=3.0
```

```

WAIT(6)=3.0
DELTA(1)= -1.00
DELTA(2)= -0.58
DELTA(3)= -0.16
DELTA(4)= 0.16
DELTA(5)= 0.58
DELTA(6)= 1.00
READ 21,(OMEGA(I),I=1,N)
21 FORMAT(F5.3)
PRINT 25, (DELTA(I),OMEGA(I),WAIT(I),I=1,N)
25 FORMAT(3F6.3)
PCVEL =0.0166666
AAB=(130*PCVEL)/2
AAC=45*PCVEL
AAD= -(AAB+AAC)
PRINT 30, AAD
30 FORMAT(10X,'AAD=',F10.6)
PRINT 26,PCVEL
26 FORMAT('PCVEL=',F10.7)
PRINT 40,ETA,YSCAL
40 FORMAT(5X,'ETA=',F10.2,5X,'YSCAL=',F10.2)
DO 45 IA=1,N
PRINT 41,OMEGA(IA)
41 FORMAT('OMEGA(IA)=',F10.6)

```

```

45  CONTINUE
    ETASQ=ETA*ETA
    AA=(ETASQ-1)
    AB=(1-ETA)
    AC=AB*AB
    SOME(1)=(-1.333332)
    DO 55 J=1.200
    AINTE=0.0
    DO 60 I=1,N
    DEL=DELTA(I)*DELTA(I)
    ETADE=ETA*DELTA(I)
    AD=(4*OMEGA(1)*OMEGA(I))/AC
    SOMESQ=SOME(J)*SOME(J)
    ETSOD=2*SOME(J)*DELTA(I)*ETA
    ANUM=(AA*DEL*2*OMEGA(I))/AB
    BNUM=(DEL+SOMESQ+AD-ETSOD)
    CNUM=ANLW*BNUM
    ANUMER=(ANUM-CNUM)
    ADENOM=(DEL-SOMESQ)*(DEL-SOMESQ)
    BDENOM=(SOME(J)+ETADE)*(SOME(J)+ETADE)
    CDENOM=AD*BDENOM
    DDENOM=(SOMESQ+DEL+ETSOD)
    EDENOM=(DDENOM*4*OMEGA(I)*ANLW)/AB
    DENOM=(ADENOM+CDENOM+EDENOM)

```

```
SIME=(ANUMER/DENOM)*WAIT(I)
AINTI=AINTI+SIME
60  CONTINUE
ANEWY=AINTI/YSCAL
BNEWY=AINTI/YSCAL1
CNEWY=AINTI/YSCAL2
CHA(J)=SOME(J)/PCVEL
PRINT 65,SOME(J),CHA(J),AINTI,ANEWY,BNEWY,CNEWY
65  FORMAT(5X,2F12.6,10X,2F10.6,10X,2F10.6)
SOME(J+1)=SOME(J)+0.0166666
55  CONTINUE
16  CONTINUE
STOP
END
```

APPENDIX III

Computer programme for the least square fit of angular variation data of  $\text{Cu}^{2+}$  ESR spectra:

$$g^2(\theta) = U + V \cos 2\theta + W \sin 2\theta \quad \dots (6.7)$$

The experimental  $g^2(\theta)$  and  $g^2A^2(\theta)$  values for the three laboratory crystal planes were fitted to the above equation. Experimental values of  $g^2$ ,  $g^2A^2$  and  $\theta$  are given as input parameters and the values of U, V and W are evaluated by setting up the appropriate minimisation conditions viz.,

$$\Sigma (g^2(\text{cal}) - g^2(\text{obs}))^2 = \text{minimum}$$

$$\text{and } \Sigma ((g^2A^2)(\text{cal}) - (g^2A^2)(\text{obs}))^2 = \text{minimum}$$

are satisfied.

```

LPRINTER WIDTH 130
REM CALCULATION OF U,V,W IN THE EQ.  $Y = U + V \cos 2X + W \sin X$ 
REM BY THE METHOD OF LEAST SQUARES
DIM Y(100), X(100), C(100), S(100), YCAL(100), TIT(5)
INPUT 'NAME='; NAME
100 INPUT 'N='; N
INPUT 'YFILNAME='; A $
INPUT 'K,L='; K,L
PRINT TAB(10); NAME; TAB(20); N; TAB(35); K; TAB(60); L
IF N=0 THEN 1200
IF END ## 1 THEN 25
IF END ## 2 THEN 26
OPEN 'X.FIL' AS 1
OPEN A $ AS 2
PRINT TAB(40); 'X(I)'; TAB(80); 'Y(I)'
FOR I = 1 TO N
  READ ## 1; X(I)
  READ ## 2; Y(I)
  PRINT TAB(40); X(I); TAB(80); Y(I)
NEXT I
25 CLOSE 1
26 CLOSE 2

```

```

SUMY = 0.0
SUMX = 0.0
SUMCC = 0.0
SUMS = 0.0; SUMSS = 0.0; SUMCS = 0.0
SUMYC = 0.0; SUMYS = 0.0
FOR I = 1 TO N
  C(I) = COS(X(I)*3.1416/90)
  S(I) = SIN(X(I)*3.1416/90)
  CC = C(I)*C(I); SS = S(I)*S(I)
  CS = C(I)*S(I); YC = Y(I)*C(I)
  YS = Y(I)*S(I)
  SUMY = SUMY+Y(I)
  SUMC = SUMC+C(I)
  SUMCC = SUMCC + CC
  SUMS = SUMS + S(I)
  SUMSS = SUMSS + SS; SUMCS = SUMCS + CS
  SUMYC = SUMYC + YC; SUMYS = SUMYS + YS
NEXT I
E = SUMC*SUMC -N*SUMCC
G = SUMS*SUMS -N*SUMSS
H = SUMC*SUMY -N*SUMYC
T = SUMS*SUMY -N*SUMYS
F = SUMC*SUMS -N*SUMCS
D = F*F -E*G

```

```

W = (H*F-T*E)/D
V = (T*F-H*G)/D
U = (SUMY-(SUMC*V+SUMS*W))/N
PRINT TAB(10); 'W='; W; TAB(40); 'V='; V; TAB(70); 'U='; U
TRUDY = W/V
TANIA = ATN(TRUDY)
THETA1 = TANIA/2
THETA2 = (TANIA/2.0)+1.5/08
YTETA1 = U+V*COS(2.*THETA1)+W*SIN(2.*THETA1)
YTETA2 = U+V*COS(2.*THETA2)+W*SIN(2.*THETA2)
TD1 = THETA1*180.0/3.1416
TD2 = THETA2*180.0/3.1416
YEX1 = (YTETA1) 0.5
YEX2 = (YTETA2) 0.5
PRINT TAB(10); 'TD1='; TD1
PRINT TAB(10); 'TD2='; TD2 ; TAB(30); 'YEX1='; YEX1; TAB(55);
      'YEX2='; YEX2
PRINT TAB(10); 'X(I)'; TAB(30); 'Y(I); TAB(50):, 'YCAL(I)'
FOR I = 1 TO N
YCAL(I) = U+V*C(I)+W*S(I)
PRINT TAB(10); X(I); TAB(30); Y(I); TAB(50); YCAL(I)
NEXT I
IF N = 19 THEN 100
PRINT TAB(10); 'J'; TAB(30); 'X(J)'; TAB(50); 'YCAL(J)'

```



```
FOR J = N TO K
  IF K = N THEN 1150
  YCAL(J) = U+V*COS(X(J)*3.1416/90)+W*SIN(X(J)*3.1416/90
  PRINT TAB(10); J; TAB(30); X(J); TAB(50); YCAL(J)
  1100 X(J+1) = X(J)+L
NEXT J
1150 GO TO 100
1200 STOP
END
```

APPENDIX IVEvaluation of spin-Hamiltonian parameters D, E, a and A  
using Eqs. 6.13 and 6.14:

A computer programme is written in HI-BASIC to evaluate the spin-Hamiltonian parameters viz., D, E, a and A based on the simultaneous equations 6.13 and 6.14. Experimental positions of the five sextets ( $H_i$ ) and the trial D value are given as input parameters. The calculation is carried out self-consistently till a good match between  $H_i(\text{cal})$  and  $H_i(\text{obs})$  is obtained.

LPRINTER WIDTH 130

REM THIS PROGRAMME CALCULATES, 'A', 'E', 'D' AND H(ZERO) USING

REM P.VENKATESHWARLU'S EXPRESSIONS KON1 IS '(H1+H5) --(H2-H4)'

REM KON2 IS '[(H1-H5)\*5] + [(H2-H4)\*4]'

INPUT 'D = '; D

INPUT 'KON2 = '; KON2

INPUT 'KON1 = '; KON1

INPUT 'H1 = '; H1

INPUT 'H2 = '; H2

INPUT 'H4 = '; H4

INPUT 'H5 = '; H5

$100 \times 1 = 9/(H1+D)$

$X2 = 5/(H1+(3*D))$

$X3 = 9/(H5-D)$

$X4 = 5/(H5-(/*D))$

$X5 = 9/(H2+D)$

$X6 = 9/(H2-D)$

$X7 = 5/(H2+(3*D))$

$X8 = 9/(H4+D)$

$X9 = 9/(H4-D)$

$X10 = 5/(H4-(3*D))$

$XX = (X1 - X2 + X3 - X4 + X5 - X6 + X7 - X8 + X9 + X10)$

```

PRINT 'XY = '; XX
EE = KON1/XX
EEE = (EE) (0.5)
PRINT 'EEE = '; EEE
Y1 = 45/(H1+D)
Y2 = 25/(H1+(3*D))
Y3 = 45/(H5 -D)
Y4 = 25/(H5-(3*D))
Y5 = 36/(H2+D)
Y6 = 36/(H2-D)
Y7 = 20/(H2+(3*D))
Y8 = 36/(H4+D)
Y9 = 36/(H4-D)
Y10 = 20/(H4-(3*D))
YY = (Y1-Y2-Y3+Y4-Y5+Y6-Y7-Y8+Y9+Y10)
YYY = YY*EEE*EEE
PRINT 'YYY = '; YYY
SUM = YYY-(56*D)
PRINT 'SUM = '; SUM
PRINT
PRINT 'D = '; D
DIF = (SUM-KON2)
IF(ABS(DIF)<= 1) THEN 10
IF((DIF)<0.01) THEN 20

```

```

IF((DIF)>0.01) THEN 30
20 D = D-0.01
GO TO 100
30 D = D+0.01
GO TO 100
10 PRINT TAB(10); 'D'; TAB(40); 'EEE'; TAB(60); 'KON1';
    TAB (80); 'KON2'; TAB(100); 'SUM
PRINT
PRINT TAB(10); D; TAB(40); EEE; TAB(60); KON1; TAB(80);
    KON2; TAB(100); SUM
TWOHO = H1+H5-(9*EE)/(H1+D)+(5*EE)/(H1+(3*D))-(9*EE)/(H5-D)
    +(5*EE)/(H5-(3*D))
HO = TWOHO/2
PRINT
PRINT TAB(10); 'HO = '; HO
TWOAA = HO-4*D+(9*EE)/(H1+D) - (5*EE)/(H1+(3*D))-H1
AA = TWOAA/2
PRINT
PRINT TAB(10); 'AA ='; AA
H1CAL = HO-4*D+(9*EE)/(H1+D)-(5*EE)/(H1+(3*D))
H5CAL = HO+4*D+(9*EE)/(H5-D)-(5*EE)/(H5-(3*D))+2*AA
H2CAL = HO-2*D-(9*EE)/(H2+D)+(9*EE)/(H2-D)-(5*EE)/(H2+(3*D))
    +2.5*AA

```

```
H4CAL = H0+2*D+(9*EE/(H4+D))-(9*EE/(H4-D))-(5*EE/(H4-(3*D)))
      -2.5*A/L
```

```
PRINT TAB(10); 'H1 ='; H1; TAB(50); 'H1CAL ='; H1CAL
PRINT TAB(10); 'H2='; H2; TAB(50); 'H2CAL='; H2CAL
PRINT TAB(10); 'H4='; H4; TAB(50); 'H4CAL='; H4CAL
PRINT TAB(10); 'H5='; H5; TAB(50); 'H5CAL='; H5CAL
STOP
END
```

APPENDIX V(a) Evaluation of  $Q'$  and  $Q''$ 

A computer programme is written in HI-BASIC to evaluate  $Q'$  and  $Q''$  based on the equation

$$\begin{aligned}
 M &= +1/2 \longrightarrow -1/2 \\
 \Delta m &= \pm 1 \text{ transition} \\
 H &= H |1/2, m+1\rangle \longrightarrow |-1/2, m\rangle - H |1/2, m\rangle \longrightarrow |-1/2, m+1\rangle \\
 &= (17 A^2/2 H_0) + (2 \gamma \beta_N H_0 / g \beta) - (2m+1) [2P - (\delta A^2 \sigma / H_0^2) + \\
 &\quad (25A^3/2H_0^2) + (\gamma \beta_N A / g \beta)] \quad \dots (6.18)
 \end{aligned}$$

Two sets of experimental  $\Delta H(\text{obs})$  values corresponding to two different  $\theta$  values are given as input parameters to evaluate two  $P$  values, where  $P$  is a function of  $\theta$  of the form

$$P = \frac{1}{2} [Q'(3\cos^2\theta - 1) + 3Q'' \sin^2\theta \cos^2\phi].$$

Using the values of  $P(\theta)$  two simultaneous equations are set up and solved for  $Q'$  and  $Q''$ . The programme used is reproduced here.

```

LPRINTER WIDTH 130

REM THIS PROGRAMME IS TO CALCULATE Q' AND Q'' USING THIRD
REM SEXTET AT TWO DIFFERENT ANGLES. SM(I) IS SMALL M. (DH(I)
REM IS DELTA H(OBSERVED)).
DIM DH(10), DHCAL(10), SM(10)
INPUT 'A='; A
INPUT 'HZERO='; HZERO
GBNGB = 0.00037
INPUT 'SIG='; SIG
FOR I = 1 TO 5
INPUT 'DH(I)='; DH(I)
NEXT I
INPUT 'P='; P
PRINT
PRINT TAB(10); 'A'; TAB(20); 'HZERO'; TAB(30); 'GBNGB';
      TAB(50); 'SIG'; TAB(60); 'P'
PRINT
PRINT TAB(10); A; TAB(20); HZERO; TAB(30); GBNGB; TAB(50); SIG;
      TAB(60); P
FOR I = 1 TO 5
PRINT 'DH(I)='; DH(I)
NEXT I

```



```

HZEROS=HZERO*HZERO
100 SM(1)= -2.5
SUM = 0.0
FOR I = 1 TO 5
  BB = (17*A*A)/(2*HZERO)
  CC = (2*GBNGB*HZERO)
  DD = (8*A*A*SIG)/HZEROS
  EE = (A*A*A*12.5)/HZEROS
  FF = (GBNGB*A)
  GG = ((2*P)-DD+EE+FF)
  MM = (2*SM(I))+1
  NN = (MM*GG)
  DHCAL(I) = (BB+CC-NN)
  DIFF = DH(I)-DHCAL(I)
  DIFFS = DIFF*DIFF
  SUM = SUM+DIFFS
  SM(I+1) = SM(I)+1.0
NEXT I
PRINT 'SUM='; SUM
PRINT
PRINT TAB(10); 'A='; TAB(20); 'P='; P
IF SUM < = 20.0 THEN GO TO 200 ELSE
  GO TO 300
200 FOR I = 1 TO 5

```

```
PRINT TAB(10); DH(I); TAB(30); DHCAL(I); TAB(50); SM(I);  
      TAB(70); SUM; TAB(90); A  
NEXT I  
GO TO 500  
300 P = P+0.01  
GO TO 100  
500 STOP  
END.
```

APPENDIX V

(b) Evaluation of  $\Delta H_{cal}$  for the transitions

$$\underline{|M, m_I\rangle \longrightarrow |M \pm 1, m_I\rangle:}$$

A computer programme is written in HI-BASIC language to calculate the  $\Delta H$  values for the analysis of forbidden transitions in pairs based on the equations 6.18. The  $Q'$  and  $Q''$  values obtained in the previous output (Appendix Va) along with the  $D$ ,  $E$ ,  $a$  and  $A$  spin-Hamiltonian parameters obtained from Appendix IV are given as input parameters for these equations to calculate  $\Delta H$ , and compare with the experimental values.

```

REM THIS PROGRAMME CALCULATES THE DISTANCE BETWEEN TWO
REM FORBIDDEN TRANSITIONS. REF. UPRETI, J. MAG. RES. 13,
REM 339 (1974). 'A' IS HYPERFINE COUPLING CONSTANT AND 'Q'
REM IS Q-PRIME AND 'QQ' IS Q-DOUBLE PRIME 'SM' IS SMALL M.
REM 'ABC' IS  $\text{GAMMA} * \text{BETA}(N) / G * \text{BETA}$ . 'DH' IS DELTA H FOR
REM  $\pm 1$  FORBIDDEN TRANSITIONS. 'D', 'HZERO' AND 'E' VALUES
REM ARE CALCULATED FROM PUTCHA'S EXPRESSIONS. 'THES' AND
REM 'PHYS' ARE ANGLES IN DEGREES. 'LAM' IS LAMDA
DIM SM(10), DH(10), DHH(10)
ABC = 0.00037
20 INPUT 'A='; A
INPUT 'D='; D
INPUT 'E='; E
INPUT 'THES='; THES
INPUT 'PHYS='; PHYS
55 INPUT 'HZERO='; HZERO
INPUT 'Q='; Q
INPUT 'QQ='; QQ
320 PRINT TAB(10); 'D'; TAB(20); 'E'; TAB(30); 'THES'; TAB(40)
      'PHYS'; TAB(50); 'A'; TAB(60); 'Q'; TAB(70); 'QQ'
PRINT TAB(10); D; TAB(20); E; TAB(30); THES; TAB(40); PHYS;
      TAB(50); A; TAB(60); Q; TAB(70); QQ

```

```

THE =(THES*22)/(180*7)
PHY = (PHYS*22)/(180*7)
PRINT TAB(10); 'THE='; THE ; TAB(30); 'PHY.='; PHY
AA = COS( THE )
BB = (3*AA*AA)-1
CC = SIN( THE )
DD = CC*CC
TPHY = (2*PHY)
EE = COS( PHY )
FF = SIN( PHY )
P = 0.5*((Q*BB)+(3*QQ*DD*EE))
LAM = CC*((D-(E*EE))*AA)
ROW = 0.25*((D*DD)+(E*((AA*AA*EE) - (FF*FF))))
SIG = 0.5*((D*BB)+(3*E*DD*EE))
PRINT TAB(10); 'P'; TAB(40); 'LAM'; TAB(70); 'ROW'; TAB(110);
      'SIG'
PRINT TAB(10); P; TAB(40); LAM; TAB(70); ROW; TAB(110); SIG.
PRINT 'M=+1/2 TO -1/2 SEXTET, DELTA-M = ±1 TRANSITIONS'
AAA = (17*A*A)/HZERO
HZEROS = HZERO*HZERO
BBB = (2*ABC*HZERO)
CCC = (8*A*A*SIG)/HZEROS
DDD = (12.5*A*A*A)/HZEROS
EEE = A*ABC

```

```

PRINT TAB(15); 'SM(I)'; TAB(30); 'DH(I)'
SM(1) = -2.5
FOR I = 1 TO 5
DH(I) = (AAA/2)+BBB - ((2*SM(I))+1)*((2*P) -CCC+DDD+(ABC*A)
PRINT TAB(15); SM(I); TAB(30); DH(I)
IF SM(I) = 2.5 THEN GO TO 100
SM(I+1) = SM(I)+1.0
NEXT I
100 SM(I) = -1.5
PRINT TAB(10); 'SM(I)'; TAB(25); 'DHH(I)'
FOR I = 1 TO 4
DHH(I) = AAA*(2*BBB)-(2*SM(I))*((4*P)+(2*CCC)+(2*DDD)+(2*ABC*A))
PRINT TAB(10);SM(I); TAB(25); DHH(I)
IF SM(I) = 2.5 THEN GO TO 200
SM(I+1) = SM(I)+1.0
NEXT I
200 PRINT TAB(50); 'M= +3/2 TO +1/2 TRANSITIONS'
SM(1) = -2.5
PRINT TAB(30); 'SM(I)'; TAB(50); 'DH(I)'
FOR I = 1 TO 5
155 GGG = 2*P*((2*SM(I))+1)
KKK = ((ABS(LAM*LAM))*A*256)/(HZEROS*3)
LLL = ((ABS(ROW*ROW))*52*A)/HZEROS
MMM = ((A*A)/HZERO)*((2*SM(I))+8.5

```

```

NNN = ((A*A*SIG)/(HZEROS))*((14*SM(I))+9)
OOO = ((A*A*A)/(HZEROS))*((SM(I)*SM(I))+(19*SM(I)) -(51/4))
DH(I) = (-(2*A)+BBB-GGG-KKK+LLL+MMM+NNN-OOO)
PRINT TAB(20); SM(I); TAB(50); DH(I)
IF SM(I) = 2.5 THEN GO TO 300
SM(I+1) = SM(I)+1.0
NEXT I

300 PRINT TAB(40); 'M = -3/2 TO -1/2 TRANSITIONS'
SM(1) = -2.5
PRINT TAB(20); 'SM(I)'; TAB(50); 'DH(I)'
FOR I = 1 TO 5
GGG = 2*P*((2*SM(I))+1)
KKK = ((ABS(LAM*LAM))*A*256)/(HZEROS*3)
LLL = ((ABS(ROW*ROW))*52*A)/HZEROS
MMM = ((A*A)/HZERO)*((2*SM(I)) - 6.5)
NNN = ((A*A*SIG)/(HZEROS))*((14*SM(I))+5)
OOO = ((A*A*A)/(HZEROS))*((SM(I)*SM(I) -(17*SM(I)) - (123/4)))
DH(I) = (-(2*A) - BBB + GGG - KKK + LLL + MMM - NNN -OOO)
PRINT TAB(20); SM(I); TAB(50); DH(I)
IF SM(I) = 2.5 THEN GO TO 400
SM(I+1) = SM(I)+1.0
NEXT I

400 PRINT TAB(40); 'M = +5/2 TO +3/2 TRANSITIONS'
SM(1) = -2.5

```

```

PRINT TAB(30); 'SM(I)'; TAB(60); 'DH(I)'
FOR I = 1 TO 5
  PP = 2*ABC*HZERO
  QQQ = ((2*SM(I))+1)*(2*P)
  RR = (ABS(LAM*LAM)*A*40)/(HZEROS*3)
  SS = (ABS(ROW*ROW)*56*A)/HZEROS
  TT = ((4*SM(I))+6.5)*((A*A)/HZERO)
  UU = ((8*SM(I))+8)*((A*A*SIG)/HZEROS)
  VV = ((2*SM(I)*SM(I)) - SM(I) - 33)*((A*A*A)/HZEROS)
  DH(I) = ((-(4*A))+PP-QQQ-RR+SS+TT+UU-VV)
  PRINT TAB(30); SM(I); TAB(60); DH(I)
  IF SM(I) = 2.5 THEN GO TO 500
  SM(I+1) = SM(I)+1.0
NEXT I

500 PRINT TAB(40); 'M = -5/2 TO -3/2 TRANSITIONS
SM(1) = -2.5
PRINT TAB(30); 'SM(I)'; TAB(60); 'DH(I)'
FOR I = 1 TO 5
  WW = 2*ABC*HZERO
  XX = ((2*SM(I))+1)*(2*P)
  YY = (ABS(LAM*LAM)*A*40)/(HZEROS*3)
  ZZ = (ABS(ROW*ROW)*56*A)/HZEROS
  PPP = ((4*SM(I)) - 2.5)*((A*A)/HZERO)
  QQQ = (18*SM(I)*SIG*A*A)/HZEROS

```



```
RRR = ((2*SM(I)*SM(I))+(5*SM(I))-30)*((A*A*A)/HZEROS)
DH(I) = ((-(4*A)) - WW + XX - YY + ZZ + PPP - QQQ -RRR)
PRINT TAB(30); SM(I); TAB(60); DH(I)
IF SM(I) = 2.5 THEN GO TO 600
SM(I+1) = SM(I) + 1.0
NEXT I
STOP
END
```

VITAE

Born on 15th July 1957 at Adilabad, A.P., the author had his early education at Govt. High School, Adilabad, A.P. and then joined Govt. College, Adilabad from where he received his B.Sc., Degree (First class) from Osmania University in 1977. Later he studied at Kakatiya University and obtained his Master's Degree in Chemistry (First class) in 1979. He then joined University of Hyderabad and obtained M.Phil. Degree in Chemistry (First class) in 1980. Subsequently he continued for Ph.D. degree in 1980. He was a Junior Research Fellow (UGC) from August 1980 to September 1983 and a Senior Research Fellow (CSIR) from October 1983 to February 1985. At present he is working as Scientist in the Regional Research Laboratory, Hyderabad.